Order Number 9129679

Application of a novel multiple-scattering approach to photoelectron diffraction and Auger electron diffraction

Kaduwela, Ajith P., Ph.D.

University of Hawaii, 1991

U·M·I

300 N. Zeeb Rd.
Ann Arbor, MI 48106

APPLICATION OF A NOVEL MULTIPLE-SCATTERING APPROACH TO PHOTOELECTRON DIFFRACTION AND AUGER ELECTRON DIFFRACTION

A DISSERTATION SUBMITTED TO THE GRADUATE DIVISION OF THE UNIVERSITY OF HAWAII IN PARTIAL FULFILLMENT OF THE REQUIREMENTS FOR THE DEGREE OF

DOCTOR OF PHILOSOPHY

IN

CHEMISTRY

MAY 1991

By

Ajith P. Kaduwela

Dissertation Committee:

Charles S. Fadley, Chairperson
John D. Head
Che-Chen Chang
William L. Pong
James W. Holm-Kennedy

DEDICATION

I dedicate this dissertation to my mother Mrs. G. N. Kaduwela and my father Mr. P. K. Kaduwela for their love and guidance; to my wife Arunika for her love and endurance.

ACKNOWLEDGMENTS

I thank Professor Charles S. Fadley for his valuble advice and support; Professor John D. Head for his numerous attempts to teach me theoretical and computational chemistry; Professor John J. Rehr and Dr. Jose Mustre de Leon for a very productive collaboration; Dr. Jurg Osterwalder and Dr. Daniel J. Friedman for their assistance with mathematics and computer programming; Mr. Gregory S. Herman and Mr. Yong-Joo Kim for their help with computations; Mr. Donald Cole and his associates for keeping the computers alive and well connected to the outside world; members of the Fadley group for being helpful, understanding and accomodating.

This work was supported by the Office of Naval Research (Contract No. 00014-87-k-0512) and the National Science Foundation (Grant CHE-83-20200). The calculations discussed here were performed at the San Diego Supercomputing Center.

ABSTRACT

We apply a new separable-Green's-function matrix method due to Rehr and Albers (Phys. Rev. B41 (1990) 8139) to a multiple scattering treatment of photoelectron diffraction and Auger electron diffraction. This cluster-based method permits building up successive orders of scattering and judging the approach to convergence in a convenient and time-saving way. We include multiple scattering up to tenth order and can treat photoelectron emission from any initial state (s, p, d, or f) with full final-state interference, as well as Auger emission in the s-final-state approximation. This new approach is used to simulate emission from linear and bent chains of atoms, from epitaxial overlayers and multilayer substrates and from atomic and molecular adsorbates. The method appears to have a very broad range of utility. We also discuss the types of geometric structures for which multiple scattering effects must be considered, and the nature of the effects expected.

TABLE OF CONTENTS

LIST OF TABLES

LIST OF FIGURES

LIST OF ACRONYMS

AED	Auger electron diffraction
APD	azimuthal photoelectron diffraction
ARPEFS	angle-resolved photoemission extended fine structure
B-S	Barton and Shirley
CPU	central processing unit
CTSS	Cray time sharing system
EXAFS	extended x-ray absorption fine structure
FPU	floating point unit
FWHM	full width at half maximum
Gb	giga byte
IU	integer unit
LEED	low energy electron diffraction
MS	multiple scattering
MSC-SW	multiple scattering cluster spherical wave
Mb	mega byte
MTL	missing top layer
MW	mega word
NEXAFS	near edge x-ray adsorption fine structure
NPD	normal photoelectron diffraction
OPD	off-normal photoelectron diffraction
PD	photoelectron diffraction
PPD	polar photoelectron diffraction

PW	plane wave
PWA	plane wave approximation
R-A	Rehr and Albers
RAM	random access memory
RISC	reduced instruction set
SDSC	San Diego Supercomputer Center
SPARC	scalable processor architecture
SS	single scattering
SSC	single scattering cluster
SSC-PW	single scattering cluster plane wave
SSC-SW	single scattering cluster spherical wave
SW	spherical wave
TS-MQNE	Tayler series magnetic quantum number expansion
XAFS	x-ray absorption fine structure
XPD	x-ray photoelectron diffraction

CHAPTER 1.

GENERAL INTRODUCTION

Photoelectron diffraction (PD) and its close relative, Auger electron diffraction (AED), are by now valuable tools for determining the atomic structure of surfaces [1]. A surface is the result of an abrupt termination of the bulk sructure. Due to the short inelastic attenuation lengths of ~5-15 Å for the electrons used in these diffraction techniques, they probe principally the first few layers inwards from such a bulk termination. A knowledge of the detailed atomic structure of a surface is an essential first step in understanding its electronic and vibrational properties. These properties are in turn the basis of the physical and chemical nature of a surface and are important for understanding catalytic activity, oxidation and corrosion, adhesion, interface formation, and many other surface phenomena of both basic scientific and technological interest.

The photoelectron diffraction experiment begins when an atom near a surface is exposed to x-rays of high enough energy to eject a core electron, leaving behind a hole. The ejected electron is termed a photoelectron. This phenomena was first explained by Einstein in 1905 [2], and it obeys the following energy conservation law:

$$E_{kin} = h\nu - E_b^V(n\ell_i) = h\nu - E_b^F(n\ell_i) - \phi_{sp} \qquad (1\text{-}1)$$

where E_{kin} is the kinetic energy of the photoelectron at the detector, $h\nu$ is the energy of the incoming radiation, $n\ell_i$ denotes the core subshell from which emission occurs, $E_b^V(n\ell_i)$ is the binding energy of this subshell measured with respect to the vacuum level, $E_b^F(n\ell_i)$ is the same binding energy measured with respect to the Fermi level, and ϕ_{sp} is the spectrometer work function. This ejection process has two selection rules in the dipole approximation for the electron-photon interaction [3]. They are

$$\Delta\ell = \ell_f - \ell_i = \pm 1 \tag{1-2}$$

$$\Delta m = m_f - m_i = 0, \pm 1 \tag{1-3}$$

where $L_i = (\ell_i, m_i)$ are the angular momentum and magnetic quantum numbers of the initial core atomic state and $L_f = (\ell_f, m_f)$ are the corresponding numbers for the final state in the continuum. Once ejected from somewhere at or below the surface, a photoelectron wave can either leave the surface without being scattered by another atom (a component of the total wave represented by ϕ_0) or can undergo scattering from other atoms along some path j in the solid (represented by ϕ_j). The ϕ_j's can have contributions from both single and multiple scattering events. The observed photocurrent outside the solid contains interference effects between these two types of components. The intensity of the photocurrent at a detector placed along a direction defined by the final wave vector $\vec{k}$ or its associated polar and azimuthal angles (θ,ϕ) can be written as,

$$I(k,\theta,\phi) \propto \left|\phi_0 + \sum_j \phi_j\right|^2 \qquad (1\text{-}4)$$

where j represents all possible scattering paths inside the solid and k is the magnitude of $\vec{k}$. Figure 1.1 gives the definitions of θ and ϕ that will be used throughout this dissertation. The magnitude of $\vec{k}$, which is proportional the momentum of the photoelectron through $p = hk/2\pi$, is thus proportional in a non-relativistic limit to the square root of the kinetic energy of the photoelectron and can be calculated conveniently as

$$k = |\vec{k}| = 2\pi\ (E_{kin}/150.2)^{1/2}. \qquad (1\text{-}5)$$

If the angular momentum quantum number of the initial state is not equal to zero (i.e., a non s-initial state), then, according to Equation (1-2), there are two possible channels for the photoelectron. Contributions from these two channels should thus be added up with the relevant phase factors in such a case. The importance of such final state interference effects between channels in photoelectron diffraction was first discussed in a systematic way by Friedman and Fadley [4], who used a single scattering approximation. These effects are explicitly included in the more accurate multiple scattering calculations to be described in this dissertation.

A given atom in different materials can have different binding energies for a certain core level. Also, a given core level of an

atom in different environments within a single surface region can have slightly different binding energies. Such difference are known as chemical shifts [6]. Thus, Equation (1-1) can be used to identify an atomic level $n\ell_i$, as well as its chemical states. By separately measuring the angular or energy dependences of the intensites of chemically-shifted peaks, a state-specific determination of structure can be made [1(c)].

In Auger emission a different process is involved. The $n_1\ell_1$ hole left behind in a first core subshell by either photoelectron ejection or inelastic electron scattering can be filled by an electron in an outer $n_2\ell_2$ subshell. During this process the atom can end up singly or doubly charged. In the first case, the energy difference between the core hole and the outer electron hole comes out as radiation at energy $h\nu'$, leaving a hole in an outer shell. This energy is given by

$$h\nu' = E_b(n_1\ell_1) - E_b(n_2\ell_2), \tag{1-6}$$

where $E_b(n_1\ell_1)$ and $E_b(n_2\ell_2)$ are the binding energies of electrons in subshells $n_1\ell_1$ and $n_2\ell_2$, respectively. This is known as radiative decay and it results in x-ray fluorescence [5]. The second possibility is that the excess energy can go into ejecting another electron in an outer subshell $n_3\ell_3$, finally leaving two holes in outer shells:

$$E_{kin} = - E_b(n_1\ell_1) + E_b(n_2\ell_2) - E_b^*(n_3\ell_3) \tag{1-7}$$

where E_{kin} is the kinetic energy of the ejected electron and $E_b^*(n_3\ell_3)$ is the binding energy of the an $n_3\ell_3$ electron in an atom which already has an $n_2\ell_2$ hole. This process is known as Auger emission [5(a)]. The probability of ejecting an Auger electron relative to that of fluorescent decay generally decreases as atomic number increases for a given $n_1\ell_1$ hole [5(a)]. The selection rules on Auger emission are not as strict as those in photoelectron emission, so that a number of final state (ℓ_f,m_f) combinations can be involved; however, the effective averaging over these combinations which occures has been shown to allow approximating the final state of the Auger electron as an s-wave or $(\ell_f,m_f) = (0,0)$ [6]. Except for these differences in the final state associated with the emission process, a scattering Auger electron will behave identically to a scattering photoelectron at the same energy, in spite of erroneous statements to the contrary in the recent literature [7]. Since the final kinetic energy of an Auger electron depends on the internal energy levels of the emitter, Auger electron diffraction also is sensitive to the nature and the chemical state of the emitter [5(a)].

A typical experimental geometry has been shown in Fig 1.1. Measurements can be done in three different modes, as shown in Figure 1.2. These modes are, scanning azimuthal angle (θ and E_{kin} are kept constant while ϕ is varied), scanning polar angle (ϕ and E_{kin} are kept constant while θ is varied) and scanning energy (θ and ϕ are kept constant while photoelectron energy E_{kin} is varied by sweeping $h\nu$).

The scanned energy mode is often referred to as angle-resolved photoemission extended fine structure (ARPEFS). The first two modes can be carried out in a normal laboratory environment with a conventional x-ray tube (or for Auger, also an electron gun) as excitation source, but the scanned energy mode requires a tunable photon source such as a synchrotron radiation facility. Scanning energy is obviously not possible for Auger emission, since the energy is determined by the atomic levels involved. Laboratory sources generally yield unpolarized radiation, so some sort of averaging over the polarization $\hat{\epsilon}$ is involved. With highly polarized synchrotron radiation, the direction of $\hat{\epsilon}$ can be a very useful experimental variable. Details of experimental procedures are found elsewhere [1].

In varying the polar angle θ, the azimuthal angle ϕ, or the kinetic energy of the photoelectron E_{kin}, one also varies the amplitudes and phase differences between ϕ_0 and ϕ_j in Equation (1-4). The amplitude changes are due to the angle and energy dependences of the photoexcitation process and the atomic scattering factors. The phase differences are due to both path length differences between waves (the aspect that carries all structural information) and the scattering process itself. These differences in amplitude and phase cause modulations in intensity. These intensity modulations, known as diffraction patterns, can then in principle be traced back to the geometric arrangement of the atoms around the emitter of the photoelectrons or Auger electrons. However, this last step requires the comparison of theoretical simulations of diffraction patterns for

different trial structures with the experimental patterns. Deriving a better method for carrying out these simulations is the topic of this dissertation. A brief history of photoelectron and Auger electron diffraction is given in the next paragraph, with an emphasis on the previous theoretical developments leading up to the work discussed here.

The first experimental work in x-ray photoelectron diffraction (XPD) was by Siegbahn, Gelius, and Olson [8] who studied NaCl in 1970, and by Fadley and Bergstrom [9(a)] who studied Au in 1971. The first interpretations of such high-energy data at $E_{kin} \simeq 1$ keV involved the Bragg-like reflections in Kikuchi-band theory and were only qualitatively successful in describing the experimental data [8,9].

The first quantitative theoretical explanation of these diffraction patterns was by Liebsch in 1974 [10], who considered emission at much lower energies. A more detailed presentation of this theory, including multiple-scattering effects, appeared in 1976 [11]. This theory was based on methods developed for describing low energy electron diffraction (LEED) and hence required the assumption of full translational symmetry parallel to the surface for the system under investigation. It was limited to emission from atomic-like core orbitals. In 1976, Pendry [12(a)], and subsequently in 1978, Li, Lubinsky, and Tong [12(b)], presented similar theories for valence photoelectron emission at typical ultraviolet energies including the more complex nature of both the initial and final states involved.

The first cluster-based theories of such processes utilized the plane-wave approximation and single scattering, and were applied to explaining extended x-ray absorption fine structure (EXAFS) by Lee [13] and to low-energy Auger emission by Woodruff et al. [14]. The cluster model was then applied for the first time to predicting photoelectron diffraction curves by Kono et al. in 1978 and 1980 [15,16]. Cluster-based theories are inherently very suitable for PD and AED in view of the spherical outgoing waves involved, the short inelastic attenuation lengths, and the short-range order sensitivity of these techniques. Within the framework of a cluster model, the importance of forward scattering along low-index directions at high energies > 500 eV was first discussed by Kono et al. [16] and the use of these effects to determine bond directions was first demonstrated by Petersson et al. [17].

The next major theoretical contribution was by Poon and Tong in 1984 [18] and by Tong, Poon, and Snider [19] in 1985; they made the important observation that multiple scattering along low-index rows of atoms tends to supress forward scattering intensity along rows, an effect they called "defocussing". Further experimental work by our group [1(b), 1(c)], by Egelhoff and co-workers [20], by Chambers and co-workers [1(d)], and by Bonzel and coworkers [21] further developed the use of forward-scattering peaks in both XPD and AED for studying epitaxial structures and adsorbed molecules.

The first cluster-based theory which included both spherical-wave scattering corrections and multiple-scattering effects was due to

Barton and Shirley in 1985 [22]. This method relies on a Taylor series expansion in the magnetic quantum numbers to reduce the complexity of the calculation. In 1985 and 1986, Rehr et al. [23] proposed spherical-wave corrections to single-scattering calculations of angle-resolved photoemission fine structure (ARPEFS) based on a separable approximation to the scattering Green's function. This also is a cluster-based method. This method was generalized further for single-scattering PD in 1989 by Mustre de Leon et al. [24]. Further extensions to include multiple-scattering with application to both x-ray absorption fine structure [XAFS] and photoelectron diffraction were reported in 1990 by Rehr and Albers [25], and this paper is a key starting point for the work of this dissertation. The differences between the treatments of Barton and Shirley [22] and Rehr and Albers are discussed elsewhere [25] and in sections 2.4.7 and 3.2.4 to follow. These approaches are similar in that they both use scattering matrices to uncouple the nested sums over angular momentum indices that plague full-sum theories such as those used in LEED. They are different primarily in the way the scattering matrices are defined and calculated. As noted, the method of Barton and Shirley (B-S) is based on a Taylor expansion in magnetic quantum numbers. The Rehr-Albers (R-A) approach is based on a separable approximation for the propagator and has the correct behavior in both high and low energy limits at low order; this gives the R-A method improved convergence properties. (i.e. it appears that smaller matrices are needed to achieve a given degree of convergence). In particular, the

Rehr-Albers method reduces to the point scattering approximation at lowest order.

The above summary is not intended to contain all important theoretical work in the field, but rather the major contributions relevant to the work of this dissertation. The aim of this dissertation was to adopt and implement the method of Rehr and Albers [25] to the simulation of multiple-scattering photoelectron and Auger electron diffraction. We have also included the proper final state interferences for PD from a non-s subshell; this has not been done previously for a cluster-based multiple-scattering theory. The rest of this dissertation contains two major chapters. Chapter 2 is devoted to the details of the formalism by Rehr and Albers [25] as applied to multiple-scattering PD and AED. It also contains computational details, a guide to the use of the computer program involved, and comparisons of our results to prior theoretical and experimental results as test cases. Chapter 3 is primerily new results and will be submitted for publication. (Other short papers based upon this dissertation have already appeared [26-28].)

REFERENCES:

[1]. (a) C.S. Fadley, Prog. in Surf. Sci. 16 (1984) 275; (b) C.S. Fadley, Phys. Scripta T17 (1989) 39; (c) C.S. Fadley in "Synchrotron Radiation Research: Advances in Surface Science", R.Z. Bachrach , Ed., (Plenum, New York, 1990); (d) S.A. Chambers, I.M. Vitomirov, S.B. Anderson, H.W. Chen, T.J. Wagener, and J.H. Weaver, Superlatt. and Microstruct. 3 (1987) 563.

[2]. A. Einstein, Ann. Physik 17 (1905) 132.

[3]. S.M. Goldberg, R.J. Baird, S. Kono, N.F.T. Hall, and C.S. Fadley, J. Electron Spectrose. Relat. Phenom. 21 (1980) 1.

[4]. D.J. Friedman and C.S. Fadley, J. Electron Spectrose. Relat. Phenom. 51 (1990) 689.

[5]. (a) T.A. Carlson in "Photoelectron and Auger Spectroscopy", Modern Analytical Chemistry, David Herucules Ed., (Plenum, New York and London, 1978); (b) C.S. Fadley in "Electron Spectroscopy: Theory, Technique, and Applications", C.R. Brundle and A.D. Baker Eds., (Academic, London, 1978), Vol. 2, Ch. 1.

[6]. H. Hilferink, E. Lang, and K. Heinz, Surf.Sci. 93 (1980) 398; R.G. Weissman and K. Muller, Surf. Sci. Repts. 1 (1981) 251; M.-L. Xu, and M. A. Van Hove, Surf. Sci. 207 (1989) 215.

[7]. D.G. Frank, N. Batina, T. Golden, F. Lu, and A.T. Hubbard, Science 247 (1990) 182.

[8]. K. Siegbahn, U. Gelius, and E. Olson, Phys. Lett. 32A (1970) 221.

[9]. (a) C.S. Fadley and S.A.L. Bergstrom, Phys. Lett. 35A (1971) 375; (b) R.J. Baird, C.S. Fadley and L.F. Wagner, Phys. Rev. B 15 (1977) 666.

[10]. A. Liebsch, Phys. Rev. Lett. 32 (1974) 1203.

[11]. A. Liebsch, Phys. Rev. B 13 (1976) 544.

[12]. (a) J.B. Pendry, Surf. Sci. 57 (1976) 697; (b) C.H. Li, A.R. Lubinsky, and S.Y. Tong, Phys. Rev. B17 (1978) 3128.

[13]. P.A. Lee, Phys. Rev. B 13 (1976) 5261.

[14]. L. McDonnell, D.P. Woodruff, and B.W. Holland, Surf. Sci. 51 (1975) 249.

[15]. S. Kono, S. M. Goldberg, N.F.T. Hall, and C.S. Fadley, Phys. Rev. Lett. 41 (1978) 1831.

[16]. S. Kono, S.M. Goldberg, N.F.T. Hall, and C.S. Fadley, Phys. Rev. B 22, 6085 (1980).

[17]. L.-G. Peterson, S. Kono, N.F.T. Hall, C.S. Fadley and J.B. Pendry, Phys. Rev. Lett. 42 (1979) 1545.

[18]. H.C. Poon and S.Y. Tong, Phys.Rev. B 30 (1984) 6211.

[19]. S.Y. Tong, H.C. Poon, and D.R. Snider, Phys. Rev. B 32 (1985) 2096.

[20]. W.F. Egelhoff Jr., Phys. Rev. B 30 (1984) 1052.

[21]. D.A. Wesner, F.P. Coenen, and H.P. Bonzel, Surf. Sci. 199 (1988) L419.

[22]. J.J. Barton and D.A. Shirley, Phys. Rev. B 32 (1985) 1892; J.J. Barton and D.A. Shirley, Phys. Rev. B 32 (1985) 1906.

[23]. J.J. Rehr and R.C. Albers, Bull. Am. Phys. Soc. 30 (1985) 524; J.J. Rehr, J. Mustre de Leon, C.R. Natoli, and C.S. Fadley, Journal de Physique, Colloque C8, Suppliment an n 12, Thome 47 (1986) 213.

[24]. J. Mustre de Leon, J.J. Rehr, C.R. Natoli, C.S. Fadley, and J. Osterwalder, Phys. Rev. B 39 (1989) 5632.

[25]. J.J. Rehr and R.C. Albers, Phys. Rev. B 41 (1990) 8139.

[26]. A.P. Kaduwela, G.S. Herman, J. Osterwalder, C.S. Fadley, J.J. Rehr, and J. Mustre de Leon, Physica B 158 (1989) 564.

[27]. A.P. Kaduwela, G.S. Herman, D.J. Friedman, C.S. Fadley and J.J. Rehr, Physica Scripta 41 (1990) 948.

[28]. A.P. Kaduwela, D.J. Friedman, Y.J. Kim, T.T. Tran, G.S. Herman, C.S. Fadley, J.J. Rehr, J. Osterwalder, H. Aebischer and A. Stuck, to appear in "The Structure of Surfaces III", M.A. Van Hove, K. Takayanagi, and Xie Xide Eds. (Springer-Verlag, Heidelberg, 1991).

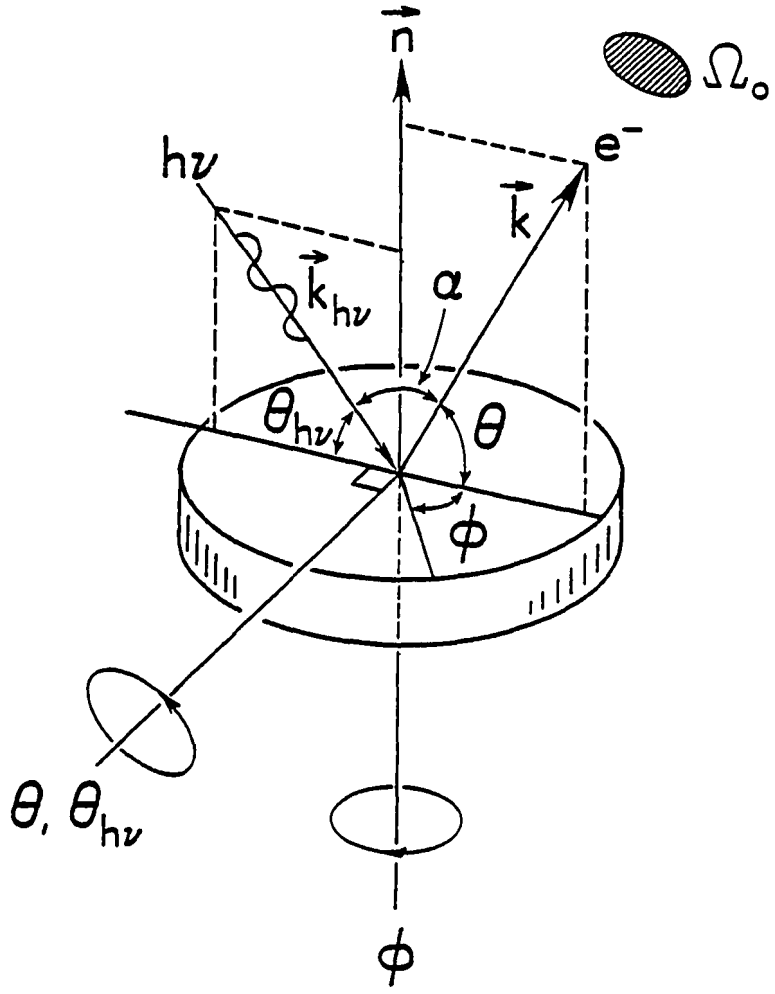

Figure 1.1. The general geometry for a photoelectron or Auger electron diffraction experiment. The azimuthal angle ϕ is defined with respect to an axis fixed in the sample surface. The polar takeoff angle θ is measured from the surface. The angle between the incoming radiation and the outgoing wave vector $\vec{k}$ is α. The polar angle of the incoming radiation with respect to the surface is $\theta_{h\nu}$, $\vec{k}_{h\nu}$ is the wave vector, and $\hat{\epsilon}$ is the polarization vector of the radiation. The solid angle accepted by the detector is Ω_0.

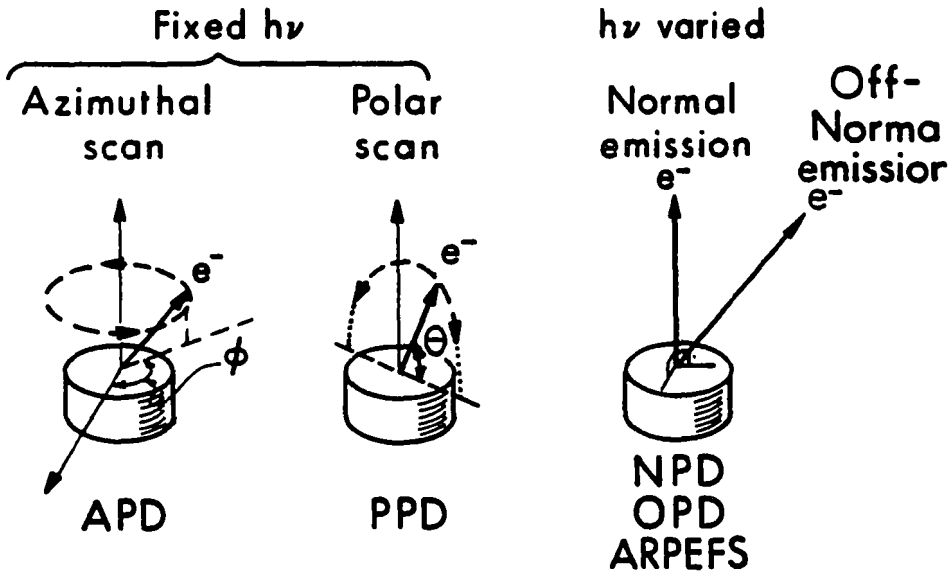

Figure 1.2. The three basic types of photoelectron diffraction measurements: (1) an azimuthal (ϕ) scan at constant polar angle, sometimes referred to as azimuthal photoelectron diffraction or APD; (2) a polar scan (θ) at constant azimuthal angle, referred to as polar photoelectron diffraction PPD; and (3) a scan of $h\nu$ in fixed geometry that can be done for emission either normal or off-normal to the surface (denoted NPD or OPD, respectively). The scanned-energy type has also been referred to as angle resolved photoemission extended fine structure or ARPEFS. Note that θ is measured with respect to the surface. Auger electron diffraction can be carried out either in mode (1) or (2).

CHAPTER 2.

THEORETICAL AND COMPUTATIONAL METHODOLOGY

2.1. INTRODUCTION:

In this chapter, we will discuss various aspects of the theoretical simulation of photoelectron and Auger electron diffraction. We will begin with the simplest approximation of single-scattering in a finite cluster (SSC), with the scattering being calculated in the plane wave (PW) limit [1-3]. This approximation, discussed in detail in Section 2.2, is very easy to understand and contains almost all of the crucial physical features of the scattering. Then we will discuss the limitations of this approach and consider first spherical-wave (SW) corrections [4-6] as a possible improvement to it (Section 2.3). The agreement between experiment and simulation is generally very satisfactory at this level of the theory. But for a fully quantitative treatment that is applicable to all geometries and energies, we must go further and explore the effects of multiple-scattering [5-9] on the simulated diffraction curves. Details of a new approach to multiple-scattering will be discussed in Section 2.4. Section 2.5 discusses our methods for computing certain important intermediate quantities. A user's guide to the FORTRAN-77 computer code used in these simulations is in Section 2.6. The several computing environments in which the code has been run are described in Section 2.7. Section 2.8 contains some applications to

test cases and comparisons to prior theoretical and experimental results, together with a discussion of the sensitivity of results to input parameters. Section 2.9 contains our general conclusions concerning the new method and our implementation of it.

2.2. SINGLE-SCATTERING CLUSTER MODEL IN THE PLANE-WAVE LIMIT:

The simplest approach to photoelectron diffraction simulations is to use the single-scattering cluster approximation in the plane-wave limit (SSC-PW) [1,2]. In this model, it is assumed that the portion of the photoelectron incident on the scatterer has sufficiently low curvature compared to the dimensions of the scattering potential that it can be represented as a plane-wave at each scatterer (see Figure 2.1). This is the so-called small-atom approximation [3]. If it is further assumed that the final state before scattering is a p-wave (i.e., that apprpriate to s photoemission), then the final expression for the intensity $I(\vec{k})$ is [2]:

$$I(\vec{k}) \alpha \left| \hat{\epsilon}\cdot\hat{k} \exp\{-L_0/2\Lambda_e\} + \sum_j \hat{\epsilon}\cdot\hat{R}_j \frac{f_j(\theta_j)}{R_j} W_j \exp\{-L_j/2\Lambda_e\} \exp\{-ikR_j(1-\cos\theta_j) + \Psi_j(\theta_j)\} \right|^2 \qquad (2\text{-}2\text{-}1)$$

where $\vec{k}$ is the wave vector of the photoelectron and k its magnitude, θ_j is the scattering angle as shown in Figure 2.2, $\hat{\epsilon}$ is the radiation

polarization vector, and $\vec{R}_j$ is the vector pointing from the emitter to the first scatterer, L_0 is the distance from the emitter to the surface, and L_j is the total path length from the emitter to the scatterer to the surface. W_j is a Debye-Waller factor representing the attenuation of diffraction by the thermal vibrations of the scatterer. $f_j(\theta_j)$ is the complex plane-wave scattering factor with magnitude $|f_j(\theta_j)|$ and phase $\Psi_j(\theta_j)$. It can be calculated from

$$f_j(\theta_j) = (2ik)^{-1} \sum_{\ell_j=0}^{\ell_{max}} (2\ell_j+1)\,(\exp\{2i\delta_{\ell_j}\} - 1)\, P_{\ell_j}(\cos\theta_j), \quad (2\text{-}2\text{-}2)$$

where ℓ_j is the angular momentum of each partial wave, δ_{ℓ_j} is the phase shift of the ℓ_j^{th} partial wave for the j^{th} scatterer, and P_{ℓ_j} is the Legendre polynomial of order ℓ_j. The limit on the sum is $\ell_{max} \approx kR_{MT}$, where R_{MT} is the effective or muffin-tin radius of the scattering potential, as shown in Figure 2.1. For a typical case of a Cu scatterer in Cu metal with $R_{MT} = 1.28$ Å, this yields $\ell_{max} = 7$ for 100 eV, 21 for 1,000 eV, and 66 for 10,000 eV.

The magnitude and phase of this scattering factor for scattering from Cu at energies from 500 eV upwards are shown in Figures 2.3(a) and 2.3(b) respectively. It is interesting to note that the amplitude of the scattering factor has a prominent peak in the forward scattering direction and, only for the lowest energies less than 500.0 eV, does it have also a weaker and broader peak in the back scattering

direction. The generally small phase shift in forward scattering (cf. Figure 2.3(b)) also implies that this peak in forward scattering magnitude will produce enhanced intensity in that direction. This effect has been termed simply "forward scattering" [2] or also "forward focussing" [10]. This feature is very valuable in the extraction of structural information from experimental data [2]. But not all of the peaks seen in experimental data at higher energies are due to forward focussing; significant features can also arise due to scattering at larger angles that produce higher-order interference effects, as illustrated in Figure 2.3(c) for the simple case of a two-atom Cu chain. We can thus denote the forward-scattering peak as "0^{th} order" with 1^{st}, 2^{nd}, 3^{rd}, etc. order peaks expected at larger angles [2]. Therefore, a full scattering calculation is required for unambiguous assignment of all experimental peaks.

The quantity $kR_j(1-\cos\theta_j)$ in Equation (2-2-1) represents the geometric phase shift associated with scattering. This arises due to the different distances traveled by the primary wave, ϕ_0, and the scattered wave, ϕ_j, as shown by the darker lines in Figure 2.2. This phase shift thus contains bond length information. The $1/R_j$ attenuation of the outgoing spherical wave as it passes to each scatterer shown in Equation (2-2-1) makes both photoelectron and Auger electron diffraction short-range-order probes. There is an additional attenuation of the photoelectron or the Auger electron due to the inelastic mean free path in the solid, as represented by the factors $\exp\{-L_0/2\Lambda_e\}$ and $\exp\{-L_j/2\Lambda_e\}$ in Equation (2-2-1). $\hat{\epsilon}\cdot\hat{k}$ and $\hat{\epsilon}\cdot\hat{R}_j$

represent the s-level emission cross-section of the photoelectron in the direction of the detector and the scatterer, respectively.

The plane wave approximation is computationally very efficient. But it has the drawback of overestimating the intensity of the forward-scattering peaks [4], as shown in one prior comparison of plane-wave (PW) and spherical-wave (SW) results in Figure 2.4. In this case, emission from an s-level ($\ell_i = 0$, $\ell_f = 1$) towards a single Ni scatterer 2.49 Å away is considered. The polarization $\hat{\epsilon}$ is kept parallel to $\vec{k}$. The PW results consistently overestimate the scattered intensity in the forward direction over the entire energy range studied: for energies less than about 200 eV, additional differences are seen between the PW and SW results. The overestimation of the forward peak is larger at higher energies, and it has in previous work been corrected in an ad hoc manner by introducing an empirical reduction factor of ~0.4-0.5 to all scattering factors [11]. However, without such corrections the simple PW approximation still yields results that are very similar in form to those using spherical wave scattering. Hence, it has been used to draw useful structural conclusions for a number of systems [2].

2.3. SPHERICAL-WAVE AND MULTIPLE-SCATTERING MODIFICATIONS:

A first improvement possible to the SSC-PW model is thus to add spherical-wave (SW) corrections. Here the assumption that the curvature of the photoelectron is small compared to the scattering

potential is abandoned and the photoelectron is represented by a spherical wave [4-6,12-17]. As expected from Figure 2.4, this modification results in a reduction in intensity of forward scattering peaks, and it does improve the agreement between experiment and theory for some cases. For example, Figure 2.5 shows a comparison of PW and SW modeling as applied to a cluster representing c(2×2)O/Ni(001) [4,19,20]. At $\theta = 7.0^{\circ}$ and $\phi = 0^{\circ}$, we are just 7° away from the chain of O atoms in the [100] direction. The PW results have a very pronounced peak in this direction, but the experiment has only a small peak that appears to be a doublet. SW theory is here able to correctly predict a weaker doublet, although it is still too pronounced. This last difference might be due to the neglect of multiple-scattering effects along linear chains of atoms, an effect we consider in more detail below.

In single scattering, we assume that there is only one scatterer per path between the emitter and the detector. At higher electron energies, this is a good approximation, provided that there are no linear chains of atoms in the path. A single-scattering picture is thus expected to be valid at higher energies when the emitter is in the first 1-2 layers of the surface and/or the emission direction is not parallel to dense rows of scatterers in low-index directions. If there are linear or nearly linear chains of atoms in the path, one must account for the 'shadowing' of some scatterers by others [5,21]. This shadowing leads to a significant reduction in intensity along the chain axis, an effect that has been termed 'defocussing' [5]. There

are several prior investigations of this shadowing or defocussing effect using different theoretical methods [5,7-9]. All of them reach very similar conclusions.

The rest of this chapter is devoted to the first use of a new theoretical method by Rehr and Albers [17] for treating multiple scattering in photoelectron and Auger electron diffraction. We will also present some simulations of experimental results in an attempt to test the method and derive a general set of rules to determine when and where multiple-scattering (MS) effects will be important.

2.4. APPLICATION OF THE SEPARABLE GREEN'S FUNCTION APPROACH OF REHR AND ALBERS TO SINGLE- AND MULTIPLE-SCATTERING:

In this section we will discuss the application of the scattering-matrix formalism of Rehr and Albers [17] to single and multiple scattering in both photoelectron and Auger electron diffraction. This full spherical wave method approximates the system by a cluster of individual atoms. This is a sensible alternative to LEED-type methods which require full translational symmetry along the surface [5]. The cluster approach [2,13-15] is very appropriate to short-range-order probes such as photoelectron and Auger electron diffraction. In a recent work, the R-A method has been used in SSC-SW calculations by our group for treating emission form a general $n_i\ell_i$ subshell [18]. The multiple-scattering version of this approach has been termed the multiple-scattering cluster-spherical wave (MSC-SW)

method to distinguish it from the SSC-PW and SSC-SW methods. In the following paragraphs we present the crucial points of a new method for doing MSC-SW calculations by Rehr and Albers [17]. In the equations to follow, we will for simplicity not include effects due to inelastic scattering or vibrational motion, but the form in which these have been incorporated will be indicated later.

We begin with some essential definitions and equations used by Rehr and Albers [17]. From Equation (25) of reference 17, the photoelectron diffraction intensity at the detector is given by

$$\frac{d\sigma}{d\Omega} \alpha \left| \sum_{L_f,N} G^{(N-1)}_{00,L_f}(\vec{R}_1,\vec{R}_2,\ldots,\vec{R}_N)\, m_{L_f,c}(\hat{\epsilon})\, \exp(i\delta^c_{\ell_f}) \right|^2 \qquad (2\text{-}4\text{-}1)$$

where $G^{(N-1)}_{00,L_f}$ is the $(N-1)^{th}$ order multiple-scattering Green's function for a path from $\vec{R}_0 = \vec{R}_{emitter}$ (taken to be the origin) via scatterers at $\vec{R}_1$, $\vec{R}_2$, ..., $\vec{R}_{N-1}$ to $\vec{R}_N = \vec{R}_{detector} = \vec{R}_d$ at ∞, $m_{L_f,c}$ is the amplitude and $\delta^c_{\ell_f}$ is the phase of the dipole matrix element into a given final-state $L_f = (\ell_f, m_f)$ contained in $\langle \Psi_{E_{kin},\hat{k}} | \hat{\epsilon}\cdot\vec{r} | \phi_{n_i \ell_i m_i} \rangle$. Within the matrix element, $\Psi_{E_{kin},\hat{k}}$ denotes the final continuum state of the photoelectron corresponding to emission into direction $\vec{k}$ (which must be parallel to $\vec{R}_N = \vec{R}_d$), $\phi_{n_i \ell_i m_i}$ is the initial core orbital from which the photoelectron is emitted, and $\hat{\epsilon}$ is the radiation polarization vector. The sum is over $L_f = (\ell_f, m_f)$ and over all combinations of N, the number of atoms in a given scattering path from

single-scattering (N = 2) to the highest order considered (usually 10^{th} order or N = 11).

Let us now look at this matrix element in detail for the case in which there are no scatterers, which is

$$\langle \Psi_{E_{kin},\hat{k}} | \hat{\epsilon}\cdot\vec{r} | \phi_{n_i \ell_i m_i} \rangle = \langle \Psi_{E_{kin},\hat{k}} | (\epsilon_x x/r + \epsilon_y y/r + \epsilon_z z/r) r | \phi_{n_i \ell_i m_i} \rangle. \tag{2-4-2}$$

But,

$$x/r \propto \sin\theta \cos\phi \propto -Y_{11} + Y_{1-1}, \tag{2-4-3a}$$

$$y/r \propto \sin\theta \sin\phi \propto Y_{11} + Y_{1-1}, \tag{2-4-3b}$$

$$z/r \propto \cos\theta \propto Y_{10}, \tag{2-4-3c}$$

where $Y_{\ell m}$ is a spherical harmonic. Now we choose for convenience the $\hat{\epsilon}$ vector to lie in the $\hat{z}$ direction: $\epsilon_x = \epsilon_y = 0$ and $\epsilon_z = 1$. Substituting these values, together with Equation (2-4-3c) into Equation (2-4-2) we obtain

$$\langle \Psi_{E_{kin},\hat{k}} | \hat{\epsilon}\cdot\vec{r} | \phi_{n\ell_i m_i} \rangle = \langle \Psi_{E_{kin},\hat{k}} | Y_{10} r | \phi_{n_i \ell_i m_i} \rangle. \tag{2-4-4}$$

We now expand both $\Psi_{E_{kin},\hat{k}}$ and $\phi_{n_i \ell_i m_i}$ in products of appropriate radial and angular parts. In expanding $\Psi_{E_{kin},\hat{k}}$ we make use of the fact that it is a plane wave at the detector and then use the standard ingoing-wave expansion for it [22] to get

$$\Psi_{E_{kin},\hat{k}} = 4\pi \sum_{\ell_f=0}^{\infty} \sum_{m_f=-\ell_f}^{\ell_f} \Big[i^{\ell_f} \exp\{-i\delta^c_{\ell_f}\} \times Y^*_{\ell_f m_f}(\theta_k,\phi_k)\, Y_{\ell_f m_f}(\theta,\phi)\, R_{E_{kin},\ell_f}(r) \Big]. \quad (2\text{-}4\text{-}5)$$

For $\phi_{n_i \ell_i m_i}$, we can simply write

$$\phi_{n_i \ell_i m_i} = R_{n_i \ell_i}(r)\, Y_{\ell_i m_i}(\theta,\phi). \quad (2\text{-}4\text{-}6)$$

Here, $R_{E_{kin},\ell_f}(r)$ and $R_{n_i \ell_i}(r)$ are radial parts of the continuum orbital at ℓ_f and a given core orbital with quantum numbers n_i and ℓ_i, respectively. The angles defining the detector along $\vec{k}$ or $\vec{R}_d$ are (θ_k,ϕ_k), although after integration over θ and ϕ in the matrix element, we will later simplify this rotation to be (θ,ϕ).

By substituting Equations (2-4-5) and (2-4-6) into (2-4-4) and by doing some simplifications, one arrives at

$$\langle \Psi_{E_{kin},\hat{k}} | \hat{\epsilon}\cdot\vec{r} | \phi_{n_i \ell_i m_i} \rangle = 4\pi \sum_{\ell_f=0}^{\infty} \sum_{m_f=-\ell_<}^{\ell_<} \Big[(-i)^{\ell_f} \exp\{i\delta^c_{\ell_f}\}\, Y_{\ell_f m_f}(\theta_k,\phi_k) \times \langle Y_{\ell_f m_f}(\theta,\phi)\, R_{E_{kin},\ell_f}(r) \times Y_{10}(\theta,\phi) r | R_{n_i \ell_i}(r) Y_{\ell_i m_i}(\theta,\phi) \rangle \Big], \quad (2\text{-}4\text{-}7)$$

where $\ell_<$ is the lesser of the pair ℓ_i and ℓ_f. Since r, θ and ϕ are independent variables, this reduces further to:

$$\langle \Psi_{E_{kin},\hat{k}} | \hat{\epsilon}\cdot\vec{r} | \phi_{n_i \ell_i m_i} \rangle = 4\pi \sum_{\ell_f=0}^{\infty} \sum_{m_f=-\ell_<}^{\ell_<} \Big[(-i)^{\ell_f} \exp\{i\delta^c_{\ell_f}\}\ Y_{\ell_f m_f}(\theta_k,\phi_k) \times \langle R_{E_{kin},\ell_f}(r) | r | R_{n_i \ell_i}(r) \rangle \times \langle Y_{\ell_f m_f}(\theta,\phi) | Y_{10}(\theta,\phi) | Y_{\ell_i m_i}(\theta,\phi) \rangle \Big]. \quad (2\text{-}4\text{-}8)$$

The last factor in the summation in Equation (2-4-8) has (since Y_{10} is real) the general form $\langle Y_{\ell_1 m_1}(\theta,\phi)\ Y_{\ell_2 m_2}(\theta,\phi) | Y_{\ell_3 m_3}(\theta,\phi) \rangle$ and is known as a Gaunt coefficient. These coefficients are non-zero only when: (1) $|\ell_2-\ell_3| < \ell_1 < \ell_2+\ell_3$. For $\ell_2 = 1$, this yields the well-known dipole selection rule in photoelectron emission: $\ell_f = \ell_i \pm 1$. (2) $|m_1 - m_3| = m_2$. When $\hat{\epsilon} \parallel \hat{z}$ (as assumed also by Rehr and Albers [17]) this condition forces $m_f = m_i$. This makes the final expressions simpler, and it also prevents cross transition in m and thus makes the calculation more efficient.

These two proporties of Gaunt coefficients can be used to simplify Equation (4-2-8) further to yield,

$$\langle \Psi_{E_{kin},\hat{k}} | \hat{\epsilon}\cdot\vec{r} | \phi_{n_i \ell_i m_i} \rangle = 4\pi \sum_{\ell_f=\ell_i\pm1} \sum_{m_i=-\ell_<}^{\ell_<} \Big[(-i)^{\ell_f} \exp\{i\delta^c_{\ell_f}\}\ Y_{\ell_f m_i}(\theta_k,\phi_k) \times \langle R_{E_{kin},\ell_f}(r) | r | R_{n_i \ell_i}(r) \rangle \times \langle Y_{\ell_f m_i}(\theta,\phi)\ Y_{10}(\theta,\phi) | Y_{\ell_i m_i}(\theta,\phi) \rangle \Big]. \quad (2\text{-}4\text{-}9)$$

It is now convenient to define a core-to-ℓ_f matrix element $m_{L_f,c}$ (where $L_f = (\ell_f, m_f)$) in the notation of Rehr and Albers (R-A) [17] as

$$m_{L_f,c} = (-i)^{\ell_f} \langle R_{E_{kin},\ell_f}(r)|r|R_{n_i\ell_i}(r)\rangle \times \langle Y_{\ell_f m_i}(\theta,\phi)|Y_{10}(\theta,\phi)|\, Y_{\ell_i m_i}(\theta,\phi)\rangle, \quad (2\text{-}4\text{-}10)$$

so that Equation (2-4-9) becomes

$$\langle \Psi_{E_{kin},\hat{k}}|\hat{\epsilon}\cdot\vec{r}|\phi_{n_i\ell_i m_i}\rangle = 4\pi \sum_{\ell_f=\ell_i\pm 1} \sum_{m_i=-\ell_f}^{\ell_f} m_{L_f,c} \exp\{i\delta^c_{\ell_f}\} \times Y_{\ell_f m_i}(\theta_k,\phi_k) \quad (2\text{-}4\text{-}9')$$

Equation (2-4-10) for $m_{L_f,c}$ can also be written in a shorthand notation as

$$m_{L_f,c} = (3/4\pi)^{1/2}\ (-i)^{\ell_f}\ R_{\ell_f}(E_{kin})\ C^1(\ell_f,m_i,\ell_i,m_i) \quad (2\text{-}4\text{-}11)$$

where $R_{\ell_f} = \langle R_{E_{kin},\ell_f}(r)|r|R_{n_i\ell_i}(r)\rangle$ and $C^1(\ell_f,m_i,\ell_i,m_i) = (4\pi/3)^{1/2}$ $\langle Y_{\ell_f m_i}(\theta,\phi)\ Y_{10}(\theta,\phi)|\ Y_{\ell_i m_i}(\theta,\phi)\rangle$. In the special case of emission into a single final state, (as, for example, for s emission ($\ell_i = m_i = 0$) to a p final-state ($\ell_f = 1$, $m_f = m_i = 0$)), we can ignore these matrix element prefactors, as they become just scaling factors for the

overall intensity. But they are extremely important in calculations to more complex final states involving emission from $\ell_i \neq 0$ to the two channels $\ell_i \pm 1$. In general, it is thus necessary to know both R_{ℓ_f} and $\delta^c_{\ell_f}$ for this general case. As one source, R_{ℓ_f} and $\delta^c_{\ell_f}$ have been tabulated for a number of free atoms at several energies by Goldberg, Fadley, and Kono [22]. In this treatment, we will introduce these factors only in the last sections to account for fully general emission into the $\ell_i \pm 1$ channels.

As noted previously, $G^{(N-1)}_{00,L_f}$ in Equation (2-4-1) is the exact multiple-scattering expansion for an N-leg scattering path with (N-1) scattering events. It can be written, using Equation (14) of Reference 17, as,

$$G^{(N-1)}_{00,L_f}(\vec{R}_1, \ldots, \vec{R}_N) = \sum_{\{\text{paths}\}} \sum_{\{L_i\}} G_{00,L_{N-1}}(\vec{\rho}_N)\, t_{\ell_{N-1}}(\vec{R}_{N-1}) \times G_{L_{N-1},L_{N-2}}(\vec{\rho}_{N-1})\, t_{\ell_{N-2}}(\vec{R}_{N-2}) \cdots\cdots\cdots \cdots\cdots\cdots t_{\ell_1}(\vec{R}_1)\, G_{L_1,L_f}(\vec{\rho}_1) \qquad (2\text{-}4\text{-}12)$$

where, $G_{L_{j+1},L_j}(\vec{\rho}_{j+1})$ is a matrix element of the free-electron propagator in an angular momentum and site basis with $L_{j+1} = (\ell_{j+1},m_{j+1})$, $L_j = (\ell_j,m_j)$, $\vec{\rho}_{j+1} = k(\vec{R}_{j+1}-\vec{R}_j)$ is a "bond vector" in units of 2π(number of electron wave lengths), and $t_\ell = \exp\{i\delta_\ell\}\sin\delta_\ell$ is a diagonal elements of the t-matrix for scattering. A graphical representation of one of the paths in $G^{(N-1)}_{00,L_f}$ is given in Figure

2.6(a). The summation is over all combinations of intermidiate L_i and all possible scattering paths of (N-1) order in the cluster. The matrix elements or intermediate propagators $G_{L_{j+1},L_j}(\vec{\rho}_{j+1})$ in the above expression can thus be thought of as giving the strength of a given L_{j+1} component of spherical waves centered on $\vec{R}_{j+1}$ as contained in the component L_j propagating outward from $\vec{R}_j$. At each $\vec{R}_{j+1}$, $t_{\ell_{j+1}}(\vec{R}_{j+1})$ then accounts for the effects of scattering on the next outgoing components. The last $L_N = (\ell_N, m_N)$ is restricted to (0,0) because it represents the projection of L_{N-1} at the last scattering center into a plane-wave at the detector $\vec{R}_d$ an infinite distance away. One can qualitatively see this limiting character in the expansion of Equation (2-4-5), for which, since $\vec{R}_d \parallel \vec{k}$, $\theta \to \theta_k$ and $\phi \to \phi_k$ at infinity, the sum over m_f becomes $\sum_{m_f} |Y_{\ell_f m_f}|^2 = (2\ell+1)/4\pi$ via the Unsold Theorem. A form frequently used for $G_{L_{j+1},L_j}(\vec{\rho}_{j+1}) = G_{L,L'}(\rho)$ [23] is, in R-A notation:

$$G_{L,L'}(\vec{\rho}) = 4\pi \sum_{L''} \langle Y_{\ell m}\, Y_{\ell'' m''} | Y_{\ell' m'} \rangle\, h_{L''}(\vec{\rho}) \qquad (2\text{-}4\text{-}13)$$

where, $h_L(\vec{\rho}) = i^{\ell}\, h_{\ell}^{(+)}(k\rho)\, Y_{\ell m}(\hat{\rho})$, $\hat{\rho} = \vec{\rho}/\rho$, and $h_{\ell}^{(+)}$ is an outgoing spherical Hankel function that can be written in its usual form as

$$h_{\ell}^{(+)}(\rho) = i^{-\ell}\, \exp(i\rho)/\rho\; C_{\ell}(\rho), \qquad (2\text{-}4\text{-}14)$$

or, in terms of the variable $z = 1/i\rho$ as

$$h_\ell^{(+)}(z) = i^{-(\ell-1)} \exp(1/z)\ z\ C_\ell(z). \qquad (2\text{-}4\text{-}15)$$

Another use of the coefficient $G_{L,L'}$ is in the so-called addition formula for the translation of spherical waves from one center at the origin to another at $\vec{a}$:

$$h_L(\vec{r}) = i^\ell\ h_\ell^{(+)}(kr)\ Y_{\ell m}(\hat{r})$$
$$= \sum_{L'} G_{L,L'}(k\vec{a})\ j_\ell(k|\vec{r} - \vec{a}|)\ Y_{\ell m}((\vec{r}-\vec{a})/|\vec{r}-\vec{a}|), \qquad (2\text{-}4\text{-}16)$$

where j_ℓ is the ℓ^{th} spherical Bessel function.

A more convenient form for subsequent development is the defining integral for $G_{L,L'}(\rho)$ [17]:

$$G_{L,L'}(\vec{\rho}) = \frac{-(4\pi)^2}{2k}$$
$$\int \frac{d^3k}{(2\pi)^3} \frac{Y_L^*(\hat{k})\ Y_{L'}(\hat{k})\ \exp\{i\vec{k}\cdot(\vec{R}-\vec{R}')\}\ j_\ell(kr)\ j_{\ell'}(kr')}{(\epsilon - k^2/2 + i0^+)\ j_\ell(\sqrt{(2\epsilon)}r)\ j_{\ell'}(\sqrt{(2\epsilon)}r')} \qquad (2\text{-}4\text{-}17)$$

where the Y_L's are spherical harmonics with $L = (\ell,m)$ and the j_ℓ's again spherical Bessal functions. $\vec{r}$ and $\vec{r}'$ are arbitrary displacements about $\vec{R}$ and $\vec{R}'$, respectively.

The major contribution of Rehr and Albers [17] was to develop a convergent separable approximation to $G_{L,L'}(\vec{\rho})$. Details of their

procedure are given elsewhere [17] and we will thus present only a brief outline of their method and results. The first step is to use rotation matrices to rotate a given bond direction corresponding to $\vec{\rho} = k(\vec{R}-\vec{R}')$ onto the z axis to simplify the calculation. Then one has after some manipulation,

$$G_{L,L'}(\vec{\rho}) = [\exp(i\rho)/\rho] \sum_{\mu=-\ell}^{\ell} R^{\ell}_{m\mu}(\hat{\rho}^{-1})\, g^{(|\mu|)}_{\ell\ell'}(\rho)\, R^{\ell'}_{\mu m'}(\hat{\rho}) \qquad (2\text{-}4\text{-}18)$$

where $R^{\ell}_{\mu m'}(\hat{\rho})$ is a rotation matrix which rotates $\hat{\rho}$ onto the z-axis, $R^{\ell}_{\mu m}(\hat{\rho}^{-1})$ is the inverse of this matrix, and $g^{(|\mu|)}_{\ell\ell'}$ is a reduced, dimensionless z-axis propagator. The general Euler angles (α,β,γ) associated with the rotation are shown in Figure 2.7. They start at XYZ, rotate by α about Z to yield X'Y'Z, rotate by β about Y' to yield X"Y'z, and finally rotate by γ about z to yield xyz. The associated rotation matrices have the property that, if $R^{\ell}_{m\mu}(\hat{\rho}) = R^{\ell}_{m\mu}(\alpha,\beta,\gamma)$, then $R^{\ell}_{m\mu}(\hat{\rho}^{-1}) = R^{\ell}_{m\mu}(-\gamma,-\beta,-\alpha)$. For more details on rotation angles and matrices see Sections 2.5.2 and 2.5.3. Equation (2-4-18) is equivalent to Equation (9) of Reference 17, but we have used $\hat{\rho}$ to represent the Euler angles of $\vec{R}-\vec{R}'$ with respect to $\hat{z}$, in place of the $\Omega_{\hat{\rho}}$ used by R-A. The first step thus separates $G_{L,L'}(\vec{\rho})$ into purely angle-dependent rotation matrices and a radial z-axis propagator $g^{(|\mu|)}_{\ell\ell'}$ that depends, through k, on energy.

The second step in the R-A method is to achieve a separable approximation to the radial z-axis propagator $g^{(|\mu|)}_{\ell\ell'}$. This proceeds

by deriving the following form for $g_{\ell\ell'}^{(|\mu|)}$ [Appendix A of Reference 17]:

$$g_{\ell\ell'}^{(|\mu|)} = N_{\ell\mu}\, N_{\ell'\mu} \int_0^\infty \frac{dx}{z}\, e^{-(x/z)}\, P_\ell^\mu(1-x)\, P_{\ell'}^\mu(1-x), \qquad (2\text{-}4\text{-}19)$$

where $N_{\ell\mu}$ and $N_{\ell'\mu}$ are normalization constants for spherical harmonics as $N_{\ell\mu} = [(2\ell+1)(\ell-\mu)!/(\ell+\mu)!]^{1/2}$, $z = 1/i\rho$, $P_\ell^\mu(\cos\theta)$ are associated Legendre polynomials, and $\cos\theta = (1-x)$. This form can be further simplified using contour integration methods to yield the final fully-separated equation for $g_{\ell\ell'}^{(|\mu|)}$ [Appendix B of Reference 17]:

$$g_{\ell\ell'}^{(|\mu|)}(\rho) = \sum_{\nu=0}^{\min[\ell,\ell'-|\mu|]} \tilde{\gamma}_{\mu\nu}^{\ell}(\rho)\, \gamma_{\mu\nu}^{\ell'}(\rho) \qquad (2\text{-}4\text{-}20)$$

where, $\min[\ell,\ell'-|\mu|]$ = the minimum of ℓ and $\ell-|\mu| \equiv [\ell,\ell'-|\mu|]$, $\rho = kR$,

$$\gamma_{\mu\nu}^{\ell}(\rho) = (-1)^\mu\, N_{\ell\mu}\, C_\ell^{(\mu+\nu)}(z)\, z^{\mu+\nu}/(\mu+\nu)!, \qquad (2\text{-}4\text{-}21)$$

and

$$\tilde{\gamma}_{\mu\nu}^{\ell}(\rho) = (2\ell+1)\, C_\ell^{(\nu)}(z)\, z^\nu/(N_{\ell\mu}\, \nu!). \qquad (2\text{-}4\text{-}22)$$

Here, $C_\ell(z)$ is the polynomial part of the spherical Hankel function as defined previously in Equation (2-4-15), and $C_\ell^{(\nu)}(z) = \partial^\nu C_\ell/\partial z^\nu$. Computational details concerning the evaluation of the C_ℓ's and $C_\ell^{(\nu)}$'s are given in Section 2.5.1.

Combining Equations (2-4-18) and (2-4-20) now yields the final form of the R-A separation:

$$G_{L,L'}(\vec{\rho}) = \frac{e^{i\rho}}{\rho} \sum_{\mu=-\ell}^{\ell} R^{\ell}_{m\mu}(\hat{\rho}^{-1}) \sum_{\nu=0}^{\min[\ell,\ell'-|\mu|]} \tilde{\gamma}^{\ell}_{\mu\nu}(\rho)\ \gamma^{\ell'}_{\mu\nu}(\rho)\ R^{\ell'}_{\mu m'}(\hat{\rho}),$$

which can be rearranged as

$$G_{L,L'}(\vec{\rho}) = \frac{e^{i\rho}}{\rho} \sum_{\mu=-\ell}^{\ell} \sum_{\nu=0}^{\min[\ell,\ell'-|\mu|]} \times [R^{\ell}_{m\mu}(\hat{\rho}^{-1})\ \tilde{\gamma}^{\ell}_{\mu\nu}(\rho)]\ [\gamma^{\ell'}_{\mu\nu}(\rho)\ R^{\ell'}_{\mu m'}(\hat{\rho})]. \qquad (2\text{-}4\text{-}23)$$

This can be further simplified by letting λ represent the expansion indices (μ,ν) and by defining the two bracketed quantities to be

$$\tilde{\Gamma}^{L}_{\lambda}(\vec{\rho}) = R^{\ell}_{m\mu}(\hat{\rho}^{-1})\ \tilde{\gamma}^{\ell}_{\mu\nu}(\rho) \qquad (2\text{-}4\text{-}24)$$

and,

$$\Gamma^{L'}_{\lambda}(\vec{\rho}) = R^{\ell'}_{\mu m'}(\hat{\rho})\ \gamma^{\ell'}_{\mu\nu}(\rho) \qquad (2\text{-}4\text{-}25)$$

to yield finally

$$G_{L,L'}(\vec{\rho}) = \frac{e^{i\rho}}{\rho} \sum_{\lambda} \bar{\Gamma}^{L}_{\lambda}(\vec{\rho})\ \Gamma^{L'}_{\lambda}(\vec{\rho}). \tag{2-4-26}$$

The factors involving L and L' are thus fully separated in this description, a key advantage of the R-A method, as we will see below in applying it to various cases in single- and multiple-scattering.

In addition, the sums in Equation (2-4-23) are found to be rapidly convergent, so that in practice results of very high accuracy are obtained with $|\mu| \leq 2$ and $\nu \leq 1$. This is the principal advantage of using this method as far as calculation times are concerned. We comment more on the consequences of working at this level in Section 3.2.1.

The results of this separable approximation can now be substituted into Equation (2-4-12) to yield the principal equation of the R-A method as applied to photoelectron and Auger electron diffraction:

$$\begin{aligned} G^{(N-1)}_{00,L_f}(\vec{R}_1,\vec{R}_2\ ..,\vec{R}_N=\vec{R}_d) = \sum_{\{\text{paths}\}} & \exp\{i(\rho_1+\rho_2+\ \ldots\ +\rho_N)\}/ \\ & (\rho_1\ \rho_2\ \ldots\rho_N) \sum_{\{\lambda_i\}} F_{\lambda_N,\lambda_{N-1}}(\vec{\rho}_N,\vec{\rho}_{N-1})\ \ldots \\ & \times F_{\lambda_3,\lambda_2}(\vec{\rho}_3,\vec{\rho}_2)\ F_{\lambda_2,\lambda_1}(\vec{\rho}_2,\vec{\rho}_1) \\ & \times W^{00,L_f}_{\lambda_N,\lambda_1}(\vec{\rho}_N,\vec{\rho}_1), \end{aligned} \tag{2-4-27}$$

where the quantities $F_{\lambda_k,\lambda_{k-1}}(\vec{\rho}_k,\vec{\rho}_{k-1}) = F_{\mu_k\nu_k,\mu_{k-1}\nu_{k-1}}(\vec{\rho}_k,\vec{\rho}_{k-1})$ are termed "scattering amplitude matrices" and are given by

$$F_{\lambda_k,\lambda_{k-1}}(\vec{\rho}_k,\vec{\rho}_{k-1}) = \sum_{L_{k-1}}^{\ell_{max}} t_{\ell_k}\, \Gamma^{L_k}_{\lambda_k}(\vec{\rho}_k)\, \tilde{\Gamma}^{L_k}_{\lambda_{k-1}}(\vec{\rho}_{k-1})$$
$$- \sum_{\ell_{k-1}=0}^{\ell_{max}} t_{\ell_k}\, \gamma^{\ell_k}_{\mu_k\nu_k}(\rho_k)\, R^{\ell_k}_{\mu_k\mu_{k-1}}(\hat{\rho}_k,\hat{\rho}_{k-1}^{-1})\, \tilde{\gamma}^{\ell_{k-1}}_{\mu_{k-1},\nu_{k-1}}(\rho_{k-1}), \quad (2\text{-}4\text{-}28)$$

with the composite rotation matrix $R^{\ell_k}_{\mu_k\mu_k}(\hat{\rho}_k,\hat{\rho}_{k-1}^{-1})$ corresponding to a rotation first of $\hat{\rho}_k$ into $\hat{z}$ and then $\hat{z}$ into $\hat{\rho}_{k-1}$. The scattering amplitude matrix $F_{\lambda_k,\lambda_{k-1}}(\vec{\rho}_k,\vec{\rho}_{k-1})$ can thus be thought of as a generalized spherical-wave scattering factor associated with the site at $\vec{R}_k$ and specific choices of scatterers at $\vec{R}_k$ and $\vec{R}_{k-2}$ (cf. Figure 2.6(b)).

The "termination matrix" involving the first and last factors in $G^{(N-1)}_{00,L_f}$ is given by

$$W^{00,L_f}_{\lambda_N,\lambda_1}(\vec{\rho}_N,\vec{\rho}_1) = \tilde{\Gamma}^{00}_{\lambda_N}(\vec{\rho}_N)\, \Gamma^{L_f}_{\lambda_1}(\vec{\rho}_1). \quad (2\text{-}4\text{-}29)$$

Our $W^{00,L_f}_{\lambda_N,\lambda_1}(\vec{\rho}_N,\vec{\rho}_1)$ is equivalent to $M^{L_f,00}_{\lambda_1,\lambda_N}(\vec{\rho}_1,\vec{\rho}_N)$ used by Rehr and Albers [17]. For photoelectron and Auger electron diffraction, where the detector is at infinity, W can be simplified further via

$$\tilde{\Gamma}^{00}_{\lambda_N}(\vec{\rho}_N) = R^0_{\mu_N 0}(\hat{\rho}_N^{-1})\ \tilde{\gamma}^0_{\mu_N \nu_N}(\rho_N), \tag{2-4-30}$$

where we have dropped the subscript N on λ and ρ for the simplicity. Note that because $R^{\ell}_{\mu 0}(\hat{\rho}^{-1}) = [4\pi/(2\ell+1)]^{1/2}\ Y_{\ell\mu}(\hat{\rho}^{-1})$, then $R^0_{\mu 0}(\hat{\rho}^{-1}) = 0$ for all $\mu \neq 0$ and $R^0_{\mu 0}(\hat{\rho}^{-1}) = 1$ for $\mu = 0$. Then Equation (2-4-30) becomes, from Equation (2-4-22),

$$\tilde{\Gamma}^{00}_{\lambda_N}(\vec{\rho}_N) = C_0^{(\nu)}(z)\ z^{\nu}/(N_{00}\ \nu!). \tag{2-4-31}$$

When the detector is at infinity, $\rho \to \infty$, $C_0(\infty) \to 1$, $C_0^{(\nu)}(\infty) = 0$ for all $\nu \neq 0$, and $C_0^{(\nu)}(\infty) = 1$ for $\nu = 0$. Hence from Equations (2-4-30) and (2-4-31), $\tilde{\Gamma}^{00}_{\lambda_N}(\rho_N \to \infty) = 1$, and

$$W^{00,L_f}_{\lambda_N,\lambda_1}(\vec{\rho}_N,\vec{\rho}_1) = \Gamma^{L_f}_{\lambda_1}(\vec{\rho}_1) = \gamma^{\ell_f}_{\mu_1\nu_1}(\hat{\rho}_1)\ R^{\ell_f}_{\mu_1 m_i}(\rho_1). \tag{2-4-32}$$

Note that this important termination quantity does not depend on $\vec{\rho}_N = \vec{\rho}_d$.

As indicated before in connection with Equation (2-4-4), the z axis is assumed to be along the polarization vector $\hat{\epsilon}$, as it simplifies the resulting expressions by requiring $m_i = m_f$. This means that whan a photoelectron is ejected for an initial state (ℓ_i, m_i) the final state should be $(\ell_i \pm 1, m_i)$. We will include this simplification in all applications of the R-A method to follow.

2.4.1. The General Single-Scattering Intensity in Photoelectron Diffraction:

The single-scattering intensity in photoelectron emission from a general $L_i = (\ell_i, m_i)$ core level can now be written from Equation (2-4-1) for N = 2 as

$$\frac{d\sigma}{d\Omega}(n_i,\ell_i,m_i \rightarrow E_{kin},\ell_{i\pm1},m_i) \propto \Big| \sum_{L_f=(\ell_{i\pm1},m_i)} m_{L_f,c}(\hat{\epsilon}) \exp(i\delta^c_{\ell_f}) \times \Big[G^{(0)}_{00,L_f}(\vec{R}_d \rightarrow \infty) + G^{(1)}_{00,L_f}(\vec{R}_j,\vec{R}_d \rightarrow \infty)\Big]\Big|^2 \qquad (2\text{-}4\text{-}33)$$

with the emitter as usual at the origin, $\vec{\rho}_j = k\vec{R}_j$, $\vec{\rho}_d = k\vec{R}_d$ in the first or direct wave term and $\vec{\rho}_d = k(\vec{R}_d - \vec{R}_j)$ in the second or scattered wave term.

$G^{(1)}_{00,L_f}$ must involve a sum over j = 1,2, ... ,M, where M is the number of single-scattering centers at positions $\vec{R}_1$, $\vec{R}_2$, ... ,$\vec{R}_M$. ($\vec{R}_1$, $\vec{R}_2$,.... here thus have a slightly different meaning from the general-path $\vec{R}_i$'s in Equation (2-4-1) and Figure 2.6). The first sum on L_f thus represents what can be termed the "direct" or "unscattered" wave ϕ_0 (cf. Figure 2.2) and the second sum on L_f and, within $G^{(1)}_{00,L_f}$, also on j represents all of the singly scattered waves ϕ_j. Since a non-s core level will, in general, have $(2\ell_i+1)$ degenerate sublevels, the final intensity observed must sum over emission from them

$$\frac{d\sigma_{n_i \ell_i}}{d\Omega} = \sum_{m_i=-\ell_i}^{\ell_i} \frac{d\sigma}{d\Omega} (n_i, \ell_i, m_i \rightarrow E_{kin}, \ell_{i\pm1}, m_i). \qquad (2\text{-}4\text{-}34)$$

For the $\ell_f = \ell_i - 1$ channel, there will only be $2(\ell_i-1) + 1$ terms in this sum. For the $\ell_f = \ell_i + 1$ channel, $(2\ell_i+1)$ terms must be included.

First we concentrate on the direct-wave which is represented by the Green's function $G^{(0)}_{00,L_f}(\vec{R}_d)$. From Equations (2-4-12) and (2-4-18)

$$G^{(0)}_{00,L_f}(\vec{R}_d) = G_{00,L_f}(\vec{R}_d)$$
$$- [\exp\{i\rho_d\}/\rho_d] \sum_{\mu=-\ell}^{\ell} R^{0}_{0\mu}(\hat{\rho}_d^{-1})\, g^{(|\mu|)}_{0\ell_f}(\rho_d)\, R^{\ell_f}_{\mu m_i}(\hat{\rho}_d). \qquad (2\text{-}4\text{-}35)$$

As stated earlier, $R^{0}_{0\mu}(\hat{\rho}^{-1})$ is zero for $\mu \neq 0$, and the only surviving term in the summation is $\mu = 0$. This allows us to use the following relations to simplify the expression for the direct-wave Green's function:

$$R^{\ell}_{0\mu}(\theta) = [4\pi/(2\ell+1)]^{1/2}\, Y_{\ell\mu}(\theta), \qquad (2\text{-}4\text{-}36a)$$

and a special case ($\ell = 0$ and $\mu = 0$) of Equation (2-4-36a),

$$R^{0}_{00}(\hat{\rho}) = 1.0, \qquad (2\text{-}4\text{-}36b)$$

and another special case ($\mu = 0$ and $\ell = 0$) of Equations (2-4-20) - (2-4-22)

$$g^{(0)}_{0\ell'}(\infty) = (2\ell'+1)^{1/2}. \qquad (2\text{-}4\text{-}36c)$$

By defining (θ_k,ϕ_k) to be the angles of $\vec{k}$ with respect to the polarization vector $\hat{\epsilon}$ (and hence the z axis), one can thus rewrite the direct-wave Green's function as

$$G^{(0)}_{00,L_f}(\vec{R}_d) = [\exp\{i\rho_d\}/\rho_d]\ (4\pi)^{1/2}\ Y_{\ell_f m_i}(\theta_k,\phi_k), \qquad (2\text{-}4\text{-}37)$$

or, since $\vec{k} \parallel \vec{R}_d$, $Y_{\ell_f m_i}(\theta_k,\phi_k) = Y_{\ell_f m_i}(\theta_d,\phi_d)$, where (θ_d,ϕ_d) are the angles of $\vec{R}_d$ with respect to the z axis.

The single-scattering Green's function, $G^{(1)}_{00,L_f}(\vec{R}_j,\vec{R}_d)$, can be expressed, using Equation (2-4-12), as follows:

$$G^{(1)}_{00,L_f}(\vec{R}_j,\vec{R}_d) = \sum_{\{j\},\{L_j\}} G_{00,L_j}(\vec{\rho}_d)\ t_{\ell_j}(\vec{R}_j)\ G_{L_j,L_f}(\vec{\rho}_j), \qquad (2\text{-}4\text{-}38)$$

where $\vec{\rho}_j = k(\vec{R}_j-(\vec{R}_0=0))$ and $\vec{\rho}_d = k(\vec{R}_d-\vec{R}_j)$. This geometry is shown in Figure 2.8. As noted previously, one can express t_ℓ in terms of partial wave phase shifts δ_ℓ as $t_\ell = \exp\{i\delta_\ell\}\sin(\delta_\ell)$.

Using Equation (2-4-18) one gets the following expression for $G^{(1)}_{00,L_f}$:

$$G^{(1)}_{00,L_f}(\vec{R}_j,\vec{R}_d) = \sum_{\{j\},\{L_j\}} [\exp\{i\rho_d\}/\rho_d] \times \sum_{\mu'} R^{0}_{0\mu'}(\hat{\rho}_d^{-1})\; g^{(|\mu'|)}_{0\ell_j}(\rho_d)\; R^{\ell_j}_{\mu' m_j}(\hat{\rho}_d)\; t_{\ell_j}(\vec{R}_j)\; [\exp\{i\rho_j\}/\rho_j] \times \sum_{\mu''} R^{\ell_j}_{m_j\mu''}(\hat{\rho}_j^{-1})\; g^{(|\mu''|)}_{\ell_j\ell_f}(\rho_j)\; R^{\ell_f}_{\mu'' m_i}(\hat{\rho}_j). \quad (2\text{-}4\text{-}39)$$

Writing g in terms of γ and $\tilde{\gamma}$ from Equation (2-4-20), one now gets,

$$= \sum_{\{j\},\{L_j\}} [\exp\{i\rho_d\}/\rho_d] \sum_{\mu'} R^{0}_{0\mu'}(\hat{\rho}_d^{-1}) \left[\sum_{\nu'=0}^{[0,\ell_j-|\mu'|]} \tilde{\gamma}^{0}_{\mu'\nu'}(\rho_d)\; \gamma^{\ell_j}_{\mu'\nu'}(\rho_d)\right] \times R^{\ell_j}_{\mu' m_j}(\hat{\rho}_d)\; t_{\ell_j}(\vec{R}_j)\; [\exp\{i\rho_j\}/\rho_j] \sum_{\mu''} R^{\ell_j}_{m_j\mu''}(\hat{\rho}_j^{-1}) \times \left[\sum_{\nu''=0}^{[0,\ell_j-|\mu''|]} \tilde{\gamma}^{\ell_j}_{\mu''\nu''}(\rho_j)\; \gamma^{\ell_f}_{\mu''\nu''}(\rho_j)\right] R^{\ell_f}_{\mu'' m_i}(\hat{\rho}_j). \quad (2\text{-}4\text{-}40)$$

Since the (μ,ν) combination occurs frequently, we will often use the simpler notation in which $\lambda = (\mu,\nu)$; when they do not occur together we will keep the original notation.

As another important simplification, note from Figure 2.8 that when $\vec{R}_d >> \vec{R}_j$, one can write $|\vec{R}_d - \vec{R}_j| \simeq |\vec{R}_d| - |\vec{R}_j| \cos\theta'$. Also as $\vec{R}_d \to \infty$, $\theta' \to \theta_j$ and hence the above expression becomes $|\vec{R}_d - \vec{R}_j| =$

$|\vec{R}_d| - |\vec{R}_j| \cos\theta_j$. Thus, $|\vec{R}_d - \vec{R}_j| = |\vec{R}_d| - R_j \cos\theta_j$, and ρ_d from the scatterer is found to be $k|\vec{R}_d - \vec{R}_j| = k|\vec{R}_d| - \rho_j\cos\theta_j$. The exponentials in Equation (2-4-40) thus become $\exp\{i\rho_d\}\exp\{i\rho_j\} = \exp\{i(k|\vec{R}_d| - \rho_j\cos\theta_j + \rho_j)\} = \exp\{ik|\vec{R}_d|\}\exp\{i\rho_j(1-\cos\theta_j)\} = \exp\{i\rho_d\}\exp\{i\rho_j(1-\cos\theta_j)\}$ with $\rho_d = kR_d$ now defined as in the direct wave case considered earlier. $\rho_j(1-\cos\theta_j)$ is thus simply the phase shift difference between the direct wave and the j^{th} scattered wave, as caused by the path length difference $R_j(1-\cos\theta_j)$. Equation (2-4-40) can thus be written as

$$G^{(1)}_{00,L_f}(\vec{R}_j,\vec{R}_d) = [\exp\{i\rho_d\}/\rho_d] \sum_{\{j\},\{L_j\}} [\exp\{i\rho_j(1-\cos\theta_j)\}/\rho_j]$$
$$\times \sum_{\lambda'\lambda''} R^0_{0\mu'}(\hat{\rho}_d^{-1})\, \tilde{\gamma}^0_{\lambda'}(\rho_d)\, t_{\ell_j}(\vec{R}_j)\, \gamma^{\ell_j}_{\lambda'}(\rho_d)\, R^{\ell_j}_{\mu' m_j}(\hat{\rho}_d)\, R^{\ell_j}_{m_j\mu''}(\hat{\rho}_j^{-1})$$
$$\times \tilde{\gamma}^{\ell_j}_{\lambda''}(\rho_j)\, \gamma^{\ell_f}_{\lambda''}(\rho_j)\, R^{\ell_f}_{\mu'' m_i}(\hat{\rho}_j). \qquad (2\text{-}4\text{-}41)$$

By considering explicit sums on ℓ_j and m_j and by realizing from Equation (2-4-36a) that $R^0_{0\mu'}(\alpha,\beta,\gamma) = (4\pi)^{1/2} Y_{0\mu'}(\beta,\gamma)$ is defined only when $\mu'=0$, one can simplify this expression. The facts that $\gamma^0_{0\nu'}(\rho_d) = C_0^{\nu'}(z_d)\, z_d^{\nu'} / \nu'!$ (cf. Equation (2-4-21)) and $C_0(z_d) = 1$ imply that $\gamma^0_{0\nu'}(\rho_d) \neq 0$ only when $\nu' \neq 0$. This makes $\nu' = 0$ the only surviving term in that summation. Hence $\lambda' = (\mu',\nu') = (0,0)$ for single-scattering. This makes $R^0_{00}(\hat{\rho}_d) = 1.0$ and $\tilde{\gamma}^0_{00}(\rho_d) = 1.0$ and we have

$$G^{(1)}_{00,L_f}(\vec{R}_j,\vec{R}_d) = [\exp\{i\rho_d\}/\rho_d] \sum_{\{j\}} [\exp\{i\rho_j(1-\cos\theta_j)\}/\rho_j]$$
$$\times \sum_{\ell_j} t_{\ell_j}(\vec{R}_j)\ \gamma^{\ell_j}_{00}(\rho_d) \sum_{\lambda''} \Big[\sum_{m_j} R^{\ell_j}_{0m_j}(\hat{\rho}_d)\ R^{\ell_j}_{m_j\mu''}(\hat{\rho}_j^{-1}) \Big]\ \tilde{\gamma}^{\ell_j}_{\lambda''}(\rho_j)$$
$$\times \gamma^{\ell_f}_{\lambda''}(\rho_j)\ R^{\ell_f}_{\mu''m_i}(\hat{\rho}_j). \qquad (2\text{-}4\text{-}42)$$

Notice that the m_j sum can considered to be a composite rotation. Hence, it can be written in general as

$$\sum_{m_j} R^{\ell_j}_{\mu' m_j}(\hat{\rho}_d)\ R^{\ell_j}_{m_j\mu''}(\hat{\rho}_j^{-1}) = R^{\ell_j}_{\mu'\mu''}(\hat{\rho}_d,\hat{\rho}_j^{-1}) \qquad (2\text{-}4\text{-}43)$$

where this composite rotation is $\hat{\rho}_d$ into $\hat{z}$ and $\hat{z}$ into $\hat{\rho}_j$. Combining Equations (2-4-42) and (2-4-43) yields,

$$G^{(1)}_{00,L_f}(\vec{R}_j,\vec{R}_d) = [\exp\{i\rho_d\}/\rho_d] \sum_{\{j\}} [\exp\{i\rho_j(1-\cos\theta_j)\}/\rho_j]$$
$$\times \sum_{\lambda''} F_{00,\lambda''}(\vec{\rho}_d,\vec{\rho}_j)\ W^{00,L_f}_{00,\lambda''}(\vec{\rho}_j) \qquad (2\text{-}4\text{-}44)$$

where, with suppression of the j subscript on ℓ,

$$F_{00,\lambda''}(\vec{\rho}_d,\vec{\rho}_j) = \sum_{\ell} t_\ell(\vec{R}_j)\ \gamma^{\ell}_{00}(\rho_d)\ R^{\ell}_{0\mu''}(\hat{\rho}_d,\hat{\rho}_j^{-1})\ \tilde{\gamma}^{\ell}_{\lambda''}(\rho_j),$$

and,

$$W^{00,L_f}_{00,\lambda''}(\vec{\rho}_j) - \gamma^{\ell_f}_{\lambda''}(\rho_j)\, R^{\ell_f}_{\mu'' m_i}(\hat{\rho}_j).$$

As noted previously, the quantities $W^{00,L_f}_{\lambda_N,\lambda_1}$ are equal to the quantities $M^{L,00}_{\lambda_1,\lambda_N}$ discussed by R-A. Note also that $W^{00,L_f}_{\lambda_N,\lambda_1}$ do not depend on $\vec{\rho}_d$ due the fact that the detector is at infinity (cf. Equations (2-4-29) - (2-4-32)). (See also for example, Equation 7 in reference 18.)

The total intensity for a single final state $L_f=(\ell_f,m_f)$ is thus calculated for single scattering from:

$$I^{(1)}_{L_f}(k,\theta,\phi) \alpha \left| (-i)^{\ell_f} \exp(i\delta^c_{\ell_f})\, R_{\ell_f}(E_{kin}) \langle \ell_f m_i | 10 | \ell_i m_i \rangle \times \left[G^{(0)}_{00,L_f}(\vec{R}_d) + G^{(1)}_{00,L_f}(\vec{R}_j,\vec{R}_d) \right] \right|^2, \qquad (2\text{-}4\text{-}45)$$

where we have now let $\theta_k \rightarrow \theta_d \rightarrow \theta$ and $\phi_k \rightarrow \phi_d \rightarrow \phi$ for simplicity. We have also cancelled out a trivial factor of $\exp\{-i\rho_d\}\exp\{i\rho_d\}/\rho_d^2 = \rho_d^{-2}$ that simply allows for the spherical-wave character of the outgoing flux. Examples of such single final states would be the p-wave final state in s photoelectron emission ($L_i=(0,0) \rightarrow L_f=(1,0)$), noting again that we take $\hat{\epsilon} \parallel \hat{z}$, and the often used s-wave final state approximation for Auger electron emission ($L_f=(0,0)$). For such cases, the excitation matrix elements and phase shifts in Equation (2-4-45) can simply be omitted, as they yield only a constant factor. In a

more general case such as p-wave initial state photoemission into s- and d-wave final states, one has to add final amplitudes with correct relative phases and to sum over the various m_i excitations possible. In general, the final intensity in this case can be written with Equation (2-4-34) as

$$I^{(1)}_{n_i \ell_i}(k,\theta,\phi) \alpha \sum_{m_i} \left| \sum_{\ell_f}^{\ell_i \pm 1} (-i)^{\ell_f} \exp(i\delta^c_{\ell_f}) R_{\ell_f}(E_{kin}) \langle \ell_f m_i | 10 | \ell_i m_i \rangle \right.$$
$$\left. \times [G^{(0)}_{00,L_f}(\vec{R}_d) + G^{(1)}_{00,L_f}(\vec{R}_j,\vec{R}_d)] \right|^2 \qquad (2\text{-}4\text{-}46)$$

where $\delta^c_{\ell_f}$ is the core level phase shift and $R_{\ell_f}(E_{kin})$ is defined previously. The integral $\langle \ell_f m_i | 10 | \ell_i m_i \rangle$ is a Gaunt coefficient to within a multiplication factor of $(4\pi/3)^{1/2}$. The explicit form of Equation (2-4-46) is

$$I^{(1)}_{n_i \ell_i}(k,\theta,\phi) \alpha \sum_{m_i} \left| \sum_{\ell_f}^{\ell_i \pm 1} (-i)^{\ell_f} \exp(i\delta^c_{\ell_f}) R_{\ell_f}(E_{kin}) \langle \ell_f m_i | 10 | \ell_i m_i \rangle \right.$$
$$\times \left[(4\pi)^{1/2} Y_{\ell_f m_i}(\theta,\phi) + \sum_{j=1}^{M} [\exp\{i\rho_j(1-\cos\theta_j)\}/\rho_j] \right.$$
$$\left. \left. \times \sum_{\lambda''} F_{00,\lambda''}(\vec{\rho}_d,\vec{\rho}_j) \, W^{00,L_f}_{00,\lambda''}(\vec{\rho}_j) \right] \right|^2 . \qquad (2\text{-}4\text{-}47)$$

which is a generalization of of the equivalent Equation (26) in Reference 17.

We also note that W is dependent only on the initial (L_f = (ℓ_f,m_f)) and final ($L_d = L_N$ = (0,0)) states. We will thus find that W has to be calculated only once for given L_f channel, whether it passes through a single or a multiple scattering path. Thus, one can perform multiple-scattering calculations for non-s initial states without much additional computer time. As an example, for a 23 atom ($\sqrt{3}\times\sqrt{3}$)R30° Ag on Si(111) cluster the correct d → f + s final state calculation takes only 5% more time than an approximate s → p final state calculation.

The range of the index ν is given in Equation (2-4-20): 0 to min[ℓ,ℓ'-|μ|]. So far we have not imposed restrictions on the summation index μ. The dependence of the coefficients $\tilde{\gamma}_{\mu\nu}(\rho)$ and $\gamma_{\mu\nu}(\rho)$ on ρ implies that $F_{\lambda\lambda'}(\vec{\rho},\vec{\rho}') \propto (\rho)^{-(2\nu+\mu)} (\rho')^{-(2\nu'+\mu')}$ for large ρ and ρ'. $\rho_j = kR_j$ is generally greater than unity, even for the smallest bond lengths, since nearest neighbor distances are always several atomic units and k for excitation above threshold is greater than the Fermi momentum k_f ($\approx$ 1.0 in atomic units) [17]. This suggests the possibility of truncating the summations on μ and ν, and we now consider several levels for doing this. Keeping only the largest matrix element yields the effective curved-wave scatttering amplitude $F^{(0)}_{00,00}$ for point scattering and a (1×1) matrix. Going beyond this requires recalling the restrictions on (μ,ν) set by prior definitions:

$$|\mu| \leq \ell, \tag{2-4-48a}$$

$$\nu \geq 0, \tag{2-4-48b}$$

$$\nu + |\mu| \leq \ell. \tag{2-4-48c}$$

In view of these, a calculation that is first order in $1/\rho$ for larger ρ could contain only non-zero (μ,ν) = (0,1), (+1,0) and (-1,0), leading to a (1×3) matrix for $F^{(1)}_{0\lambda'}$ whose elements are given in single scattering by Equation (2-4-44). (Note here that F is a column matrix due to the fact that the detector is at the infinity.) Going to second order in $1/\rho$ permits including additional non-zero (μ,ν) = (0,1), (2,0) and (-2,0) to yield a symmetric (1×6) matrix whose elements are given again by Equation (2-4-44). This second-order level of truncation, fortunately turns out be fully adequate for accurate numerical calculations, as discussed both by Rehr and Albers [17] and in Section 3.2.1. For third order one has to consider four additional combinations; they are (0,3), (0,-3), (1,1) and (1,-1). Third order thus corresponds to a (1×10) matrix for $F^{(3)}_{0\lambda'}$. Fourth order corresponds to a (1×15) matrix for $F^{(4)}_{0\lambda'}$.

We also note that since $R^{\ell_f}_{\mu'' m_i}(\hat{\rho}_j)$ is not defined when $\mu'' > \ell_f$ or $m_i > \ell_f$ [29], $W^{00,L_f}_{00,\lambda''}(\vec{\rho}_j)$ is also not defined under these conditions. These restrictions thus impose a limit on μ values allowed by order $(|\mu| + 2\nu)$ in <u>single scattering</u>. For example, in $\ell_f = 0$ to simulate Auger emission, only $\mu = 0$ is allowed. Therefore, only the first term in the F matrix has to be calculated in single scattering. Thus, for Auger emission 0^{th} order or (1×1) matrix theory is exact in single

scattering. For $\ell_f = 1$, the largest μ value allowed is 1 and hence, 2^{nd} order or (1×4) matrix theory is exact in the single-scattering level and the allowed (μ,ν) combinations are (0,0), (±1,0), and (0,1). (Note that in single scattering the F is a column matrix due the fact that the detector is at infinity.) For $\ell_f = 2$, the next two combinations (±2,0) allowed by the 2^{nd} order and (±1,1) allowed by 3^{rd}order theory makes the (1×8) matrix theory exact. For $\ell_f = 3$, it is a (1×13) and for $\ell_f = 4$ it is (1×15). It should be stressed that the aforementioned conclusions are true only for single scattering. In multiple scattering more than one scattering matrix is involved and such straightforward conclusions can not be made.

In the next three subsections we explore in detail a few final states of specific interest. This includes $\ell_f = 0$, which can be used to approximate the final state in Auger electron diffraction [2b], $\ell_f = 1$ to represent p-wave final state photoelectron diffraction and $\ell_f = 0,2$ to describe p → s + d photoelectron diffraction. In the section following these three subsections we extend this formalism to the fully general case of non-s emission with multiple-scattring.

2.4.2. Single-Scattering Intensity for an s-Wave Final State:

The most simple case we consider in scattering is the s-wave final state, an approximation often used in Auger electron emission

[2(c)]. In this case $\ell_f = m_f = 0$. Hence the direct-wave is

$$G^{(0)}_{00,00}(\vec{R}_d) = [\exp\{i\rho_d\}/\rho_d]. \qquad (2\text{-}4\text{-}49)$$

According to Equation (2-4-48b), the fact that $L_f = (0,0)$ forces W to be a (1×1) unit matrix. That is,

$$W^{00,00}_{00,00}(\vec{\rho}_j) = 1.0. \qquad (2\text{-}4\text{-}50)$$

Therefore, the only contributing term in the F matrix is $F_{00,00}$. This indicates that the R-A formalism is exact at the zeroth order for s-wave single-scattering. Now one can write,

$$G^{(1)}_{00,00}(\vec{R}_j,\vec{R}_d) = [\exp\{i\rho_d\}/\rho_d] \times \sum_j [\exp\{i\rho_j(1-\cos\theta_j)\}/\rho_j]\ F_{00,00}(\vec{\rho}_d,\vec{\rho}_j) \qquad (2\text{-}4\text{-}51)$$

where, again with the supression of the j subscript of ℓ,

$$F_{00,00}(\vec{\rho}_d,\vec{\rho}_j) = \sum_\ell t_\ell(\vec{R}_j)\ \gamma^\ell_{00}(\rho_d)\ R^\ell_{00}(\hat{\rho}_d,\hat{\rho}_j^{-1})\ \tilde{\gamma}^\ell_{00}(\rho_j)$$
$$= \sum_\ell (2\ell+1)\ t_\ell(\vec{R}_j)\ P_\ell(\cos\theta_j)\ C_\ell(z_j)$$

where, θ_j is as before the scattering angle or the angle between $\hat{R}_d$ and $\hat{R}_j$, and $z_j = 1/i\rho_j$. Note that this scattering factor is proportional to the plane wave result in Equation (2-2-2), but with

correction factors introduced via the C_ℓ's. This type of correction was first introduced by Rehr et al. in an earlier less general version of this method [24].

The final intensity in this case is thus

$$I_0^{(1)}(k,\theta,\phi) \propto \Big|1.0 + \sum_{j=1}^{M} [\exp\{i\rho_j(1-\cos\theta_j)\}/\rho_j] \times \sum_{\ell_j} (2\ell_j+1)\ t_{\ell_j}(\vec{R}_j)\ P_{\ell_j}(\cos\theta_j)\ C_{\ell_j}(z_j)\Big|^2, \qquad (2\text{-}4\text{-}52)$$

and we have neglected the $(1/\rho_d)^2$ and $|m_{00,c}e^{i\delta_0^0}|^2$ factors on the right hand side of the equation as they are common to both the primary and singly-scattered waves.

2.4.3. Single-Scattering Intensity for a s-Emission into a p-Wave Final State:

We now write down the intensity for a p-wave final state in single-scattering, as would correspond to s → p emission. Here we will use the following identities that can be derived or taken from our prior discussion and definitions:

$$L_f = (1,0), \qquad (2\text{-}4\text{-}53a)$$

$$R_{00}^0(\alpha,\beta,\gamma) = 1.0, \qquad (2\text{-}4\text{-}53b)$$

$$R_{00}^1(\alpha,\beta,\gamma) = (4\pi/3)^{1/2}\ Y_{10}(\beta,\gamma) = \cos\beta, \qquad (2\text{-}4\text{-}53c)$$

$$\tilde{\gamma}^{0}_{00}(\rho_d) = \gamma^{0}_{00}(\rho_d) = 1.0, \tag{2-4-53d}$$

$$\gamma^{1}_{00}(\rho_d) = \sqrt{3}\, c^{0}_{1}(z_d) = \sqrt{3}, \tag{2-4-53e}$$

$$g^{(0)}_{01}(\rho_d) = \tilde{\gamma}^{0}_{00}(\rho_d)\, \gamma^{1}_{00}(\rho_d). \tag{2-4-53f}$$

We now begin with the direct-wave; which is, from Equation (2-4-18):

$$G^{(0)}_{00,10}(\vec{R}_d) = [\exp\{i\rho_d\}/\rho_d] \times \sum_{\mu} R^{0}_{0\mu}(\hat{\rho}_d^{-1})\, g^{(|\mu|)}_{01}(\rho_d)\, R^{1}_{\mu 0}(\hat{\rho}_d). \tag{2-4-54}$$

Here the $R^{0}_{0\mu}$ term requires μ to be 0, as stated previously. Then we have

$$G^{(0)}_{00,10}(\vec{R}_d) = [\exp\{i\rho_d\}/\rho_d]\, g^{0}_{01}(\rho_d)\, R^{1}_{00}(\alpha,\beta,\gamma), \tag{2-4-55}$$

where (α,β,γ) are the Euler angles of $\hat{R}_d$ (or $\hat{k}$) with respect to the polarization vecter $\hat{\epsilon}$. Then, from Equation (2-4-53),

$$G^{(0)}_{00,10}(\vec{R}_d) = [\exp\{i\rho_d\}/\rho_d]\, \sqrt{3}\, \cos\beta. \tag{2-4-56}$$

One can choose the rotation so that the first Euler angle $\alpha = 0$ and $(0,\beta,\gamma) = (0,\theta,\phi)$ such that (θ,ϕ) are the polar and azimuthal angles between $\hat{\epsilon}$ and $\hat{R}_d$ (or $\hat{k}$). In that case,

$$G^{(0)}_{00,10}(\vec{R}_d) = [\exp\{i\rho_d\}/\rho_d]\, \sqrt{3}\, \cos\theta, \tag{2-4-57}$$

with $\cos\theta$ then also being equal to $\hat{\epsilon}\cdot\hat{k}$, the form seen in Equation (2-2-1).

Now let us turn to the single-scattering amplitude, which can be taken from Equation (2-4-44) as:

$$G^{(1)}_{00,10}(\vec{R}_j,\vec{R}_d) = [\exp\{i\rho_d\}/\rho_d] \sum_{j=1}^{M} [\exp\{i\rho_j(1-\cos\theta_j)\}/\rho_j] \times \sum_{\lambda''} F_{00,\lambda''}(\vec{\rho}_d,\vec{\rho}_j)\ W^{00,10}_{00,\lambda''}(\vec{\rho}_j) \qquad (2\text{-}4\text{-}58)$$

where, with the supression of the j index on ℓ,

$$F_{00,\lambda''}(\vec{\rho}_d,\vec{\rho}_j) = \sum_{\ell} t_\ell(\vec{R}_j)\ \gamma^{\ell}_{00}(\rho_d)\ R^{\ell}_{0\mu''}(\hat{\rho}_d,\hat{\rho}_j^{-1})\ \tilde{\gamma}^{\ell}_{\lambda''}(\rho_j),$$

and,

$$W^{00,10}_{00,\lambda''}(\vec{\rho}_j) = \gamma^{1}_{\lambda''}(\rho_j)\ R^{1}_{\mu''0}\ (\hat{\rho}_j).$$

The rotation matrices in the above equations are complex in nature and deserve further scrutiny. In the convention used by Edmonds [25],

$$R^{\ell}_{\mu\mu'}(\hat{\rho}) = R^{\ell}_{\mu\mu'}(\hat{z}\leftarrow\hat{\rho}) = R^{\ell}_{\mu\mu'}(\alpha,\beta,\gamma) = e^{i\mu\alpha}\ d^{\ell}_{\mu\mu'}(\beta)\ e^{i\mu'\gamma}, \qquad (2\text{-}4\text{-}59)$$

with $d^{\ell}_{\mu\mu'}(\beta)$ satisfying the symmetry relations $d^{\ell}_{\mu\mu'} = d^{\ell}_{-\mu',-\mu} = (-1)^{\mu+\mu'} d^{\ell}_{\mu'\mu}$.

For a simple matrix like $R^{1}_{\mu"0}(\hat{\rho}_j) = R^{1}_{\mu"0}(\alpha,\beta,\gamma)$ in W of Equation (2-4-58), one can choose the rotation such that $\alpha = 0$, $\beta = \theta_r$ and $\gamma = \phi_r$ where (θ_r,ϕ_r) are the azimuthal and polar angles of $\hat{\rho}_j$ with respect to the z axis. Therefore, the rotation matrix in W can be written as

$$R^{1}_{\mu"0}(\hat{\rho}_j) = R^{1}_{\mu"0}(0,\theta_r,\phi_r) = d^{1}_{\mu"0}(\theta_r). \qquad (2\text{-}4\text{-}60)$$

Unfortunately, the composite rotation is not that simple. The one for this case implies

$$R^{\ell}_{0\mu"}(\hat{\rho}_d,\hat{\rho}_j^{-1}) = R^{\ell}_{0\mu"}(\hat{\rho}_d \to \hat{z} \to \hat{\rho}_j). \qquad (2\text{-}4\text{-}61)$$

Let (θ_k,ϕ_k) and (θ_r,ϕ_r) be the spherical polar coordinates of $\hat{\rho}_d$ (which is parallel to $\vec{k}$) and $\hat{\rho}_j$ with respect to the z axis, respectively, and denote the composite rotation angles by (α,β,γ). Remember that the composite rotation is $\hat{\rho}_d \to \hat{z} \to \hat{\rho}_j$. Since $(0,\theta_r,\phi_r)$ corresponds to the $\hat{z} \leftarrow \hat{\rho}_j$ rotation, one has to use Euler angles for the inverse rotation, $(-\phi_r,-\theta_r,0)$, in place of $(0,\theta_r,\phi_r)$ in the composite rotation. Then we have after multiplying the two matrices and solving [18b]:

$$\alpha = \arg[(\sin\theta_k \cos\theta_r - \sin\theta_r \cos\theta_k \cos(\phi_k-\phi_r)) + i(\sin\theta_r \sin(\phi_r-\phi_k))], \qquad (2\text{-}4\text{-}62a)$$

$$\beta = \text{acos}[\sin\theta_k \sin\theta_r \cos(\phi_k-\phi_r) + \cos\theta_r \cos\theta_k], \qquad (2\text{-}4\text{-}62b)$$

$$\gamma = \arg[(\sin\theta_k \cos\theta_r \cos(\phi_k-\phi_r) - \cos\theta_k \sin\theta_r) - i(\sin\theta_k \sin(\phi_r-\phi_k))], \qquad (2\text{-}4\text{-}62c)$$

with the derivation of these angles being given in Section 2.5.2. Now the composite rotation matrix can be written as:

$$R^{\ell}_{0\mu"}(\hat{\rho}_d,\hat{\rho}_j^{-1}) = R^{\ell}_{0\mu"}(\hat{\rho}_d \rightarrow \hat{z} \rightarrow \hat{\rho}_j) = d^{\ell}_{0\mu"}(\beta)\ e^{i\mu"\gamma}. \qquad (2\text{-}4\text{-}63)$$

Computational details of the determination of $d^{\ell}_{\mu\mu}$, are given in Section 2.5.3. Equations (2-4-58), (2-4-60) and (2-4-63) can be combined to yield the final expression for s-emission and/or p-wave final-state single-scattering:

$$G^{(1)}_{00,10}(\vec{R}_j,\vec{R}_d) = [\exp\{i\rho_d\}/\rho_d] \sum_j [\exp\{i\rho_j(1-\cos\theta_j)\}/\rho_j] \times \sum_{\lambda"} F_{00,\lambda"}(\vec{\rho}_d,\vec{\rho}_j)\ W^{00,10}_{00,\lambda"}(\vec{\rho}_j) \qquad (2\text{-}4\text{-}64)$$

where, with the supression of the j index on ℓ,

$$F_{00,\lambda"}(\vec{\rho}_d,\vec{\rho}_j) = e^{i\mu"\gamma} \sum_{\ell} t_{\ell}(\vec{R}_j)\ \gamma^{\ell}_{00}(\rho_d)\ d^{\ell}_{0\mu"}(\beta)\ \tilde{\gamma}^{\ell}_{\lambda"}(\rho_j),$$

with β from Equation (2-4-62b), and,

$$W^{00,10}_{00,\lambda''}(\vec{\rho}_j) = \gamma^1_{\lambda''}(\rho_j)\ d^1_{\mu''0}(\theta_r).$$

Finally, the intensity is given by

$$I^{(1)}_1(k,\theta,\phi) \propto \left| G^{(0)}_{00,10}(\vec{R}_d) + G^{(1)}_{00,10}(\vec{R}_j,\vec{R}_d) \right|^2$$

$$\propto \Big| \sqrt{3}\cos\theta + \sum_j [\exp\{i\rho_j(1-\cos\theta_j)\}/\rho_j]$$
$$\times \sum_{\lambda''} F_{00,\lambda''}(\vec{\rho}_d,\vec{\rho}_j)\ W^{00,10}_{00,\lambda''}(\vec{\rho}_j) \Big|^2 \qquad (2\text{-}4\text{-}65)$$

with $F_{00,\lambda''}(\vec{\rho}_d,\vec{\rho}_j)$ and $W^{00,10}_{00,\lambda''}(\vec{\rho}_j)$ defined just above.

2.4.4. Single-Scattering Intensity for p-Emission into s and d Final-State Channels:

In the case of p emission, one has two final-state ℓ channels: s-wave and d-wave. Once they are calculated they should be added with the appropriate phase factors to get the final amplitude. We have already worked out the simple s-wave final state in detail. Now we consider the d-wave final state. This case, in contrast to those considered previously, has five possible channels. They are $m_f = -2$, -1, 0, 1, 2. But our continuing choice of $\hat{\epsilon}$ to be along the z axis imposes the restriction $m_i = m_f$. Since the initial p-state has only

m_i = -1, 0, 1, there are thus only three possible channels corresponding to m_f= -1, 0 and +1. Hence one has three possible direct d waves and three corresponding W matrices. The F matrices, as we have noted earlier, do not depend on the final state. Calculating the direct-wave Green's function for the cases of relevance yields, from Equation (2-4-35) the general expression:

$$G^{(0)}_{00,2m_i}(\vec{R}_d) = [\exp\{i\rho_d\}/\rho_d]\; g^0_{02}(\rho_d)\; R^2_{0m_i}(0,\theta,\phi). \qquad (2\text{-}4\text{-}66a)$$

The specific values of the above expression are, from Equations (2-4-36):

$$G^{(0)}_{00,20}(\vec{R}_d) = [\exp\{i\rho_d\}/\rho_d]\; \sqrt{5}\; (3\cos^2\theta - 1)\; /\; 2, \qquad (2\text{-}4\text{-}66b)$$

$$G^{(0)}_{00,2\pm1}(\vec{R}_d) = \pm[\exp\{i\rho_d\}/\rho_d]\; (15/2)^{1/2}\cos\theta\; \sin\theta\; \exp\{\pm i\phi\}. \qquad (2\text{-}4\text{-}66c)$$

To get the single-scattering wave, we begin with Equation (2-4-44) and substitute L_f = (2,-1), (2,0) and (2,1):

$$G^{(1)}_{00,2m_i}(\vec{R}_j,\vec{R}_d) = [\exp\{i\rho_d\}/\rho_d] \sum_{j=1}^{M} [\exp\{i\rho_j(1-\cos\theta_j)\}/\rho_j] \times \sum_{\lambda''} F_{00,\lambda''}(\vec{\rho}_d,\vec{\rho}_j)\; W^{00,2m_i}_{00,\lambda''}(\vec{\rho}_j) \qquad (2\text{-}4\text{-}67)$$

where, with the supression of the j index on ℓ,

$$F_{00,\lambda''}(\vec{\rho}_d,\vec{\rho}_j) = \sum_{\ell} t_\ell(\vec{R}_j)\ \gamma^{\ell}_{00}(\rho_d)\ R^{\ell}_{0\mu''}(\vec{\rho}_d,\vec{\rho}_j^{-1})\ \tilde{\gamma}^{\ell}_{\lambda''}(\rho_j),$$

and,

$$W^{00,2m_i}_{00,\lambda''}(\vec{\rho}_j) = \gamma^2_{\lambda''}(\rho_j)\ R^2_{\mu''m_i}(\hat{\rho}_j).$$

As we have stated earlier, only the W factor changes with the precise specifications of L_f. Everything we said previously about rotation matrices still holds. This is true for all higher ℓ's. That is, the derivation for other final states of interest is trivial. The final intensity for the p-wave initial state problem in single scattering is thus:

$$I^{(1)}_{0+2}(k,\theta,\phi) \propto \sum_{m_i} \Big|\sum_{\ell_f} (-i)^{\ell_f} \exp(i\delta^c_{\ell_f})\ R_{\ell_f}(E_{kin})\ \langle \ell_i m_i | 10 | \ell_f m_i \rangle \times [G^{(0)}_{00,\ell_f m_i}(\vec{R}_d) + G^{(1)}_{00,\ell_f m_i}(\vec{R}_j,\vec{R}_d)]\Big|^2,$$

$$\propto \Big| (-i)^2 \exp(i\delta^c_2)\ R_2(E_{kin})\ \langle 1\text{-}1|10|2\text{-}1\rangle \times [(15/2)^{1/2} \cos\theta \sin\theta \exp(-i\phi) + \sum_{j=1}^{M} [\exp\{i\rho_j(1-\cos\theta_j)\}/\rho_j] \times \sum_{\lambda''} F_{00,\lambda''}(\vec{\rho}_d,\vec{\rho}_j)\ W^{00,2\text{-}1}_{00,\lambda''}(\vec{\rho}_j)]\Big|^2$$

$$+ \Big| \{(-i)^0 \exp(i\delta_0^c)\, R_0(E_{kin}) \langle 10|10|00\rangle \Big[1+\sum_{j=1}^{M} [\exp\{i\rho_j(1-\cos\theta_j)\}/\rho_j]$$

$$\times \sum_{\ell_j} (2\ell_j+1)\, t_{\ell_j}(\vec{R}_j)\, P_{\ell_j}(\cos\theta)\, C_{\ell_j}(z_j)\Big]\} +$$

$$\{(-i)^2 \exp(i\delta_2^c)\, R_2(E_{kin}) \langle 10|10|20\rangle \Big[\sqrt{5}\,(3\cos^2\theta - 1)/2$$

$$+\sum_{j} [\exp\{i\rho_j(1-\cos\theta_j)\}/\rho_j]$$

$$\times \sum_{\lambda''} F_{00,\lambda''}(\vec{\rho}_d\, \vec{\rho}_j)\, W^{00,20}_{00,\lambda''}(\vec{\rho}_j)\Big]\}\Big|^2$$

$$+ \Big| (-i)^2 \exp(i\delta_2^c)\, R_2(E_{kin}) \langle 11|10|21\rangle$$

$$\times \Big[-(15/2)^{1/2} \cos\theta \sin\theta \exp(i\phi) + \sum_{j=1}^{M} [\exp\{i\rho_j(1-\cos\theta_j)\}/\rho_j]$$

$$\times \sum_{\lambda''} F_{00,\lambda''}(\vec{\rho}_d,\vec{\rho}_j)\, W^{00,21}_{00,\lambda''}(\vec{\rho}_j)\Big]\Big|^2 \qquad (2\text{-}4\text{-}68)$$

with $F_{00,\lambda''}(\vec{\rho}_d,\vec{\rho}_j)$ and $W^{00,2m_i}_{00,\lambda''}(\vec{\rho}_j)$ defined just above. Again $t_{\ell_j} = \exp\{i\delta_{\ell_j}\} \sin\delta_{\ell_j}$ is a t-matrix element at site j. $P_{\ell_j}(\cos\theta)$ is a Legendre polynomial of order ℓ_j, and $C_{\ell_j}(z)$ is the polynomial part of the spherical Hankel functions in the variable $z = 1/i\rho$.

This expression illustrates a general feature of the final-state inteference between $\ell_f = \ell_i \pm 1$ channels that will convay through all our results: inteference can only occur between final-state channels with the same $m_f = m_i$ values. Thus, we can see it only between $L_f = (0,0)$ and $L_f = (2,0)$. For the more general case to be treated below,

this will mean that inteference arises between $\ell_i + 1$ and $\ell_i - 1$ only for the $m_f = m_i$ values of $\ell_i - 1$, $\ell_i - 2$, ..., $-(\ell_i - 1)$.

It is known in general that, at the higher energies of $\geq$ 500 eV typical in x-ray photoelectron diffraction, the $(\ell-1)$ component becomes less significant compared to the $(\ell+1)$ component in emission from a state with angular momentum ℓ [22]; that is, one might here be able to make the assumption, $R_2(E_{kin}) >> R_0(E_{kin})$, thus neglecting the s-wave contribution in emission from a p-initial state. This approximation, however, should be tested for each individual system involved, as a calculation of these matrix elements for a number of elements up to the 1 keV range yield ratios R_2/R_0 that are only as large as ~2-4 [22].

2.4.5. Multiple-Scattering Intensity for Emission from a General Initial State:

We here discuss emission from a general $L_i = (\ell_i, m_i)$ initial state to a set of general final states, but with the important addition that multiple-scattering paths of arbitrary order are considered. The direct wave in this case is identical to that given in Equation (2-4-37). By definition a multiple scattering path contains the emitter and more than one scatterer. Different aspects of a typical multiple-scattering path are shown in Figure 2.6. Our notation for the various vectors needed to unambiguously describe a complete set of multiple-scattering paths will be more explicit than

that of R-A, although we will remain as close to it as possible. Specifically the emitter is still taken to be at $\vec{R}_0 = 0$ and the vectors of all other scatterers $\vec{R}_j$ and the detector $\vec{R}_d$ are measured with respect to this origin. To keep track of a given typical scattering path $\vec{R}_0, \vec{R}_1, \vec{R}_2, \ldots, \vec{R}_N, \vec{R}_{N+1} = \vec{R}_d$, we will designate all possible first scatterers by $\vec{R}_{j_1}$, all possible second scatterers by $\vec{R}_{j_2}$, etc., up to a general k^{th} order $\vec{R}_{j_k}$. The vector used in the arguments of the F and W matrices we can then calculate from $\vec{\rho}_{j_k j_{k-1}} = k\,(\vec{R}_{j_k} - \vec{R}_{j_{k-1}})$, with two indices now required due to the many paths involved. For the first step in a path, this is simply $\vec{\rho}_{j_1} = k\,\vec{R}_{j_1} = \vec{\rho}_j$ in the single-scattering discussion of the prior section. For the last step in any N-event path, $\vec{\rho}_{d,j_N} = k\,(\vec{R}_d - \vec{R}_{j_N}) = \vec{\rho}_d$ for simplicity, since this vector always points from the last scatterer to the detector at ∞. In multiple scattering, there may be several consecutive scattering events, including those in which the photoelectron is scattered off the emitter at some step after a first scattering event on another site. In this case, we will treat the emitter as a neutral atom even though it contains a core hole. The presence of this core hole could affect the phase shifts $\delta_{\ell_0}(\vec{R}_0)$ somewhat, but final state screening is expected to reduce this effect, so we have chosen to ignore it here. The restriction on $\vec{\rho}_{j_k j_{k-1}}$ is that $j_k \neq j_{k-1}$ for all k: that is, the photoelectron cannot be scattered off the same atom twice in a row. In this notation, j_i can

represent any atom of the M atoms in the cluster, including the emitter. The summations in any of the multiple-scattering paths to follow will thus be over (M-1) j_k values at each order in a path, with the restriction that $j_k \neq j_{k-1}$ for all k. We will not write this restriction explicitly in equations, but indicate such sums only with the set of indices $\{j_i\}$.

The N^{th} order multiple-scattering Green's function in photoemission to a state $L_f = (\ell_f, m_i)$, can now be written following Equation (2-4-12) as,

$$G^{(N)}_{00,L_f}(\vec{R}_{j_1},\vec{R}_{j_2},\ \ldots\ ,\vec{R}_{j_N},\vec{R}_d) = \sum_{\{j_i\},\{L_i\}} G_{00,L_N}(\hat{\rho}_d)\ t_{\ell_N}(\vec{R}_{j_N})\ G_{L_N L_{N-1}}(\hat{\rho}_{j_N j_{N-1}}) \ldots\ldots\ldots \ldots\ t_{\ell_2}(\vec{R}_{j_2})\ G_{L_2 L_1}(\hat{\rho}_{j_2 j_1})\ t_{\ell_1}(\vec{R}_{j_1})\ G_{L_1 L_f}(\hat{\rho}_{j_1}) \qquad (2\text{-}4\text{-}69)$$

where we have now added $\vec{R}_{N+1} \equiv \vec{R}_d$ so that the scattering order is directly given in $G^{(N)}_{00,L_f}$. This general Green's function can now be written in terms of the prior W and F matrices, again using the notation $\lambda = (\mu,\nu)$ to make expressions more compact. This is very useful in multiple scattering where several (μ,ν) combinations are involved.

The steps leading to a specific evaluation of this $G^{(N)}_{00,L_f}$ are very similar to those shown in detail for the single-scattering cases. Therefore, we will omit details here and directly write from Equations (2-4-27) and (2-4-69)

$$G^{(N)}_{00,L_f}(\vec{R}_{j_1},\vec{R}_{j_2},\ \ldots\ ,\vec{R}_{j_N},\vec{R}_d) =$$

$$\sum_{(j_i)} [\exp\{i\rho_d+\rho_{j_N j_{N-1}}+\ldots+\rho_{j_1}\}/(\rho_d\ \rho_{j_N j_{N-1}}\cdots\rho_{j_1})]$$

$$\times \sum_{(\lambda_i)} F_{00,\lambda_N}(\vec{\rho}_d,\vec{\rho}_{j_N j_{N-1}})\ F_{\lambda_N\lambda_{N-1}}(\vec{\rho}_{j_N j_{N-1}},\vec{\rho}_{j_{N-1} j_{N-2}})\cdots\cdot$$

$$\cdots\cdots\ F_{\lambda_2\lambda_1}(\vec{\rho}_{j_2 j_1},\vec{\rho}_{j_1})\ W^{00,L_f}_{00,\lambda_N}(\vec{\rho}_{j_1}), \qquad (2\text{-}4\text{-}70)$$

with the second subscript of W equals to 0 due to the fact that the detector is at ∞.

Now we look at each factor in the above expression in detail. First, we consider the prefactor involving the exponential term. This can be written in terms of scattering angles. The notation we use for angles is as follows.

$$\theta_{j_k j_{k-1}} = \text{angle between vectors } \hat{\rho}_{j_{k+1} j_k} \text{ and } \hat{\rho}_{j_k j_{k-1}}, \qquad (2\text{-}4\text{-}70a)$$

which is the true scattering angle for the event at $\vec{R}_{j_k}$, and

$$\theta'_{j_k j_{k-1}} = \text{angle between vectors } \hat{\rho}_d \text{ and } \hat{\rho}_{j_k j_{k-1}}, \qquad (2\text{-}4\text{-}70b)$$

which is the angle required for calculating the path length difference along $\hat{\rho}_{j_k j_{k-1}}$ leading to the event at $\vec{R}_{j_k}$. Then, by repeated usage of the argument used to obtain Equation (2-4-41), we can show that

$$\exp(i\rho_d + \rho_{j_N j_{N-1}} + \ldots + \rho_{j_1}) \,/\, (\rho_d\, \rho_{j_N j_{N-1}} \ldots \rho_{j_1}) =$$

$$(\exp(i\rho_d)/\rho_d) \prod_{k=1}^{N} [\exp(i\rho_{j_k j_{k-1}} (1-\cos\theta'_{j_k j_{k-1}})/\rho_{j_k j_{k-1}}]. \qquad (2\text{-}4\text{-}71)$$

After the last scattering event, the photoelectron escapes towards the detector. This last event, or the first event in a time reversed sense, involves a finite and an infinite distance and is represented by $F_{00,\lambda_N}(\vec{\rho}_d, \vec{\rho}_{j_N j_{N-1}})$. This F matrix is identical in structure to the one we worked out in the single-scattering case. The W matrix as defined in Equation (2-4-44) depends only on the polarization the incoming radiation and the position of the first scatterer relative to the emitter; thus it does not require any modification either. The only other factors left to calculate are the matrices $F_{\lambda_k \lambda_{k-1}}(\vec{\rho}_{j_k j_{k-1}}, \vec{\rho}_{j_{k-1} j_{k-2}})$ involving two finite distances. The general form of these is identical to that given in Equation (2-4-28) for the two bond vectors $\vec{\rho}_1$ and $\vec{\rho}_2$ connecting these atomic positions:

$$F_{\lambda',\lambda''}(\vec{\rho}_1, \vec{\rho}_2) = \sum_{\ell} t_\ell\, \gamma^{\ell}_{\lambda'}(\rho_1)\, R^{\ell}_{\mu',\mu''}(\hat{\rho}_1, \hat{\rho}_2^{-1})\, \tilde{\gamma}^{\ell}_{\lambda''}(\rho_2). \qquad (2\text{-}4\text{-}72)$$

Now combining the above equations, we have,

$$G^{(N)}_{00,L_f}(\vec{R}_{j_1},\vec{R}_{j_2},\ \ldots\ ,\vec{R}_{j_N},\vec{R}_d) =$$

$$(\exp\{i\rho_d\}/\rho_d) \sum_{\{j_i\}} \Big[\prod_{k=1}^{N} [\exp\{i\rho_{j_k j_{k-1}}(1-\cos\theta'_{j_k j_{k-1}})\}/\rho_{j_k j_{k-1}}]$$

$$\times \sum_{\{\lambda_i\}} F_{00,\lambda_N}(\vec{\rho}_d,\vec{\rho}_{j_N j_{N-1}})\ F_{\lambda_N\lambda_{N-1}}(\vec{\rho}_{j_N j_{N-1}},\vec{\rho}_{j_{N-1} j_{N-2}}) \cdots\cdots$$

$$\times F_{\lambda_2\lambda_1}(\vec{\rho}_{j_2 j_1},\vec{\rho}_{j_1})\ W^{00,L_f}_{00,\lambda_1}(\vec{\rho}_{j_1})\Big] \qquad (2\text{-}4\text{-}73)$$

where,

$$F_{00,\lambda_N}(\vec{\rho}_d,\vec{\rho}_{j_N j_{N-1}}) = \sum_{\ell} t_\ell\ \gamma^{\ell}_{00}(\rho_d)\ R^{\ell}_{0\mu_N}(\hat{\rho}_d,\hat{\rho}^{-1}_{j_N j_{N-1}})\ \tilde{\gamma}^{\ell}_{\lambda_N}(\rho_{j_N j_{N-1}})$$

$$F_{\lambda_k,\lambda_{k-1}}(\vec{\rho}_{j_k j_{k-1}},\vec{\rho}_{j_{k-1} j_{k-2}}) =$$

$$\sum_{\ell_{k-1}} t_{\ell_{k-1}}\ \gamma^{\ell}_{\lambda_k}(\rho_{j_k j_{k-1}})\ R^{\ell}_{\mu_k\mu_{k-1}}(\hat{\rho}_{j_k j_{k-1}},\hat{\rho}^{-1}_{j_{k-1} j_{k-2}})\ \tilde{\gamma}^{\ell}_{\lambda_{k-1}}(\rho_{j_{k-1} j_{k-2}}),$$

and,

$$W^{00,L_f}_{00,\lambda_1}(\vec{\rho}_{j_1}) = \gamma^{\ell_f}_{\lambda_1}(\rho_{j_1})\ R^{\ell_f}_{\mu_1 m_i}(\hat{\rho}_{j_1}).$$

Now, as an specific example, we write out the above general equation explicitly for fifth-order multiple-scattering:

$$G^{(5)}_{00,L_f}(\vec{R}_{j_1},\vec{R}_{j_2},\vec{R}_{j_3},\vec{R}_{j_4},\vec{R}_{j_5},\vec{R}_d) =$$

$$(\exp\{i\rho_d\}/\rho_d) \sum_{\{j_i\}} \Big[\prod_{k=1}^{N} [\exp\{i\rho_{j_k j_{k-1}}(1-\cos\theta'_{j_k j_{k-1}})\}/\rho_{j_k j_{k-1}}]$$

$$\times \sum_{\{\lambda_i\}} F_{00,\lambda_5}(\vec{\rho}_d,\vec{\rho}_{j_5 j_4})\, F_{\lambda_5\lambda_4}(\vec{\rho}_{j_5 j_4},\vec{\rho}_{j_4 j_3})\, F_{\lambda_4\lambda_3}(\vec{\rho}_{j_4 j_3},\vec{\rho}_{j_3 j_2})$$

$$\times F_{\lambda_3\lambda_2}(\vec{\rho}_{j_3 j_2},\vec{\rho}_{j_2 j_1})\, F_{\lambda_2\lambda_1}(\vec{\rho}_{j_2 j_1},\vec{\rho}_{j_1})\, W^{00,L_f}_{00,\lambda_1}(\vec{\rho}_{j_1}) \Big] \qquad (2\text{-}4\text{-}74)$$

$$- (\exp\{i\rho_d\}/\rho_d) \sum_{\{j_i\}} \Big[[\exp\{i\rho_{j_1}(1-\cos\theta'_{j_1})\}/\rho_{j_1}]$$

$$\times [\exp\{i\rho_{j_2 j_1}(1-\cos\theta'_{j_2 j_1})\}/\rho_{j_2 j_1}]\, [\exp\{i\rho_{j_3 j_2}(1-\cos\theta'_{j_3 j_2})\}/\rho_{j_3 j_2}]$$

$$\times [\exp\{i\rho_{j_4 j_3}(1-\cos\theta'_{j_4 j_3})\}/\rho_{j_4 j_3}]\, [\exp\{i\rho_{j_5 j_4}(1-\cos\theta'_{j_5 j_4})\}/\rho_{j_5 j_4}]$$

$$\times F_{00,\lambda_5}(\vec{\rho}_d,\vec{\rho}_{j_5 j_4})\, F_{\lambda_5\lambda_4}(\vec{\rho}_{j_5 j_4},\vec{\rho}_{j_4 j_3})\, F_{\lambda_4\lambda_3}(\vec{\rho}_{j_4 j_3},\vec{\rho}_{j_3 j_2})$$

$$\times F_{\lambda_3\lambda_2}(\vec{\rho}_{j_3 j_2},\vec{\rho}_{j_2 j_1})\, F_{\lambda_2\lambda_1}(\vec{\rho}_{j_2 j_1},\vec{\rho}_{j_1})\, W^{00,L_f}_{00,\lambda_1}(\vec{\rho}_{j_1}) \Big]. \qquad (2\text{-}4\text{-}75)$$

In some of our numerical simulations involving small clusters of ≤ 40 atoms, we have used the equivalent expressions up to tenth-order multiple-scattering.We will later use the above expansion in the discussion of structure of the computer code used for numerical simulations.

The final expression for the intensity for a single final-state $L_f = (\ell_f, m_i)$ is thus

$$I_{L_f}^{(N_{max})}(k,\theta,\phi) \propto \sum_{m_i} \left| \left[G^{(0)}_{00,\ell_f m_i}(\vec{R}_d) + G^{(1)}_{00,\ell_f m_i}(\vec{R}_{j_1},\vec{R}_d) + \sum_{N=2}^{\infty} G^{(N)}_{00,\ell_f m_i}(\vec{R}_{j_1},\vec{R}_{j_2}, \ldots ,\vec{R}_{j_N},\vec{R}_d) \right] \right|^2. \quad (2\text{-}4\text{-}76)$$

where N_{max} is the highest scattering order included. On the right hand side of the above expression, the first term represents the direct wave, the second the singly-scattered waves and the final summation the multiply-scattered waves up to all orders. In practice we go only up to the tenth order multiple-scattring ($N_{max} = 10$).

For emission from all the initial magnetic sublevels $\ell_i m_i$ into two final state channels $\ell_f = \ell_i \pm 1, m_i$ we have the fully general result

$$I_{n_i \ell_i}^{(N_{max})}(k,\theta,\phi) \propto \sum_{m_i} \left| \sum_{\ell_f} (-i)^{\ell_f} \exp(i\delta^c_{\ell_f}) R_{\ell_f}(E_{kin}) \langle \ell_f m_i | 10 | \ell_i m_i \rangle \times \left[G^{(0)}_{00,\ell_f m_i}(\vec{R}_d) + G^{(1)}_{00,\ell_f m_i}(R_{j_1},\vec{R}_d) + \sum_{N=2}^{N_{max}} G^{(N)}_{00,\ell_f m_i}(\vec{R}_{j_1},\vec{R}_{j_2}, \ldots ,\vec{R}_{j_N},\vec{R}_d) \right] \right|^2. \quad (2\text{-}4\text{-}77)$$

In the above expression $G^{(0)}_{00,\ell_f m_i}$ represents the direct wave, $G^{(1)}_{00,\ell_f m_i}$ the singly-scattered waves, and $G^{(N)}_{00,\ell_f m_i}$ in the summation represents the N^{th} order multiply-scattered waves. Equation (2-4-77) can be written more explicitly as,

$$I_{n_i \ell_i}^{(N_{max})}(k,\theta,\phi) \propto \sum_{m_i} \left| \sum_{\ell_f} (-i)^{\ell_f} \exp(i\delta_{\ell_f}^{c}) \, R_{\ell_f}(E_{kin}) \, \langle \ell_f m_i | 10 | \ell_i m_i \rangle \right.$$

$$\times \left[(4\pi)^{1/2} \, Y_{\ell_f m_i}(\theta) + \right.$$

$$\sum_{j_1} \left[\exp\{ i\rho_{j_1} (1-\cos\theta_{j_1}) \} / \rho_{j_1} \right] \sum_{\lambda_1} F_{00,\lambda_1}(\vec{\rho}_d, \vec{\rho}_{j_1}) \, W_{00,\lambda_1}^{00,L_f}(\vec{\rho}_{j_1}) +$$

$$\sum_{N=2}^{N_{max}} \sum_{\{j_i\}} \left[\prod_{k=1}^{N} \left[\exp\{ i\rho_{j_k j_{k-1}} (1-\cos\theta'_{j_k j_{k-1}}) \} / \rho_{j_k j_{k-1}} \right] \right.$$

$$\sum_{\{\lambda_i\}} F_{00,\lambda_N}(\vec{\rho}_d, \vec{\rho}_{j_N j_{N-1}}) \, F_{\lambda_N \lambda_{N-1}}(\vec{\rho}_{j_N j_{N-1}}, \vec{\rho}_{j_{N-1} j_{N-2}}) \cdots\cdots$$

$$\left. \left. \cdots\cdots\cdots F_{\lambda_2 \lambda_1}(\vec{\rho}_{j_2 j_1}, \vec{\rho}_{j_1}) \, W_{00,\lambda_1}^{00,L_f}(\vec{\rho}_{j_1}) \right] \right] \Big|^2, \qquad (2\text{-}4\text{-}78)$$

where F_{00,λ_N}, $F_{\lambda_k \lambda_{k-1}}$, and $W_{00,\lambda_1}^{00,L_f}$ are given with Equation (2-4-73).

2.4.6. Inclusion of Inelastic Scattering, Vibrational Effects, Instrumental Angular Averaging and Unpolarized Radiation:

We now consider the inclusion of several additional effects that are essential for a quantitative comparison of theory and experiment: inelastic scattering, vibrational effects, intrumental angular averaging, and the possible use of unpolarized radiation.

A fully rigorous method for including inelestic attenuation is so far not available, and thus we use the common phenomenological approach of an exponential decay of the amplititude of each component

of the photoelectron wave with the distance travelled in the solid before escaping through the "surface". The surface here is a plane used to define both the cutoff of inelastic scattering and the location of possible refraction effects due to the inner potential V_0 (as discussed below). If the distance travelled along a given path is L and the inelastic attenuation length for photoelectron <u>intensity</u> is Λ_e, then the exponential decay factor for the <u>amplitude</u> is $\exp\{-L/2\Lambda_e\}$. Incorporating such factors into Equation (2-4-78) yields:

$$
\begin{aligned}
I^{(N_{max})}_{n_i\ell_i}(k,\theta,\phi) \;\alpha\; & \sum_{m_i} \Big| \sum_{\ell_f} (-i)^{\ell_f} \exp(i\delta^c_{\ell_f})\, R_{\ell_f}(E_{kin}) \,\langle \ell_f m_i \; 10 | \ell_i m_i \rangle \\
\times \Bigg[& (4\pi)^{1/2}\, Y_{\ell_f m_i}(\theta)\, \exp\{-|\vec{R}_{0S}|/2\Lambda_e\} + \\
& \sum_{j_1} [\exp\{i\rho_{j_1}(1-\cos\theta_{j_1})\}/\rho_{j_1}]\, \exp\{-|\vec{R}_{j_1 S}|/2\Lambda_e\}\, \exp\{-|\vec{R}_{j_1}|/2\Lambda_e\} \\
& \times \sum_{\lambda_1} F_{00,\lambda_1}(\vec{\rho}_d, \vec{\rho}_{j_1})\, W^{00,L_f}_{00,\lambda_1}(\vec{\rho}_{j_1}) + \\
& \sum_{N=2}^{N_{max}} \sum_{\{j_i\}} \Bigg[\prod_{k=1}^{N} [\exp\{i\rho_{j_k j_{k-1}}(1-\cos\theta'_{j_k j_{k-1}})\}/\rho_{j_k j_{k-1}}]\, \exp\{-|\vec{R}_{j_N S}|/2\Lambda_e\} \\
& \times \exp\{-|\vec{R}_{j_N j_{N-1}}|/2\Lambda_e\} \,..\, \exp\{-|\vec{R}_{j_2 j_1}|/2\Lambda_e\}\, \exp\{-|\vec{R}_{j_1}|/2\Lambda_e\} \\
& \times \sum_{\{\lambda_i\}} F_{00,\lambda_N}(\vec{\rho}_d, \vec{\rho}_{j_N j_{N-1}})\, F_{\lambda_N \lambda_{N-1}}(\vec{\rho}_{j_N j_{N-1}}, \vec{\rho}_{j_{N-1} j_{N-2}}) \,..... \\
& \qquad ..... F_{\lambda_2 \lambda_1}(\vec{\rho}_{j_2 j_1}, \vec{\rho}_{j_1})\, W^{00,L_f}_{00,\lambda_1}(\vec{\rho}_{j_1}) \Bigg] \Bigg] \Bigg|^2
\end{aligned}
\qquad (2\text{-}4\text{-}79)
$$

where, as shown in Figure 2.6(c), $\vec{R}_{0S}$ is the vector from the emitter to the surface in the direction of $\vec{k}$. $\vec{R}_{j_k j_{k-1}} = \vec{R}_{j_k} - \vec{R}_{j_{k-1}} = \vec{\rho}_{j_k j_{k-1}}/k$, and $\vec{R}_{j_N S}$ is the vector from atom j_N to the surface in the direction of $\vec{k}$ (see Figure 2.6(c)).

Thermal vibrations can be treated most simply in an isotropic uncorrelated fashion, although anisotropic correlated vibrations are a more accurate description for the more important near-neighbor scatterers [15,18]. There is no generally applicable yet accurate model for including both anisotropy and correlation in single or multiple scattering calculations, although different methods for approximating these effects have been discussed previously by Sagurton et al. [4(b)] and by Barton et al. [15].

In the simplest case of isotropic uncorrelated vibrations, inclusion of them in Equation (2-4-79) can be effected by multiplying each scattered amplitude by a simple Debye-Waller factor $W^{uc}_{j_k}$ representing the motion of a given scatterer j_k; if $\Delta\vec{k}_{j_k j_{k-1}}$ is the change in $\vec{k}$ on scattering at the $j_k{}^{th}$ atom, $\theta_{j_k j_{k-1}}$ is the scattering angle defined in equation (2-4-70(a)) and $\overline{U^2_{j_k}}$ is the absolute mean square displacement of the $j_k{}^{th}$ atom, this simple uncorrelated Debye-Waller factor is given by

$$W^{uc}_{j_k} = \exp\{-\Delta k^2_{j_k j_{k-1}} \overline{U^2_{j_k}}\} = \exp\{-2k^2(1-\cos\theta_{j_k j_{k-1}})\,\overline{U^2_{j_k}}\}. \qquad (2\text{-}4\text{-}80)$$

But for correlated vibrations, this factor is expected to depend on the distance between the present scatterer and the previous scatterer. We represent this by $W^{c}_{j_k j_{k-1}}$. When the distance between the present and the previous scatterer is large enough $W^{c}_{j_k j_{k-1}}$ will approach the uncorrelated $W^{uc}_{j_k}$. But in general, it will depend on the displacement of atom j_k relative to the previous scatterer, which we denote by $\vec{U}_{j_k j_{k-1}}$. With the definition of the effective mean square displacement with thermal averaging (indicated by $<\cdots>$) of $\sigma^2_{j_k j_{k-1}} = <(\hat{\Delta k}_{j_k j_{k-1}} \cdot \vec{U}_{j_k j_{k-1}})>$, the equivalent correlated Debye-Waller-type attenuation factor is given by [4(c)]:

$$W^{c}_{j_k j_{k-1}} = <\exp\{-i\Delta\vec{k}_{j_k j_{k-1}} \cdot \vec{U}_{j_k j_{k-1}}\}> = \exp\{-1/2<(\Delta\vec{k}_{j_k j_{k-1}} \cdot \vec{U}_{j_k j_{k-1}})^2>\}$$
$$= \exp\{-1/2(\Delta k_{j_k j_{k-1}})^2 \sigma^2_{j_k j_{k-1}}\} = \exp\{-k^2(1-\cos\theta_{j_k j_{k-1}})\sigma^2_{j_k j_{k-1}}\}. \quad (2\text{-}4\text{-}81)$$

$\sigma^2_{j_k j_{k-1}}$ we have calculated from a sum over phonon modes in the "substrate" crystal, usually neglecting surface-specific effects. The method is one due to Beni and Platzmann [26], but with simplifications introduced by Sagurton et al. [4(b)]. The relevant equation is [(4(b)]:

$$\sigma^2_{j_k j_{k-1}} = \frac{3(h/2\pi)^2}{2M_S k_B \theta_D q_D^2}\left\{q_D^2 + \frac{4q_D^2}{\alpha^2}\left[\frac{\pi^2}{6} - \sum_{n=1}^{\infty}\left(\frac{1}{n^2} + \frac{\alpha}{n}\right) e^{-\alpha n}\right]\right.$$

$$- \frac{2}{|\vec{R}_{j_k} - \vec{R}_{j_{k-1}}|^2}\left(1-\cos\beta_{j_k j_{k-1}}\right)$$

$$+ \frac{4q_D}{|\vec{R}_{j_k} - \vec{R}_{j_{k-1}}|\alpha}\sum_{n=1}^{\infty}\frac{1}{n^2 + (\beta_{j_k j_{k-1}}/\alpha)^2}\left(e^{-na}\left[n\sin\beta_{j_k j_{k-1}}\right.\right.$$

$$\left.\left. + (\beta_{j_k j_{k-1}}/\alpha)\cos\beta_{j_k j_{k-1}}\right] - \beta_{j_k j_{k-1}}/\alpha\right)\Big\} \qquad (2\text{-}4\text{-}82)$$

where M_S is the substrate or "average-atom" atomic mass, k_B is the Boltzmann constant, θ_D is the effective or "average-atom" Debye temperature, q_D is the associated Debye wave vector, $\alpha = \theta_D/T(K)$, and $\beta_{j_k j_{k-1}} = q_D|\vec{R}_{j_k} - \vec{R}_{j_{k-1}}|$. The curve in Figure 2.9 shows some typical results obtained for $\sigma^2_{j_k j_{k-1}}$ with this method. The way in which it is input the program is discussed below.

Additional details of calculating $W_{j_N j_{N-1}}$'s including the allowance for surface-specific affects are found elsewhere [4(b)]. In the calculations reported here, the $W_{j_N j_{N-1}}$'s have been determined from Equations (2-4-81) and (2-4-82) and then inserted into Equation (2-4-79) as follows:

$$I^{(N_{max})}_{n_i \ell_i}(k,\theta,\phi) \propto \sum_{m_i}\left|\sum_{\ell_f}(-i)^{\ell_f}\exp(i\delta^c_{\ell_f})\, R_{\ell_f}(E_{kin})\, \langle \ell_f m_i | 10 | \ell_i m_i\rangle\right.$$

$$\times\left[(4\pi)^{1/2}\, Y_{\ell_f m_i}(\theta,\phi)\exp\{-|\vec{R}_{0S}|/2\Lambda_e\} + \right.$$

$$\sum_{j_1} [\exp\{i\rho_{j_1}(1-\cos\theta_{j_1})\}/\rho_{j_1}] \exp\{-|R_{j_1 S}|/2\Lambda_e\} \exp\{-|\vec{R}_{j_1}|/2\Lambda_e\} W_{j_1 0}$$

$$\times \sum_{\lambda_1} F_{00,\lambda_1}(\vec{\rho}_d,\vec{\rho}_{j_1}) W_{00,\lambda_1}^{00,L_f}(\vec{\rho}_{j_1}) +$$

$$\sum_{N=2}^{N_{max}} \sum_{\{j_i\}} \Big[\prod_{k=1}^{N} [\exp\{i\rho_{j_k j_{k-1}}(1-\cos\theta'_{j_k j_{k-1}})\}/\rho_{j_k j_{k-1}}] \exp\{-|\vec{R}_{j_N S}|/2\Lambda_e\}$$

$$\times \exp\{-|\vec{R}_{j_N j_{N-1}}|/2\Lambda_e\} \cdots \exp\{-|\vec{R}_{j_2 j_1}|/2\Lambda_e\} \exp\{-|\vec{R}_j|/2\Lambda_e\}$$

$$\times W_{j_N j_{N-1}} W_{j_{N-1} j_{N-2}} \cdots\cdots\cdots\cdots W_{j_2 j_1} W_{j_1 0}$$

$$\times \sum_{\{\lambda_i\}} F_{00,\lambda_N}(\vec{\rho}_d,\vec{\rho}_{j_N j_{N-1}}) F_{\lambda_{N-1}\lambda_{N-2}}(\vec{\rho}_{j_N j_{N-1}},\vec{\rho}_{j_{N-1} j_{N-2}}) \cdots\cdots$$

$$\cdots\cdots F_{\lambda_2\lambda_1}(\vec{\rho}_{j_2 j_1},\vec{\rho}_{j_1}) W_{00,\lambda_1}^{00,L_f}(\vec{\rho}_{j_1}) \Big] \Big]|^2. \qquad (2\text{-}4\text{-}83)$$

where the physical origin of each W factor in indicated in Figure 3.6(c).

For convenience in calculations, we also note that defining $\tilde{F}$ and $\tilde{W}$ factors that are damped by inelastic scattering and vibrational motion again yields the same simple from of Equation (2-4-78). That is we can let,

$$\tilde{F}_{00,\lambda_1}(\vec{\rho}_d,\vec{\rho}_{j_1}) = F_{00,\lambda_1}(\vec{\rho}_d,\vec{\rho}_{j_1}) \exp\{-|\vec{R}_{j_1 S}|/2\Lambda_e\}$$

$$\times \exp\{-|\vec{R}_{j_1}|/2\Lambda_e\} W_{j_1 0} \qquad (2\text{-}4\text{-}84)$$

$$\tilde{W}_{00,\lambda_1}^{00,L_f}(\vec{\rho}_{j_1}) = W_{00,\lambda_1}^{00,L_f}(\vec{\rho}_{j_1}) \qquad (2\text{-}4\text{-}85)$$

$$\tilde{F}_{00,\lambda_N}(\vec{\rho}_d,\vec{\rho}_{j_N j_{N-1}}) = F_{00,\lambda_N}(\vec{\rho}_d,\vec{\rho}_{j_N j_{N-1}}) \exp\{-|R_{j_N S}|/2\Lambda_e\} \times \exp\{-|\vec{R}_{j_N j_{N-1}}|/2\Lambda_e\} W_{j_N j_{N-1}} \quad (2\text{-}4\text{-}86)$$

$$\tilde{F}_{\lambda_k,\lambda_{k-1}}(\vec{\rho}_{j_k j_{k-1}},\vec{\rho}_{j_{k-1} j_{k-2}}) = F_{\lambda_k,\lambda_{k-1}}(\vec{\rho}_{j_k j_{k-1}},\vec{\rho}_{j_{k-1} j_{k-2}}) \times \exp\{-|\vec{R}_{j_k j_{k-1}}|/2\Lambda_e\} W_{j_k j_{k-1}}, \quad (2\text{-}4\text{-}87)$$

and then substituting these tilde quantities into Equation (2-4-78) yields the equivalent of Equation (2-4-83) with both inelastic and vibrational effects included. These F's and W's (or $\tilde{F}$'s and $\tilde{W}$'s) can then in principle be calculated once and for all for all scatterer-to-detector combinations ($\tilde{F}_{00,\lambda_1}$ and $\tilde{W}_{00,\lambda_N}^{00,L_f}$), all scatterer-to-scatterer-to-detector combinations ($\tilde{F}_{00,\lambda_N}$ for $N \geq 2$), and all scatterer-to-scatterer-to-scatterer "vertices" centered at scatterer j_{k-1} ($\tilde{F}_{\lambda_k,\lambda_{k-1}}$). We comment below on the time saving possible in this way.

In addition, we must also include the important effects of instrumental angular averaging due to the finite aperture of the detector. This is done by summing the photoelectron intensities over a grid of points on a circular aperture centered on the nominal emission direction as defined by $\vec{k}$. The direct wave and the singly-scattered waves have to be recalculated for each grid point on the aperture. For multiply scattered waves, only the path length differences represented by $\rho_{j_k j_{k-1}}(1-\cos\theta'_{j_k j_{k-1}})$ and the last scattering matrix represented by $F_{00,\lambda_N}(\vec{\rho}_d,\vec{\rho}_{j_N j_{N-1}})$ need to be

recalculated (cf. Equation (2-4-73). This calculation has been made much more efficient by further assuming that the scattering matricies are slowly varying functions of the angles (θ,ϕ) in $\vec{k}$. Then only the geometric phase factors due to path length differences need to be recalculated.

If (θ,ϕ) are now taken to be the mean angles of the nominal emission direction $\vec{k}$ and $\sum_b$ is a sum over the (θ_b,ϕ_b) combinations on a grid spanning the acceptance aperture, usually in a centered circular pattern, we can include angular broadening in Equation (2-4-83) as:

$$
\begin{aligned}
&\bar{I}^{(N_{max})}_{n_i \ell_i}(k,\theta,\phi) \;\alpha\; \sum_b \sum_{m_i} \Big| \sum_{\ell_f} (-i)^{\ell_f} \exp(i\delta^c_{\ell_f})\, R_{\ell_f}(E_{kin})\, \langle \ell_f m_i | 10 | \ell_i m_i \rangle \\
&\times \Big[(4\pi)^{1/2}\, Y_{\ell_f m_i}(\theta_b,\phi_b)\, \exp\{-|\vec{R}_{0S}|/2\Lambda_e\} + \\
&\quad \sum_{j_1} [\exp\{i\rho_{j_1}(1-\cos\theta_{bj_1})\}/\rho_{j_1}]\, \exp\{-|\vec{R}_{j_1 S}|/2\Lambda_e\}\, \exp\{-|\vec{R}_{j_1}|/2\Lambda_e\}\, W_{j_1 0} \\
&\quad \times \sum_{\lambda_1} F_{00,\lambda_1}(\vec{\rho}_d,\vec{\rho}_{j_1})\, W^{00,L_f}_{00,\lambda_1}(\vec{\rho}_{j_1}) + \\
&\quad \sum_{N=2}^{N_{max}} \sum_{(j_i)} \Big[\prod_{k=1}^{N} [\exp\{i\rho_{j_k j_{k-1}}(1 - \cos\theta'_{bj_k j_{k-1}})\}/\rho_{j_k j_{k-1}}] \\
&\quad \times \exp\{-|\vec{R}_{j_N S}|/2\Lambda_e\} \exp\{-|\vec{R}_{j_N j_{N-1}}|/2\Lambda_e\} .. \exp\{-|\vec{R}_{j_2 j_1}|/2\Lambda_e\} \\
&\quad \times \exp\{-|\vec{R}_{j_1}|/2\Lambda_e\}\, W_{j_N j_{N-1}} W_{j_{N-1} j_{N-2}} \cdots\cdots\cdots\cdots W_{j_2 j_1} W_{j_1 0}
\end{aligned}
$$

$$\times \sum_{(\lambda_i)} F_{00,\lambda_N}(\vec{\rho}_d, \vec{\rho}_{j_N j_{N-1}}) \, F_{\lambda_{N-1}\lambda_{N-2}}(\vec{\rho}_{j_N j_{N-1}}, \vec{\rho}_{j_{N-1} j_{N-2}}) \cdots\cdots$$

$$\cdots\cdots F_{\lambda_2\lambda_1}(\vec{\rho}_{j_2 j_1}, \vec{\rho}_{j_1}) \, W^{00,L_f}_{00,\lambda_1}(\vec{\rho}_{j_1}) \Big]\Big]\Big|^2. \qquad (2\text{-}4\text{-}88)$$

The direct wave is thus recalculated for each grid point (θ_b, ϕ_b) but only the geometric phase differences due to path length difference are recalculated for each scattered waves via the angle $\theta'_{bj_k j_{k-1}}$ as indicated by the added "b" subscript.

An additional correction in our calculations is that all of the external exit angles with respect to the surface θ_{ext} have been adjusted relative to the internal angles of propogating to the surface θ_{int} using the following refraction equation [1];

$$\theta_{ext} = \tan^{-1}[(\sin^2\theta_{int} - V_0/E'_{kin})^{1/2}/\cos\theta_{int}], \qquad (2\text{-}4\text{-}89)$$

where V_0 is the inner potential and E'_{kin} is the <u>internal</u> kinetic energy such that $E_{kin}(\text{external}) = E'_{kin}(\text{internal}) - V_0$. Thus all different paths are calculated for $\vec{k}$ corresponding to θ_{int}, but angular averaging is over the actual θ_{ext}.

Finally, all of the above equations are valid only for radiation of a definite polarization, as usual with the coordinates chosen so that $\hat{\epsilon} \parallel \hat{z}$. Normally, we choose this polarization vector $\hat{\epsilon}$ to lie somewhere in the plane defined by the directions of the incoming radiation $(\hat{k}_{h\nu})$ and the outgoing electron $(\hat{k})$, as indicated in Figure 2.2. However, if the source is unpolarized, a second polarization $\hat{\epsilon}'$

perpendicular to this plane must be considered, with I(unpolarized) = $I(\hat{\epsilon}) + I(\hat{\epsilon}')$. However, our past experience with single-scattering calculations has shown that the other polarization component can safely be neglected; this is because $\hat{\epsilon}$ in most experimental geometries is usually aproximately parallel to $\hat{k}$, and thus more strongly excites the direct and scattered waves towards it, whereas $\hat{\epsilon}'$ is perpendicular to $\hat{k}$ and therefore is much less important.

We have used Equation (2-4-88) in all of the photoelectron diffraction calculations discussed here. For simulations of Auger electron diffraction, the program was simply forced by the input choices of R_{ℓ_f} and $\delta^c_{\ell_f}$ to treat a fictitious case of p emission into a single s channel. This method yields the correct final state for scattering if it is assumed that the final state of the Auger process is an s-wave [7]. The only trivial drawback in using Equation (2-4-88) for Auger electron diffraction is that it includes the evaluation of an unnecssary Gaunt coefficient characteristic of the p → s process; however, this produces only a multiplicative constant in the final intensity. Equation (2-4-88) should be applicable to any final state and over a broad range of energy.

2.4.7. Comparison to the Multiple-Scattering Treatment by Barton and Shirley:

We now compare the Rehr-Albers [17] approach to another similar spherical-wave multiple-scattering method by Barton and Shirley (B-S)

[15]. Both of these methods are cluster based in contrast to traditional LEED multiple-scattering methods which rely on the translational symmetry of the system under investigation. We will first introduce the essential elements of the Barton-Shirley [17] method briefly.

The B-S method is based upon a Taylor series magnetic-quantum-number expansion (TS-MQNE). These authors note that the addition formula for the translation of spherical waves in Equation (2-4-13) can be derived by first taking the Fourier transform of the spherical wave and then doing the inverse transform. They then return to the transform and expand it in a Taylor series about the origin-shift vector $\vec{a}$, which is the bond vector of a particular scatterer. The z-axis is also rotated parallel to $\vec{a}$ to simplify the calculation just as in the R-A method. They finally obtain an angular momentum series when each term in the translation is subjected to the inverse Fourier transform. This is done to obtain a workable approximation to the Gaunt-integral summation formula of Equation (2-4-13). This results in the following expression for the single-scattering portion of a p-wave final state at the detector ($\vec{R}_d$) due to an atom at $\vec{a}$ with respect to the emitter [17], the case we will treat as our comparative example:

$$\psi_a^{(1)}(\vec{R}_d) = -ik\,[\exp\{i\rho_d\}/\rho_d]\,[\exp\{i\rho_a(1-\cos\theta_{aR_d})\}/\rho_a] \sum_{q=-1}^{1} \sum_{p=0}^{1-|q|} F_{pq}^{00}(\vec{\rho}_a,\vec{\rho}_d)\, e^{iq\phi_{\epsilon aR_d}}\, P_{10}^{pq}(\hat{a},\hat{\epsilon}), \qquad (2\text{-}4\text{-}90)$$

where $\hat{\epsilon}$ is the radiation polarization, $\phi_{\epsilon a R_d}$ is the azimuth of $\hat{R}_d$ with respect to $\hat{\epsilon}$ as rotated around $\vec{a}$ or $\vec{\rho}_a$,

$$F_{pq}^{00}(\vec{\rho}_a,\vec{\rho}_d) = \frac{1}{ik} \sum_{\ell=|q|}^{\ell_{max}} i\ (2\ell+1)\ t_\ell(\vec{a})\ H_\ell^{pq}(\rho_a)\ P_\ell^{|q|}(\cos\theta_{aR_d}),$$

$$P_{10}^{pq}(\hat{a},\hat{\epsilon}) = N_{\ell q}\ R_{|q|0}^{(1)}(0,\theta_{\epsilon a},\pi-\phi_{x\epsilon a})\ C_{pq}^{1}\ ,$$

$$H_\ell^{pq}(\rho_a) = \frac{(\ell+q)!}{(\ell-q)!}\ \frac{(-1)^p}{(i\rho_a)^{q+p}}\ \frac{p!}{q!} \sum_{s=0}^{p} \frac{(q+p-s)!}{s!\ (p-s)!}\ (\rho_a)^s\ \frac{\partial^s C_\ell(\rho_a)}{[\partial(\rho_a)]^s}\ ,$$

$P_\ell^{|q|}(\cos\theta_{aR_d})$ is an associated Legendre polynomial, θ_{aR_d} is the dihedral angle between vectors $\vec{a}$ and $\vec{R}_d$ (also equal to the single scattering angle), $N_{\ell q}$ is a normalization constant for spherical harmonics, $R_{|q|0}^{(1)}(0,\theta_{\epsilon a},\pi-\phi_{x\epsilon a})$ is a rotation matrix element with angles defined in the same format, $\theta_{\epsilon a}$ and $\phi_{x\epsilon a}$ are the polar and azimuthal angles of $\vec{a}$ with respect to $\hat{\epsilon} \parallel \hat{z}$, and

$$C_{pq}^{1} = \frac{(\ell+|q|+p)!}{(\ell-|q|-p)!}\ \frac{1}{p!\ (2|q|+2p)!!}\ .$$

The expansion index q is found to correct the zeroth order origin-shift term in an arc perpendicular to the bond vector that moves away from the center of the scattering potential, where as the index p corrects outward from the center along this bond vector [17].

One can compare the above equation with Equation (2-4-44) by making some minor modifications to the latter. Note first that, from the discussion just above Equation (2-4-41), the exponential prefactors above can be rewritten as $-ik[\exp\{i\rho_a\}/\rho_a] \times [\exp\{ik|\vec{R}_d| - \rho_a \cos\theta_{aR_d}\}/\rho_d] = \exp\{i\rho_d/\rho_d\} \times \exp\{i\rho_a(1-\cos\theta_{aR_d})/\rho_a\}$; this is thus the same prefactor as in Equation (2-4-44). Then note that Equation (2-4-44) includes the sum over atoms in the cluster while Equation (2-4-90) does not; thus the sum over j in Equation (2-4-44) can be removed, with $\vec{R}_j$ being replaced by $\vec{a}$ and ρ_j by ρ_a. Then Equation (2-4-44) becomes

$$G^{(1)}_{00,10}(\vec{a},\vec{R}_d) = [\exp\{i\rho_d\}/\rho_d]\ [\exp\{i\rho_a(1-\cos\theta_{aR_d})\}/\rho_a] \times \sum_{\lambda''} F_{00,\lambda''}(\vec{\rho}_d,\vec{\rho}_a)\ W^{00,10}_{00,\lambda''}(\vec{\rho}_a) \qquad (2\text{-}4\text{-}91)$$

where, with the simplification of Equation (2-4-60) in both F and W,

$$F_{00,\lambda''}(\rho_d,\vec{\rho}_a) = e^{i\mu''\gamma} \sum_{\ell=0}^{\ell_{max}} t_\ell(\vec{a})\ \gamma^\ell_{00}(\rho_d)\ d^\ell_{0\mu''}(\theta_{aR_d})\ \tilde{\gamma}^\ell_{\lambda''}(\rho_a),$$

and

$$W^{00,10}_{00,\lambda''}(\vec{\rho}_a) = \gamma^1_{\lambda''}(\rho_a)\ d^1_{\mu''0}(\theta_{\epsilon a}),$$

and again θ_{aR_d} is the angle between vectors $\vec{a}$ and $\vec{R}_d$,.

We note at once some similarities between these two expressions. The summation limits in Equation (2-4-90), which is a first order Taylor Series in m, and Equation (2-4-91), which is a second order expansion in the parameter $1/\rho$, lead to an equivalant number of terms. In Equation (2-4-90), q = -1, 0, +1 and p = 0, 1, and these are in fact happen to be equal to the allowed values for $\mu"$ and $\nu"$ in $\lambda" = (\mu",\nu")$. It is also evident that the summations in Equations (2-4-90) and (2-4-91) can be broken into two major factors. The first factors, $F^{00}_{pq}(\vec{\rho}_a,\vec{\rho}_d)\ e^{iq\phi_{\epsilon aR_d}}$ in Equation (2-4-90) and $F_{00,\lambda"}(\vec{\rho}_d,\vec{\rho}_a)$ in Equation (2-4-91), are independent of the exact initial and final states involved, while the second factors, $P^{pq}_{10}(\hat{a},\hat{\epsilon})$ in Equation (2-4-90) and $W^{00,10}_{00,\lambda"}(\vec{\rho}_a)$ in Equation (2-4-91), are not. Also, the "effective scattering factors" in the two approximations are similar in that both $F^{00}_{pq}(k\vec{a},\hat{R}_d)$ and $F_{00,\lambda"}(\vec{\rho}_d,\vec{\rho}_a)$ represent the scattering of a given angular momentum component ((p,q) or $(\mu",\nu")$ respectively) incident on scatterer "a" into the correct (0,0) component at the detector.

To compare these models further, we modify Equation (2-4-91) futher. First we substitute explicit expressions for γ and $\tilde{\gamma}$. Also $d^{\ell}_{\mu\nu}$'s be written in terms of the associated Legendre polynomials P^{m}_{ℓ}. Then we get,

$$F_{00,\lambda"}(\vec{\rho}_d,\vec{\rho}_a) = e^{i\mu"\gamma} \sum_{\ell=0}^{\ell max} t_\ell(\vec{a})\ (2\ell+1)^{1/2}\ C_\ell(z_a)$$
$$\times\ [4\pi/(2\ell+1)]^{1/2}\ N_{\ell\mu"}\ P_\ell^{|\mu"|}(\cos\theta_{aR_d})$$

$$\times (2\ell+1)\ [\partial^{\nu"} C_\ell(z_a)/\partial z_a^{\nu"})]\ z_a^{\nu"}/N_{\ell\mu"}\ \nu"!, \qquad (2\text{-}4\text{-}92)$$

and,

$$W^{00,10}_{\lambda",00}(\vec{\rho}_a) = [(-1)^{\nu"}\ N_{1\mu"}\ [\partial^{\nu"+\mu"} C_1(z_a)/\partial z^{\nu"+\mu"}]\ z^{\nu"+\mu"} / (\nu"+\mu")!]\ d^1_{\mu"0}(\theta_{\epsilon a}). \qquad (2\text{-}4\text{-}93)$$

Equation (2-4-92) can be simplified further, as

$$F_{00,\lambda"}(\vec{\rho}_d,\vec{\rho}_a) = e^{i\mu"\gamma}\ [4\pi]^{1/2} \sum_\ell (2\ell+1)\ t_\ell(\vec{a}) \times [C_\ell(z_a)\ (\partial^{\nu"} C_\ell(z_a)/\partial z_a^{\nu"})\ z_a^{\nu"}/\nu"!] \times P_\ell^{|\mu"|}(\cos\theta_{aR_d}). \qquad (2\text{-}4\text{-}94)$$

Now, if we compare the effective scattering factor $F_{00,\lambda"}(\vec{\rho}_d,\vec{\rho}_a)$ in Equation (2-4-94) with that of $F^{00}_{pq}(\vec{\rho}_a,\vec{\rho}_d)$ in Equation (2-4-90), it is evident that they have some similarities, but also some important differences. Both involve the t-matrix elements t_ℓ and the associated Legendre polynomials $P^m_\ell(\cos\theta_{aR_d})$. But the Barton-Shirley method has a sum of derivatives of the C_ℓ's in H^{pq}_ℓ, and the Rehr-Albers formalism contains products of C_ℓ's and their derivatives.

In comparing $W^{00,10}_{00,\lambda"}(\vec{\rho}_a)$ in Equation (2-4-93) with $P^{pq}_{10}(\hat{a},\hat{\epsilon})$ in Equation (2-4-90), we note that, while $W^{00,10}_{00,\lambda"}(\vec{\rho}_a)$ is dependent on the distance between the emitter and the first scatterer, $P^{pq}_{10}(\hat{a},\hat{\epsilon})$ is independent of any distance. This is also true for the analogous

multiple-scattering comparisons. For example, we can compare double-scattering terms in a similar manner, and it is clear that they exhibit distinct differences.

From the point of view of computational time, inspection of the number and types of factors to be calculated in the two methods in single-scattering indicates a comparable amount of numerical work. However, in general multiple-scattering, the cleaner separability of the $F_{\lambda_k,\lambda_{k-1}}(\vec{\rho}_k,\vec{\rho}_{k-1})$ for each scattering vertex defined by $\vec{R}_k \leftarrow \vec{R}_{k-1} \leftarrow \vec{R}_{k-2}$ would appear to furnish a computational advantage in the R-A approach.

As final comparative comments, we believe that the R-A approach has better convergence and formal properties, as discussed also eleswhere [17]. In particular, the R-A formalism reduces to effective curved wave scattering amplitude in a point scattering approximation in zeroth order (i.e., (1×1)), whereas that of B-S does not. For a given degree of convergence smaller matrices should be needed in R-A calculations. The R-A method also does not distinguish between forward and backward scattering, whereas the B-S method appears to converge faster in back scattering [15]. The R-A method at the (6×6) level assumed here also should be applicable to a broader range of energies, with the B-S approach representing more of a low-energy Taylor expansion. We will illustrate some of these comments in subsequent numerical calculations with the R-A method.

In conclusion, the R-A and B-S methods are fundamentally different in the kind of truncation and approximation they make in the

expansion of $G_{L,L'}(\rho)$. But the R-A separation appears to be inherently applicable to a broader range of energies, to be more readily generalizable to higher order expansions (even though the second order (6×6) seems fully adequate to date), and to be more easily adopted to a variety of situations such as, e.g., emission from a general $n_i\ell_i$ subshell treated here (a case which has not yet been dealt with using the B-S approach).

2.5. COMPUTATIONAL DETAILS OF IMPORTANT INTERMEDIATE QUANTITIES:

In this section we present the computational details of the several quantities which are important for applying this method in numerical simulations. (Additional useful comments appear in reference 18(b).) Whenever possible, we will provide at least two alternative methods for calculating a quantity, including a non-recursive option. These non-recursive methods are suitable for computers with compilers which can vectorize a code, as such compilers usually cannot vectorize segments with recurrence relations. The efficient recursive methods are most suitable for non-vectorizing machines. But it is advisable to try both options on a given machine to assess both speed and accuracy before settling on one.

2.5.1. Polynomial Part of the Spherical Hankel Function C_ℓ and its Derivatives $C_\ell^{(n)}$:

As noted above we can decompose the spherical Hankel function as,

$$h^{(+)}_\ell(\rho) = i^{-\ell} \frac{e^{i\rho}}{\rho} C_\ell(\rho). \qquad (2\text{-}5\text{-}1)$$

To calculate the C_ℓ's one can use the following recurrence relation for $h_\ell^{(+)}(\rho)$ [27],

$$h_{\ell-1}(\rho) + h_{\ell+1}(\rho) = (2\ell+1)\ \rho^{-1}\ h_\ell(\rho). \qquad (2\text{-}5\text{-}2)$$

Substituting Equation (2-5-1) in Equation (2-5-2) and changing variables from ρ to $z = 1/i\rho$, we have, for $\ell > 1$:

$$C_{\ell+1}(z) = C_{\ell-1}(z) + (2\ell+1)\ z\ C_\ell(z). \qquad (2\text{-}5\text{-}3)$$

The initial values are $C_0(z) = 1.0$ and $C_1(z) = 1\text{-}z$.

One can also use a non-recursive approximate method to calculate the C_ℓ's [17]:

$$C_\ell(z) \simeq (1.0 + \ell(\ell+1)\ z^2)^{1/2} \exp\left[-\frac{\ell(\ell+1)\ z^2}{2}\right]. \qquad (2\text{-}5\text{-}4)$$

In the computer code discussed below we have used recurrence relations to calculate the C_ℓ's for the sake of accuracy.

Next we discuss a method for calculating the derivatives $C_\ell^{(n)}(z)$ which are given by

$$C_\ell^{(n)}(z) = \partial^n C_\ell(z) \; / \; \partial z^n. \tag{2-5-5}$$

A consideration of the C_ℓ's needed in calculating both F and W shows that, in a second order (6×6) treatment, we will need $C_\ell^{(1)}$ for $\ell = 0, 1, \ldots, \ell_{max}$ and $C_\ell^{(2)}$ for $\ell = \ell_i \pm 1$.

We can obtain the following recurrence relation for the $C_\ell^{(n)}$'s by partially differentiating Equation (2-5-3) n times with respect to z. This yields

$$C_{\ell+1}^{(n)}(z) = C_{\ell-1}^{(n)}(z) - (2\ell+1)\left[z\, C_\ell^{(n)}(z) + n\, C_\ell^{(n-1)}(z)\right]. \tag{2-5-6}$$

In practice, we used the following two relations, which are special cases of Equation (2-5-6), for second order calculations:

$$C_{\ell+1}^{(1)}(z) = C_{\ell-1}^{(1)}(z) - (2\ell+1)\left[z\, C_\ell^{(1)}(z) + C_\ell^{(0)}(z)\right], \tag{2-5-7}$$

$$C_{\ell+1}^{(2)}(z) = C_{\ell-1}^{(2)}(z) - (2\ell+1)\left[z\, C_\ell^{(2)}(z) + 2\, C_\ell^{(1)}(z)\right]. \tag{2-5-8}$$

The initial conditions for these are

$$C_0^{(0)}(z) = 1.0, \tag{2-5-9}$$

$$C_0^{(1)}(z) = 0.0, \tag{2-5-10}$$

$$C_0^{(2)}(z) = 0.0, \tag{2-5-11}$$

$$C_1^{(0)}(z) = 1 - z, \tag{2-5-12}$$

$$C_1^{(1)}(z) = -1.0. \tag{2-5-13}$$

(The above recurrence relations can be vectorized by making the do loop on n the innermost loop. But for the purpose of second order calculations, we need only $0 \leq n \leq 2$ and hence the length of this vector is not large enough to gain significantly by vectorization.)

A final useful property of the C_ℓ's is that $\lim_{z \to 0} C_\ell(z) = 1.0$.

2.5.2. Euler Angles, α, β, γ:

First we consider the simple rotation, $R^{\ell}_{\mu\mu'}(\hat{\rho}_1)$. From Equation (2-4-59) we have that

$$R^{\ell}_{\mu\mu'}(\hat{\rho}_1) = R^{\ell}_{\mu\mu'}(\hat{z} \leftarrow \hat{\rho}_1) = R^{\ell}_{\mu\mu'}(\alpha,\beta,\gamma) = e^{i\mu\alpha}\, d^{\ell}_{\mu\mu'}(\beta)\, e^{i\mu'\gamma}, \tag{2-5-14}$$

with the angles α, β, and γ defined as in Figure 2.7(a).

If θ_1 and ϕ_1 are polar and aximuthal angles of $\hat{\rho}_1$ with respect to the z axis and x axis, respectively (cf. Figure 2.7(c)) we can choose $\alpha = 0$, $\beta = \theta_1$ and $\gamma = \phi_1$. Therefore this rotation matrix simplifies to:

$$R^{\ell}_{\mu\mu'}(\hat{\rho}_1) = d^{\ell}_{\mu\mu'}(\theta_1)\, e^{i\mu'\phi_1}. \tag{2-5-15}$$

The rotation matrix occuring in the W matrix is even simpler:

$$R^1_{\mu 0}(\hat{\rho}_1) = R^1_{\mu 0}(0,\theta_1,\phi_1) = d^1_{\mu 0}(\theta_1). \tag{2-5-16}$$

In rotating the polarization vector $\hat{\epsilon}$ onto the z axis, the initial step of the R-A method, we make use of the same expression, but with $(\theta_\epsilon,\phi_\epsilon)$ replacing (θ_1,ϕ_1), as shown in Figure 2.7(b).

The composite rotation given by $R^{\ell}_{\mu\mu'}(\hat{\rho}_1,\hat{\rho}_2^{-1})$, as shown in Figures 2.7(c) and (d), is more complicated:

$$R^{\ell}_{\mu\mu'}(\hat{\rho}_1,\hat{\rho}_2^{-1}) = R^{\ell}_{\mu\mu'}(\hat{\rho}_1 \rightarrow \hat{z} \rightarrow \hat{\rho}_2). \tag{2-5-17}$$

Let (θ_1,ϕ_1) and (θ_2,ϕ_2) be the spherical polar coordinates of $\hat{\rho}_1$ and $\hat{\rho}_2$ with respect to the x and z-axes. Also, let (α,β,γ) be the Euler angles of the composite rotation $\hat{\rho}_1 \rightarrow \hat{z} \rightarrow \hat{\rho}_2$. The Euler angles for the rotation $\hat{\rho}_1 \rightarrow \hat{z}$ are $(0,\theta_1,\phi_1)$. For the $\hat{z} \rightarrow \hat{\rho}_2$ rotation they are as for the inverse of $\hat{\rho}_2 \rightarrow \hat{z}$ with $(0,\theta_2,\phi_2)$ or $(-\phi_2,-\theta_2,0)$.

Any coordinate rotation through (α,β,γ) can be represented by the matrix [28],

$$R(\alpha,\beta,\gamma) = \begin{bmatrix} \cos\alpha\cos\beta\cos\gamma-\sin\alpha\sin\gamma & \cos\alpha\cos\beta\sin\gamma-\sin\alpha\cos\gamma & -\cos\alpha\sin\beta \\ -\sin\alpha\cos\beta\cos\gamma-\cos\alpha\sin\gamma & -\sin\alpha\cos\beta\sin\gamma+\cos\alpha\cos\gamma & \sin\alpha\sin\beta \\ \sin\beta\cos\gamma & \sin\beta\sin\gamma & \cos\beta \end{bmatrix}. \tag{2-5-18}$$

To now determine (α,β,γ) for the composite rotation, we have to consider the following matrix equation, which equates $R(\alpha\beta\gamma)$ to the product $R(0,\theta_1,\phi_1) \times R(-\phi_2,-\theta_2,0)$:

$$\begin{bmatrix} \cos\alpha\cos\beta\cos\gamma-\sin\alpha\sin\gamma & \cos\alpha\cos\beta\sin\gamma-\sin\alpha\cos\gamma & -\cos\alpha\sin\beta \\ -\sin\alpha\cos\beta\cos\gamma-\cos\alpha\sin\gamma & -\sin\alpha\cos\beta\sin\gamma+\cos\alpha\cos\gamma & \sin\alpha\sin\beta \\ \sin\beta\cos\gamma & \sin\beta\sin\gamma & \cos\beta \end{bmatrix} =$$

$$\begin{bmatrix} \cos\theta_1\cos\phi_1 & \cos\theta_1\sin\phi_1 & -\sin\theta_1 \\ -\sin\phi_1 & \cos\phi_1 & 0 \\ \sin\theta_1\cos\phi_1 & \sin\theta_1\sin\phi_1 & \cos\theta_1 \end{bmatrix} \times$$

$$\begin{bmatrix} \cos\theta_2\cos\phi_2 & \sin\phi_2 & \sin\theta_2\cos\phi_2 \\ \cos\theta_2\sin\phi_2 & \cos\phi_2 & \sin\theta_2\sin\phi_2 \\ -\sin\theta_2 & 0 & \cos\theta_2 \end{bmatrix}. \qquad (2\text{-}5\text{-}19)$$

By comparing the matrix elements on the left and right sides of the above equation one finally gets the following expression for the Euler angles [18b]:

$$\alpha = \arg[(\sin\theta_1 \cos\theta_2 - \sin\theta_2 \cos\theta_1 \cos(\phi_1-\phi_2)) + i(\sin\theta_2 \sin(\phi_2-\phi_1))], \qquad (2\text{-}5\text{-}20)$$

$$\beta = \cos^{-1}[\sin\theta_1 \sin\theta_2 \cos(\phi_2-\phi_1) + \cos\theta_2 \cos\theta_1], \qquad (2\text{-}5\text{-}21)$$

$$\gamma = \arg[(\sin\theta_1 \cos\theta_2 \cos(\phi_1-\phi_2) - \cos\theta_1 \sin\theta_2) - i(\sin\theta_1 \sin(\phi_2-\phi_1))]. \qquad (2\text{-}5\text{-}22)$$

2.5.3. Rotation Matricies, $R^{\ell}_{\mu\mu'}(\alpha,\beta,\gamma)$:

From Equation (2-4-59), we have again

$$R^{\ell}_{\mu\mu'}(\alpha,\beta,\gamma) = e^{i\mu\alpha}\, d^{\ell}_{\mu\mu'}(\beta)\, e^{i\mu'\gamma}. \tag{2-5-23}$$

Beginning from Equation (a4) of Reference 25, we can arrive at the following recurrence relation for $d^{\ell}_{\mu\mu'}(\beta)$. Here θ has been replaced by $-\theta$ to switch from the Messiah [29] to Edmonds [25] convention to be used here. Also, row-column indicies have been switched using Equation (2-5-29) to get,

$$\begin{aligned} 2[(\ell+\mu)(\ell+\mu-1)]^{1/2} d^{\ell}_{\mu\mu'}(\beta) = {} & [(\ell+\mu')(\ell+\mu'-1)]^{1/2}(1+\cos\theta) \\ & \times d^{\ell-1}_{\mu-1,\mu'-1}(\beta) + 2(\ell^2-(\mu')^2)^{1/2} \sin\theta\, d^{\ell-1}_{\mu-1,\mu'}(\beta) + \\ & [(\ell-\mu')(\ell-\mu'-1)]^{1/2}(1-\cos\theta)\, d^{\ell-1}_{\mu-1,\mu'+1}(\beta). \end{aligned} \tag{2-5-24}$$

The initial conditions are:

$$d^{0}_{00}(\beta) = 1.0 \tag{2-5-25}$$

$$d^{1}_{\mu\mu'}(\beta) = \begin{bmatrix} (1+\cos\theta)/2 & \sin\theta/\sqrt{2} & (1-\cos\theta)/2 \\ -\sin\theta/\sqrt{2} & \cos\theta & \sin\theta/\sqrt{2} \\ (1-\cos\theta)/2 & -\sin\theta/\sqrt{2} & (1+\cos\theta)/2 \end{bmatrix} \tag{2-5-26}$$

where columns (or rows) are labeled in the order μ (or μ') = 1, 0, -1.

Although generally efficient, there are a few drawbacks in this method. The first is that it may require the calculation of

intermediate terms that are not used, especially in the case of multiple-scattering. Second, and a direct consequence of the first, it can require very large arrays to hold these intermediate terms. Both of these features are undesirable in time-consuming large-scale computations. Hence we have used in the computer code the non-recursive method described below [30]:

$$d^{\ell}_{\mu\mu'}(\beta) = [(\ell+\mu)(\ell-\mu)(\ell+\mu')(\ell-\mu')]^{1/2} \times \sum_{\nu} \frac{(-1)^{\nu}}{(\ell-\mu-\nu)!\ (\ell+\mu'-\nu)!\ (\nu+\mu-\mu')!\ \nu!} \times [\cos(\beta/2)]^{2\ell+\mu'-\mu-2\nu}\ [-\sin(\beta/2)]^{\mu-\mu'+2\nu}. \qquad (2\text{-}5\text{-}27)$$

Since the arguments of the factorials should be greater than or equal to zero, we have to impose the following limits on the summation index ν:

$$\max(0,\ \mu-\mu') \le \nu \le \min(\ell-\mu,\ \ell+\mu'). \qquad (2\text{-}5\text{-}28)$$

In this approach it is possible to calculate factors that are independent of β once and hold them in arrays. Also, it can be used to calculate only the required (μ,μ') combinations. In addition, it is vectorizable.

The $d^{\ell}_{\mu\mu'}(\beta)$, and hence also the $F_{\lambda,\lambda'}(\vec{\rho}_1,\vec{\rho}_2)$, have very useful symmetry relations which can be used to reduce the computation time

[30]. Two of these are:

$$d^{\ell}_{\mu\mu'}(\beta) = d^{\ell}_{-\mu',-\mu}(\beta) = (-1)^{\mu-\mu'} d^{\ell}_{-\mu,-\mu'}(\beta). \qquad (2\text{-}5\text{-}29)$$

Other symmetry relations of the $d^{\ell}_{\mu\mu'}(\beta)$ also can be used to reduce their computation time.

2.5.4. Gaunt Coefficients, $\langle \ell_f m_i | 10 | \ell_i m_i \rangle$:

From Reference 28, we find for the Gaunt cefficients required in our calculation when $\hat{z}$ is rotated to be parallel to $\hat{\epsilon}$:

$$\langle \ell_f m_i | 10 | \ell_i m_i \rangle = \langle \ell_f m_i \; 10 | \ell_i m_i \rangle$$
$$= (-1)^{m_i} (3/4\pi) (2\ell_f+1) (2\ell_i+1) A, \qquad (2\text{-}5\text{-}30)$$

where, A is a product of two 3j symbols:

$$A = \begin{matrix} \ell_f & 1 & \ell_i & \ell_f & 1 & \ell_i \\ -m & 0 & m & 0 & 0 & 0 \end{matrix} .$$

To calculate this product, we define $\ell_> \equiv \max(\ell_f, \ell_i)$ and $\ell_< = \min(\ell_f, \ell_i)$, and use the properties of the 3j symbols [31], to show that,

$$A = (-1)^{m_i} \frac{[(\ell_<+m_i+1)(\ell_<-m_i+1)]^{1/2}}{(2\ell_<+3)(2\ell_<+1)} \qquad (2\text{-}5\text{-}31)$$

where, $|\ell_f - \ell_i| = 1$, or finally,

$$<\ell_f m_i \; 10 | \ell_i m_i> = \left[\frac{(\ell_< + m_i + 1)(\ell_< - m_i + 1)}{(2\ell_< + 3)\;(2\ell_< + 1)} \right]^{1/2} . \qquad (2\text{-}5\text{-}32)$$

2.5.5. Associate Legendre Polynomicals, $P_\ell^{|m|}(\cos\theta)$:

We can calculate the $P_\ell^{|m|}$ from the recusion relation [27]:

$$P_\ell^{|m|}(\cos\theta) = \frac{1}{\ell - m} \left[(2\ell-1) \cos\theta \; P_{\ell-1}^{|m|}(\cos\theta) + (\ell - |m| - 1) \; P_{\ell-2}^{|m|}(\cos\theta) \right]. \qquad (2\text{-}5\text{-}33)$$

To start the recursion above, we need for each m both $P_m^{|m|}$ and $P_{m+1}^{|m|}$. We can get these from,

$$P_m^{|m|}(\cos\theta) = (2m-1) \sin\theta \; P_{m-1}^{|m-1|}(\cos\theta), \qquad (2\text{-}5\text{-}34)$$

and,

$$P_{m+1}^{|m|}(\cos\theta) = (2m+1) \cos\theta \; P_m^{|m|}(\cos\theta). \qquad (2\text{-}5\text{-}35)$$

Finally we need the initial conditions of, $P_0^0(\cos\theta) = 1.0$ and $P_1^{(0)}(\cos\theta) = \cos\theta$.

2.6. USER'S GUIDE TO THE FORTRAN CODE:

This section is intended as the User's Guide to the FORTRAN-77 code. For simplicity, we do not provide any machine specific information here, although the several computing environments on which the code has been run are discussed below. At present, we have a single code capable of doing both scanned-angle photoelectron and Auger electron diffraction, and scanned-energy photoelectron diffraction (ARPEFS). Both the polar and azimuthal angles can be scanned in scanned-angle mode. Multiple-scattering up to tenth order events can be included; single-scattering output is an option in any run. For photoelectron diffraction, emission from any $n_i \ell_i$ subshell also can be treated. This is thus the most general cluster-based code for such diffraction calculations of which we are aware. As an estimate of the program size, the present version named XPD.F (version of 08/90) requires about 75 kW of high speed memory and about 5 MW of fast disk storage. (On a supercomputer such as a Cray, one word (W) is 64 bytes, whereas on a work station such as a Sun SPARCstation a word is equal to 32 bytes). In Section 2.6.1, we discuss the general structure of this program. In Section 2.6.2, we provide examples of all input and output files for this code. In Section 2.6.3, we discuss the minor changes needed in one of the input files to simulate scanned-angle Auger electron diffraction. In Section 2.6.4, possible methods for more accelerated calculations and geometry optimization are discussed.

2.6.1. General Structure of the FORTRAN code:

In this section the structure of the code will be discussed. At the beginning the code reads the input files to be discussed in detail in the next section and immediately writes input information to output files. Next it calculates and stores some frequently used prefactors. They are used in subroutines for the scattering factors $F_{\lambda\lambda'}$ and the rotation matrices. The bond length matrix $R_{j_k j_{k+1}}$ also is stored for future reference. Then comes the angular or energy stepping loops. Inside these loops usually the (6x6) matrices $F_{\lambda_k \lambda_{k-1}}(\vec{\rho}_k \cdot \vec{\rho}_{k-1})$ for all scattering centers or verticies are calculated. Typical scattering verticies are shown in Figure 2.6(b). At each such scattering vertex, the first atom in the sequence can be any atom in the cluster. The second atom can be any other atom except for the first one. The third atom can also be any other atom except for the second one. Hence, there are [Mx(M-1)x(M-1)] such scattering verticies in an M-atom cluster that includes the emitter as a scatterer. That is, we are typically dealing with 36 times this value of complex numbers, or 2.9×10^4 for a 10-atom cluster, 4.3×10^6 for a 50-atom cluster, and 3.5×10^7 for a 100-atom cluster (which is larger than anything attempted to date). The last atom of the three can also be replaced by the vector pointing towards the detector; the number of such verticies is [Mx(M-1)] and they represent either all single-scattering events or the last events in all multiple-scattering paths (that is

$F_{00,\lambda}$). The number of these is thus 5.4×10^2 for 10 atoms, 1.5×10^4 for 50 atoms, and 5.9×10^4 for 100 atoms. All of these verticies are calculated and stored in scratch files to prevent redundancy. Provided the scratch files containing F's can be accessed quickly, this leads to a considerable savings in computer time. The W matrices have to be calculated only once for each multiple-scattering path and hence there are only M-1 of them for each final ℓ_f value; they can be stored in an array. This leads to a very small number of W matricies for a given ℓ_{max}: $54\times(2\ell_{max}+1)$ matrix elements for 10 atoms, $294\times(2\ell_{max}+1)$ for 50 atoms, and $594\times(2\ell_{max}+1)$ for 100 atoms. This method is also ideal for the approximate approach to geometry optimization that will be discussed in the next section. Once these matrices, which are the building blocks, are calculated and stored, the code proceeds to calculate intensity at each scattering order starting from single-scattering.

After each order it checks for the value of the maximum order desired (N_{max} - variable "LEVEL") to determine whether <u>all</u> paths should be extended to the next order or terminated. This gives the user a chance to go up to only a predetermined order to save time. This predetermination can be done by performing a full calculation for a given system at the beginning. Then by looking at intensities for each order one can determine the order at which the intensities are converged (i.e., the point at which $I^{(N_{max})}(k,\theta,\phi) \approx I^{(N_{max}-1)}(k,\theta,\phi)$ to with in a small enough difference). As long as atomic positions

are not changed too much, any further calculations on this system can be done only up to that order.

An additional special feature of the code is in incorporating convergence criteria at each order above 3^{rd} (varibles "cut4", "cut5", ... , "cut10") in order to decide whether each path should be calculated to that order or not. For a given order, the cutoff criterion at the n^{th} order "cutn" is defined as x% of the maximum amplitude for all events at 3^{rd} order, so that a given n^{th} order event is calculated only if the $(n-1)^{th}$event in this path is $\geq$ x% of this maximum in 3^{rd} order. A cutoff of 0.0% thus includes all events up to N_{max}. As discussed below, a satisfactory cutoff appears to be at ~5%. With a suitable cutoff in place, a second method of cheking for convergence is to watch the number of events verses order (a program output) and note the N at which they fall to a negligible numbers (see discussion in section 2.8.2 and 3.2.5, and Table 3.1).

In single-scattering, the photoelectron is propagated from the emitter to the first scatterer. Then the appropriate $F_{00,\lambda}$ value describing the scattering of this photoelectron into the direction of the detector is read from a scratch file,. In double-scattering, one starts from the emitter and reads the appropriate $F_{\lambda\lambda'}$ value for the first scatterer towards the second. The resulting scattering amplitude just before the second scatterer is saved, again in a scratch file, to be used as the starting value for triple-scatttering. After the saving is done, the photoelectron can be scattered off the second scatterer in the direction of the detector using the

appropriate $F_{00,\lambda}$ to yield the double-scattering intensity. This saving and retrieving can be extended up to 10^{th} order: this procedure is used to overcome the large memory requirements on $F_{\lambda\lambda'}$ for bigger clusters. Another advantage of this order-by-order approach is that it eliminates redundancy in calculating the building blocks of the calculation. Once the desired scattering order is reached the output files are written. The Cray version has built in timing routines to write both the CPU time and wall clock time at the end of the output file LISTOUT.

Now we discuss other features of this code in some detail. First inelastic damping. As discussed in connection with Equation (2-4-79), inelastic damping is introduced by multiplying a given wave amplitude by $\exp\{-L/2\Lambda_e\}$, where L is the total distance traveled by the photoelectron inside the solid and Λ_e is the inelastic attenuation length. The latter is calculated using the empirical approximation, $\Lambda_e = f_0 (E_{kin})^{1/2}$, where f_0 is a constant used as an input parameter to the computer code, and E_{kin} here is the internal kinetic energy. (The actual input to the code is the external kinetic energy.)

As discussed in Section 2.4.6, this code is capable of including simple correlated, parameterized correlated, and simple uncorrelated Debye-Waller vibrations. The correlated vibrations are done using a subroutine developed by M. Sagurton [4(b)] using the Equation (2-4-82). In this case the $\sigma^2_{j_k j_{k-1}}$ is generated for each diatomic combination. In the second approximate correlated vibration option, the curve of $\sigma^2_{j_k j_{k-1}}$ is calculated outside the code. Then it is

approximated by three straight line segments, as shown in Figure 2.9. The inputs to the code are the gradients (m_1,m_2,m_3) and intercepts (c_1,c_2,c_3) of each line and the distances (x_1 and x_2) below which the first two lines are applicable. The third line really requuire only the intercept, as its gradient m_3 is taken to be zero to mimic uncorrelated Debye-Waller behavior at large distances. Then the value of $\sigma^2_{j_k j_{k-1}}$ for a given distance can be calculated inside the code in a more rapid manner. The approximate correlated vibrations provide the additional freedom to use an ad hoc scheme for a given system. Finally the uncorrelated option involves simply calculating the asymptotic limit of $\sigma^2_{j_k j_{k-1}} = \sigma^2_{j_k}$ from Equation (2-4-82).

An additional important correction is for angular broadening due to the finite anlyzer acceptance solid angle. The most accurate way to do this is to sum each intensity over ≥ 10 points of $\vec{k}$ equally distributed over the solid angle of acceptance of the analyzer to be simulated. This, however, would cost a great deal of computation time, basically in proportion to the number of points. However, as noted earliar, we can simplify this calculation by noting that only factors depending on the direction of $\vec{\rho}_d$ will change as the angle averaging is done; these are only the phase factors $\exp\{i\rho_{j_k j_{k-1}}(1-\cos\theta'_{j_k j_{k-1}})\}/\rho_{j_k j_{k-1}}$ (with $\theta'_{j_k j_{k-1}}$ defined as before as the scattering angle between $\vec{\rho}_{j_k j_{k-1}}$ and $\vec{\rho}_d$) and, the scattering factors $F_{00,\lambda_N}(\vec{\rho}_d,\vec{\rho}_{j_N j_{N-1}})$. Then, we can furthermore assume that, within the small angular cone of a typical analyzer of of $\pm$ a few

degrees, the variation of the scattering factors F_{00,λ_N} with angle is much less important than that of the phase factors $\exp\{i\rho_{j_k j_{k-1}}(1-\cos\theta'_{j_k j_{k-1}})\}/\rho_{j_k j_{k-1}}$. Hence, as a first approximation, we can vary only the phase factors while keeping F; this is the very rapid method used at present. As a further improvement to the code we note that the factors F_{00,λ_N} are only as difficult to compute as in a 'single-scattering' problem and thus only moderately time consuming. The code therefore is written in such a way that it could be easily modified in the future to do exact angular broadening. However, single-scattering comparisons between the approximate and exact angular broadening results indicate that the former is fully satisfactory over a small angular cone.

2.6.2. Scanned-Angle and Scanned-Energy Photoelectron Diffraction:

(a). <u>The Inputs</u>:

There are several inputs to this code. They are listed below; begining with an example of a scanned-angle case, and then showing a scanned-energy case.

File 1 - XPDIN:

The name of File 1 should always be XPDIN. Names of other files are listed in XPDIN and, hence, can vary. For clarity, we label lines in this file as L1, L2 etc. The actual input file does not have these line numbers. The example shown below is for s → p photoemission from

a two atom Cu chain at 1000.0 eV. An azimuthal scan is done at a polar takeoff angle equal to zero. Polar angle is henceforth measured with respect to the specimen surface. The electron mean free path is effectively "infinite" with an f_0 factor of 10^7, and the inner potential is zero. Events up to 10^{th} order are included and the R-A method is used in second order ((6×6) F matrices). The convergence cutoff is 5% for all scattering orders above 3^{rd}, and is defined in the previous section.

```
L1.  XPD.F Cu 03 atoms 5% cutoff 6x6  ekin=1000.eV  v0=0  NV 1f=1
L2.  0 0.0000 0.0000000 0.0000 1.0000000
L3.  28 00 00 00 00
L4.  coord   cul000p junkp   junkp   junkp
L5.  $list1 thetab=0.0,thetar=1.0,thetas=2.0,
L6.    phib=0.0,phir=180.0,phis=2.0
L7.    energb=1000.0,energr=1.0,energs=1.0 $end
L8.  $list2 alpha=90.0,level=10,v0=0.0,order=2,
L9.    lfactr=10e+06,bangle=0.0 $end
L10. $list3 zs=0.0,cut4=5.0,cut5=5.0,cut6=5.0,cut7=5.0,cut8=5.0,
L11.   cut9=5.0,cut10=5.0 $end
L12. azimuthal
L13. full
L14. parameterized
L15. 0.00000 0.00000 0.00000 0.00000 0.00000 0.00000 00.00000
L16. 0.00000 0.00000 0.00000 0.00000 0.00000 0.00000 00.00000
```

Explanation of Lines:

L1. Title line: at user discretion

L2. $\ell_{initial}$, $\delta_{\ell-1}$(radians), $R_{\ell-1}$, $\delta_{\ell+1}$(radians), $R_{\ell+1}$

L3. Atomic number of the emitter followed by atomic numbers for up to four other elements

L4. Coordinate file and phase-shift files for each atomic type. If the number of atomic types are less than five, leave blanks for up to five names using the a8 format

L5. $listl - beginnig of listl

thetab - beginning polar angle (degrees with respect to the surface)

thetar - range of polar angle (o)

thetas - polar angle step size (o), with polar scanning being always made on an axis perpendicular to the plane containing $h\nu$ and $\vec{k}$

L6. phib - beginning azimuthal angle (o)

phir - range of azimuthal angle (o)

phis - azimuthal angle step size (o), with azimuthal scaning always being made about the speciman surface normal

L7. energb - beginning kinetic energy (eV) (E_{kin} external)

energr - range of kinetic energy (eV)

energs - kinetic energy step size (eV)

$end - end of listl

(This set of input is appropriate to scanned-energy calculations, as discussed in the next example)

L8. $list2 - beginning of list2

alpha - angle between $h\nu$ incident and $\hat{k}$ (o), from which the polar angle of the polarization vector $\hat{\epsilon}$ can be calculated. Since $\hat{\epsilon}$ is assumed to be in the plane of $h\nu$ and $\vec{k}$, $\phi_\epsilon = \phi_k$.

level - maximum order of scattering (N_{max} in prior notation)

v0 - inner potential (eV)

order - order of the R-A approximation used (0 = (1x1), 1 = (3x3), 2 = (6x6)

L9. lfactr - determines the mean free path using the empirical relation Λ_e (Å) = lfactr * k ($Å^{-1}$) with k calculate from $k = 2\pi\ [E_{kin}\ (eV)/150.2]^{1/2}$. (Again E_{kin} here is the internal kinetc energy)

bangle - half angle of the analyzer acceptance cone (o)

$end - end of list2

L10. $list3 - beginning of list3

zs - the height in Å of the region above the centers of the surface layer of atoms in which additional inelastic attenuation should be taken into account. The surface, before this modification, is taken to be at the highest z value in the coordinate file. (z is negative into the bulk and positive otherwise. The emitter is always at x = y = z = 0).

cut4 - cutoff value for fourth order

cut5 - cutoff value for fifth order

cut6 - cutoff value for sixth order

cut7 - cutoff value for seventh order

cut8 - cutoff value for eighth order

L11. cut9 - cutoff value for ninth order

cut10 - cutoff value for tenth order

$end - end of list3

(cut4 - cut10 above are measured as a % of 3^{rd} order maximum reference)

L12. azimuthal, polar or energy (selects the type of scan to be done. Once selected, only the beginning parameters and their ranges for that mode are used, and those for the others modes are ignored.)

L13. 'atomic' to calculate normalized χ curves as $[I(k,\theta,\phi) - I(k,\theta,\phi,direct)]/I(k,\theta,\phi,direct)$ or 'full' for full intensity

L14. 'parameterized' for parameterized vibrations using three linear segments or 'exact' for correlated vibrations from Equation (2-4-82).

L15. and L16. parameters for vibrations depending on the model. At present this code can handle vibrations of two-component systems only (e.g., adsorbate-substrate systems). The parameters on line L15 are for the adsorbate and those on line L16 are for the substrate. (Both lines are read

in the code using free format). For systems with more than two atomic types, set all variables to zero. (The next version of this code will be capable of handling vibrations for upto five different atomic types).

For parameterized correlated vibrations:

$m_1(\text{Å})$, $c_1(\text{Å}^2)$, $m_2(\text{Å})$, $c_2(\text{Å}^2)$, $c_3(\text{Å}^2)$, $x_1(\text{Å})$, $x_2(\text{Å})$ (see Figure 2.9).

For simple Debye-Waller vibrations:

0.0, 0.0, 0.0, 0.0, $c_3(\text{Å}^2)$, 0.0, 0.0. (again from Figure 2.9)

For exact correlated vibrations:

R_j, q_D, t_{Deb}, t_{exp}, amass (where $R_j = |\vec{R}_{j_k} - \vec{R}_{j_{k-1}}|$ - distance between the two correlated atoms (Å), q_D - magnitude of the Debye wave vector (Å^{-1}), $t_{Deb} = \theta_D$ - Debye temperature (K), $t_{exp} = T$ - experimental temperature (K), and amass = M_s - mass of the vibrating atom (g)).

A sample input file for a normal energy scan from 100 to 500 eV for the above case with emission along the x-axis ($\theta = 0^\circ$, $\phi = 0^\circ$) is given below. If an angle-resolved photoelectron extended fine structure scan is intended then line 13 should read 'atomic' so that a normalized χ function defined as [I - I(direct)] / I(direct) is calculated as a function of energy.

```
L1  XPD.F Cu 03 atoms 5% cutoff 6x6  e-scan  v0=0  NV lf=1
L2  0 0.0000 0.0000000 0.0000 1.0000000
L3  28 00 00 00 00
L4  coord   cuphase junkp   junkp   junkp
L5  $list1 thetab=0.0,thetar=1.0,thetas=2.0,
L6  phib=0.0,phir=1.0,phis=2.0
L7  energb=100.0,energr=400.,energs=5.0 $end
L8  $list2 alpha=90.0,level=5,v0=0.0,order=2,
L9  lfactr=10e+06,bangle=0.0 $end
L10 $list3 zs=0.0,cut4=5.0,cut5=5.0,cut6=5.0,cut7=5.0,cut8=5.0,
L11 cut9=5.0,cut10=5.0 $end
L12 energy
L13 full
L14 parameterized
L16 0.00000 0.00000 0.00000 0.00000 0.00000 0.00000 00.00000
L17 0.00000 0.00000 0.00000 0.00000 0.00000 0.00000 00.00000
```

File 2 - Coordinate File:

The name of the coordinate file is given on as the first entry on line 4 (L4) of XPDIN. The first line of this coordinate file has the number of atoms in the cluster. The second line represents the x, y, and z corrdinates (in Å) and the atomic number of the emitter and it must must directly follow the number of atoms in the cluster. On the following lines, the first three numbers are the x, y, and z coordinates for each atom (in Å) and the last number is the atomic

number. This version of the code handles five different atomic types. As expected, x and y are in the surface plane, with x located at $\theta = 0^{\circ}$, $\phi = 0^{\circ}$; z is thus perpendicular to the surface, with +z values lying above this plane and -z values lying in the opposite sense. The sample file shown below is for a three atom Cu chain along the x-axis.

```
3
  0.0000    0.0000    0.0000 28
  3.5000    0.0000    0.0000 28
  7.0000    0.0000    0.0000 28
```

File 3 - Phase Shift Files:

The names of phase shift files are listed on line 4, after the name of the coordinate file. Each element listed on line 3 should have a corresponding phase shift file. In the example given above there is only one such file (cul000p). It has the following structure. The first line gives the energy in eV and the number of phase shifts to be used at that energy. The next five lines list these phase shifts. The first line contains $\ell = 0$ to $\ell = 4$, the second line $\ell = 5$ to $\ell = 9$ etc. For energy scans, where multiple energy steps are involved this file must be repeated for each energy step.

```
1000.0  20
   -0.87809      0.71220     -0.61514     -1.51618      1.07160
    0.72774      0.50911      0.36592      0.26775      0.19854
    0.14799      0.11017      0.08180      0.06003      0.04318
    0.03050      0.02102      0.01368      0.00808      0.00422
    0.00193      0.00000      0.00000      0.00000      0.00000
```

(b). The Outputs:

There can be two or three output files. They are listed below. The first file is named LISTOUT. This is the long output file. In the intensity part the first column is polar angle, the second is azimuthal angle, the third is the single scattering intensity, the fourth is the double scattering intensity and so on up to the tenth order intensity. For energy scans the first column is energy in eV, the second is the k vector (in $\mathring{A}^{-1}$), the third is the single scattering intensity, the fourth is the double scattering intensity and so on up to tenth order. Shown below is the file LISTOUT corresponding to the input file for an azimuthal scan given at the beginning of this section.

```
THE LONG OUTPUT OF XPD.FOR (August/'990)
Copyright (c) 1990 by A. P. Kaduwela, D. J. Friedman and C. S. Fadley
Please acknowledge the use of this code
```

```
XPD.F Cu 03 atoms 5% cutoff 6x6  ekin=1000.eV  v0=0  NV 1f=0
&LIST1  THETAB = 0.0,  THETAR = 1.0,  THETAS = 2.0,  PHIB = 0.0,
        PHIR = 180.0,  PHIS = 2.0,  ENERGB = 1000.0,  ENERGR = 1.0,
        ENERGS = 1.0,  &END
&LIST2  ALPHA = 90.0,  LEVEL = 10,  V0 = 0.0,  ORDER = 2,
        LFACTR = 10000000.0,  BANGLE = 0.0,  &END
&LIST3  ZS = 0.0,  CUT4 = 5.0E-02,  CUT5 = 5.0E-02,  CUT6 = 5.0E-02,
        CUT7 = 5.0E-02,  CUT8 = 5.0E-02,  CUT9 = 5.0E-02,
        CUT10 = 5.0E-02,  &END

Vibrational Parameters:  adsorbate-adsorbate
 Gradients =  0.000000  0.000000 Intercepts =  0.000000  0.000000
 Critical Values: Y =  0.000000 X =  0.000000  0.000000

Vibrational Parameters:  adsorbate-substrate and substrate-substrate
 Gradients =  0.000000  0.000000 Intercepts =  0.000000  0.000000
 Critical Values: Y =  0.000000 X =  0.000000  0.000000

The number of atoms in the cluster =   3

Coordinates of the Cluster
    0.0000    0.0000    0.0000 28
    3.5000    0.0000    0.0000 28
    7.0000    0.0000    0.0000 28
```

The Z coordinate of the surface is 0.0000

The bond length matrix

0.0000	3.5000	7.0000
3.5000	0.0000	3.5000
7.0000	3.5000	0.0000

Phase-shifts for atomic number 28

1000., 20

-0.878090	0.712200	-0.615140	-1.516180	1.071600
0.727740	0.509110	0.365920	0.267750	0.198540
0.147990	0.110170	0.081800	0.060030	0.043180
0.030500	0.021020	0.013680	0.008080	0.004220
0.001930	0.000000	0.000000	0.000000	0.000000

Intensities up to 10th order

0.0	0.0	0.25874E-01	0.19670E-01	0.19532E-01	0.19339E-01
		0.19384E-01	0.19384E-01	0.19384E-01	0.19384E-01
		0.19384E-01	0.19384E-01		
0.0	2.0	0.24603E-01	0.18027E-01	0.17891E-01	0.17712E-01
		0.17755E-01	0.17755E-01	0.17755E-01	0 .17755E-01
		0.17755E-01	0.17755E-01		
0.0	4.0	0.20901E-01	0.13590E-01	0.13464E-01	0.13322E-01
		0.13361E-01	0.13361E-01	0.13361E-01	0.13361E-01
		0.13361E-01	0.13361E-01		

0.0	6.0	0.15255E-01	0.78439E-02	0.77348E-02	0.76507E-02
		0.76815E-02	0.76815E-02	0.76815E-02	0.76815E-02
		0.76815E-02	0.76815E-02		
0.0	8.0	0.88506E-02	0.30380E-02	0.29565E-02	0.29350E-02
		0.29544E-02	0.29544E-02	0.29544E-02	0.29544E-02
		0.29544E-02	0.29544E-02		
0.0	10.0	0.36152E-02	0.12626E-02	0.12142E-02	0.12397E-02
		0.12462E-02	0.12462E-02	0.12462E-02	0.12462E-02
		0.12462E-02	0.12462E-02		
.					
.					
.					
0.0	170.0	0.53175E-02	0.54698E-02	0.59504E-02	0.57292E-02
		0.57265E-02	0.57265E-02	0.57265E-02	0.57265E-02
		0.57265E-02	0.57265E-02		
0.0	172.0	0.53306E-02	0.60318E-02	0.65777E-02	0.63047E-02
		0.62999E-02	0.62999E-02	0.62999E-02	0.62999E-02
		0.62999E-02	0.62999E-02		
0.0	174.0	0.54862E-02	0.66138E-02	0.71893E-02	0.68665E-02
		0.68602E-02	0.68602E-02	0.68602E-02	0.68602E-02
		0.68602E-02	0.68602E-02		
0.0	176.0	0.56649E-02	0.70539E-02	0.76338E-02	0.72720E-02
		0.72646E-02	0.72646E-02	0.72646E-02	0.72646E-02
		0.72646E-02	0.72646E-02		

0.0 178.0	0.57931E-02	0.73119E-02	0.78862E-02	0.74999E-02
	0.74920E-02	0.74920E-02	0.74920E-02	0.74920E-02
	0.74920E-02	0.74920E-02		
0.0 180.0	0.58386E-02	0.73954E-02	0.79664E-02	0.75718E-02
	0.75637E-02	0.75637E-02	0.75637E-02	0.75637E-02
	0.75637E-02	0.75637E-02		

THE TOTAL NUMBER OF SCATTERING EVENTS

Single	:	182
Double	:	364
Triple	:	728
Quadruple	:	910
Quintuple	:	546
Sextuple	:	0
Heptuple	:	0
Octuple	:	0
9th	:	0
10th	:	0

THE BEGINNING DATE AND TIME	:	11/21/90	21:51:51
THE ENDING DATE AND TIME	:	11/21/90	21:52:12
TOTAL CPU MINUTES	:	0.4495E-01	

File 2 - PLOT1: This file is a short version of LISTOUT containing intensities up to fifth order. If "level" is greater than five then

another file named PLOT2 will appear. That contains intensites from sixth to tenth order. File PLOT1 for the above LISTOUT is shown below.

```
 XPD.F Cu 03 atoms 5% cutoff 6x6  ekin=1000.eV  v0=0  NV 1f=0
0.0  0.0 0.25874E-01 0.19670E-01 0.19532E-01 0.19339E-01 0.19384E-01
0.0  2.0 0.24603E-01 0.18027E-01 0.17891E-01 0.17712E-01 0.17755E-01
0.0  4.0 0.20901E-01 0.13590E-01 0.13464E-01 0.13322E-01 0.13361E-01
0.0  6.0 0.15255E-01 0.78439E-02 0.77348E-02 0.76507E-02 0.76815E-02
0.0  8.0 0.88506E-02 0.30380E-02 0.29565E-02 0.29350E-02 0.29544E-02
0.0 10.0 0.36152E-02 0.12626E-02 0.12142E-02 0.12397E-02 0.12462E-02
    .
    .
    .
0.0 170.0 0.53175E-02 0.54698E-02 0.59504E-02 0.57292E-02 0.57265E-02
0.0 172.0 0.53306E-02 0.60318E-02 0.65777E-02 0.63047E-02 0.62999E-02
0.0 174.0 0.54862E-02 0.66138E-02 0.71893E-02 0.68665E-02 0.68602E-02
0.0 176.0 0.56649E-02 0.70539E-02 0.76338E-02 0.72720E-02 0.72646E-02
0.0 178.0 0.57931E-02 0.73119E-02 0.78862E-02 0.74999E-02 0.74920E-02
0.0 180.0 0.58386E-02 0.73954E-02 0.79664E-02 0.75718E-02 0.75637E-02
```

File PLOT2 for this case is identical in structure to PLOT1 but contains intensities for sixth to tenth order.

2.6.3. Scanned-Angle Auger Electron Diffraction:

To prepare XPDIN for scanned-angle Auger electron diffraction the following changes are needed on line 2.

1. ℓ_i should be 1.
2. $\delta_{\ell-1}$ should be 0.0 and $R_{\ell-1}$ should be 1.0.
3. Both $\delta_{\ell+1}$ and $R_{\ell+1}$ should be 0.0.

Then the modified XPDIN for a typical case at 917 eV energy looks as,

```
L1  XPD.F Cu O2 atoms 5% cutoff 6x6  ekin=917.0 eV  v0=0  NV lf=0
L2  1 0.0000 1.0000000 0.000 0.0000000
L3  28 00 00 00 00
L4  coord   cu917p  junkp   junkp   junkp
L5  $list1 thetab=0.0,thetar=1.0,thetas=2.0,
L6    phib=0.0,phir=180.0,phis=2.0
L7    energb=917.0,energr=1.0,energs=1.0 $end
L8  $list2 alpha=90.0,level=10,v0=0.0,order=2,
L9    lfactr=10e+06,bangle=0.0 $end
L10 $list3 zs=0.0,cut4=5.0,cut5=5.0,cut6=5.0,cut7=5.0,cut8=5.0
L11   cut9=5.0,cut10=5.0 $end
L12 azimuthal
L13 atomic
L14 parametrized
```

L15 0.00000 0.00000 0.00000 0.00000 0.00000 0.00000 00.00000

L16 0.00000 0.00000 0.00000 0.00000 0.00000 0.00000 00.00000

Also, one should set ENERGB on line 7 (L7) of XPDIN to the desired energy of the Auger electron, here chosen to be 917.0 eV, a case to be considered later. Once the mode on line 12 (L12) of XPDIN is set to either polar or azimuthal, ENERGR and ENERGS become unimportant. Other input parameters are set as discussed in Section 2.6.2. Other input files are identical in structure to those described in that section.

These modifications mimic a p → s transition. Here we make the assumption that the final state of an Auger electron is an s-wave. The final single-scattering intensity for this case is given in Equation (2-4-52). Notice that the p-initial state does not yield any observable effect in that equation; this initial state appears only in the factor $C^1(\ell_f,m_i,\ell_i,m_i)$ within $m_{L,c}$ (cf. Equation (2-4-11)) which is common to both direct and scattered waves (single and multiple). Hence, the only consequence of simulating the s-wave Auger final state by using the ℓ-1 channel of a p-initial state is that the final intensities are multiplied by a constant.

2.6.4. Possible Methods for More Accelerated Calculations and Geometry Optimizations:

In comparing theoretical and experimental curves so as to determine a structure one often has to fine tune several structural parameters of the theoretical model before finding the optimum set. This is known as geometry optimization, and it can involve calculating diffraction curves for many different geometries, exactly as is done in a typical LEED analysis. In the case of an adsorbate/substrate system, for example, one of the most frequently changed structural parameters is the vertical distance of the adsorbate from the substrate; but beyond this various relaxations of the underlying substrate atoms from their bulk positions may be tried. To avoid incurring a prohibitive cost in computation time for such optimizations, it is logical then to search for a way to do such sets of calculations for different structural parameters in the most efficient way. One thing to avoid is calculating anything from one structure to another that does not change at all, or at a more approximate level, does not change very much. We discuss below two possible approximations to permit more rapid calculations and geometry optimizations.

The most time consuming part of our method is the calculation of the scattering matrices $F_{\lambda_k\lambda_{k-1}}(\vec{\rho}_k,\vec{\rho}_{k-1})$. The elegance of the Rehr-Albers approach allows us to initially calculate scattering matrices for every atom with respect to two other atoms on each side

of it in some scattering path. Each such $F_{\lambda_k\lambda_{k-1}}$ can be referred to as a vertex, as shown in Figure 2.6(b). Once all the verticies are calculated, they can be used, together with the W "termination" factors that are much easier to calculate, to build up the the actual scattering calculation. Let us now estimate the number of scattering matrices or verticies that would need to be recalculated in going from one geometry to another in an adsorbate/substrate system for which we are varying the vertical adsorbate/substrate distance only.

Let M be the total number of atoms in the cluster and f be the fraction of these atoms in the adsorbate layer. Then the number of atoms in the substrate is (1-f)M. Out of all possible M(M-1)(M-1) verticies in the cluster, only a fraction of these has to be recalculated when the vertical distance is changed. There are eight possible verticies in the notation A = adsorbate, S = substrate: A-A-A, A-A-S, A-S-A, A-S-S, S-A-A, S-A-S, S-S-A, and S-S-S, we must recalculate all types coupling S and A, or 6 out of 8. Note also that there are as many A-A-S combinations as S-A-A combinations. This is also true for A-S-S and S-S-A combinations. Therefore, the fraction of verticies to be recalculated, F, can be written as,

$$F = \{2\cdot[fM\cdot(fM-1)\cdot(1-f)M] + [fM\cdot(1-f)M\cdot fM] + 2\cdot[fM\cdot(1-f)M\cdot((1-f)M-1)] + [(1-f)M\cdot fM\cdot(1-f)M]\} / M\cdot(M-1)\cdot(M-1)$$

$$= \frac{f\ (1-f)\ M\ (3M-4)}{(M-1)^2}. \qquad (2.6.1)$$

The large M limit of F is thus,

$$F(M \to \infty) = 3\ f\ (1-f). \qquad (2\text{-}6\text{-}2)$$

Table 2.1 shows the behavior of F as a function of both M and f. It is evident from this table that about 50% of the verticies have to be recalculated for each vertical distance for a typical case of f = 0.20. This would save 50% of the time of recalculating the $F_{\lambda_k\lambda_{k-1}}$'s, and would be worth incorporating in a future version of the program. This conclusion is also valid for the case of first-layer relaxation in a substrate system. However, the situation gets worse for multilayer adsorbate/substrate relaxation where f could be as high as 0.5 and about 3/4 of the $F_{\lambda_k\lambda_{k-1}}$'s would have to be recalculated for each geometry. This approach is thus interesting, but not as generally useful as one might desire.

We now consider a more approximate approach. Small vertical relaxations or other atomic displacements will cause only slight changes in the angles in the vertices. Therefore, a perturbation approach to the problem could be a very efficient path to geometry optimization.

One such approach depends on the fact that, except in the forward and backward scattering directions, the scattering factor $F_{\lambda_k\lambda_{k-1}}$ is generally not rapidly varying with vertex angle. This suggests taking

those $F_{\lambda_k\lambda_{k-1}}$ values appropriate to some reference structure not too far from the actual structure, and varying only the geometric phase factors in which the actual path length differences of waves are accounted for. To illustrate this idea in detail let us look at the general single-scattering expression for the scattered wave as written down before in Equation (2-4-44):

$$G^{(1)}_{00,L_f}(\vec{R}_j,\vec{R}_d) = [\exp(i\rho_d)/\rho_d] \sum_j [\exp(i\rho_j(1-\cos\theta_j))/\rho_j] \times \sum_{\lambda_j} F_{00,\lambda_j}(\vec{\rho}_d,\vec{\rho}_j)\ W^{00,L_f}_{00,\lambda_j}(\vec{\rho}_j) \qquad (2\text{-}6\text{-}3)$$

where,

$$F_{00,\lambda_j}(\vec{\rho}_d,\vec{\rho}_j) = \sum_{\ell_j} t_{\ell_j} \gamma^{\ell_j}_{00}(\rho_d)\ R^{\ell_j}_{0\mu_j}(\hat{\rho}_d,\hat{\rho}_j^{-1})\ \tilde{\gamma}^{\ell_j}_{\lambda_j}(\rho_j),$$

and,

$$W^{00,L_f}_{00,\lambda_j}(\vec{\rho}_j) = \gamma^{\ell_f}_{\lambda_j}(\rho_j)\ R^{\ell_f}_{\mu_j m_f}(\hat{\rho}_j).$$

In this equation the only time consuming factor is F_{00,λ_j}. Other factors can be recalculated for each new choice of structural parameters. The approximation is then to multiply the old scattering factor, F_{00,λ_j}, by a new phase factor,

$\exp\{i(\rho_j+\delta\rho_j)(1-\cos[\theta_j+\delta\theta_j])\}/(\rho_j+\delta\rho_j)$. This approach is expected to be acceptable if the scattering angle of the vertex is at least 20° away from either forward or backward directions. Otherwise new scattering factors should be recalculated. In implementing such a scheme, the magnitudes of both $\delta\theta_j$ and $\delta\rho_j$ with respect to the reference structure could easily be calculated at each step in an optimization and criteria established as to when a given $F_{\lambda_k\lambda_{k-1}}$ needs recalculation, or when a new reference structure is needed. The same approximation could be made in a multiple scattering calculation, but here all of the associated phase factors

$$\exp\{i(\rho_{j_kj_{k-1}}+\delta\rho_{j_kj_{k-1}})(1-\cos[\theta'_{j_kj_{k-1}}+\delta\theta'_{j_kj_{k-1}}])\}/(\rho_{j_kj_{k-1}}+\delta\rho_{j_kj_{k-1}})$$

in Equation (2-4-77) would need to be recalculated. (Note that it is θ' we must use here and not θ (cf. definitions leading to Equation (2-4-71).) Such a scheme should be very efficient way to search structures, and its implementation in a future version of this program is strongly recommended. This method is also very similar in philosophy to that of "tensor LEED" proposed recently [32].

Finally we note two other procedures that could be used to speed up such calculations: (1) storing all F's and W's needed in fast-access RAM, thus eliminating slower disk retrival and (2) going to lower order F's or even plane-wave scattering) if the two distances in F become larger.

2.4.7. COMPUTING ENVIRONMENT:

We have used several computers during the development, optimization, testing, and application of this program. We briefly indicate the characteristics of these machines and point out certain machine-specific parts of the code below.

2.7.1. Cray X-MP/48 (CTSS):

This code was initially developed, optimized, and tested on the Cray X-MP/48 supercomputer at the San Diego Supercomputer Center using the CTSS operating system. The Cray X-MP/48 is a 64-bit machine with vectorizing capabilities. It has four CPU's and an eight megaword RAM shared by all CPUs. During the optimization several Cray specific functions were used. They are as follows:

call link - A call to the routine 'link' must appear as the first executable statement of the code. This is also capable of linking files to unit numbers. If you wish to open your files in the traditional FORTRAN way, then you may use the 'call dropfile(0)' statement instead of call link(.....) and then use the 'open' statement. At end of the main module you may use 'call exit'. But the 'end' statement does the equivalent.

n = cvmgz(i,j,k) - if k = 0 then n = i
if k .ne. 0 then n = j

This function is vectorizable. But "IF" statements in the equivalent Fortran soubroutine are not.

saxpy(3,-1,v1,1,v2,1) - This is equivalent to v2(1) = v2(1) - v1(1)
v2(2) = v2(2) - v1(2)
v2(3) = v2(3) - v1(3)

The first 3 means that the vector length is 3. -1 correspond to the - sign and other 1's correspond to vector strides of 1.

sdot(3,v2,1,kuv,1) - This is the dot product of two vectors. That is v2(1)xkuv(1) + v2(2)xkuv(2) + v2(2)xkuv(2). Again 3 is the vector length and 1's are strides.

wrbin(xx,yy(1,1,1),length) - This allows to unload the array yy onto unit xx in a very efficient way through a buffer. yy(1,1,1), for example, is the first element of the array and length is the number of words you want to unload.

rdbin(xx,yy,length) - This is the complement of webin. The only difference is that you specify just the array.

Another thing to notice in this code is the style, which has been written specially with vectorization in mind. To run this code on a non-vector machine efficiently requires rearranging certain parts, as we have done in converting to a Sun workstation.

This machine was replaced with a Cray Y-MP/864 in January, 1990. Modifications needed for this changeover are described in the next section.

2.7.2. Cray Y-MP/864 (UNICOS):

The current version of the code runs on the Cray Y-MP/864 at the San Diego Supercomputer Center using the UNICOS operating system. This machine has eight CPUs and 16 megawords of RAM. The inputs and outputs on the Y-MP are identical to those on the Cray X-MP. Some X-MP specific routines in the codes are replaced by corresponding Y-MP counterparts and we describe them below.

The "call link" statement is not available on the Y-MP. Hence all the files opened or created in that statement should now be opened with the standard FORTRAN-77 OPEN statement. RDBIN and WRBIN are replaced by BUFFER IN and BUFFER OUT, respectively:

buffer in (id,mode) (bloc,eloc), and,

buffer out (id,mode) (bloc,eloc).

These allow the subsequent execution sequence to proceed concurrently with the tranfer of data. Here id is the unit specifier. Use of mode ≥ 0 is for regular full record I/O and <0 for partial records, and bloc is the symbolic name of the variable, array or array element that marks the beginning location of the buffered I/O transfer.

2.7.3. Sun-4 SPARCstation (SunOS):

This 32-bit Sun-4 system with SPARC (Scalable Processor ARChitecture) runs SunOS Release 4.0. The Sun-4 CPU comprises an Integer Unit (IU) that performs basic processing and a Floating Point

Unit (FPU) that performs floating point calculations. SPARC is a RISK (Reduced Instruction Set) architecture that emphasizes simplicity and efficiency. The RAM on this machine is 8 Mb and the disk capasity is about 1.3 Gb. It is housed in the Department of Chemistry, University of Hawaii.

This SPARCstation has a FORTRAN-77 compiler. To run on this mechine, our code was rewritten in ANSI FORTRAN-77 to remove all Cray specific routines. The run times were obtained by using a simple UNIX script. Table 2.3 shows the times required for a small chain of Ge atoms, as described in Section 2.7.2. This can be compared with Table 2.2 which contains the same times on a Cray Y-MP/864. The following facts should be kept in mind during this comparison: 1. The Sun had a very light work load and was almost a single user environment. 2. The Cray had the usual work load, but these calculations were done at priority = 2, which is the highest, but nonetheless usual for such quick chain calculations. 3. The Cray is double precision and Sun is single, but the numerical results are found to agree very well. 4. The code is vectorizable on the Cray but not on the Sun. Table 2.4 shows the normalized time rations Sun/Cray without taking any of the above facts into account. As shown there, when the Cray is used at its highest priority it can be as much as 35 times faster than the SPARCstation on the wallclock. On the CPU clock the Cray is about 25 times faster. But for more time consuming jobs, the Cray should be used in a batch queue mode to stretch time allocations and this usually increases the wallclock time by an order of magnitutde, thus

making it comparable to that for the SPARCstation! Hence a single user (or nearly single user) SPARCstation environment is a viable option for running this code in production mode, and our group is proceeding to further develop this option.

2.8. SENSITIVITY TO INPUT PARAMETERS AND COMPARISON OF RESULTS WITH PREVIOUS CALCULATIONS:

2.8.1. Auger and Photoelectron Emission from Atomic Chains:

We now consider single-scattering and fully converged multiple-scattering results for simple linear chains of different atoms, an illustrative type of test case discussed first by Xu, Barton, and Van Hove [7]. To illustrate the type of diffraction pattern one expects from such chains, we show in Figure 2.3(c) a simplified drawing applicable to high-energy scattering where forward peaking is dominant and the scattering phase shift is small (here assumed to be zero). Both the 0^{th} order (forward scattering) peak and the higher-order diffraction peaks are labelled. In a real n-atom chain these features will be distorted somewhat by scattering phase shifts that depend on scattering angle, by the resulting imperfect overlap of different orders from different scatterers, by inelastic attenuation effects, and by multiple-scattering effects.

We begin by considering Cu atoms placed at 45° with respect to a fictitious "(001) surface", as shown in the inset of Figure 2.10. The

2.56 Å nearest neighbor distance is chosen to simulate emission along a [101] direction. The surface is used only to determine that region of space over which an exponential decay of intensity due to inelastic scattering is included. These chains represent the nearest-neighbor [101] direction in the fcc Cu crystal, with a single emitting atom at the bottom of the chain. The total emission from such a [101] chain in the metal would thus be the sum over the intensities of all of these emitters from the surface inward to the end of the chain. Cu LMM Auger emission at 917.0 eV is simulated using the aforementioned approximation of an s outgoing wave (ℓ_f=0 only). Λ_e is taken to be 11.7 Å at 917 eV and 3.9 Å at 100 eV in results to be discussed later. Refraction at the surface due to the inner potential V_0 has not been included. The resulting curves for 2-10 atom linear chains are shown in Figure 2.10. Figure 2.11 shows other information derived from these curves, in particular the forward-scattering along-chain intensities in both SS and MS and, in the lower panel, the amount of MS "defocussing", which is defined as $D(\%) = 100 \times [I^{SS}(\text{along chain}) - I^{MS}(\text{along chain})] / I^{SS}(\text{along chain})$, all as a function of chain length n.

From these two figures, it is evident that the longer the chain is, the greater are the MS effects: the forward-scattering peak height systematically diminishes as the number of atoms in the chain increases, eventually falling by about 6 atoms to a level equal to the background on either side of the chain axis. Such intensity reductions were termed "defocussing" in the first discussion of this

effect by Tong and co-workers [2]. It is also interesting to note that the MS peak widths are consistently narrower than those of corresponding SS peaks, becoming systematically smaller in FWHM as the number of atoms in the chain is increased. This can be qualitatively understood from a classical picture in which only those electrons with very small deflections (i.e., with large impact parameters at the edge of the scattering potential) can avoid being driven into defocussing pathways in passing several scattering centers. By contrast, for a 2-atom chain and at this high energy, MS effects are negligible, a simplifying result which is applicable to emission from an oriented diatomic molecule such as the system CO/Fe that is to be discussed later. The 4- to 10-atom cases are applicable to multilayer substrate emission or to grazing-angle emission from adsorbate/substrate systems, since in both of these cases, emitters can have more or less linear rows of atoms between them and the detector for a certain direction of emission. In such cases, one thus expects that intensity along linear or nearly-linear chains of atoms with small interatomic distances will be significantly reduced. By contrast to the MS results, the SS intensity only begins to reduce after $n = 4$-5 due to both interference effects and inelastic attenuation. But even at $n = 10$, the SS intensity shows a pronounced forward-scattering peak and is much too strong compared to the MS intensity.

These calculations provide another test of the accuracy of our method and the computer code, because a similar set of curves for the same case were reported earlier by Xu and Van Hove [7] for 2-, 3- and

5-atom Cu [101] chains at 917.0 eV; they have used the TS-MQNE method of Barton and Shirley [15] in their work. The good agreement between these two different approaches to MS is very encouraging: in fact, excellent agreement is obtained if we allow fully for the differing degrees of angular broadening used in the two sets of calculations.

We have also performed calculations on such Cu chains at the much lower energy of 100.0 eV. There is no Cu Auger peak at 100.0 eV and this energy was simply chosen to investigate the low energy behavior of multiple-scattering effects, again for an outgoing s-wave. As shown in Figures 3.9 and 3.10, the SS and MS forward-scattering intensities decay at a more nearly comparable rate than those at 917.0 eV. This is due to the lack of a strongly forward-peaked scattering factor, as well as to the shorter electron mean free path at this energy, which tends to attenuate MS effects with longer total path lengths. Although both defocussing loss of intensity and peak narrowing with increasing chain length are still present, they are less pronounced than at 917 eV and we expect this to be a general comparison between lower (~100 eV) and higher ($\geq$ 500 eV) energies with an emitter at the end of the chain.

A further noteworthy effect at lower energies is that the peak maximum systematically moves to higher takeoff angles so that it is 2-5° away from the chain axis. This is due to peak distortion by the stronger exponential damping of intensities by inelastic effects, which will go as $\exp(-Z_n/\Lambda_e \sin\theta)$, if Z_n is the depth of the emitter in the n-atom chain below the surface.

Another interesting case is that of bent chains, results from which are shown in Figure 2.14 for 917.0 eV and in Figure 2.15 for 100.0 eV. The amount of defocussing vs. the bend angle β for 2- 3- and 5-atom chains is presented. The dropoff of defocussing to zero for 917 eV at β ~25°-30° is consistent with the fact that the forward peak in the plane-wave scattering factor dies away to essentially "background" level by this angle [1]. At 100 eV, however, the forward peak is much broader, but the SS and MS intensities still converge at about the same angle. Thus, events more than about 30° off axis are expected to be rather SS in character over a broad range of energy, although we note that the chain geometry we have used here does not allow for back scattering from atom(s) just below the emitter, an effect which could become important by 100 eV.

We now investigate the dependence of these MS effects in chains on different crystallographic directions and materials. In Figures 2.16 and 2.17, we first look at 917 eV emission along the much more open [111] direction in the fcc Cu lattice, which has a nearest-neighbor distance of d_{n-n} = 6.27 Å compared to 2.56 Å for the [101] direction considered previously. In this case, the chain is placed at 35.3° with respect to a fictitious (001) surface and hence the forward-scattering peak is very close to that angle with respect to the surface. The intensities along the chain fall more rapidly with increasing chain length due to inelastic attenuation, which now goes as $\exp\{-Z_n/\Lambda_e \sin(35.3^\circ)\}$. These inelastic effects are enhanced because the interatomic distance and thus Z_n is about 2.5 times larger

than that for the [101] chains at a given n. We note here also that enhanced inelastic attenuation has shifted the peak position about 2° toward higher takeoff angles. Also, the SS and MS results are much closer to one another for [111] chains because of the increased nearest-neighbor distance and a concomitant reduction of MS defocussing effects; thus the importance of this type of MS effect will depend strongly on the direction of observation. Nonetheless, up to 50% defocussing is seen for the longest chain, and the same sort of peak narrowing in MS is observed. Both SS and MS peaks are very small after about eight atoms and hence major contributions to the photoelectron intensity are coming from the top eight layers in each case.

To further investigate the effects of interatomic distances on defocussing, we have finally studied Cu [001] chains (d_{n-n} = 3.62 Å) which are less dense than [101] chains but more dense than [111] chains . We see from Figures 2.18 and 2.19 that both single and multiple scattering intensities for [001] chains are in between those for [101] and [111] cases, but closer in behavior to the [101] case, consistent with the interatomic distance being closer.

As a final comment concerning these results for various Cu chains at 917 eV kinetic energy, we note that the higher-order diffraction features occuring for emission angles more than 10-15° away from the chain axis are always predicted reasonably well by SS theory, even though the MS curves exhibit some additional fine structure about an average that is very close to the companion SS curves. This is

another indication that SS becomes a reasonable approximation for angles sufficiently far from a near-linear chain of scatterers. (cf. also discussion of Figures 2.14 and 2.15.)

We now turn to examples of chains for different materials, and first show in Figures 2.20 and 2.21 results for linear [101] Al chains at 1336.0 eV, which corresponds to MgK_α-excited Al 2s emission. We have here assumed $\hat{\epsilon}$ and $\hat{k}$ to be parallel. Defocusing effects are again obvious, since the SS curves show a pronounced peak for an emitter as deep as ~10 layers in the solid, but the MS intensity goes essentially to background level when the emitter is about eight layers deep. Peak narrowing as chain length increases is also evident. Note also that defocussing sets in more slowly for Al than for Cu as a function of chain length, with about an additional 2 chain atoms being required to yield the same effect in Al.

A second case of Ge [11$\bar{1}$] chains is also interesting and related to a recent x-ray photoelectron diffraction study by our group of a surface phase transition on Ge(111) [10]. In this study, the intensity of a forward-scattering peak along a [11$\bar{1}$] direction at 19.0° with respect to the Ge(111) surface was monitored as a function of temperature, and it was found to show an abrupt decrease at a previously-observed surface phase transition temperature. The Ge [11$\bar{1}$] chains on which we have carried out MS calculations represent this direction. As shown in Figures 2.22 and 2.23, even though the SS peak has contributions from more than ten layers (five (111) double layers in the usual notation), the MS signal is seem to come from the

top eight layers (four double layers) only. Both defocussing intensity reduction and peak narrowing are again seen. The smooth-curve average behavior of of the defocussing effects in Figure 2.23 also make it appear that Ge defocusses intensity more rapidly than Cu.

Figure 2.23 illustrates another interesting effect in Ge: the "saw tooth" variation of the curves as the chain length increases, which is found in both the SS and MS curves. This is explained by the alternating short-long-short-long nature of the interatomic distances along this chain. That is, within a double layer d_{n-n} is 2.45 Å, but between them it is three times this or 7.35 Å. The chains with odd numbers of atoms thus have a gap of 7.35 Å between the emitter and the nearest forward scatterer, and then two foward scatterers with d_{n-n} = 2.45 Å along the chain. Chains with even numbers of atoms have a single nearest-neighbor scatterer at d_{n-n} = 2.45 Å, and then a long gap of 7.35 Å to the next scatterer. The enhanced intensity for even numbers is thus due to having a strong forward-focussing scatterer very close to the emitter. This oscillatory effect on intensity, which has not been discussed previously, could be useful in studying semiconductor epitaxial growth. The "stairstep" form of the defocussing curve also has the same origin, in that increasing from even to odd adds only a long distance scatterer that is very ineffective at defocussing.

In Figure 2.22, SS peak centroids are found to shift to higher takeoff angles by about 3° due to previously discussed inelastic

effects. We do not observe such distortions in the MS peak. This is due to the less severe inelastic distortions on the narrower MS peaks.

We continue this discussion on chains by investigating the dependence of these strong forward-scattering defocussing effects on some of the non-structural parameters used in the simulations.

First, we consider the size of the muffin-tin radius which is used in the program generating the scattering phase shifts δ_ℓ. This is motivated by recent work by Aebisher et al. [34] who have theoretically investigated the material dependence of such MS effects along chains. They concluded that the different amounts of defocussing in Cu and Al chains at a given chain length (cf. our more detailed results of this type in Figures 2.10-2.13, 2.16, and 2.17-2.23) are not due to the choice of non-structural input parameters but rather are primarily due to the differences in the scattering strengths of the constituent atoms (i.e., their atomic numbers and the resultant set of δ_ℓ's). However, an additional parameter related to the δ_ℓ's that depends on the nature of the material and also has a certain degree of arbitrariness in its choice is the muffin-tin radius R_{MT} used in the calculation of the δ_ℓ's. The usual choice is the touching-sphere radius and hence R_{MT} is clearly dependent on the lattice parameters of a given material. We have thus investigated the effects of muffin-tin radius on the final intensities for a five-atom Cu chain, as shown in Figure 2.24. Here we have chosen two non-touching radii which are 30% and 15% smaller than the touching radius, the touching radius, and two overlapping radii which

are 15% and 30% larger than the touching radius. The magnitude of the SS forward intensity increases monotonically with the size of the muffin-tin radius. This can be qualitatively explained in terms of a potential of greater radial extent being capable of better focusing the photoelectrons in the forward direction, since forward-scattering is primarily controlled by the outer portion of the potential corresponding to larger impact parameters. But the MS intensities show a much weaker variation with R_{MT} that is, if anything, the inverse of the SS intensities; that is, the strongest forward scattering in SS (the largest R_{MT}) gives the strongest defocussing and the lowest MS intensity along the chain. This can be explained via a potential of greater radial extent causing stronger defocussing and thus being capable of directing photoelectrons away from the forward direction through multiple-scattering effects. However it is evident from Figure 2.24 that the choice of muffin-tin radius has only minor effects on defocussing. Hence, the choice of muffin-tin radius alone is not sufficient to account for the different amounts of defocussing in different materials; our results show that these differences are mainly due to a combination of the differing atomic scattering strengths and the change in interatomic distance along chains of atoms, in agreement with the work of Aebisher et al. [34].

As a final comment on Figure 2.24, we note that, for angles more than 10-15° away from the chain axis, the diffraction structure is negligiblly affected by the choice of the muffin-tin radius in either SS or MS. This is useful, because as noted previously, it is such

higher-order structure that contains bond length information, or via holographic inversion, also atomic image positions.

There are other non-structural parameters that could influence chain intensities such as the precise choice of the inelastic attenuation length of the photoelectron, the finite aperture of the photoelectron detector and the inner potential. Varying the first two parameters over a reasonable range is found to cause changes in relative peak intensities of only about 1-10%; peak positions are very little affected. Increasing the inner potential is responsible for moving peak positions to lower takeoff angles due to refraction, an effect that is strong for lower energies and/or lower takeoff angles. When the inner potential is increased the peak positions move away from the surface normal. But the single and multiple scattering peaks are found to move together with no relative displacement.

We now present elapsed-time information for these calculations. As noted before, a cutoff criterion is used to discard many unimportant multiple scattering events. This cutoff becomes effective after the third order. All events which are less than, say 5%, of the maximum third order amplitude are not carried over to fourth order scattering. The same check is performed at the end of fourth order scattering and again all events that are less than 5% of the same third order cutoff are not carried over to fifth order. This is done all the way up to the maximum scattering order, which was tenth order in this case. The number of scattering events for each chain is plotted against the order of scattering in Figure 2.25 for chains of

Al atoms varying from two (1 emitter, 1 forward scatterer) to ten (1 emitter, 9 forward scatterers). Since the cutoff becomes effective after third order scattering, the numbers up to third order represent all events possible. For shorter chains the maximum number of events is at the third order. After that the number of events tails off. For longer chains there is a competition between the cutoff and the very large number of new scattering events for each order. The latter seems to dominate over the middle range of orders, but the cutoff takes over eventually. As a result the maximum moves towards higher scattering order.

As an indication of how many events are eliminated with a 5% cutoff, we note that the total number for a given length n at a given order N can be estimated from $(n-1)^N$, so that each extra order should be go up by a factor of (n-1). For n = 10, the fact that the ratio of the number of 5^{th} order events to that of 3^{rd} order is only about 8.8/5.9 = 1.27 instead of 81 indicates that 5th order has been very heavily discriminated against, with only about 0.39% of them being computed.

Figure 2.25 illustrates another simple rule for high-energy scatttering along such chains: the highest order of scattering that needs to be considered is often equal to the maximum number of forward-scattering events in sequence, that is, (n-1) for an n-atom chain. All of the curves in this figure obey this (n-1) rule. (For chains of the much higher Z scatterer W, we find however, that higher orders than predicted by this rule might have to be included.)

Finally, Figure 2.26 shows Cray Y-MP/864 CPU seconds for each chain. Times are for tenth order MS. Even with a 5% cut-off limit the increase in time is a very steep function of n. This time should vary roughly as the area under the different curves in Figure 2.25. For the four highest n values, a log-log plot of time vs. n shows that time α $n^{5.5}$, with an exponent that is not surprisingly about equal to the scattering orders with the largest numbers. This is probably a generally useful way to estimate time scaling with n: that is, if the largest number of scattering events for a given cutoff occurs at N^*, then for an n-atom cluster, the variation of time with n can be estimated from n^{N^*}.

2.8.2. Choice of Convergence Limit and the Maximum Scattering Order:

We now consider the influence of the two crucial parameters controlling both the degree of convergence of the calculation and the amount of computational time required: the cutoff criteria for 4^{th} and higher order events and the maximum of order of scattering included. The effects of these choices will be illustrated first for calculations on simple linear chains.

Shown in Figure 2.27 are the defocussing and the CPU time as a function of the cutoff. This is for a linear chain of five Cu atoms at 1000.0 eV. It is clear from this figure that the cutoff does not have much effect on the defocussing for any value above about 2-3%, as the amplitudes of the important events are much larger than the

cutoffs considered. By contrast, the CPU time falls off rapidly for smaller cutoffs but levels off after about 5-10%. The reason for this is that there are a large number of unimportant events at lower cutoffs for this case. These events are responsible for only about 1.5% of the total defocussing (the spike seen as cutoff goes to zero) and hence can be neglected to save computer time. In this case we chose a 5% cutoff as it reduces the computational time by a factor of about eight but has a negligible effect on defocussing. We have found this cutoff to be both safe and time saving in more complicated calculations with many more unimportant events.

As noted above, this example exhibits an unexpected upturn in the % defocussing as the cutoff passes 1%. As this occurs, many more events are calculated, and the CPU time also rises dramatically. However the change in the % defocussing is very small (only ~1.5-2.0% of the total peak intensity in SS), and the 5% cutoff we have chosen thus nonetherless yields quite quantitative results. This kind of small change as the cutoff goes to zero is seen in other test calculations of this type, and we tentatively attribute it to the presence of a large number of small-amplitude events in a linear chain.

As noted previously, the maximum scattering order can be selected by looking at the final intensities and watching for their convergence. For example, $I^{(N)}(k,\theta,\phi)$ can be compared with $I^{(N-1)}(k,\theta,\phi)$ visually or with an R-factor to determine where a sufficient degree of convergence has been achieved. In, the most

general approach, a preliminary calculation has be done at the maximum order possible, with inspection of the table of intensities and numbers of events versus order then showing where the N_{max} can be set so as to exclude a neglegible number of events. However, there is a shortcut for estimation at higher energies via the (n-1) rule which says that the convergence is at the $(n-1)^{th}$ order for a chain of n atoms. With this in mind, one can examine the cluster to determine the number of atoms n in the longest chain and then perform the calculation at the (n-1) and n orders to see if convergence has been reached. For medium-Z scatterers such as Cu this rule is valid when inelastic attenuations are included in the calculation. But the (n-1) rule does not seem to hold for strong high-Z scatterers such as W. In such a case, the aforementioned shortcut should be used with caution.

As a final check on the overall accuracy and convergence of this code, we have calcuated the total fluxes from a linear chain of Cu atoms at 917.0 eV (see Figure 2.28). Flux conservation between the case of no scatterers present (a 1-atom cluster) and the case of n scatterers is necessary for physical consistency: that is, the total emitted intensity with n scatterers, which can be calculated as

$$I^{(N)}_{n,tot} = \int_0^{2\pi} \int_0^{\pi} I^{(N)}_n(k,\theta,\phi)\, \sin\theta\, d\theta\, d\phi,$$

must equal that in the absence of any scatterers:

$$I_{1,tot}^{(N)} = \int_0^{2\pi} \int_0^{\pi} I_1^{(N)}(k,\theta,\phi) \sin\theta \, d\theta \, d\phi,$$

provided that we do not include any inelastic attenuations. Figure 2.28 shows that including single-scattering events alone for this case conserves flux to within a ± 1.5%. But it is also evident that, in order to achieve a reasonable flux conservation of within ± 1% in a multiple-scattering calculation, all orders up to convergence should be included. Therefore one must be cautious in going up to only a predetermined order without checking for convergence, especially for cases involving long chains. This figure also shows that the (n-1) rule we have mentioned in the previous paragraph works reasonably well, although flux conservation does improve on going 1-2 orders higher. Since we have not included inelastic attenuation in this calculation, the (n-1) rule does not hold as rigorously for this case.

2.8.3. Auger Emission From Thin Epitaxial Overlayers of Cu(001) on Ni(001) substrate:

In this section we present theoretical simulations of an Auger experiment by Egelhoff [21] on a pseudomorphic monolayer of Cu deposited on Ni(001) and then buried by successive epitaxial overlayers of Ni. The polar-angle dependence of the Cu Auger intensity at 917.0 eV was recorded for overlayers of 2, 4 and 10 monolayers (ML) in thickness. The rapid falloff with increasing thickness of the relative intensities of forward-scattering features

such as that shown in Figure 2.29(a) at 45° has been interpreted as evidence of MS effects. This conclusion was supported by qualitative arguments based on classical trajectories [21].

In order to more quantitatively assess these data, we have performed SS and fully-converged MS calculations for 1 to 4 overlayers of Ni(001). The electron mean free path used in these calculations was 11.6 Å. We have also performed SS calculations using 5.0 Å as the mean free path, since several prior studies have suggested that this empirical reduction acts to simulate some MS effects [2a,2c], for example, for the case of photoelectron diffraction from bulk Ni(001) [36].

Experimental and theoretical curves are compared in Figure 2.29. The MS theory is shown in both zeroth order (1×1) and in converged second order (6×6). Comparing Figures 2.29(a) and 2.29(b), it is clear that a quantum-mechanical treatment of the SS problem does correctly predict the diminished importance of the features at large angles with respect to the surface normal, particularly for the theoretical curves with a reduced attenuation length of 5 Å. This trend is also found in SS calculations by Herman et al. for up to a 14 ML thickness [37]. Considering now the MS results, we find reasonable agreement between the (1×1) and (6×6) curves, especially well off the [101] direction; however, the differences along [101] are large enough to illustrate that (1×1) is not converged. The (6×6) curves are in agreement with experiment for the 2 ML case as to both peak positions and approximate relative intensities, although the experimental

features are larger in width in general than predicted by theory. Going to 4 ML, we note that MS theory predicts too much of a defocussing effect for the scattering along [101], and that SS theory with a reduced attenuation length is actually in better agreement with experiment! The MS curve also has a pronounced higher-order peak about 23° away from the surface normal (67° on the scale of this figure); this is present also in the SS curves, and its more complex origin in forward-scattering plus higher order interference effects has been discussed in a previous analysis of Auger diffraction from epitaxial overlayers by Bullock and Fadley [38].

These MS results can also be compared to previous MS calculations by Xu et al. [7] on the same system, in which the intensity of this inteference peak was lower, although all other features of our MS results are in excellent agreement with their curves. In particular, they also predict a more rapid decrease in the relative intensity of the peak at 45° than is observed. The lack of better success with the MS approach for thicknesses of 4 ML or greater case could be due to several effects: the presence of some strain and disorder in the actual overlayer studied, the small cluster size of only about 40 atoms used in our calculations, our neglect of angular averaging over the spectrometer acceptance cone and/or a systematic tendency of such calculations to overestimate the degree of defocussing due to some of the simplifying assumptions made in the model (as, e.g., the muffin-tin approximation). Therefore, the full degree to which MS

defocussing is responsible for the intensity loss at 45° is not clear, although it is certainly expected to contribute to some extent.

2.8.4. Scanned-Energy (Angle-Resolved Photoemission Fine Structure) Results for the c(2×2)S/Ni(001) System:

In this section, we compare two angle-resolved photoemission fine structure (ARPEFS) experimental curves for the c(2×2)S overlayer on Ni(001) due to Barton et al. to a multiple-scattering cluster spherical-wave (MSC-SW) analysis of this data by the same authors [15], and to our reanalysis of this work using the present method. In both experiments, the photon incidence direction, the polarization $\hat{\epsilon}$, the [001] surface normal, and the electron emission direction lie in the same plane, normal to the surface. Our calculations made use of clusters of 40 atoms and non-structural inputs as described elsewhere in a SSC-SW analysis of the same data by Sagurton et al. [4(b)].

In the first case, the incoming photon beam makes an angle of $\theta_{h\nu} = 70^{\circ}$ with respect to the surface normal and the detector is placed in the direction of the surface normal ($\theta_{e-} = 0^{\circ}$). (Hence, this has been termed normal photoelectron diffraction or NPD.) The photon energy was scanned from 50 to 420 eV. Figure 2.30(a) shows the experimental curve superimposed on the MSC-SW simulation by Barton et al. [7(b)] for an optimized structure with sulfur 1.30 Å above the first Ni layer and a first-to-second Ni-Ni interlayer distance of 1.84 Å that is expanded by 4.5% with respect to the bulk value of 1.76 Å. Figure

2.30(b) shows a similar comparison of our SS and MS results to experiment. In SS, several peak positions and intensities are not predicted correctly (e.g., l, m and o, as well as the valley between k and l). By contrast, our MSC-SW simulations are in excellent agreement with the experiment, and appear to provide an overall better description of the data than the earlier calculations shown in (a). In perticular, we are better able to predict the intensities of peaks o and p, and the positions of peaks r and s are also in better agreement with experiment.

The second case is very similar to the first, except that the incoming photons are oriented at $\theta_{h\nu} = 45^{\circ}$ away from the surface normal and the detector is at $\theta_{e^-} = 45^{\circ}$ away from the surface normal. (This has been termed off-normal photoelectron diffraction or OPD.) Figure 2.31(a) again shows the experimental curve and the MSC-SW simulation by Barton et al. [15] for the optimized structure. Figure 2.31(b) shows our SS and MS results compared to the same experimental data. In SS, the position and intensity of the valley between peaks a and b are not well reproduced. For peak c, the calculated intensity is too small. Also peak i in the SS simulation is displaced by several eV. In our MS results however, the only major disagreement compared to the simulation by Barton et al. [15] is the intensity of peak f, which is overestimated. But our simulation of peaks e and j is in better agreement with experiment than that of Barton et al. [15]

The χ-scale ordinates on both Figures 2.30 and 2.31 are set by the experimental data and our calculations have not been rescaled to

fit experiment. This is an important point, as prior SSC-SW results due to Sagurton et al. [4(b)] have an adjusted χ-scale which is more expanded than the experimental scale. This difference is due to the different sets of correlated vibrational parameters used in the two calculations, which evidently oversuppressed the diffraction oscillations in the earlier work. Our parameters correspond to the alternative "correlated model 1" discussed by Sagurton at al. [4(b)].

As a final comment concerning our calculations, we note that convergence is achieved at 4^{th} order as judged from final intensities, although events through 5^{th} order were included in the calculation.

Overall, the MSC-SW results obtained using these two different methods agree very well with themselves and with experiment. This indicates that the Rehr-Albers approach [17] is reliable over low to medium energies of photoelectron diffraction and that it can provide at least as good a description of such experimental data as the method of Barton and Shirley, if not somewhat better.

2.8.5. Scanned-Angle X-ray Photoelectron Diffraction Results for the c(2×2)S/Ni(001) System:

As a final comprarison of our calculations to prior experimental data and MS theory, we consider an experimental study by Sinkovic et al., who used the intermediate kinetic energy range from 230 to 900 eV to study adsorbate core-level azimuthal photoelectron diffraction [39]. The adsorbate/substrate system employed in this study was again

the well-defined c(2×2)S overlayer on Ni(001). Again the photon incident direction, the polarization, the [001] surface normal, and the electron emission direction were in a single plane normal to the surface. They utilized two polarization orientations: s-polarization lying in the (001) surface and a specially selected p-polarization only 18° off the surface normal that maximally emphasized substrate Ni scattering relative to the primary wave. A grazing electron takeoff angle of $\theta = 10^{\circ}$ with respect to the surface was used in both cases, with the azimuthal angle ϕ being scanned. The experimental geometry for p polarization is shown in the inset of Figure 2.32.

The s-polarization results with $\hat{\epsilon}$ only 10°away from the electron emission direction and thus yielding a very strong primary wave were reasonablly well reproduced by a quite simple single-scattering cluster plane-wave (SSC-PW) model [39]. The corresponding p-polarization results were markedly different however. In order to be semiquantitatively described by the theory, the p-polarization data required a reduction in the PW scattering amplitudes and the inclusion of double-scattering events [39]. These p-polarization data were later analyzed by Sagurton et al. [40] using a single-scattering cluster spherical-wave approach, but there was no significant improvement in the agreement. From this prior work, it was concluded that the p-polarization geometry with its weaker primary wave showed evidence of MS effects [40].

Tang [41] subsequently performed a multiple-scattering spherical-wave analysis on this system and agreed in concluding that

MS is required for the accurate description of the p-polarization data. Tang's computational method is based on an inverse-LEED type final state, as described eleswhere by Tong et al. [5,42]; this method takes the translational symmetry of the system into account and thus requires the assumption of long range order. Hence it is fundamentally different from the cluster-based methods used by Barton et al. [15] and in this work. We have now performed multiple-scattering cluster spherical-wave (MSC-SW) calculations on the same system and Figure 2.32 compares this p-polarization experimental data to various theoretical curves. We considered a cluster of 36 atoms. We see that, SSC-SW theory fails to predict the peak observed in the [110] direction, and yields very poor positions for the other two peaks in experiment at $\phi \sim 22^{\circ}$ and 67°. By contrast the two MS curves agree much better with experiment, and also very well with one another. Tang's MS curve has a peak in the [110] direction, but it is too strong in relative intensity. The other peaks and shoulders at $\phi \sim 12^{\circ}$ and 82° in his curve are in good agreement with experiment. Our MS curve has a wider double peak along [110]. This may be due to our small cluster size of 36 atoms and/or our neglect of the finite aperture of the detector. But the relative intensity of our central peak is in better agreement with the experiment than that predicted by Tang [41]. The rest of the structure in our MS curve away from [110] is in excellent agreement with experiment. The strong disagreement of our SS results with experiment is consistent with the prior conclusions by both Sinkovic

et al. [39] and Tang [41] concerning the need for MS for this particular geometry. Finally, we note that convergence for this case was reached at 4^{th} order, as judged intensities.

2.9. CONCLUSIONS:

We have implemented and tested a new method for carrying out multiple-scattering (MS) photoelectron and Auger electron diffraction calculations due to Rehr and Albers, and have developed a general purpose computer program for applying it to a wide range of problems. Results obtained using this new separable Green's function matrix approach are in very good agreement with those obtained with other MS methods and with experiment. In agreement with previous work we find that Auger and photoelectron peak intensities along chains diminish rapidly due to MS defocussing effects as the number of atoms in the chain is increased. These MS effects are prominent only in a cone within about 20° of the chain axis. This implies the necessity of linear or nearly linear chains to observe MS effects at higher energies of $\geq$ 500 eV. This defocussing due to MS is found to depend on the material as well as the crystallographic directions in a given material.

REFERENCES:

[1]. (a) P.A. Lee, Phys. Rev. B 13 (1976) 5261; (b) D.P. Woodruff, Surf. Sci. 166 (1986) 377.

[2]. (a) C.S. Fadley, Prog. in Surf. Sci. 16 (1984) 275; (b) C.S. Fadley, Physica Scripta T 17 (1987) 39; (b) C.S. Fadley in "Synchrotron Radiation Research: Advances in Surface Science", R.Z. Bachrach Ed., (Plenum, NY, 1990), in press.

[3]. P.A. Lee and J.B. Pendry, Phys. Rev. B 11 (1975) 2795.

[4]. (a) M. Sagurton, E.L. Bullock, R. Saiki, A. Kaduwela, C.R. Brundle, C.S. Fadley, and J.J. Rehr, Phys. Rev. B 33 (1986) 2207; (b) M. Sagurton, E.L. Bullock, and C.S. Fadley, Surf. Sci. 182 (1987) 287.

[5]. S.Y. Tong, H.C. Poon, and D.R. Snider, Phys. Rev. B 32 (1985) 2096.

[6]. J.J. Barton, S.W. Robey, and D.A. Shirley, Phys. Rev. B 34 (1986) 778.

[7]. M.-L. Xu and M. Van Hove, Surf. Sci. 207 (1989) 215.

[8]. A.P. Kaduwela, G.S. Herman, J. Osterwalder, C.S. Fadley, J.J. Rehr, and J. Muestre de Leon, Physica B 158 (1989) 564.

[9]. A.P. Kaduwela, G.S. Herman, D.J. Friedman, C.S. Fadley, and J.J. Rehr, Physica Scripta, 41 (1990) 298.

[10]. H.C. Poon and S.Y. Tong, Phys. Rev. B 30 (1984) 6211.

[11]. S. Kono, S.M. Goldberg, N.F.T. Hall, and C.S. Fadley, Phys. Rev. Lett. 41 (1978) 1831; S. Kono, S.M. Goldberg, N.F.T. Hall, and C.S. Fadley, Phys. Rev. B 22 (1980) 6085.

[12]. A. Liebsch, Phys. Rev. Lett. 32 (1974) 1203; A. Liebsch, Phys. Rev. B 13 (1976) 544.

[13]. T. Fujikawa, J. Phys. Soc. Jpn. 50 (1981) 1321; 51 (1982) 251; 54 (1985) 2747; J. Elect. Spect. 26 (1982) 79.

[14]. L.G. Petersson, S. Kono, N.F.T. Hall, C.S. Fadley, and J.B. Pendry, Phys. Rev. Lett. 42 (1979) 1545.

[15]. J.J. Barton and D.A. Shirley, Phys. Rev. A 32 (1985) 1019; J.J. Barton and D.A. Shirley, Phys. Rev. B 32 (1985) 1892; J.J. Barton and D.A. Shirley, Phys. Rev. B 32 (1985) 1906; J.J. Barton, Ph.D. Thesis, University of California at Berkeley (1985).

[16]. J.J. Rehr, R. Albers, C. Natoli, and E.A. Stern, Phys. Rev. B 34 (1986) 4350; J.J. Rehr, J. Mustre de Leon, C.R. Natoli, and C.S. Fadley, J. de Physique C 8, suppl. 12, (1986) 213; J.J. Rehr, J. Mustre de Leon, C.R. Natoli, C.S. Fadley, and J. Osterwalder, Phys. Rev. B 39 (1989) 23.

[17]. J.J. Rehr and E.A. Albers, Phys. Rev. B 41 (1990) 8139.

[18]. (a) D.J. Friedman and C.S. Fadley, J. Electron Spectrosc. Relat. Phenom. 51 (1990) 689; (b) D.J. Friedman and C.S. Fadley, unpublished notes.

[19]. R.S. Saiki, A.P. Kaduwela, M. Sagurton, J. Osterwalder, C.S. Fadley, and C.R. Brundle, unpublished results.

[20]. E.L. Bullock, Ph.D. Thesis, Department of Chemistry, University of Hawaii, 1988.

[21]. W.F. Egelhoff, Phys. Rev. Lett. 59 (1987) 559.

[22]. S.M. Goldberg, C.S. Fadley, and S. Kono, J. Electron Spectrosc. Relat. Phenom., 21 (1981) 285.

[23]. W.L. Schaich, Phys. Rev. B 29 (1984) 6513.

[24]. J. Mustre, J.J. Rehr, C.R. Natoli, C.S. Fadley, and J. Osterwalder, Phys. Rev. B 39 (1989) 5632.

[25]. A.R. Edmonds, Angular Momentum in Quantum Mechanics (Princeton University Press, New Jersey, 1957)

[26]. G. Beni and P.M. Platzmann, Phys. Rev. B 14 (1976), 1514

[27]. Handbook of Mathematical Functions, Eds. M. Abramowitz and I.A. Stegun (Dover, New York, 1972).

[28]. M. Jacob and G.C. Wick, Ann. Physics, 7 (1959) 425.

[29]. A. Messiah, Quantum Mechanics (North Holland, Amsterdam, 1969).

[30]. R.N. Zare, Angular Momentum: Understanding of Spatial Aspects in Chemistry and Physics (Wiley, USA, 1988).

[31]. M. Weissbluth, Atoms and Molecules (Academic, 1978).

[32]. P.J. Rous, J.B. Pendry, D.K. Saldin, K. Heinz, K. Muller, and N. Bickel, Phys. Rev. Lett. 57 (1986) 2951; P.J. Rous, M.A. Van Hove, and G.A. Somorjai, Surf. Sci. 226 (1990) 15.

[33]. J. Osterwalder, T. Graber, S. Hufner, and L. Schlapbach, Phys. Rev. B 41 (1990) 12475.

[34]. H.A. Aebischer, T. Greber, J. Osterwalder, A.P. Kaduwela, D.J. Friedman, G.S. Herman, and C.S. Fadley, to appear in Surf. Sci. Lett.

[35]. T.T. Tran, D.J. Friedman, Y.J. Kim, and C.S. Fadley, to be published.

[36]. J. Osterwalder, A. Stuck, D.J. Friedman, A. Kaduwela, C.S. Fadley, J. Mustre de Leon, and J. J. Rehr, Physica Scripta 41 (1990) 990.

[37]. G.S. Herman and C.S. Fadley, unpublished results.

[38]. E.L. Bullock and C.S. Fadley, Phys. Rev. B 31 (1985) 1212.

[39]. B. Sinkovic, P.J. Orders, C.S. Fadley, R. Trehan, Z. Hussain, and J. Lecante, Phys. Rev. B 30 (1984) 1833.

[40]. M. Sagurton and C.S. Fadley, unpublished results.

[41]. J.-C. Tang, J. Vac. Sci. Technol. 5 (1987) 658.

[42]. S.Y. Tong and C.H. Li, Critical Review in Solid State and Materials Science (Chemical Rubber, Cleveland, 1981), p. 209

Table 2.1.

The fraction F of three-atom scattering verticies to be recalculated with a change in adsorbate/substrate spacing as a function of both f (the fraction of adsorbate atoms) and M (the total number of atoms in the cluster).

	F		
f	M = 10	M = 100	$M \to \infty$
0.1	0.29	0.27	0.27
0.2	0.51	0.48	0.48
0.3	0.67	0.63	0.63
0.4	0.77	0.73	0.72
0.5	0.80	0.76	0.75

Table 2.2.

Timing information on the Cray Y-MP/864 for chains of Ge atoms.
(cf. Figure 2.22)

# of atoms	Wallclock(sec)	CPU(sec)
1	4.7	0.4
2	7.2	1.1
3	15.6	7.7
4	52.6	23.8
5	119.4	52.7

Table 2.3.

Timing information on the Sun-4 SPARCstation for chains of Ge atoms.

# of atoms	Wallclock(sec)	CPU(sec)
1	37.8	2.3
2	85.6	22.1
3	547.5	189.4
4	1129.4	608.6
5	2090.2	1315.6

Table 2.4.

Timing ratio for Ge chains: Sun-4 SPARCstation/Cray Y-MP/864

# of atoms	Wallclock(sec)	CPU(sec)
1	8.0	5.8
2	11.9	20.1
3	35.1	24.6
4	21.5	25.6
5	17.5	25.0

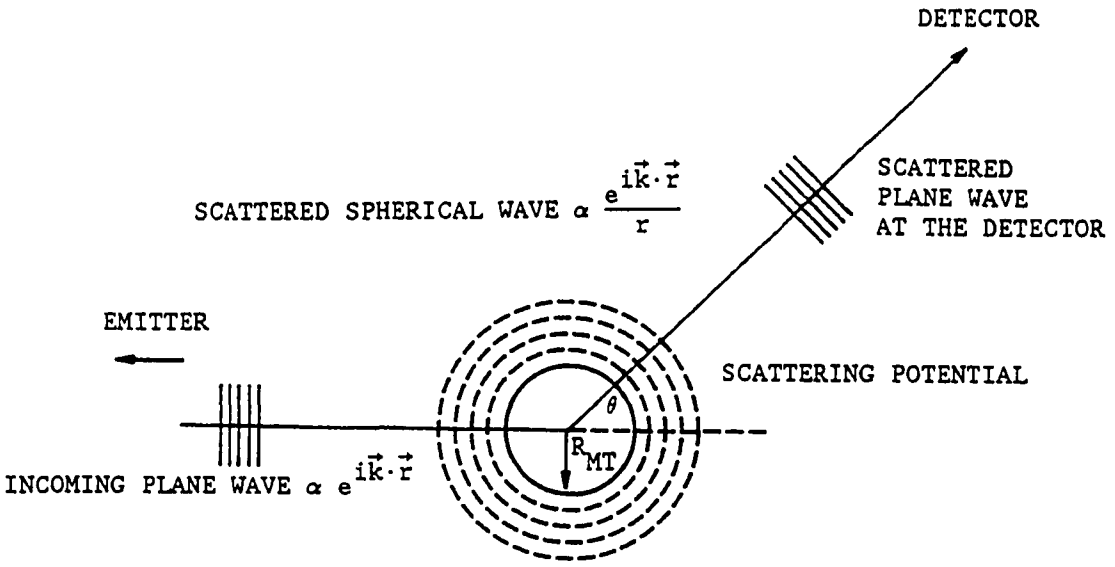

$$I(\theta,\vec{k}) \alpha \left| e^{i\vec{k}\cdot\vec{r}} + f(\theta) \frac{e^{i\vec{k}\cdot\vec{r}}}{r} \right|^2$$

Figure 2.1. Scattering of a plane-wave by a shperically symmetric atomic potential.

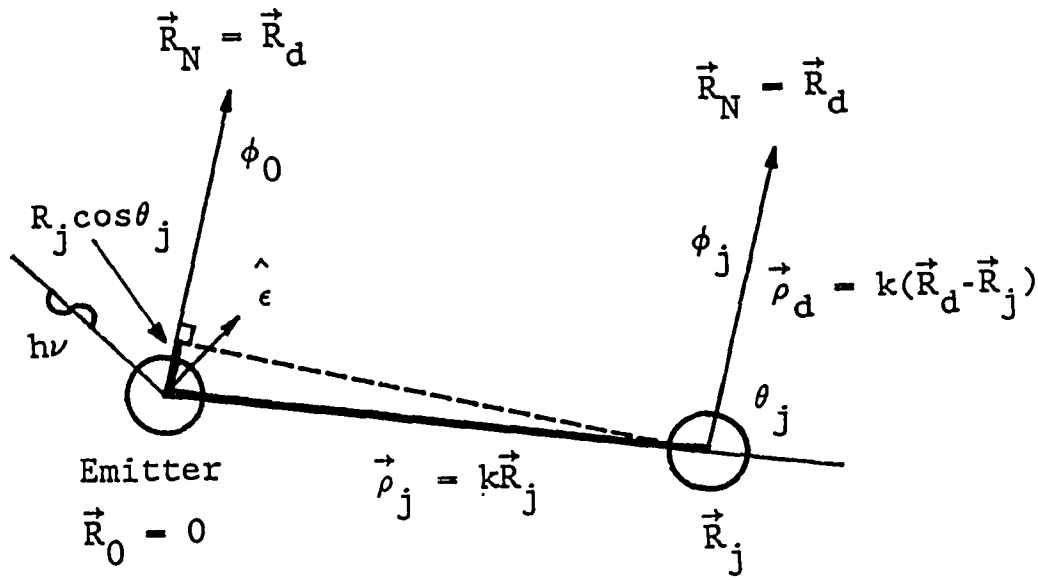

Figure 2.2. Illustration of the phase shift between the primary wave (ϕ_0) and a scattered wave (ϕ_j) due to path length difference. The polarization $\hat{\epsilon}$ is here assumed to lie in the plane of the scattering. The other component $\hat{\epsilon}'$ is perpendicular to this.

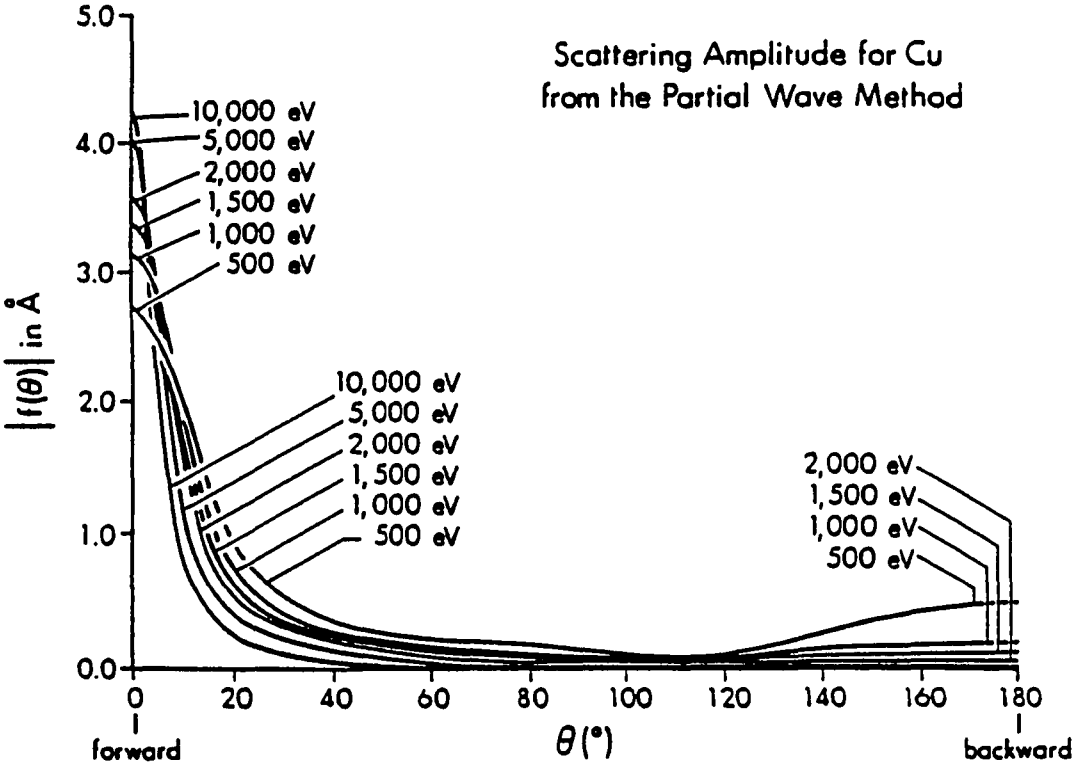

Figure 2.3.(a) The magnitude of the atomic scattering factor $|f(\theta)|$ for Cu as a function of scattering angle θ for various electron kinetic energies from 500 to 10,000 eV. Note the enhanced forward peaking as energy increases and the concomitant decrease in the importance of any back-scattering.

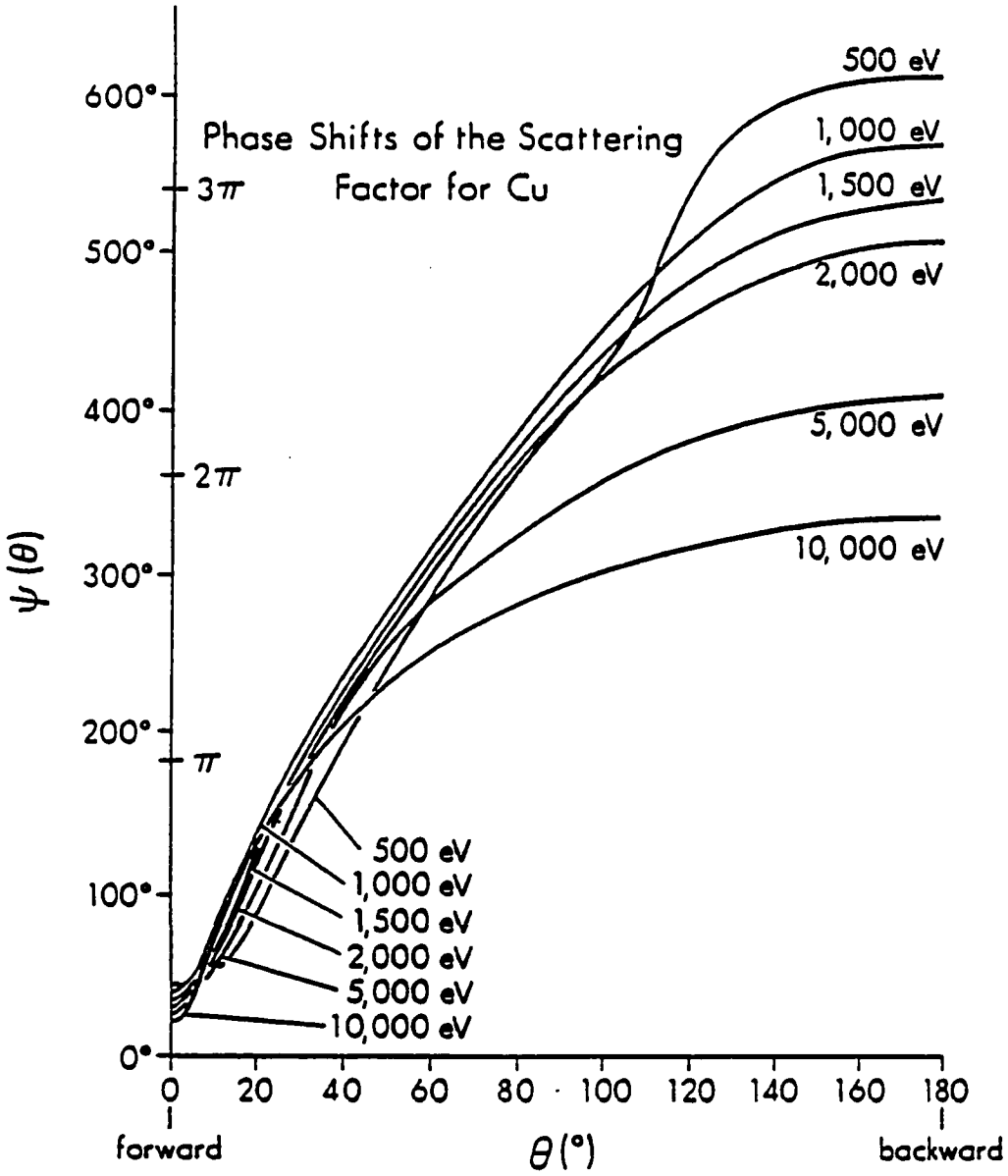

Figure 2.3.(b) The scattering phase-shift $\Psi(\theta)$ for Cu as a function of scattering angle θ for various electron kinetic energies from 500 to 10,000 eV.

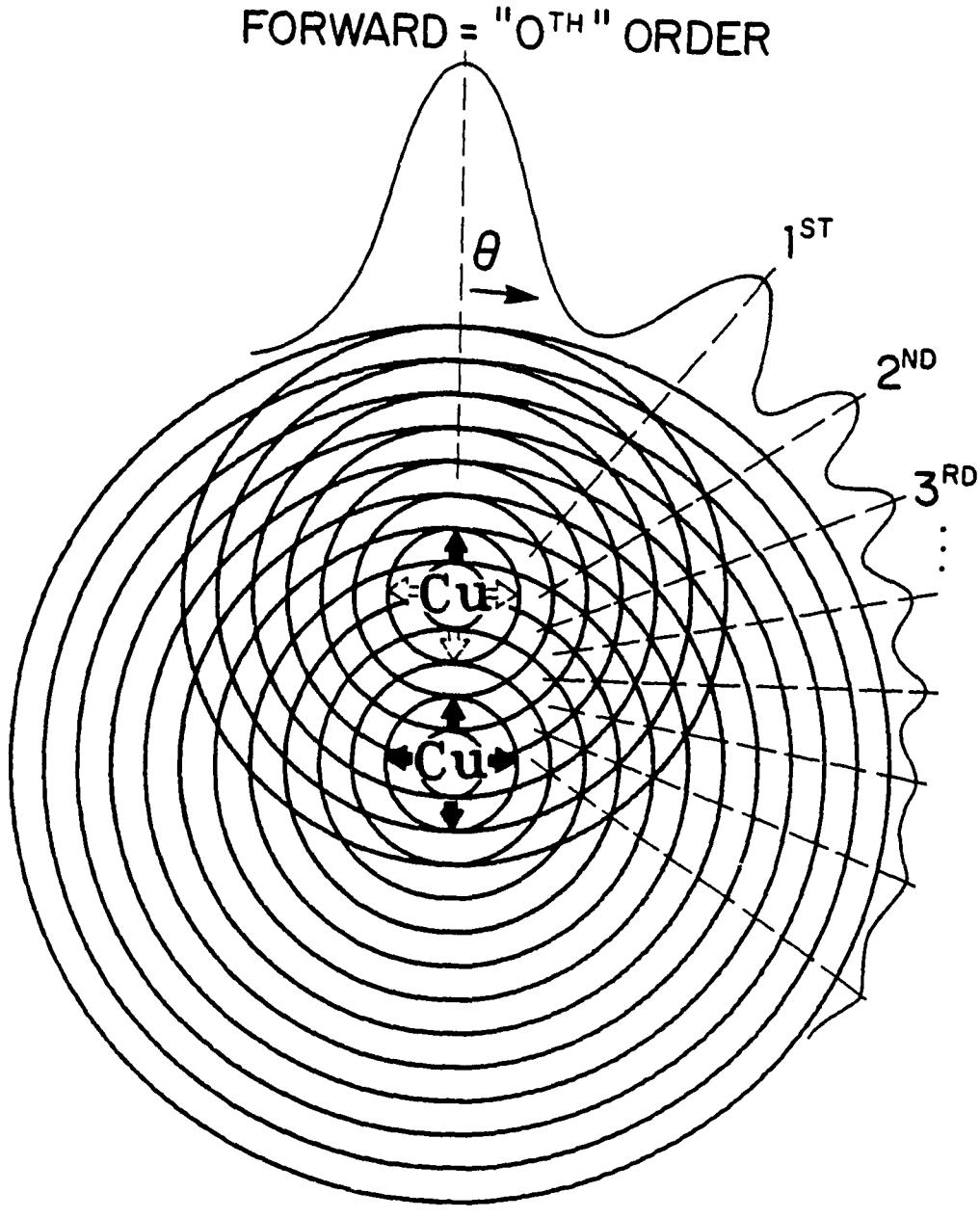

Figure 2.3.(c) The inteference patterns produced by an idealized single Cu scatterer, assuming the scattering phase shifts to be zero. Note the higher order scattering features away from the forward scattering "0^{th} order" peak.

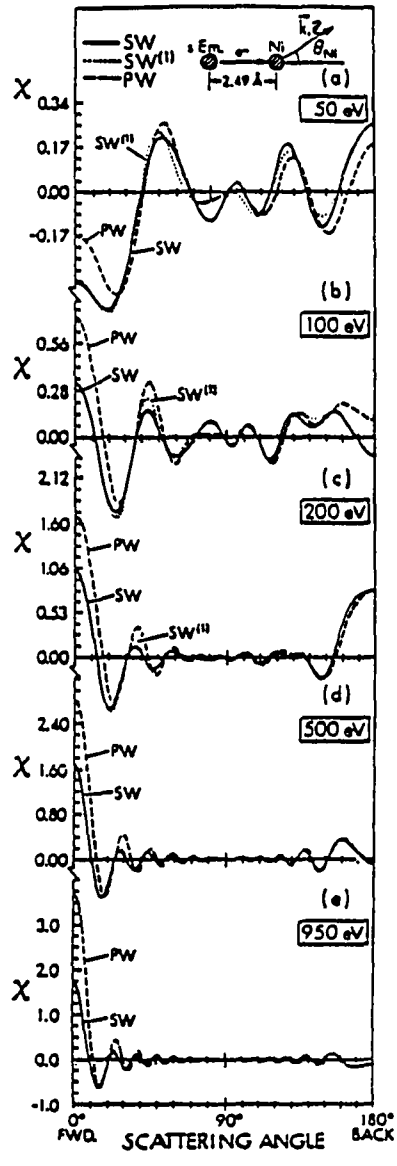

Figure 2.4. Theoretical χ curves for emission from an s-level in Ni as a function of the scattering angle θ_{Ni} for a Ni single scatterer at a distance of 2.49 Å from the emitter (Em). The radiation polarization is kept parallel to the emission direction. Results from three different approximations to the scattering (PW, SW, and $SW^{(1)}$ a lower-order spherical wave approximation) are shown for energies of 50-950 eV.

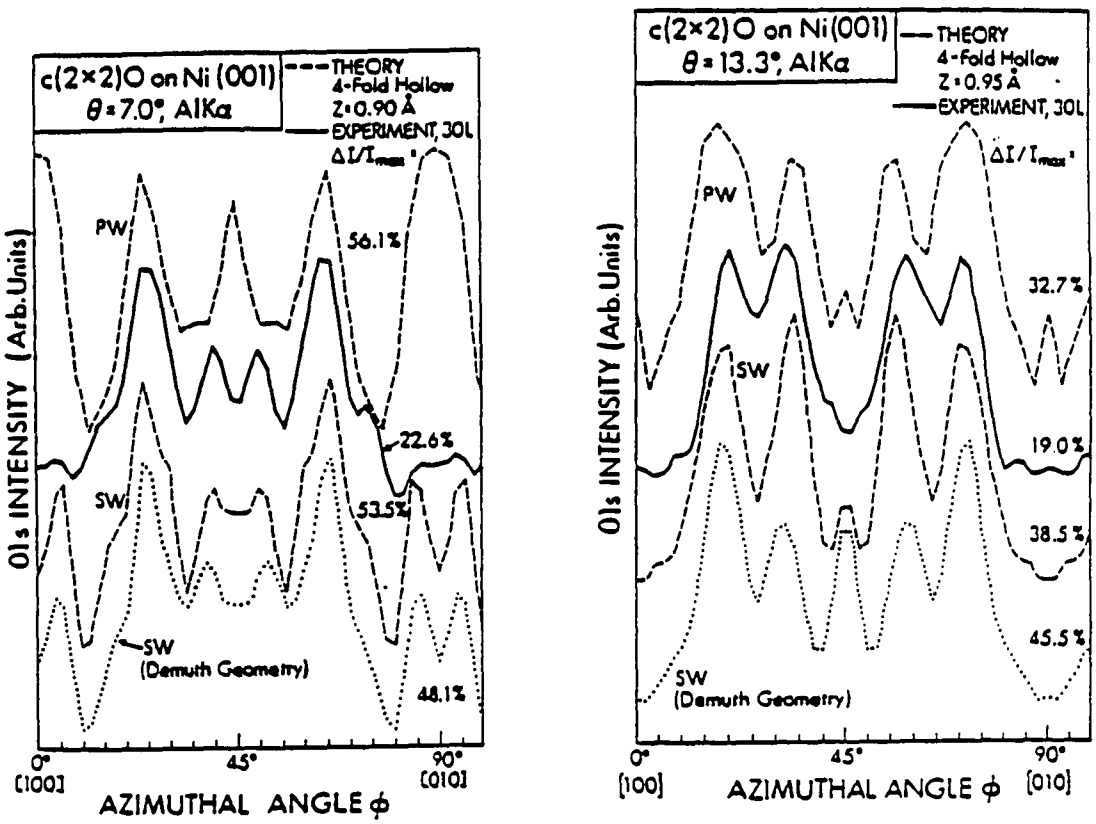

Figure 2.5. Experimental and single-scattering theoretical azimuthal scans of O 1s intensity from c(2×2)O/Ni(001) at angles θ of emission with respect to the surface of (a) 7.0° and (b) 13.3°. The experimenal data are for an exposure of 30 langmuirs (30 L) (1 L = 10^{-6} Torr-Sec). PW and SW theoretical calculations are shown.

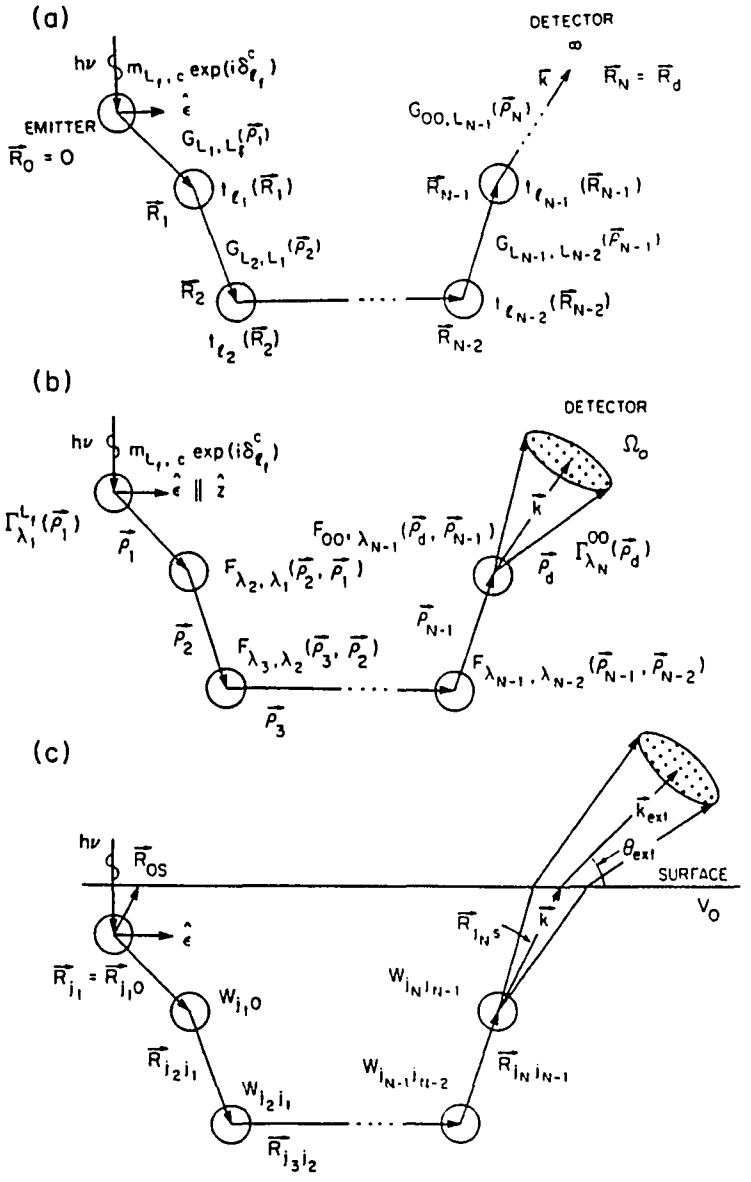

Figure 2.6. The geometry of the scattering process: (a) the initial general expression in terms of the free particle propagator $G_{L,L'}$ and the t-matrix elements t_{ℓ}; (b) the separation into scattering matrices $F_{\lambda,\lambda'}$ and termination factors $\Gamma^{L_f}_{\lambda_1}$ and $\Gamma^{00}_{\lambda_N}$ that is obtained in the Rehr-Albers method [17]; (c) the inclusion of Debye-Waller and inelastic damping, with $\vec{R}_N$ now defined as the last scatterer instead of the detector as in (a) and (b).

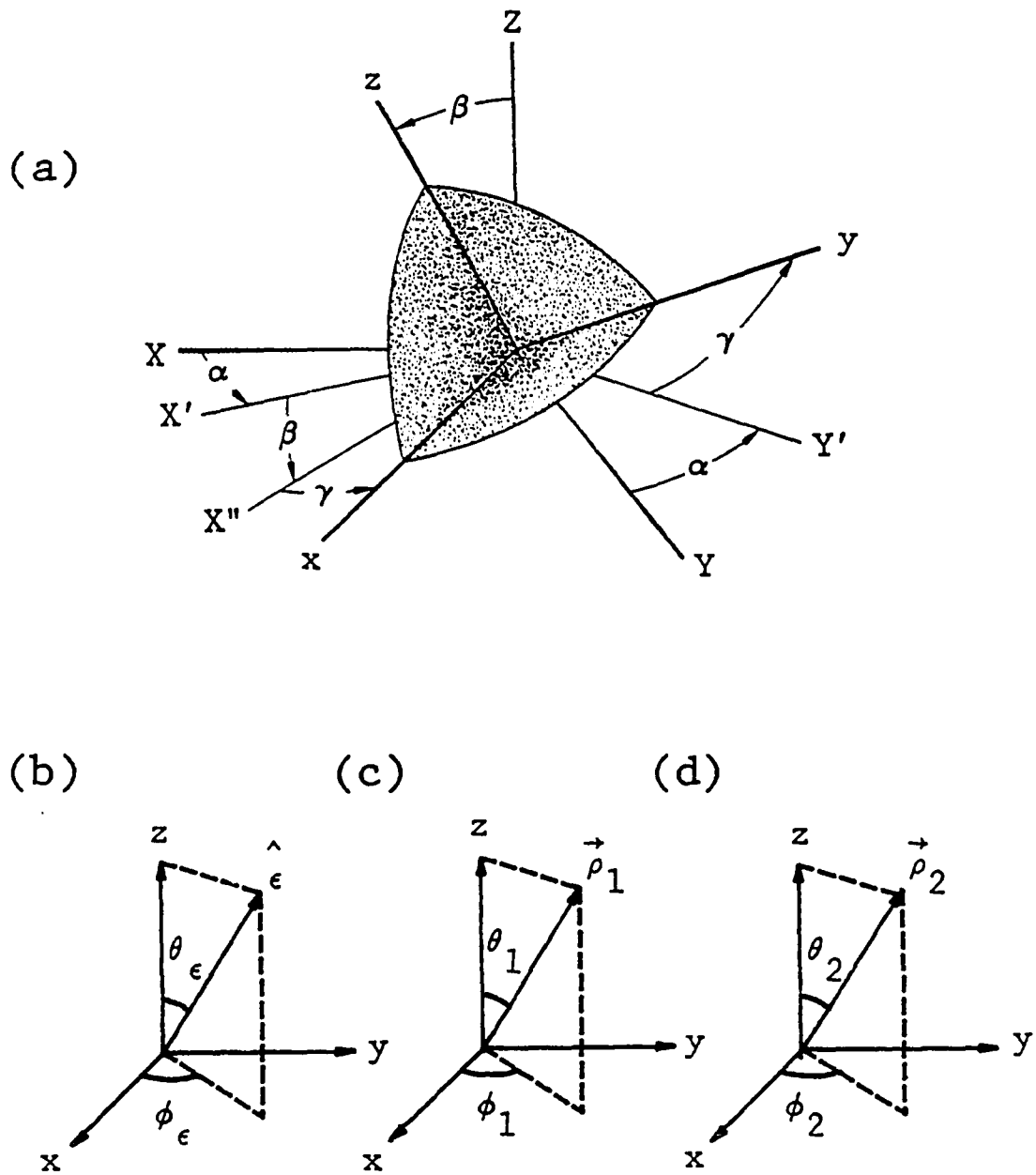

Figure 2.7. (a) Definition of the Euler rotations. (b) Polar and azimuthal angles of the vector $\hat{\epsilon}$. (c) Same as (b) but for the vector $\vec{\rho}_1$ at some atom 1. (d) Same as (b) but for the vector $\vec{\rho}_2$.

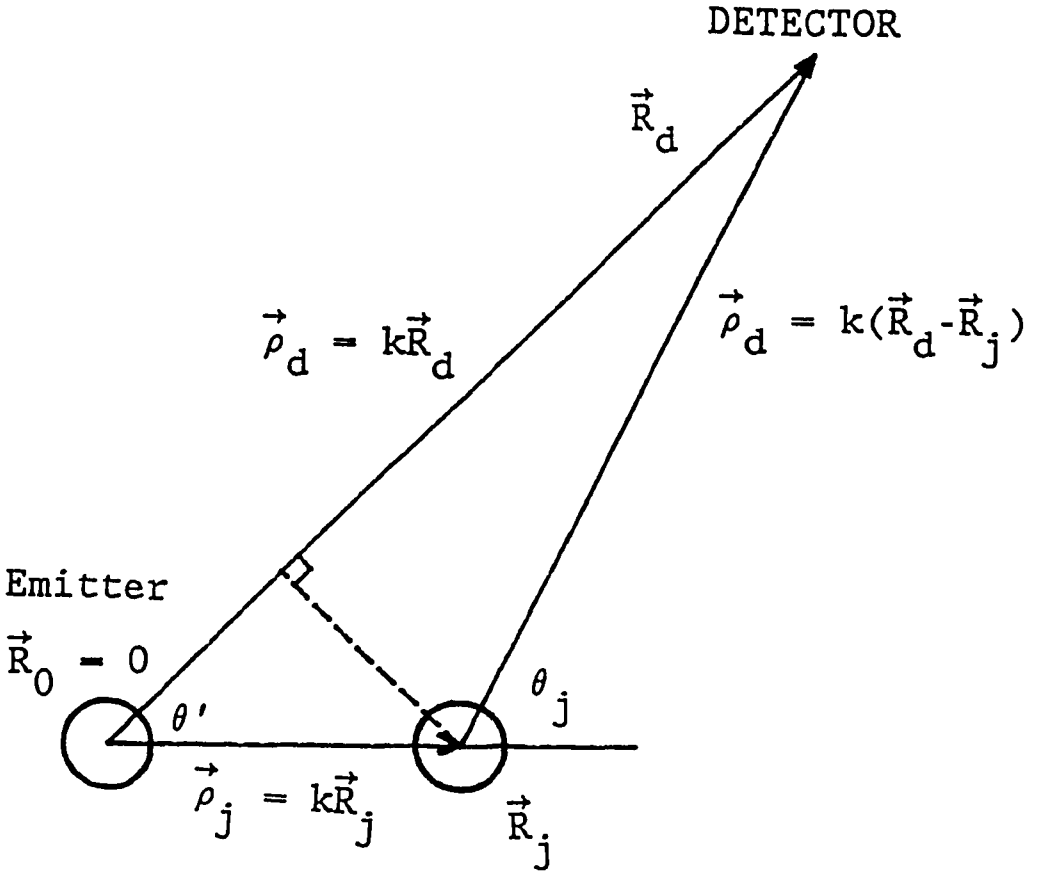

Figure 2.8. The scattering geometry for a single scatterer as used in calculating the path length difference as $|\vec{R}_d| \to \infty$.

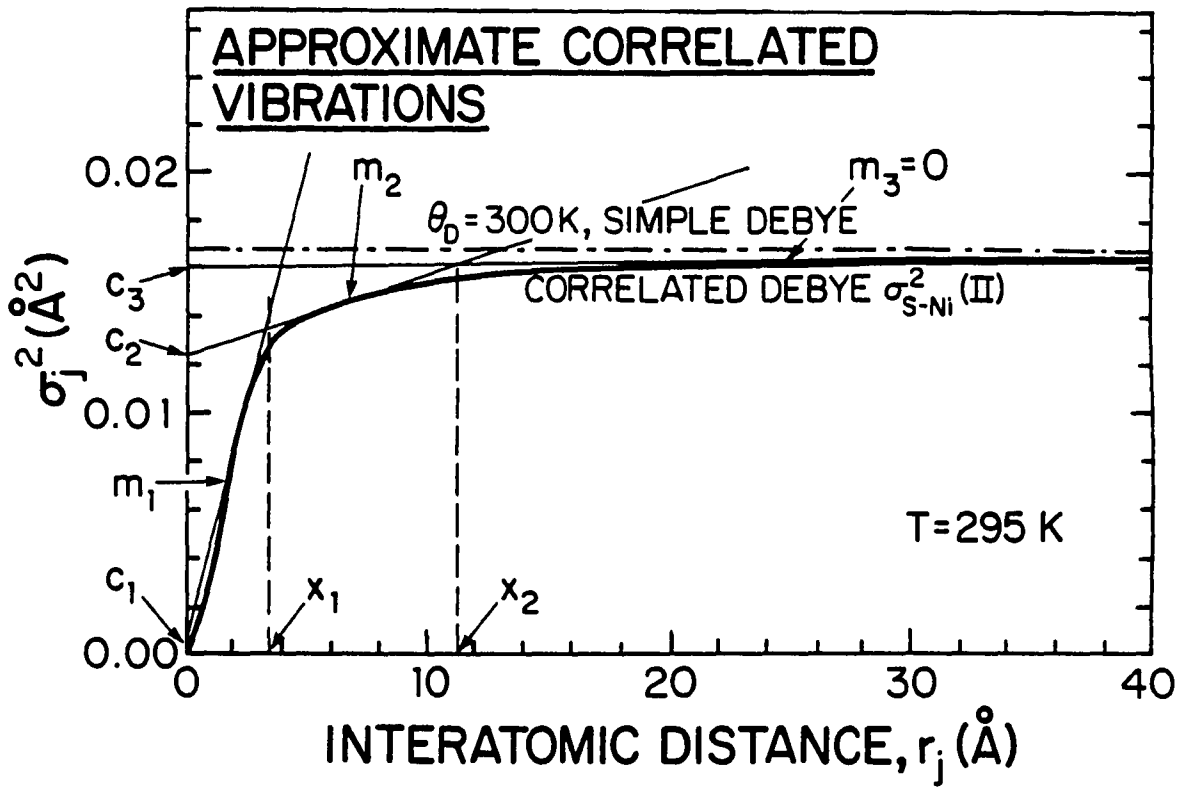

Figure 2.9. Correlated vibrations as calculated from Equation (2-4-82) (smooth curve) and in an approximation was as parametrised by three straight lines.

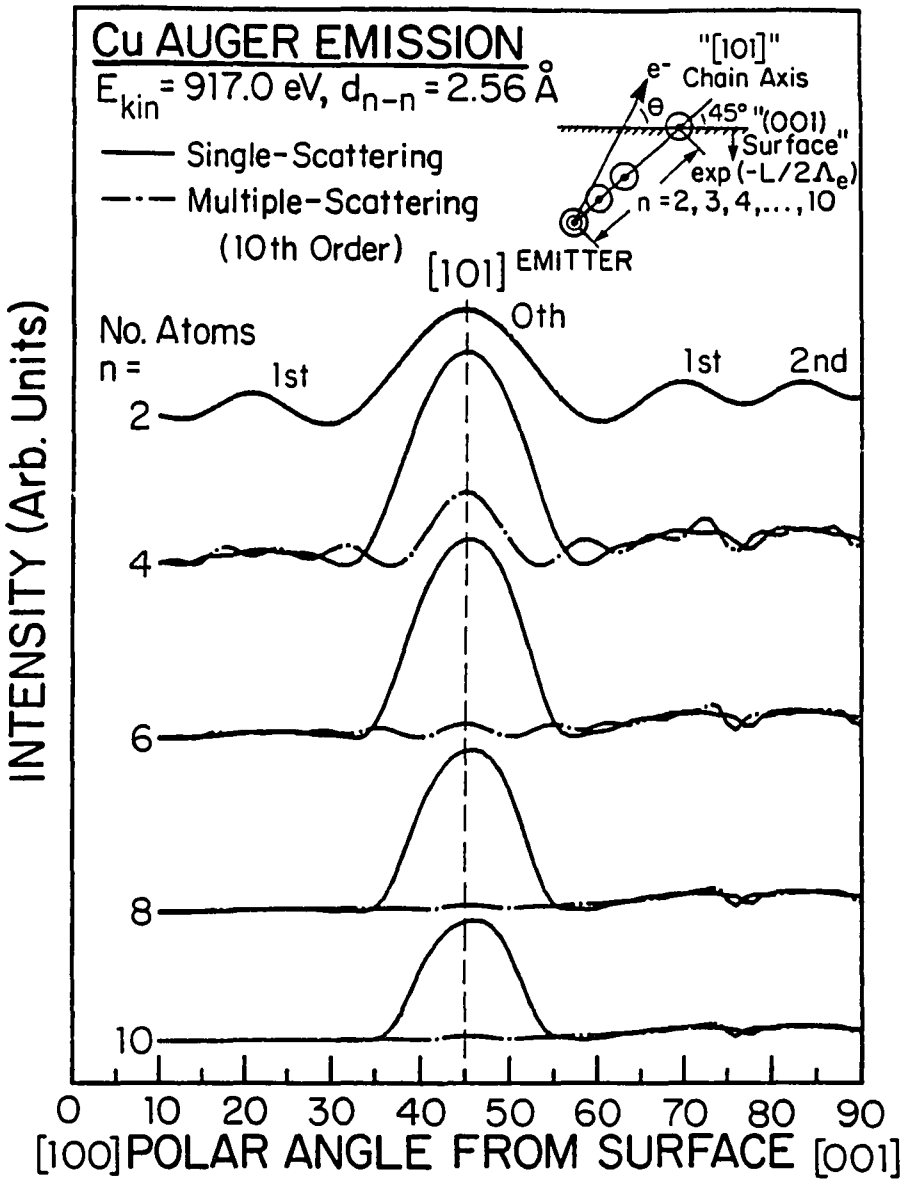

Figure 2.10. Single and Multiple scattering calculations of Auger electron diffraction from linear Cu [101] chains at 917.0 eV.

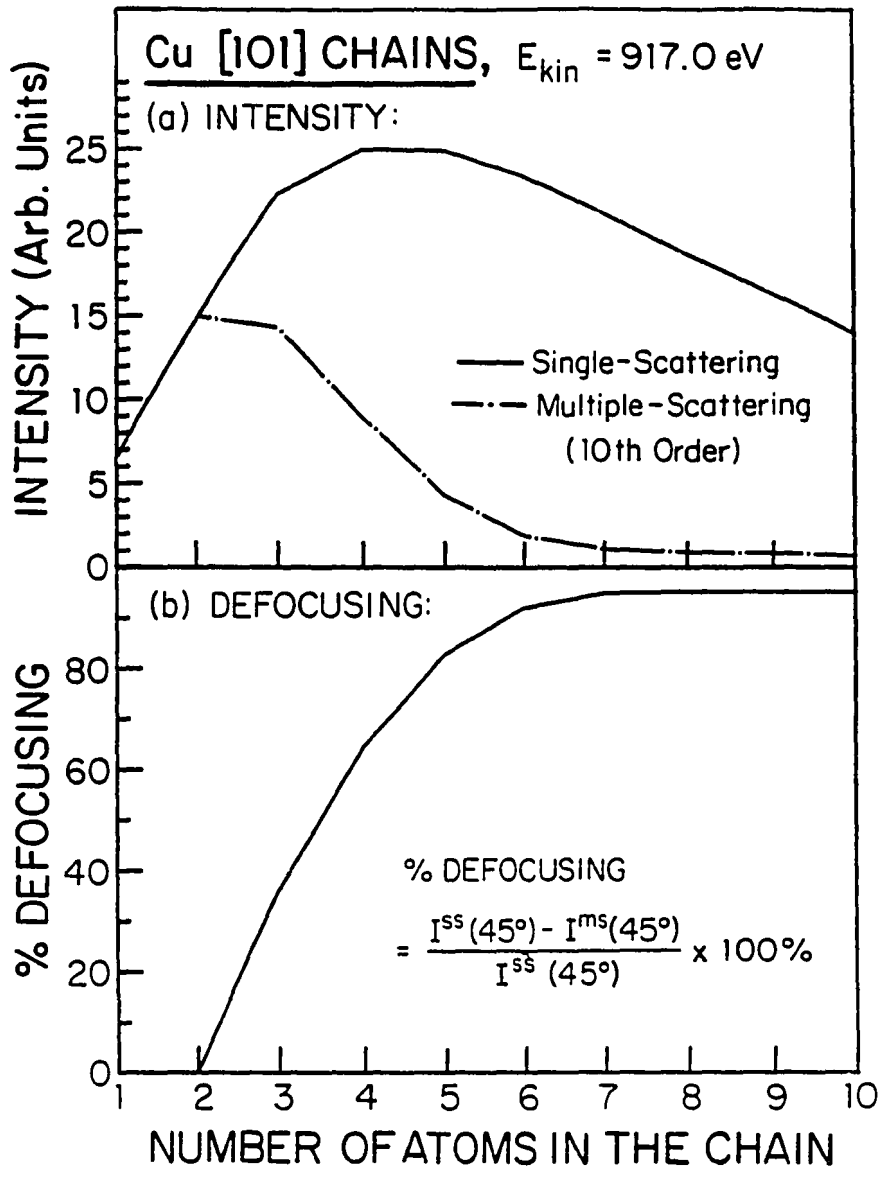

Figure 2.11. (a) Single and multiple scattering Auger electron diffraction intensities directly alomng linear Cu [101] chains at 917 eV as a function of the number of atoms in the chain. (b) The % defocussing (defined in the inset) in Auger electron diffraction intensity along linear chains of Cu [101] at 917 eV.

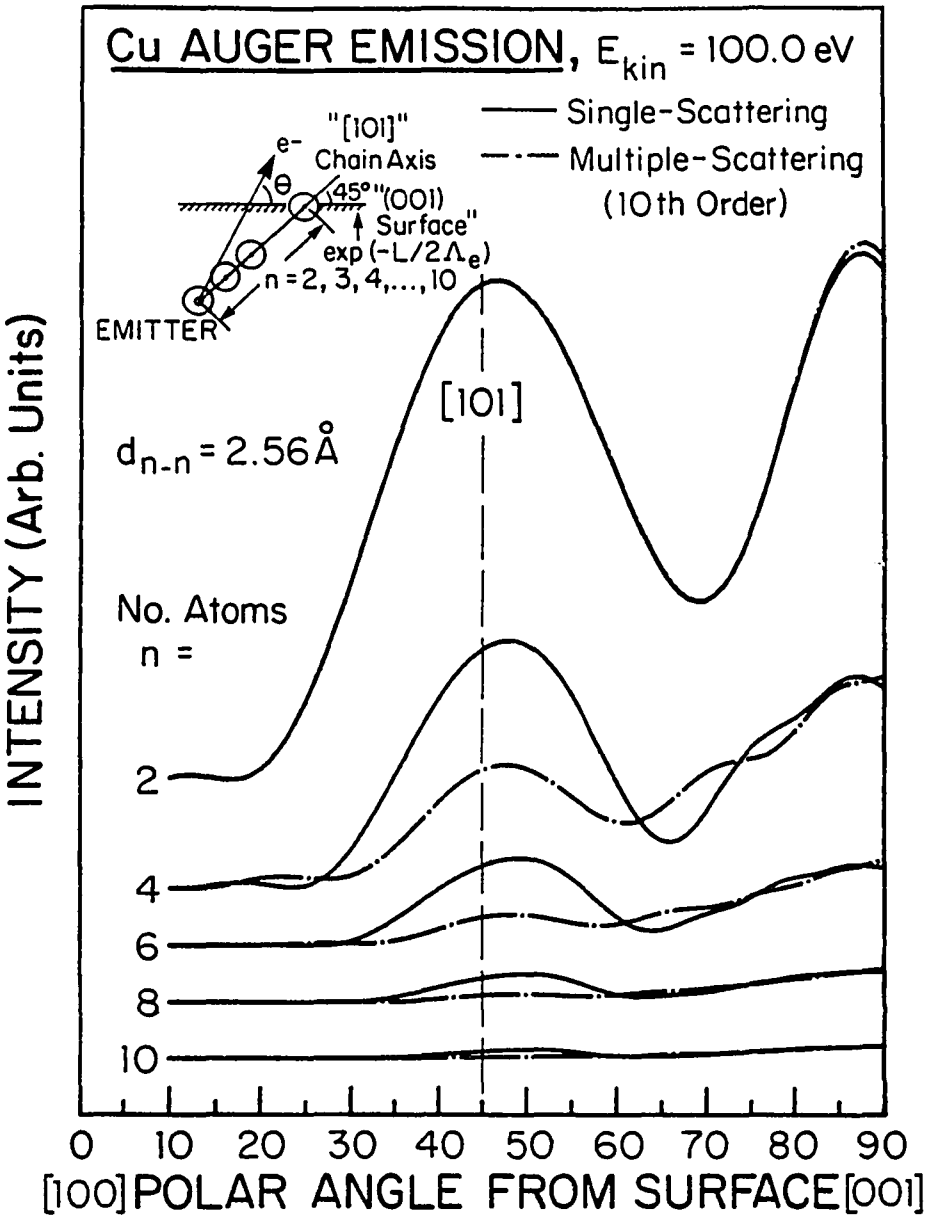

Figure 2.12. Same as Figure 2.10, but for 100 eV.

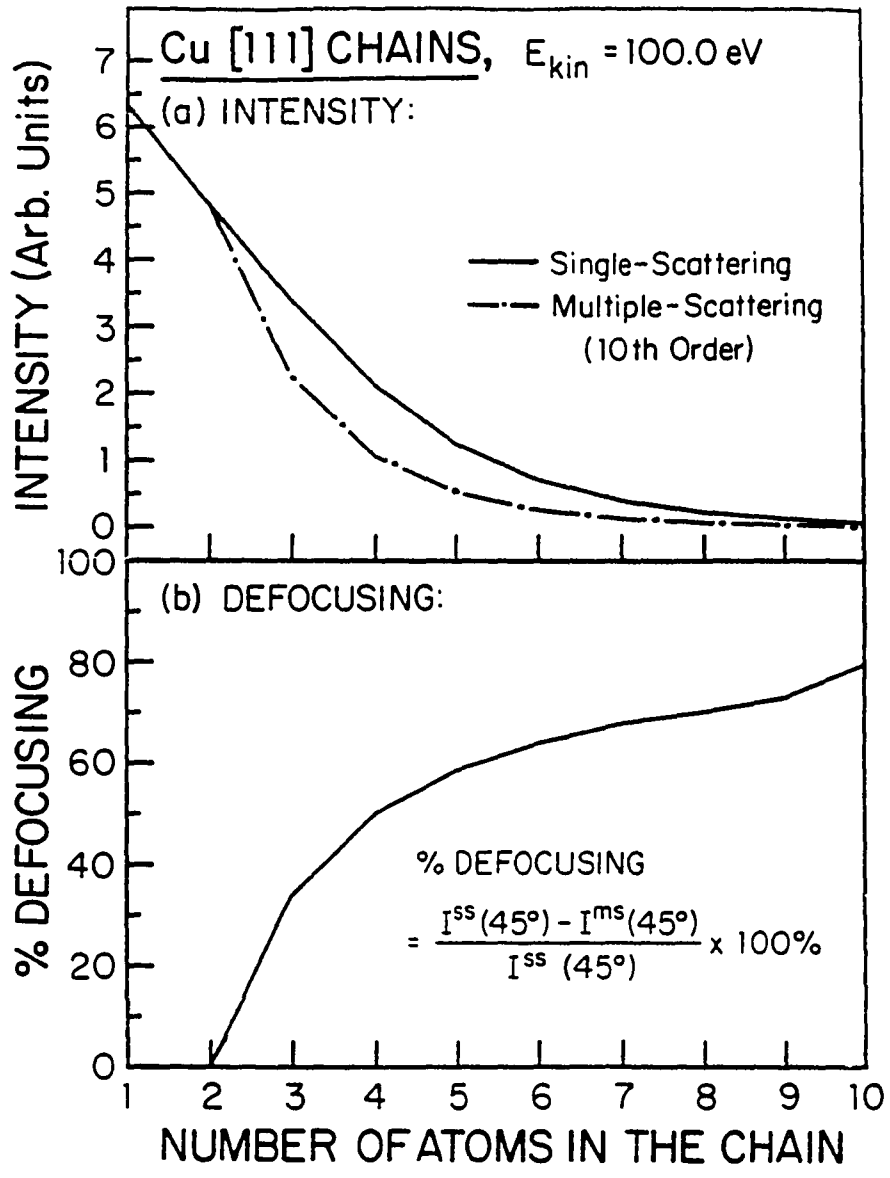

Figure 2.13. (a) Same as Figure 2.11(a), but for 100 eV. (b) Same as Figure 2.8.11(b), but for 100 eV.

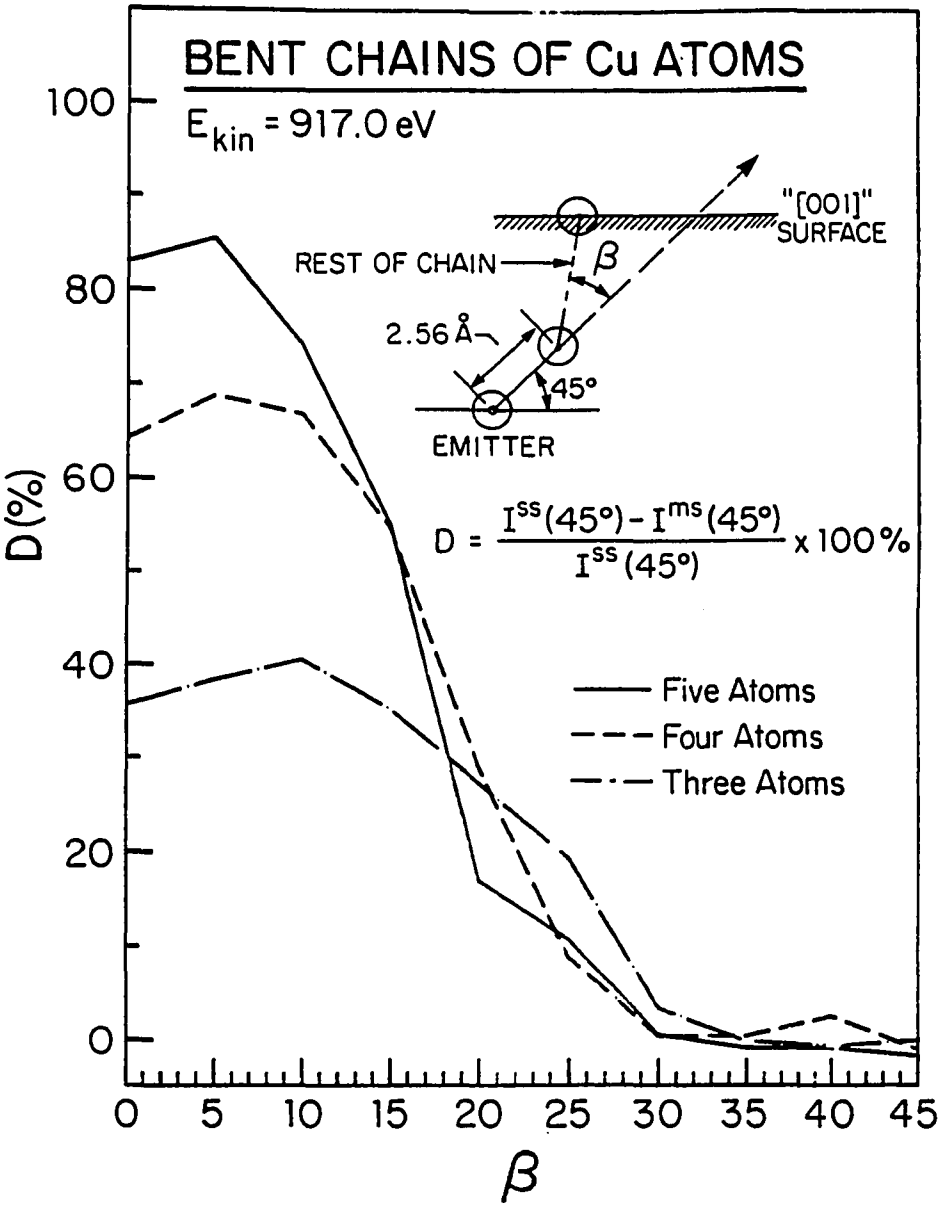

Figure 2.14. Defocussing of the Auger electron diffraction intensity at 917 eV in bent Cu [101] chains as a function of the bend angle.

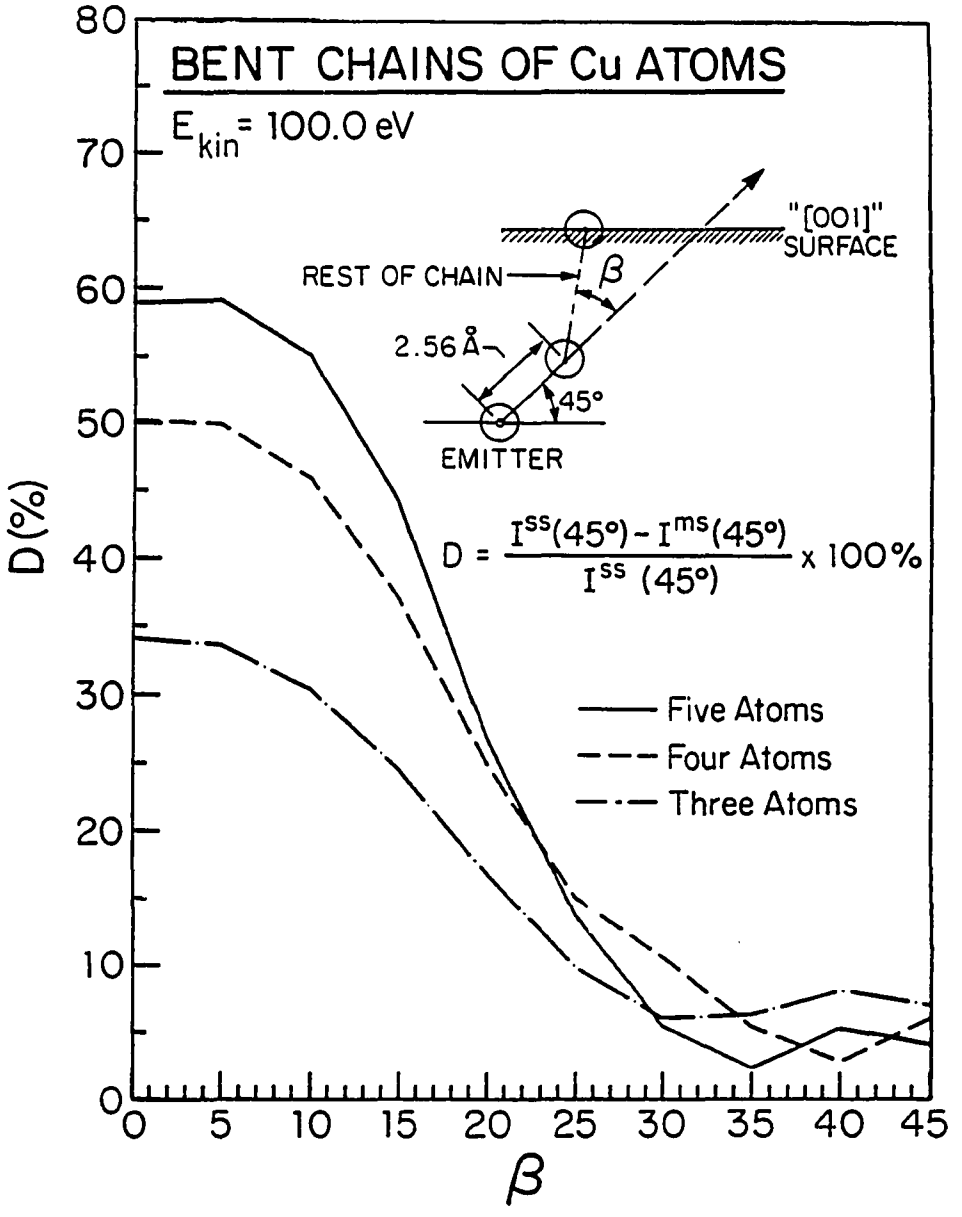

Figure 2.15. Same as Figure 2.14, but for 100 eV.

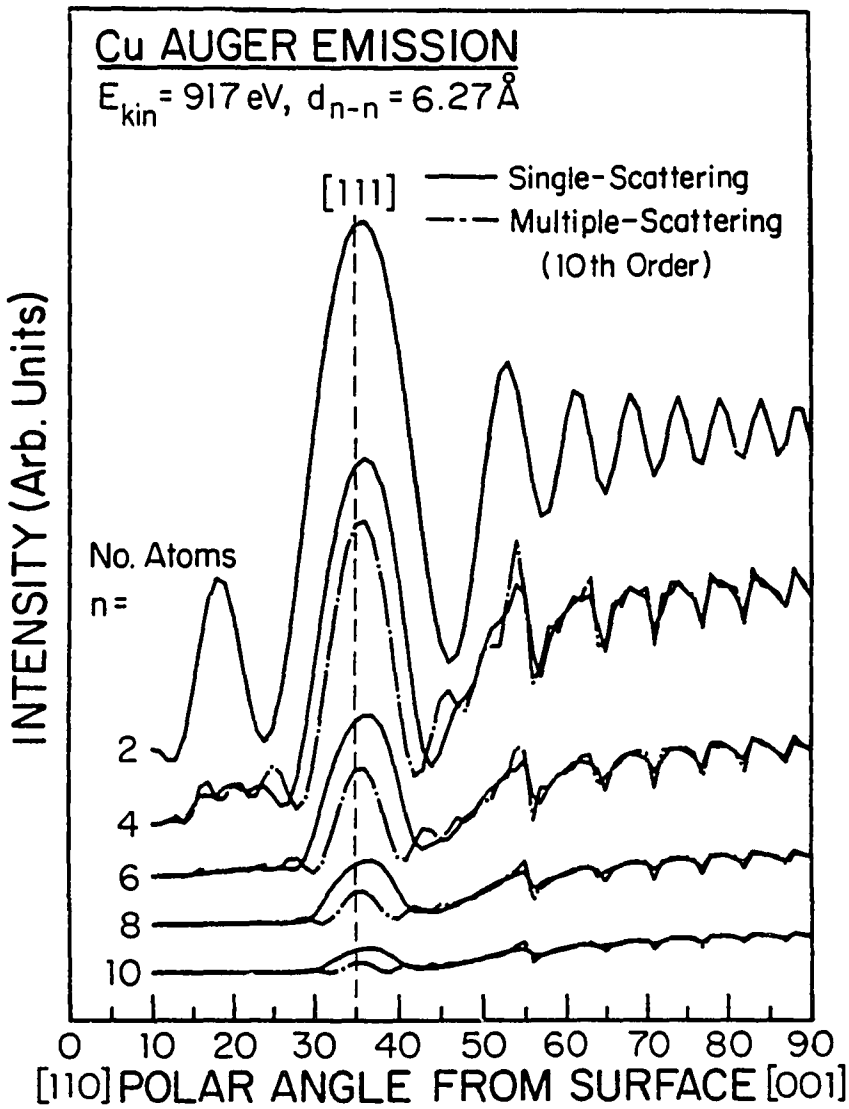

Figure 2.16. Same as Figure 2.10, but for Cu [111] chains.

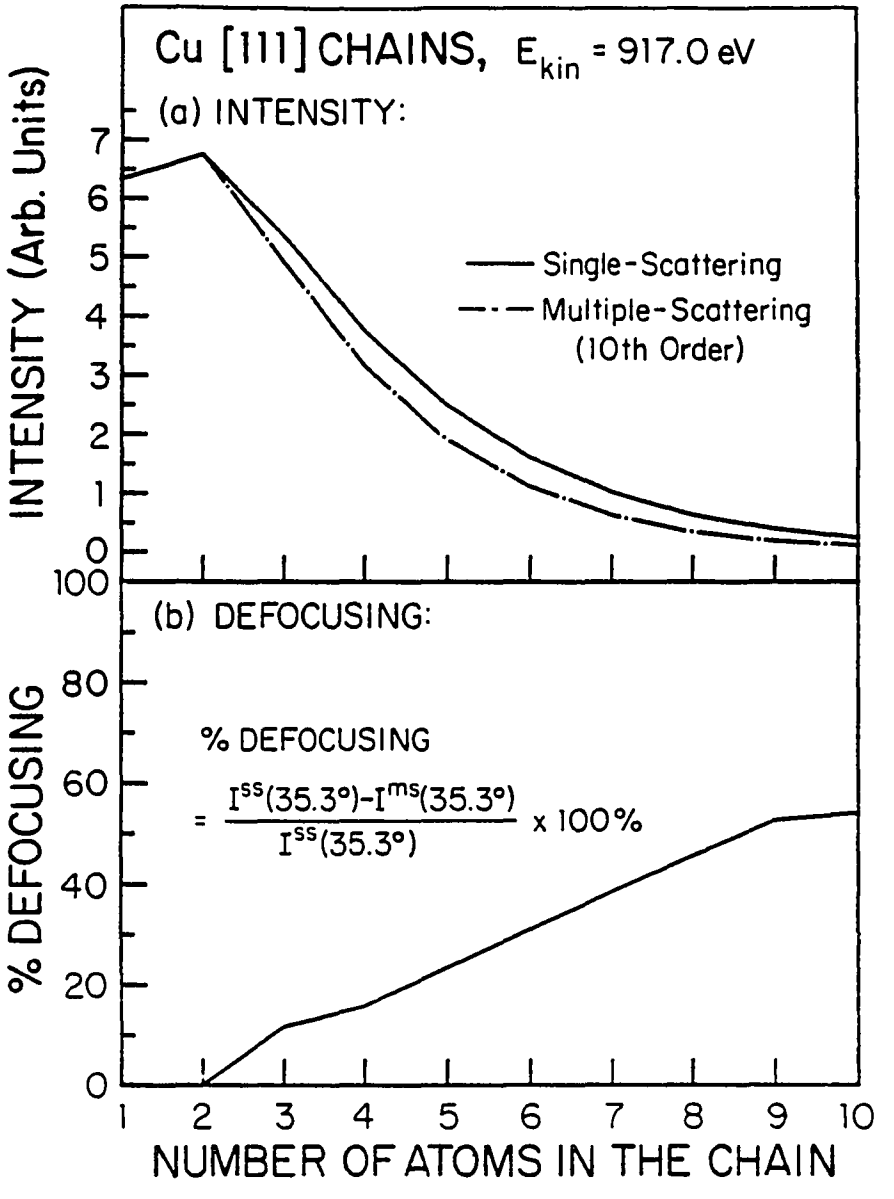

Figure 2.17. Same as Figure 2.11, but for Cu [111] chains.

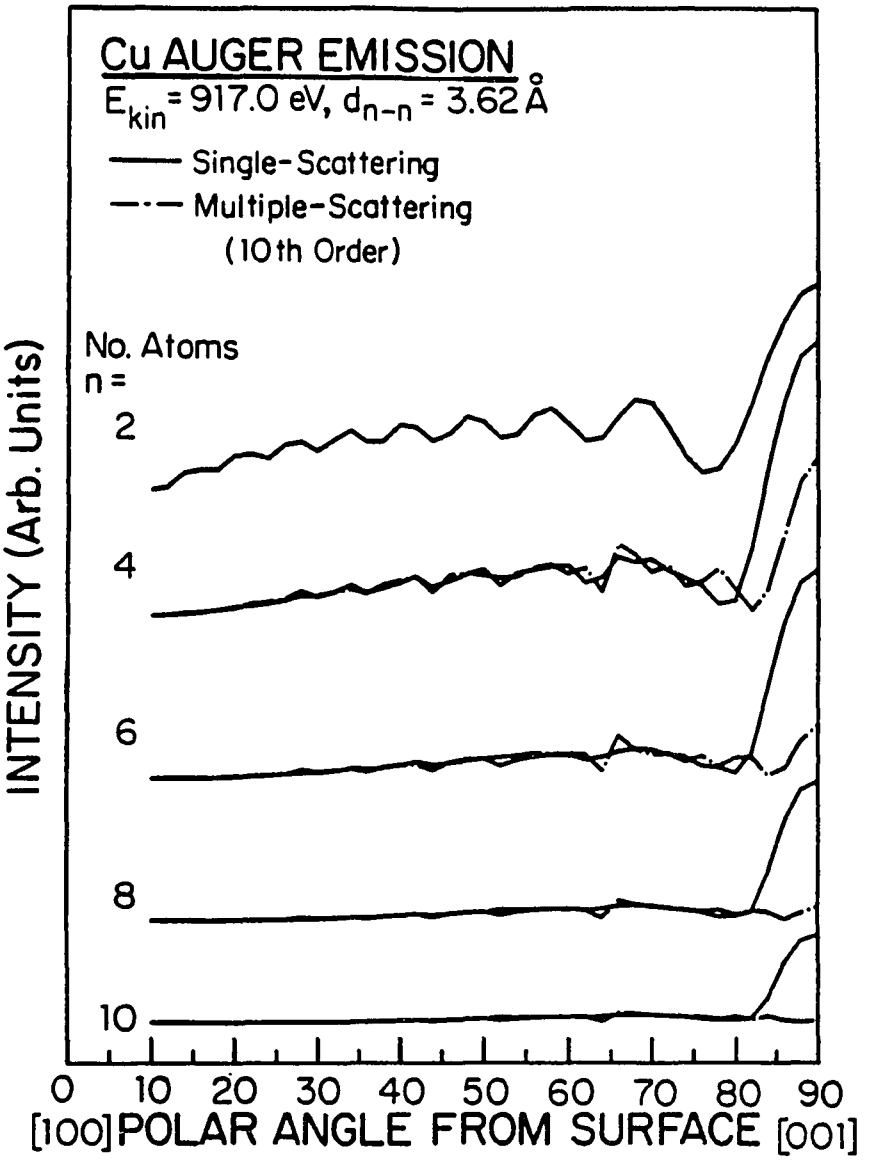

Figure 2.18. Same as Figure 2.10, but for Cu [001] chains.

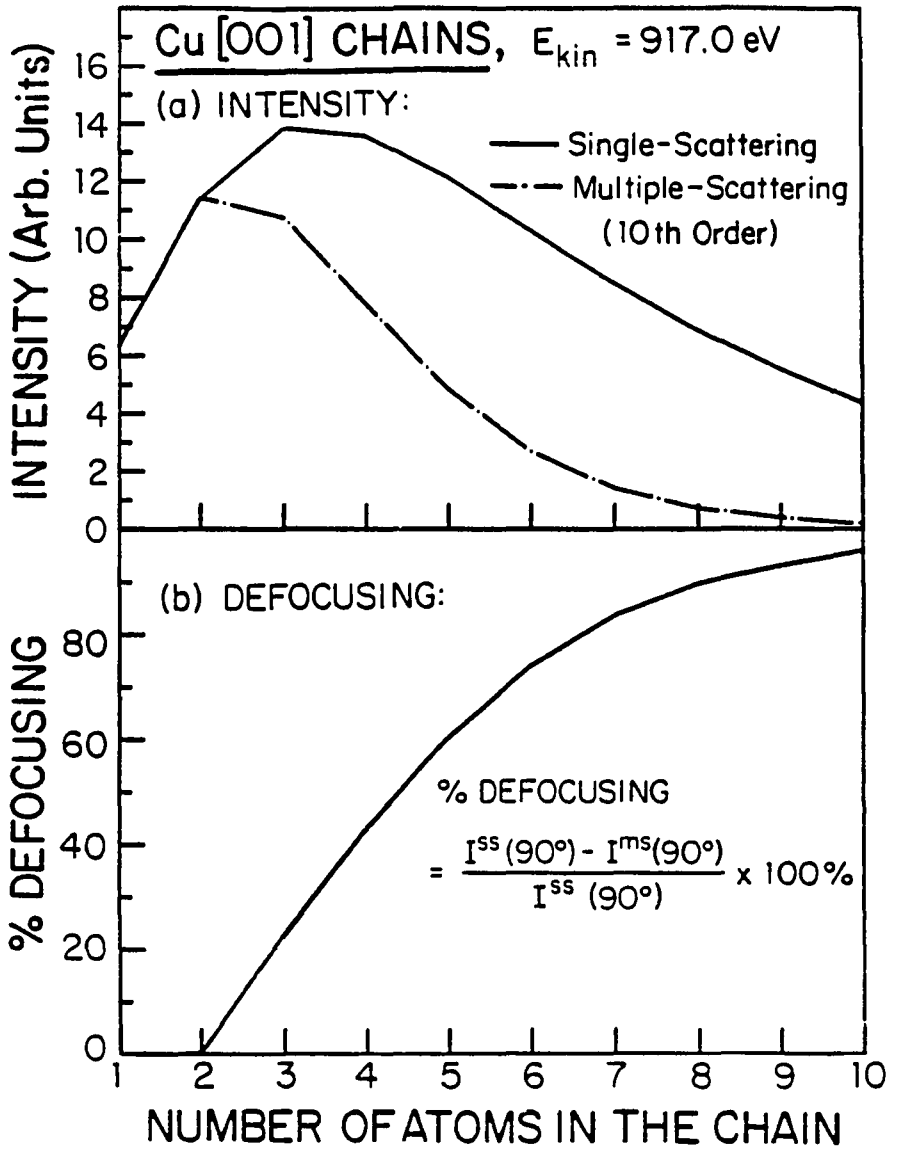

Figure 2.19. Same as Figure 2.11, but for Cu [001] chains.

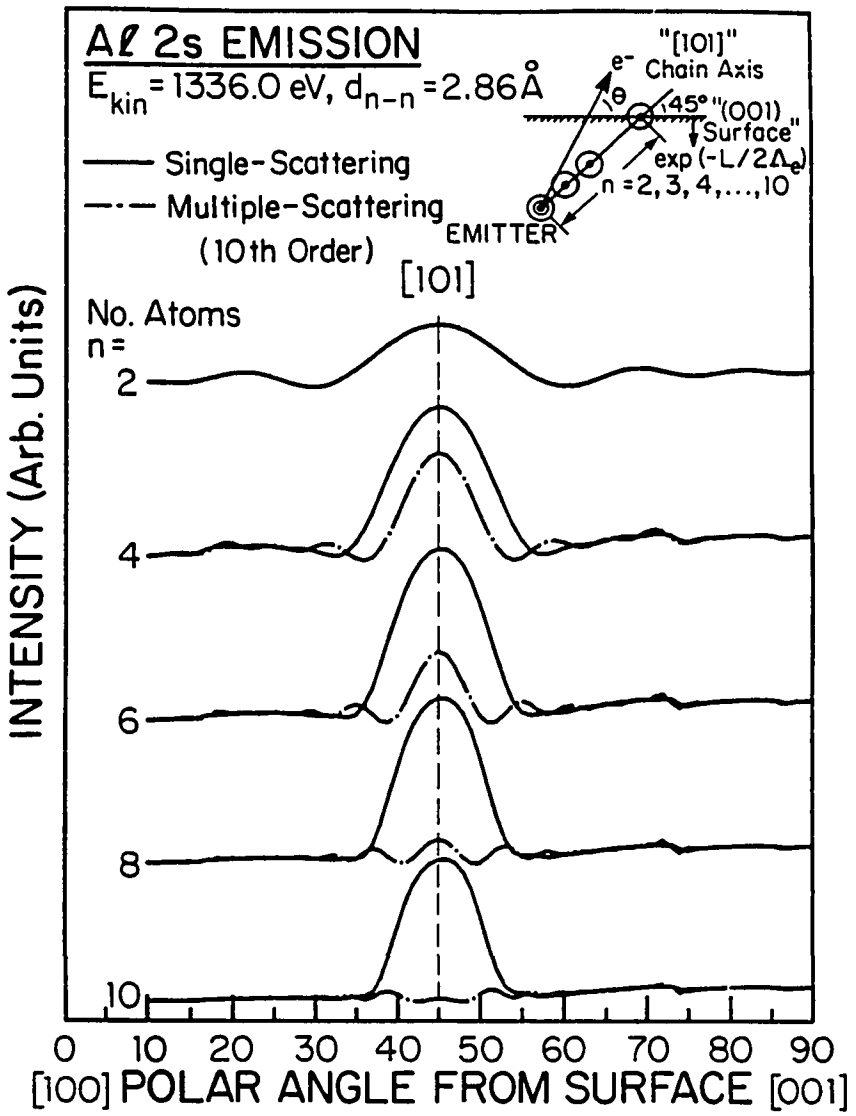

Figure 2.20. Single and multiple scattering calculations of Al 2s photoelectron diffraction from a linear Al [101] chain at 1336.0 eV. The emitter is at one end of the chain, as shown in the insert.

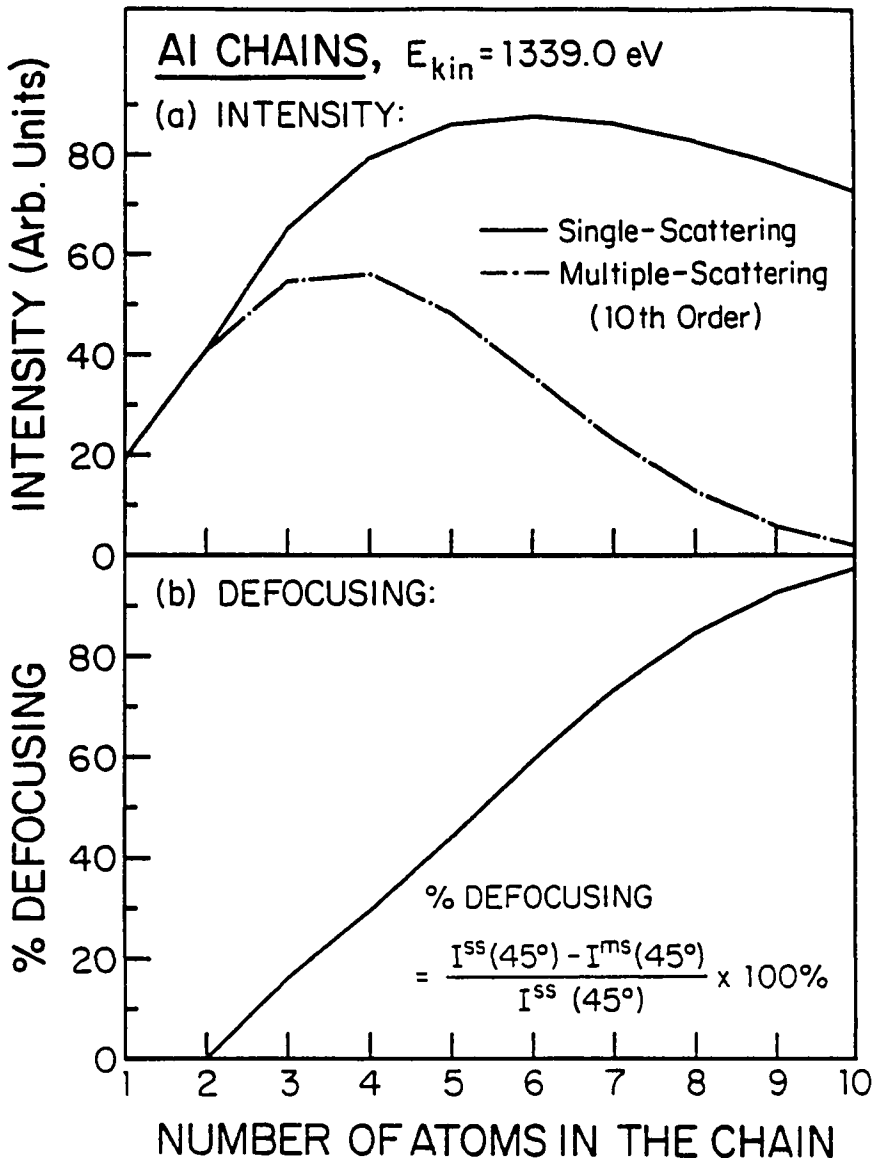

Figure 2.21.(a) Al 2s photoelectron diffraction intensity at 1336.0 eV directly along linear Al [101] chains as a function of number of atoms in the chain. (b) The % defocussing in 2s photoelectron diffraction intensity, based upon results in (a).

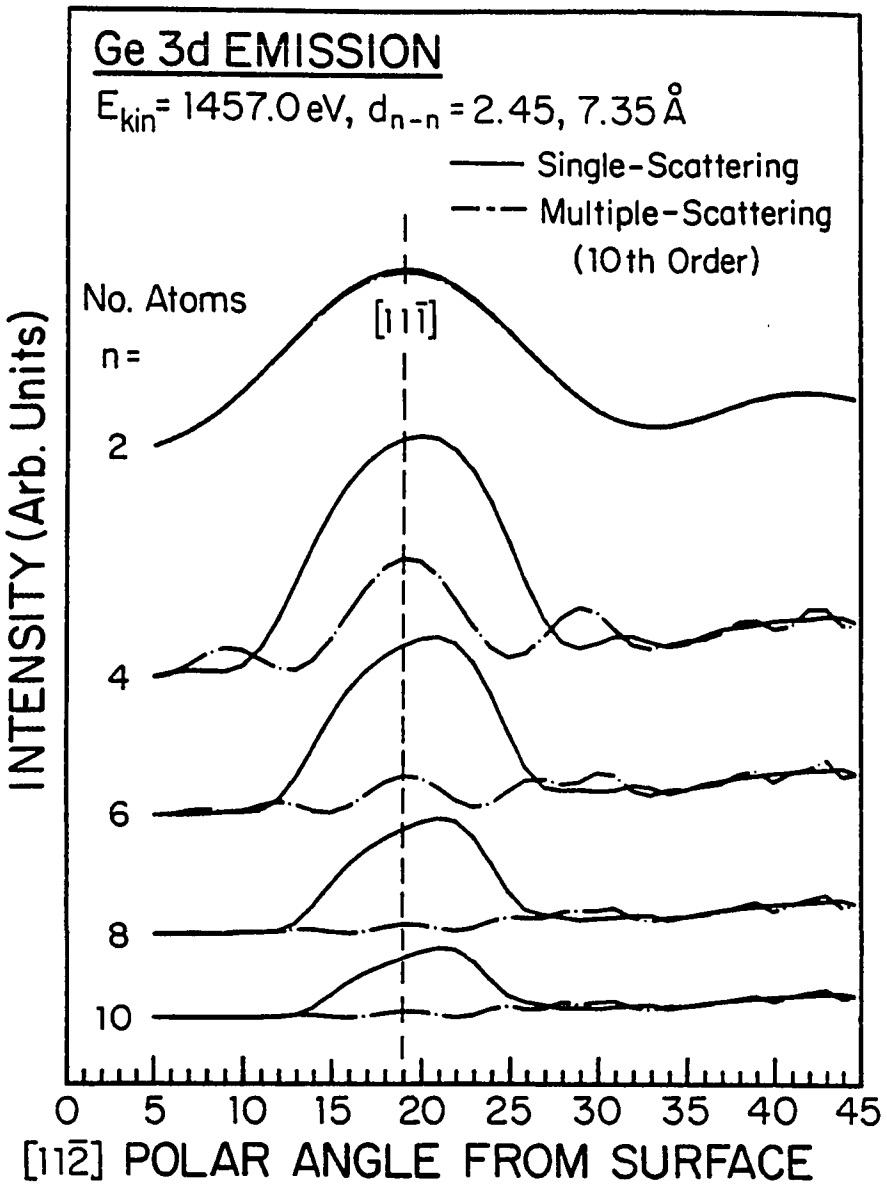

Figure 2.22. Single and multiple scattering calculations of Ge 3d photoelectron diffraction at 1457.0 eV from linear Ge [11$\bar{1}$] chains. The emitter is at one end of the chain.

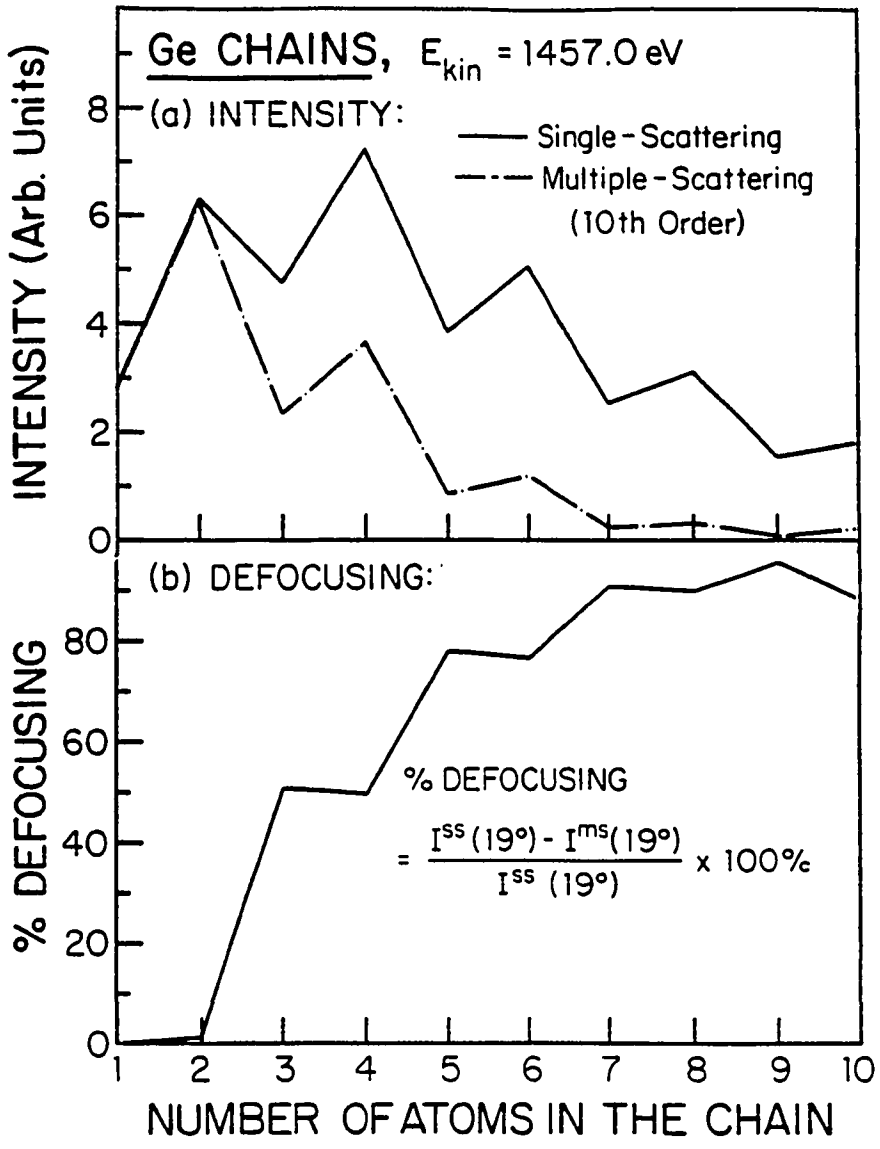

Figure 2.23.(a) Ge 3d photoelectron diffraction intensity from linear Ge [11$\bar{1}$] chains at 1457.0 eV as a function of the number of atoms in the chain. (b) The % defocussing in 3d photoelectron diffraction intensity, based upon the results in (a).

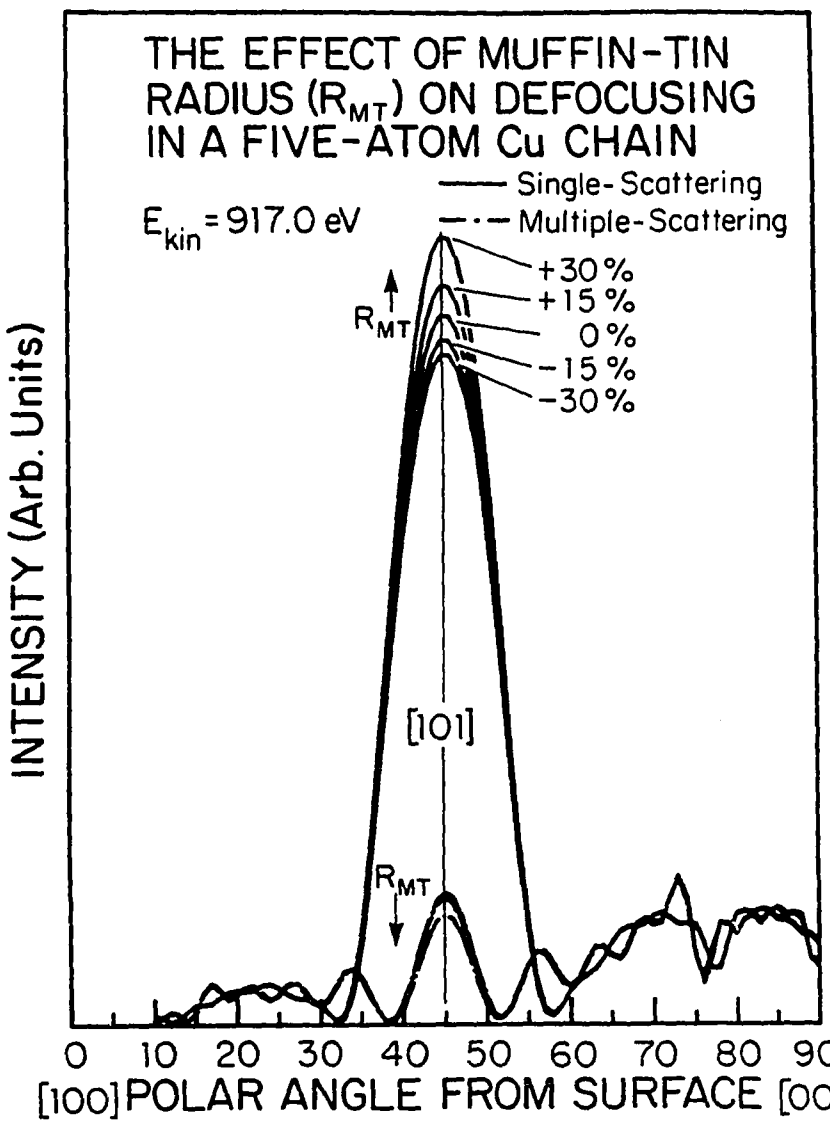

Figure 2.24. The effect of changing muffin-tin radius (R_{MT}) by ±30% on defocussing in a five atom Cu [101] chain at 917.0 eV. The multiple scattering curves all cluster very close together at the bottom of the figure. The direction of variation of R_{MT} is indicated by an arrow for each set of curves.

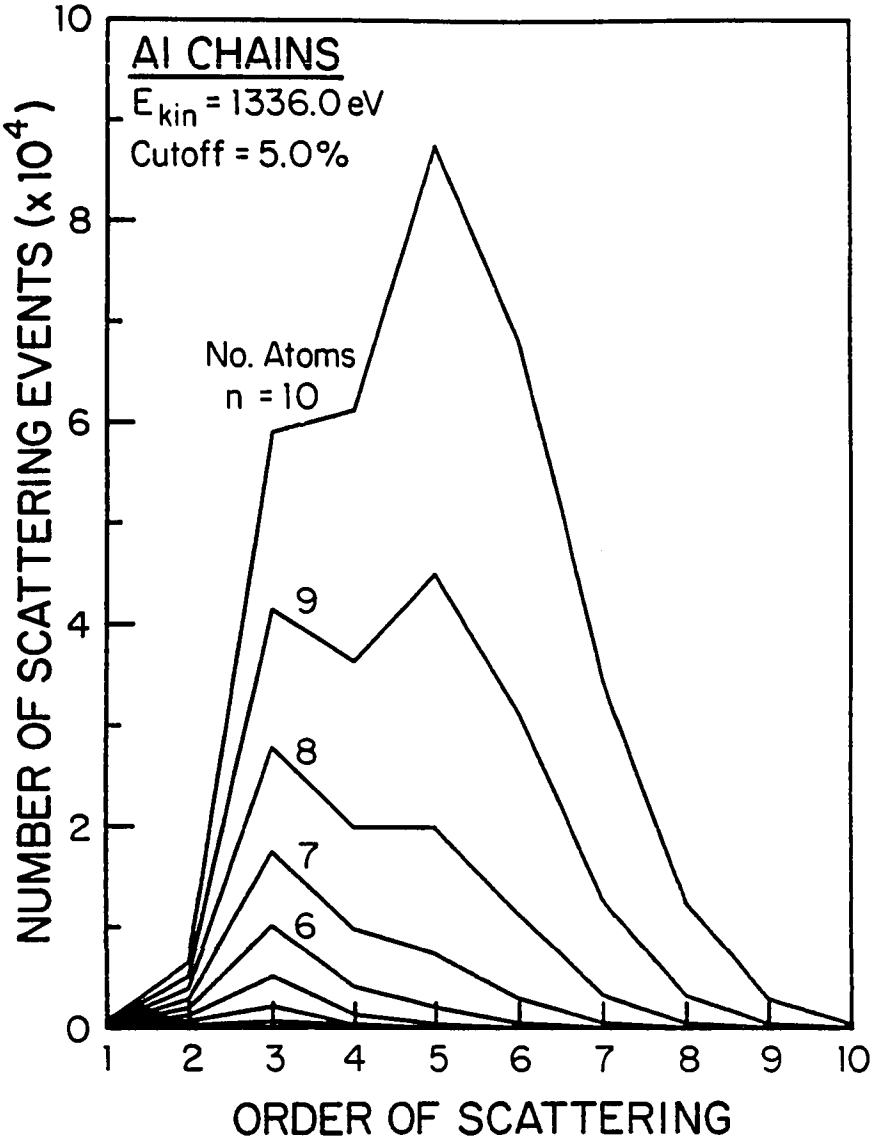

Figure 2.25. The number of scattering events in linear Al [101] chains at 1336.0 eV as a function of the scattering order. A cut-off of 5% was used for orders above 3rd in each calculation.

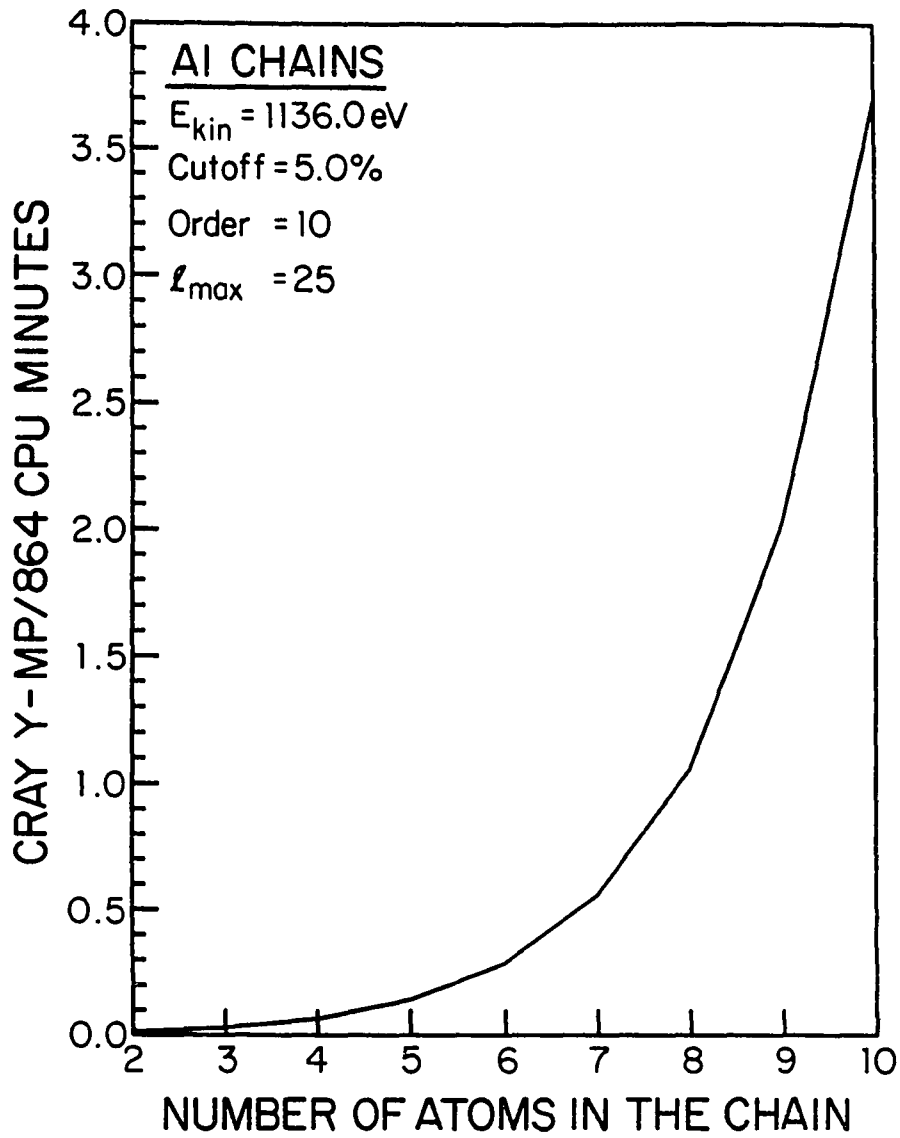

Figure 2.26. The Cray Y-MP/864 CPU time taken for the linear Al [101] chains of Figure 2.25 at tenth order scattering. A cut-off of 5% was again used.

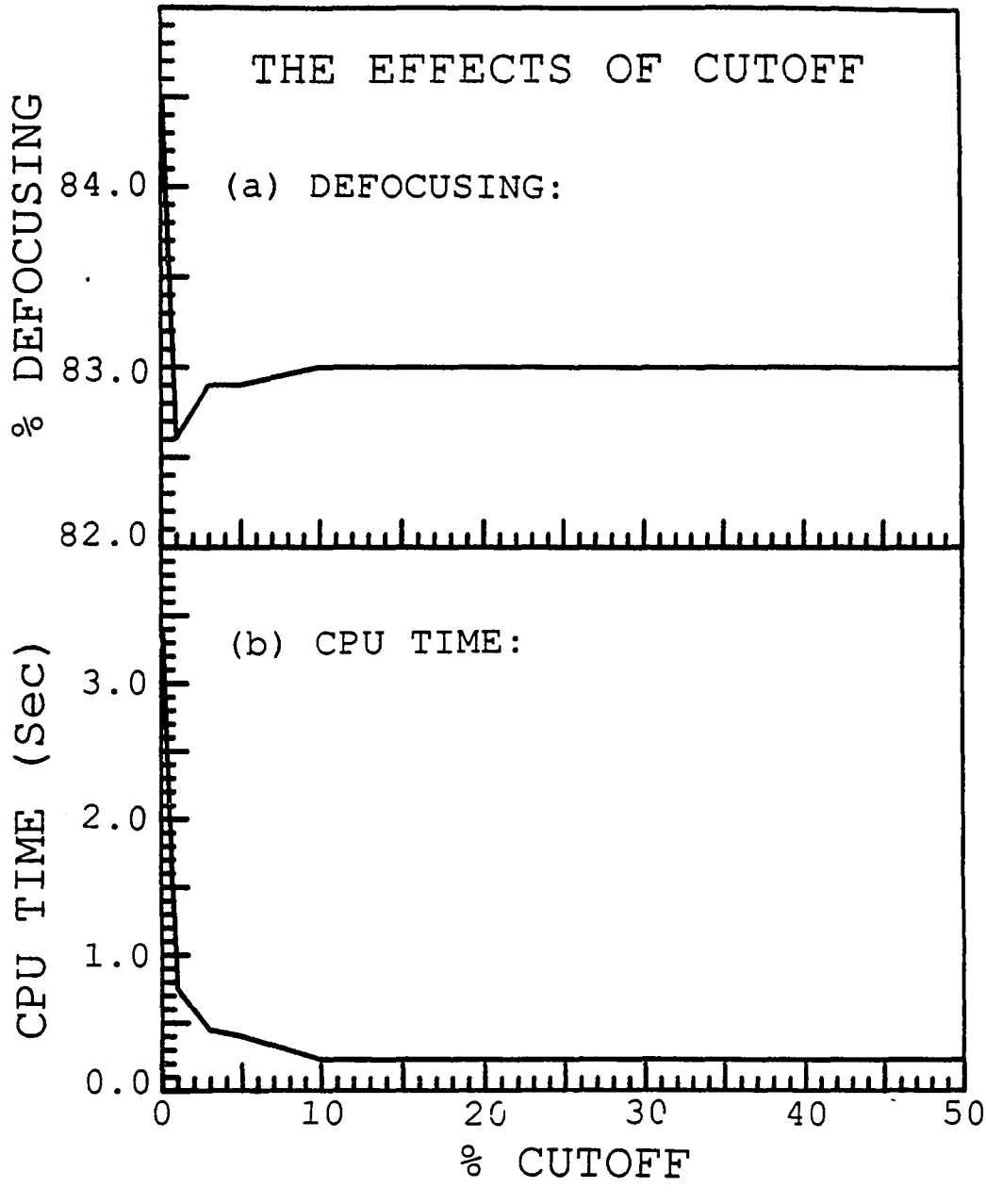

Figure 2.27. The effect of cutoff on (a) defocussing and (b) on the total CPU time for a five-atom Cu chain.

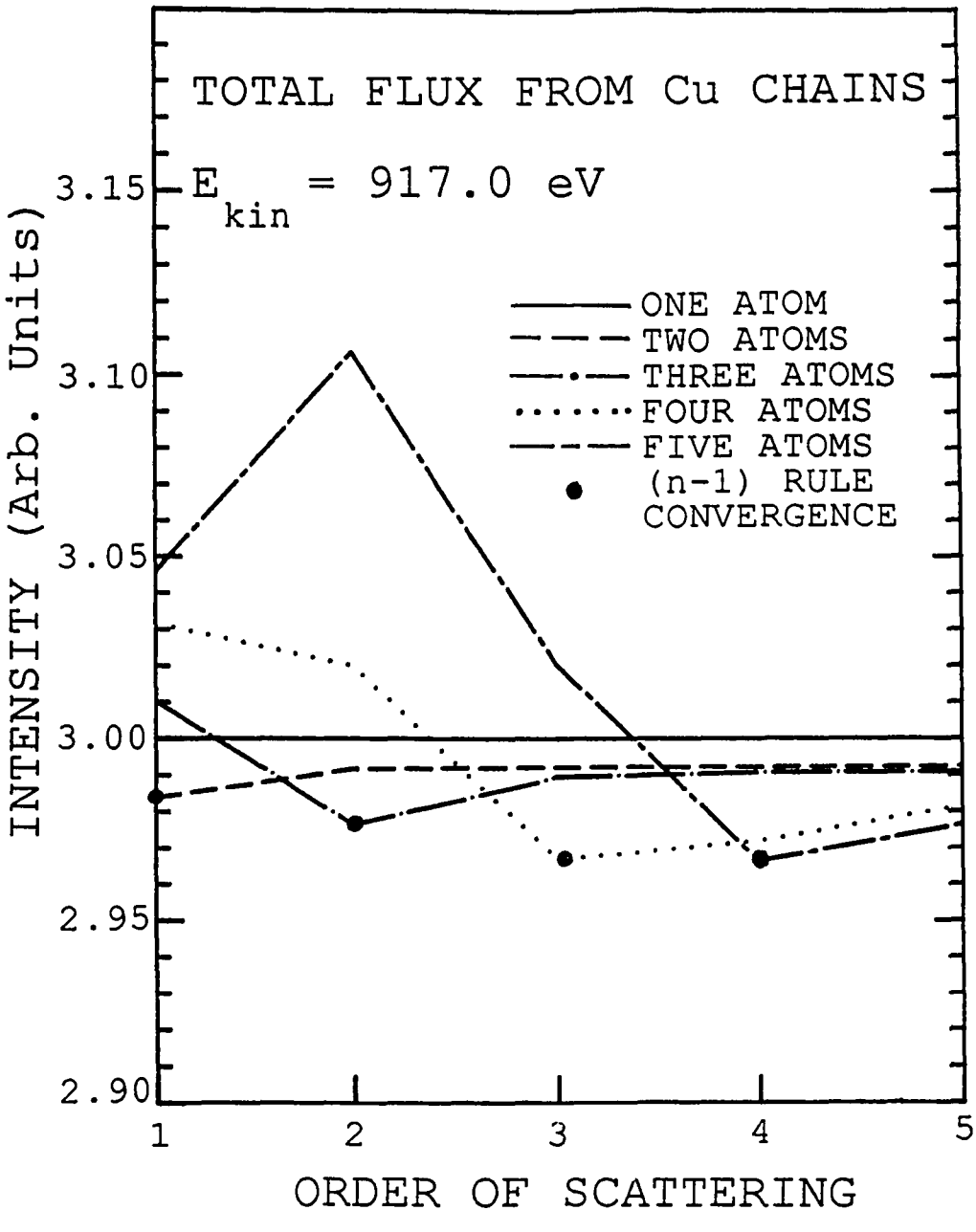

Figure 2.28. Degree of conservation of total flux from linear five-atom Cu chains as a function of scattering order.

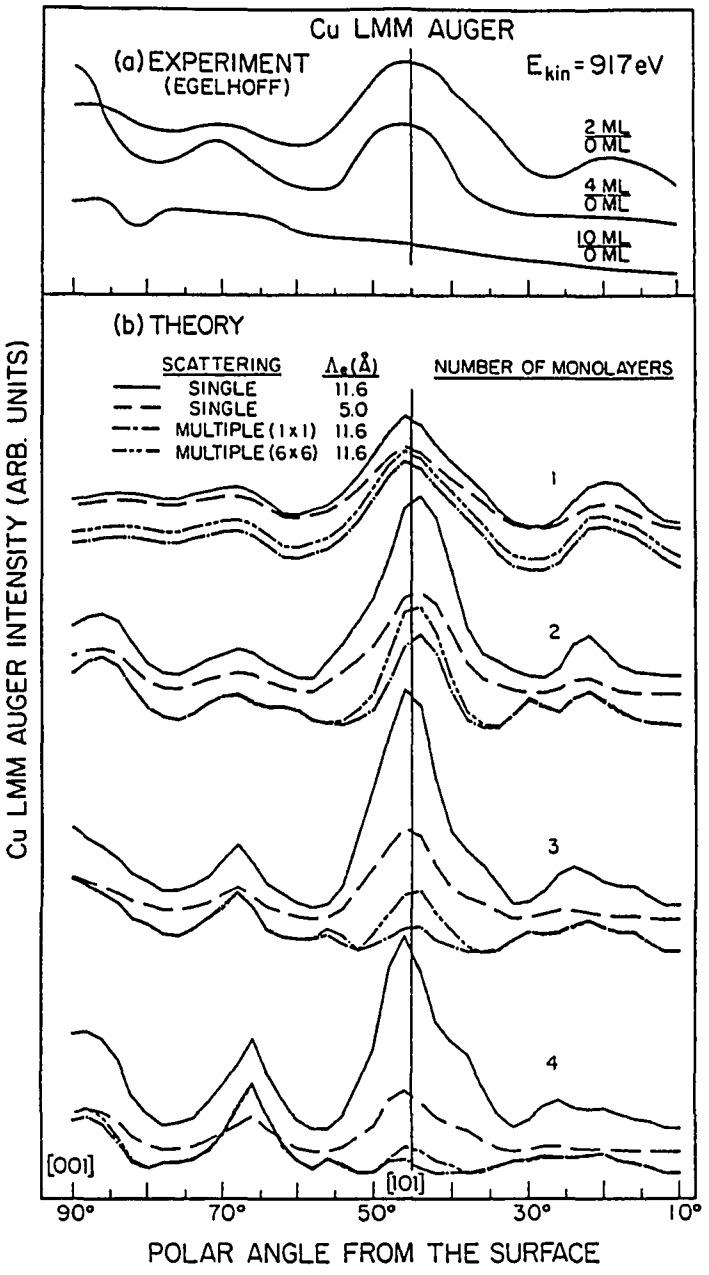

Figure 2.29. Polar angle dependence of Cu LMM Auger emission at 917.0 eV from a single monolayer of Cu buried under different thicknesses of Ni(001). The experimental data in (a) are from Reference [21]. The calculations in (b) are all form this work, and include both single and multiple scattering with two choices of inelastic attenuation length.

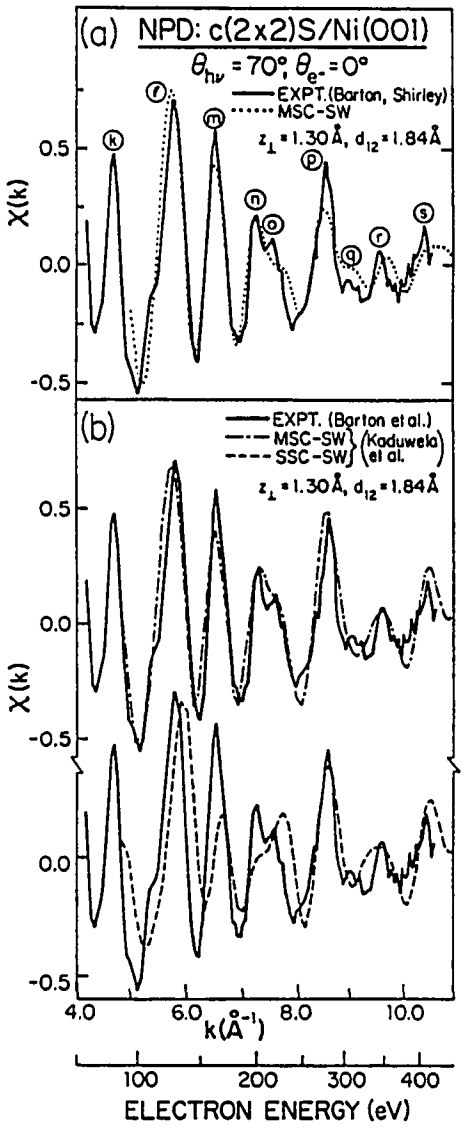

Figure 2.30. (a) Experimental and theoretical scanned-energy (ARPEFS) curves for S 1s emission from c(2×2)S/Ni(001) by Barton et al. [15]. The incoming radiation makes a 70° angle with the surface normal, and the photoelectrons are emitted along the surface normal. (b) Single and multiple-scattering simulations of the experimental data in (a) using the present method.

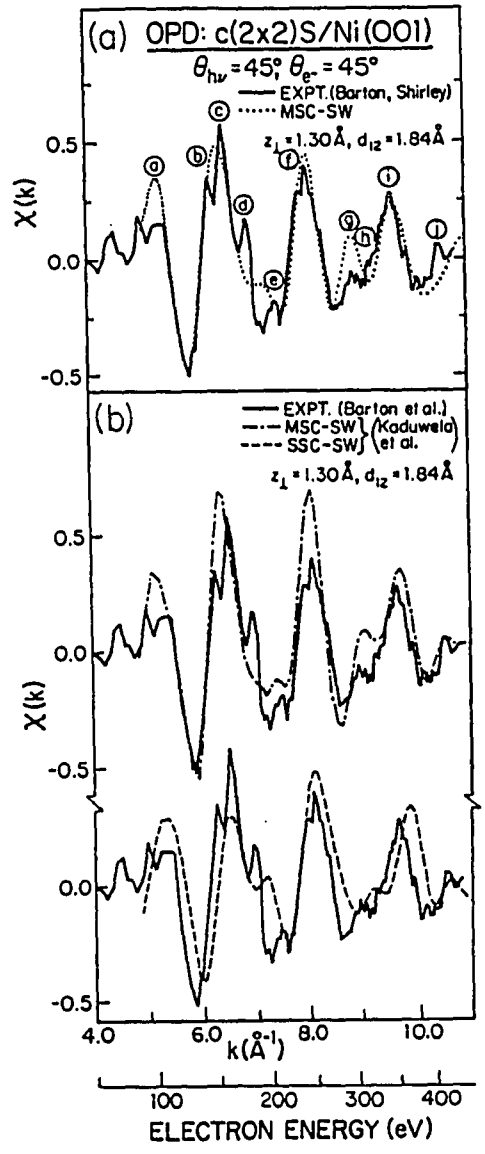

Figure 2 31. (a) Experimental and theoretical scanned-energy (ARPEFS) curves for S 1s emission from c(2x2)S/Ni(001) by Barton et al. [15]. The incoming radiation makes a 45° angle with the surface normal, and the photoelectrons are emitted at a 45° angle with respect to the surface normal. (b) Single and multiple-scattering simulations of the experimental data in (a) using the present method.

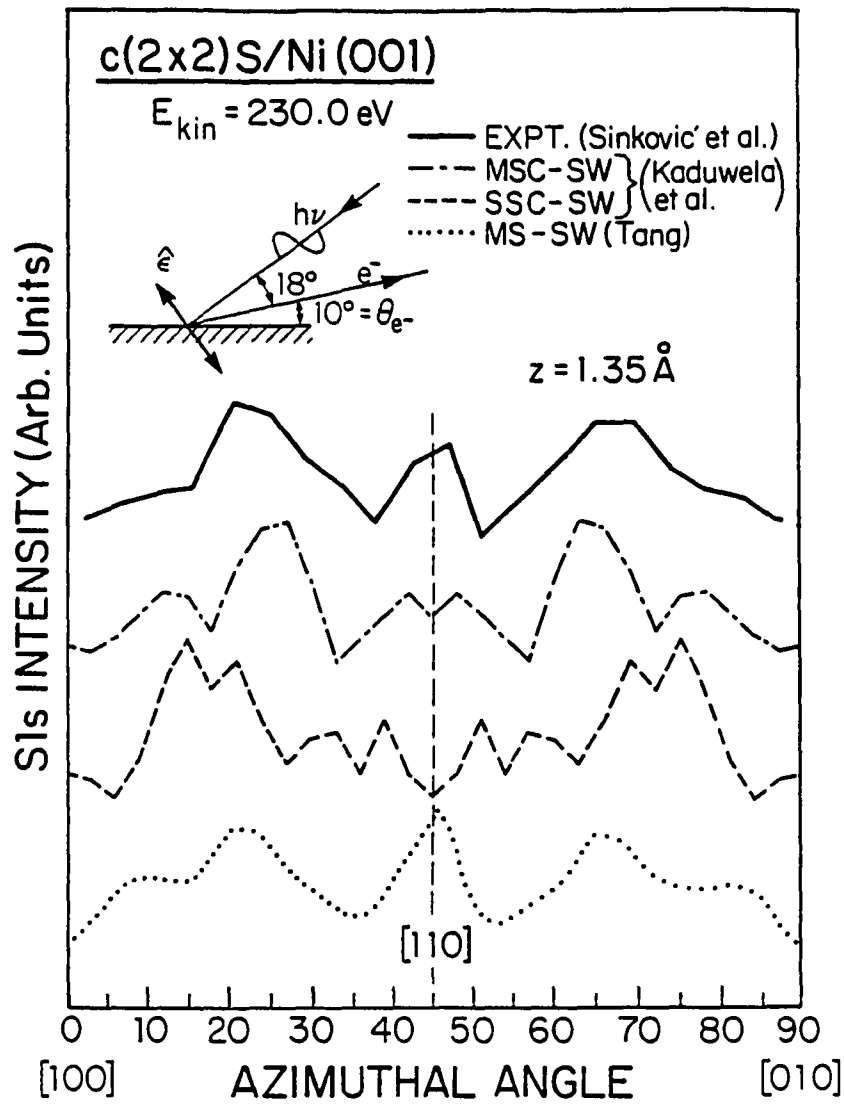

Figure 2.32. Azimuthal photoelectron diffraction for S 1s emission from c(2×2)S/Ni(001) at 230.0 eV. The experimental geometry is shown in the inset. The experimental data are from Reference 40, the bottom MS-SW curve is from Reference 41, and the rest of the theoretical curves are from this work.

CHAPTER 3.

APPLICATION OF A NOVEL MULTIPLE-SCATTERING APPROACH TO PHOTOELECTRON DIFFRACTION AND AUGER ELECTRON DIFFRACTION

3.1. INTRODUCTION:

Single-scattering cluster (SSC) theories, initially with plane wave (PW) scattering, but by now often with spherical-wave (SW) effects included, have been widely used in simulating experimental scanned-angle photoelectron diffraction (PD) and Auger electron diffraction (AED) patterns [1,2]. The same types of SSC models have also been applied with reasonable success to scanned-energy photoelectron diffraction or angle resolved photoemission extended fine structure (ARPEFS) [1(b),1(c),3]. However, the possible effects of multiple-scattering (MS) on such patterns have also been discussed by several authors [1(c),3-11]. Thus, even though a single scattering (SS) approach has been found to predict most of the diffraction features observed experimentally with enough accuracy to be useful for structure determinations [1-3], several instances where such an approach is not fully adequate in explaining experimental results have been pointed out [1(c),3,6-11]. It is thus desirable to have a quickly-convergent and versatile MS algorithm that can be applied to both photoemission from any core subshell (i.e., to s, p, d, or f emission) and to Auger emission (as treated in the common approximation of an outgoing s wave [10-12]).

In this paper, we further develop a new approach to MS due to Rehr and Albers [13] for this purpose. This method is conceptually simple and computationally efficient. It is based on a separable approximation to the scattering Green's function or free-particle propagator, and it allows building up successive orders of scattering and judging the approach to convergence in a convenient and efficient way. Scattering events up to 10^{th} order have been included in our calcuations for some cases to insure convergence. The general-purpose computer program written in this work permits treating photoelectron emission from any subshell, as well as s-wave Auger emission. The example systems studied to date and discussed here include c(2×2)S on Ni(001), linear and bent chains of several different atoms (Cu, Al, and Ge), multilayer epitaxial overlayers (Cu(001) on Ni(001)) and multilayer substrates (Ni(001)), and more complex structures of molecular or atomic adsorbates on surfaces (the tilted α_3 state of CO on Fe(001) and ($\sqrt{3}\times\sqrt{3}$)R30° Ag on Si(111)).

3.2. APPLICATION OF THE SEPARABLE GREEN'S FUNCTION APPROACH OF REHR AND ALBERS TO SINGLE AND MULTIPLE SCATTERING:

In this section we will discuss the application of the scattering-matrix formalism of Rehr and Albers (R-A) [13] to single and multiple scattering in both photoelectron and Auger electron diffraction. This full spherical-wave method approximates the system by a cluster of individual atoms. This is a sensible alternative to

prior MS methods derived from low energy electron diffraction (LEED) [4,6,9] which require full translational symmetry along the surface and are thus not as well matched to treating short-range probes such as PD, AED or ARPEFS, or the presence of any disorder. Cluster methods [1,3,7,10,11] are by contrast very appropriate to modeling all types of short-range-order effects. The most accurate version of the cluster approach we will term multiple-scattering cluster-spherical wave (MSC-SW) to distinguish it from the previously-used SSC-PW and SSC-SW methods. In the following paragraphs, we present the essential points of the treatment by Rehr and Albers [13], and then expand it to apply to MS in photoemission from any subshell or Auger emission. In the equations to follow, we will for simplicity not initially include effects due to inelastic scattering or vibrational motion, but the form in which these have been incorporated will be indicated later. The details of the original derivation by Rehr and Albers will only be discussed briefly, as they are discussed fully in the original article discribing this approach [13].

We begin with some fundarmental equations and definitions used by Rehr and Albers [13]. From Equation (25) of Reference 13, the photoelectron diffraction intensity at the detector is given by

$$I(\vec{k}) \propto \frac{d\sigma}{d\Omega}(\vec{k}) \propto \left| \sum_{L_f,N} G^{(N-1)}_{00,L_f}(\vec{R}_1,\vec{R}_2,\ldots,\vec{R}_N)\, m_{L_f,c}(\hat{\epsilon})\, \exp(i\delta^c_{\ell_f}) \right|^2 \qquad (3\text{-}2\text{-}1)$$

where $I(\vec{k})$ is the intensity at the detector for emission with wave vector $\vec{k}$, $\frac{d\sigma}{d\Omega}(\vec{k})$ is the core photoelectric cross section for emission from a given sublevel $n_i \ell_i m_i$, $G^{(N-1)}_{00,L_f}$ is the $(N-1)^{th}$ order multiple-scattering Green's function for a path from $\vec{R}_0 = \vec{R}_{emitter}$ at the origin via scatterers at $\vec{R}_1$, $\vec{R}_2$, ..., $\vec{R}_{N-1}$ to $\vec{R}_N = \vec{R}_{detector} = \vec{R}_d$ at ∞, $m_{L_f,c}(\hat{\epsilon})$ is the amplitude and $\delta^c_{\ell_f}$ is the phase of the dipole matrix element into a given final-state $L_f = (\ell_f, m_f)$ value as given by $\langle \Psi_{E_{kin},\hat{k}} | \hat{\epsilon}.\vec{r} | \phi_{n_i \ell_i m_i} \rangle$. ($L_f$ here is equal to L in the notation of R-A). $G^{(N-1)}_{00,L_f}$ thus couples the (ℓ_f, m_f) state from the emitter to the (0,0) state required at the detector an infinite distance away. Within the matrix element, $\Psi_{E_{kin},\hat{k}}$ denotes the final continuum state of the photoelectron at a kinetic energy E_{kin} and in the direction $\hat{k} = \vec{k}/k$, $\phi_{n_i \ell_i m_i}$ is the initial core orbital from which the photoelectron is emitted, and $\hat{\epsilon}$ is the radiation polarization vector. The sum is over $L_f = (\ell_f, m_f)$ and over all combinations of N, the number of atoms in a given scattering path from single-scattering (N=2) to the highest order considered (in our case 10^{th} order or N=11).

Now R-A choose the $\hat{\epsilon}$ vector in the $\hat{z}$ direction to simplify the matrix element evaluation. The expression for the matrix element then becomes [14]

$$\langle \Psi_{E_{kin},\hat{k}} | \hat{\epsilon} \cdot \vec{r} | \phi_{n_i \ell_i m_i} \rangle = \langle \Psi_{E_{kin},\hat{k}} | Y_{10}(\theta,\phi) r | \phi_{n \ell_i m_i} \rangle, \qquad (3\text{-}2\text{-}2)$$

where $Y_{10}(\theta,\phi)$ is a spherical harmonic. Both $\Psi_{E_{kin},\hat{k}}$ and $\phi_{n_i\ell_i m_i}$ are now expanded in spherical harmonics. In expanding $\Psi_{E_{kin},\hat{k}}$, use is made of the fact that it is a plane wave at the detector, thus implying the usual ingoing-wave expansion for it [14] to yield

$$\Psi_{E_{kin},\hat{k}} = 4\pi \sum_{\ell_f=0}^{\infty} \sum_{m_f=-\ell_f}^{\ell_f} \Big[i^{\ell_f} \exp\{-i\delta^c_{\ell_f}\} \times Y^*_{\ell_f m_f}(\theta_k,\phi_k)\, Y_{\ell_f m_f}(\theta,\phi)\, R_{E_{kin},\ell_f}(r) \Big], \quad (3\text{-}2\text{-}3)$$

with the angles defining the detector along $\vec{k}$ (or $\vec{R}_d$) taken to be (θ_k,ϕ_k). For $\phi_{n_i\ell_i m_i}$, we can simply write

$$\phi_{n_i\ell_i m_i} = R_{n_i\ell_i}(r)\, Y_{\ell_i m_i}(\theta,\phi). \quad (3\text{-}2\text{-}4)$$

Here, $R_{E_{kin},\ell_f}(r)$ and $R_{n_i\ell_i}(r)$ are radial parts of the continuum orbital at ℓ_f and a given core orbital with quantum numbers n_i and ℓ_i, respectively.

Substituting Equations (3-2-3) and (3-2-4) into (3-2-2) and doing some simplifications, one arrives at

$$\langle \Psi_{E_{kin},\hat{k}(\vec{k})} | \hat{\epsilon}\cdot\vec{r} | \phi_{n_i \ell_i m_i} \rangle = 4\pi \sum_{\ell_f = \ell_i \pm 1} \sum_{m_i = -\ell_<}^{\ell_<} \Big[(-i)^{\ell_f} \exp(i\delta_{\ell_f}) \times Y_{\ell_f m_i}(\theta_k, \phi_k) \langle R_{E_{kin},\ell_f}(r) | r | R_{n_i \ell_i}(r) \rangle \times \langle Y_{\ell_f m_i}(\theta,\phi) | Y_{10}(\theta,\phi) | Y_{\ell_i m_i}(\theta,\phi) \rangle \Big], \quad (3\text{-}2\text{-}5)$$

where $\ell_<$ is the lesser of the pair ℓ_i and ℓ_f. The integral in θ, ϕ yields the selection rules $\ell_f - \ell_i = \pm 1$ and $m_f - m_i = 0$ (due to polarization choice).

It is convenient now to define a core-to-ℓ_f matrix element $m_{L_f,c}$ as

$$m_{L_f,c} = (-i)^{\ell_f} \langle R_{E_{kin},\ell_f}(r) | r | R_{n_i \ell_i}(r) \rangle \times \langle Y_{\ell_f m_i}(\theta,\phi) | Y_{10}(\theta,\phi) | Y_{\ell_i m_i}(\theta,\phi) \rangle, \quad (3\text{-}2\text{-}6)$$

or in shorthand notation as

$$m_{L_f,c} = (3/4\pi)^{1/2} (-i)^{\ell_f} R_{\ell_f}(E_{kin}) C^1(\ell_f, m_i, \ell_i, m_i), \quad (3\text{-}2\text{-}7)$$

where $R_{\ell_f} = \langle R_{E_{kin},\ell_f}(r) | r | R_{n_i \ell_i}(r) \rangle$ and $C^1(\ell_f, m_i, \ell_i, m_i) = (4\pi/3)^{1/2} \langle Y_{\ell_f m_i}(\theta,\phi)\, Y_{10}(\theta,\phi) | Y_{\ell_i m_i}(\theta,\phi) \rangle$, with the last factor being a Gaunt coefficient. In the case of emission to a single final state (as, for example, for s emission ($\ell_i = 0$, $m_i = 0$) to a p final-state ($\ell_f = 1$, $m_f = m_i = 0$) or Auger emission to an assumed s final state

($\ell_f = 0$, $m_f = 0$)), we can ignore these matrix elements and phase shifts, as they produce only scaling factors of the intensity. But they are extremely important in calculations to more complex final states where ℓ_i can go into the two channels $\ell_f = \ell_i \pm 1$. As one available source of both R_{ℓ_f} and $\delta^c_{\ell_f}$, Goldberg et al. [14] have tabulated them for a a number of free atoms at several energies. We will here introduce these factors only at the end of derivations to account for fully general emission into the $\ell_i \pm 1$ channels.

As noted previously, $G^{(N-1)}_{00,L_f}$ in Equation (3-2-1) is the exact multiple-scattering expansion for an N-leg scattering path with (N-1) scattering events. It can be written, using Equation (14) of Reference 13, as,

$$G^{(N-1)}_{00,L_f}(\vec{R}_1, \ldots, \vec{R}_N) = \sum_{\text{(paths)}} \sum_{\{L_i\}} G_{00,L_{N-1}}(\vec{\rho}_N)\, t_{\ell_{N-1}}(\vec{R}_{N-1}) \times G_{L_{N-1},L_{N-2}}(\vec{\rho}_{N-1})\, t_{\ell_{N-2}}(\vec{R}_{N-2}) \cdots\cdots\cdots \cdots\cdots\cdots t_{\ell_1}(\vec{R}_1)\, G_{L_1,L_f}(\vec{\rho}_1) \qquad (3\text{-}2\text{-}8)$$

where $G_{L_{j+1},L_j}(\vec{\rho}_{j+1})$ is a matrix element of the free-electron propagator in an angular momentum and site basis, $L_{j+1} = (\ell_{j+1}, m_{j+1})$, $L_j = (\ell_j, m_j)$, $\vec{\rho}_{j+1} = k(\vec{R}_{j+1} - \vec{R}_j)$ is a "bond vector" in units of 2π(number of electron wave lengths), and $t_\ell = \exp\{i\delta_\ell\}\sin\delta_\ell$ is a diagonal element of the t-matrix for scattering. A graphical representation of one of the paths in $G^{(N-1)}_{00,L_f}$ is given in Figure 3.1.

The summations are over all combinations of intermediate L_i's and all possible scattering paths of (N-1) order in the cluster. The matrix elements or intermediate propagators $G_{L_{j+1},L_j}(\vec{\rho}_{j+1})$ in the above expression thus give the strength of a given L_{j+1} component of spherical waves centered on $\vec{R}_{j+1}$ as contained in the component L_j propagating outward from $\vec{R}_j$; at each $\vec{R}_{j+1}$, $t_{\ell_{j+1}}(\vec{R}_{j+1})$ then accounts for the effects of scattering on the next outgoing components. For a general multiple-scattering event, both L_{j+1} and L_j must take on all values from 0 up to some L_{max} at which $t_{\ell_{j+1}}$ and $t_{\ell_{j-1}}$ go to zero. The last $L_N = (\ell_N, m_N)$ can be shown to be restricted to (0,0) because it represents the projection of L_{N-1} at the last scattering center into a plane-wave at the detector $\vec{R}_d$ an infinite distance away.

The major contribution of Rehr and Albers (R-A) [13] was to develop a convergent separable approximation to the general matrix element $G_{L,L'}(\vec{\rho})$. Details of their derivation and certain extensions we have made of it for the specific case of multiple-scattering in photoelectron and Auger emission are given elsewhere [13,15] and we will thus present only a brief outline of essential steps and results. Beyond choosing the initial z axis to be parallel to the polarization vector $\hat{\epsilon}$, as noted previously, the next step is to rotate a given bond direction corresponding to $\vec{\rho} = k(\vec{R}-\vec{R}')$ onto the z-axis to further simplify the calculation. Then one has after some manipulation,

$$G_{L,L'}(\vec{\rho}) = [\exp\{i\rho\}/\rho] \sum_{\mu=-\ell}^{\ell} R^{\ell}_{m\mu}(\hat{\rho}^{-1})\, g^{(|\mu|)}_{\ell\ell'}(\rho)\, R^{\ell'}_{\mu m'}(\hat{\rho}) \qquad (3\text{-}2\text{-}9)$$

where $R^{\ell}_{m\mu}(\hat{\rho})$ is a rotation matrix which rotates the unit vector $\hat{\rho}$ onto the z-axis, $R^{\ell}_{m\mu}(\hat{\rho}^{-1})$ is the inverse of this matrix, $\rho = |\vec{\rho}|$ and $g^{(|\mu|)}_{\ell\ell'}$ is found to be a reduced, dimensionless z-axis propagator. (Equation (3-2-9) here is equivalent to Equation (9) of Reference 13.) The Euler angles (α,β,γ) associated with these rotations are defined according to the convention in reference 16: α about initial Z, β about intermediate Y', and γ about final z. The two matrices are related by the standard identities: $R^{\ell}_{m\mu'}(\hat{\rho}) = R^{\ell}_{m\mu'}(\alpha,\beta,\gamma)$ and $R^{\ell}_{m\mu'}(\hat{\rho}^{-1}) = R^{\ell}_{m\mu'}(-\gamma,-\beta,-\alpha)$. The first step in the R-A treatment thus separates $G_{L,L'}(\vec{\rho})$ into purely angle-dependent rotation matrices and a radial z-axis propagator $g^{(|\mu|)}_{\ell\ell'}$ that depends, through k in ρ, on energy.

The second step in the R-A method is to achieve a separable approximation to this z-axis propagator. This proceeds by deriving an integral expression for $g^{(|\mu|)}_{\ell\ell'}$ (Appendix A of Reference 13); and then further simplifying this using contour integration methods to yield the final fully-separated equation (Appendix B of Reference 13) as:

$$g^{(|\mu|)}_{\ell\ell'}(\rho) = \sum_{\nu=0}^{\min[\ell,\ell'-|\mu|]} \tilde{\gamma}^{\ell}_{\mu\nu}(\rho)\ \gamma^{\ell'}_{\mu\nu}(\rho), \qquad (3\text{-}2\text{-}10)$$

where $\min[\ell,\ell'-|\mu|]$ = the minimum of ℓ and $\ell-|\mu| = [\ell,\ell'-|\mu|]$ in later notation, and the new functions γ and $\tilde{\gamma}$ are defined as,

$$\gamma_{\mu\nu}^{\ell}(\rho) = (-1)^{\mu} N_{\ell\mu} C_{\ell}^{(\mu+\nu)}(z) z^{\mu+\nu}/(\mu+\nu)!, \qquad (3\text{-}2\text{-}11)$$

and

$$\tilde{\gamma}_{\mu\nu}^{\ell}(\rho) = (2\ell+1) C_{\ell}^{(\nu)}(z) z^{\nu}/(N_{\ell\mu} \nu!). \qquad (3\text{-}2\text{-}12)$$

Here, $C_{\ell}(z)$ is the polynomial part of the spherical Hankel function and $C_{\ell}^{(\nu)}(z) = \partial^{\nu} C_{\ell}/\partial z^{\nu}$.

Combining Equations (3-2-9) and (3-2-10) now yields the final form of the R-A separation:

$$G_{L,L'}(\vec{\rho}) = \frac{e^{i\rho}}{\rho} \sum_{\mu=-\ell}^{\ell} \sum_{\nu=0}^{\min[\ell,\ell'-|\mu|]} \times [R_{m\mu}^{\ell}(\hat{\rho}^{-1}) \tilde{\gamma}_{\mu\nu}^{\ell}(\rho)] [\gamma_{\mu\nu}^{\ell'}(\rho) R_{\mu m'}^{\ell'}(\hat{\rho})]. \qquad (3\text{-}2\text{-}13)$$

This can be further simplified by letting $\lambda = (\mu,\nu)$ represent the combined expansion indices and by defining the two bracketed quantities to be

$$\tilde{\Gamma}_{\lambda}^{L}(\vec{\rho}) = R_{m\mu}^{\ell}(\hat{\rho}^{-1}) \tilde{\gamma}_{\mu\nu}^{\ell}(\rho) \qquad (3\text{-}2\text{-}14)$$

and,

$$\Gamma_{\lambda}^{L'}(\vec{\rho}) = \gamma_{\mu\nu}^{\ell'}(\rho) R_{\mu m'}^{\ell'}(\hat{\rho}) \qquad (3\text{-}2\text{-}15)$$

to yield finally

$$G_{L,L'}(\vec{\rho}) = \frac{e^{i\rho}}{\rho} \sum_{\lambda} \tilde{\Gamma}_{\lambda}^{L}(\vec{\rho})\ \Gamma_{\lambda}^{L'}(\vec{\rho}). \qquad (3\text{-}2\text{-}16)$$

The factors involving L and L′ are thus fully separated in this description, a key advantage of the R-A method, as we will see below in applying it to both single and multiple scattering.

In addition, the sums in Equation (3-2-13) are found to be rapidly convergent [13], so that in practice results of very high accuracy are obtained with $|\mu| \leq 2$ and $\nu \leq 1$. This is the principal advantage of using this method as far as calculation times are concerned. We comment more on the adequacy of working at this level later.

The results of this separable approximation can now be substituted into Equation (3-2-8) to yield the principal equation of the R-A method as applied to photoelectron and Auger electron diffraction:

$$G_{00,L_f}^{(N-1)}(\vec{R}_1,\vec{R}_2 \ldots,\vec{R}_N{=}\vec{R}_d) = \sum_{\{\text{paths}\}} \exp\{i(\rho_1+\rho_2+ \ldots +\rho_N)\}/$$
$$(\rho_1\ \rho_2 \cdots \rho_N) \sum_{\{\lambda_i\}} F_{00,\lambda_{N-1}}(\vec{\rho}_N,\vec{\rho}_{N-1}) \cdots$$
$$F_{\lambda_3,\lambda_2}(\vec{\rho}_3,\vec{\rho}_2)\ F_{\lambda_2,\lambda_1}(\vec{\rho}_2,\vec{\rho}_1)\ W_{\lambda_N,\lambda_1}^{00,L_f}(\vec{\rho}_N,\vec{\rho}_1) \qquad (3\text{-}2\text{-}17)$$

where the quantities $F_{\lambda_k,\lambda_{k-1}}(\vec{\rho}_k,\vec{\rho}_{k-1}) = F_{\mu_k\nu_k,\mu_{k-1}\nu_{k-1}}(\vec{\rho}_k,\vec{\rho}_{k-1})$ are termed "scattering amplitude matrices" and are given by

$$F_{\lambda_k,\lambda_{k-1}}(\vec{\rho}_k,\vec{\rho}_{k-1}) = \sum_{L_{k-1}} t_{\ell_{k-1}} \Gamma^{L_k}_{\lambda_k}(\vec{\rho}_k)\, \tilde{\Gamma}^{L_{k-1}}_{\lambda_{k-1}}(\vec{\rho}_{k-1})$$

$$= \sum_{\ell_{k-1}=0}^{\ell_{\max}} t_{\ell_{k-1}} \gamma^{\ell_k}_{\mu_k\nu_k}(\rho_k)\, R^{\ell_k}_{\mu_k\mu_{k-1}}(\hat{\rho}_k,\hat{\rho}_{k-1}) \tilde{\gamma}^{\ell_{k-1}}_{\mu_{k-1}\nu_{k-1}}(\rho_{k-1}), \qquad (3\text{-}2\text{-}18)$$

with the composite rotation matrix $R^{\ell_k}_{\mu_k\mu_{k-1}}(\hat{\rho}_k,\hat{\rho}_{k-1})$ corresponding to a rotation first of $\hat{\rho}_k$ into $\hat{z}$ and then $\hat{z}$ into $\hat{\rho}_{k-1}$. The scattering amplitude matrix $F_{\lambda_k,\lambda_{k-1}}(\vec{\rho}_k,\vec{\rho}_{k-1})$ can thus be thought of as a generalized spherical-wave scattering factor associated with the site at $\vec{R}_{k-1}$ and specific choices of scatterers at $\vec{R}_k$ and $\vec{R}_{k-2}$. A schematic illustration of the separated form for $G^{(N-1)}_{00,L_f}$ is given in Figure 3.1(b).

A "termination matrix" involving the first and last factors in $G^{(N-1)}_{00,L_f}$ is further given by

$$W^{00,L_f}_{\lambda_N,\lambda_1}(\vec{\rho}_N-\vec{\rho}_d,\vec{\rho}_1) = \tilde{\Gamma}^{00}_{\lambda_N}(\vec{\rho}_N-\vec{\rho}_d)\, \Gamma^{L_f}_{\lambda_1}(\vec{\rho}_1). \qquad (3\text{-}2\text{-}19)$$

(Our $W^{00,L_f}_{\lambda_N,\lambda_1}(\vec{\rho}_N,\vec{\rho}_1)$ is equivalent to the $M^{L_f,00}_{\lambda_1,\lambda_N}(\vec{\rho}_1,\vec{\rho}_N)$ used by Rehr and Albers [13].) For photoelectron and Auger electron diffraction, where the detector is at infinity, W can be simplified further via

$$\tilde{\Gamma}^{00}_{\lambda_N}(\vec{\rho}_N) = R^{0}_{\mu_N 0}(\hat{\rho}_N^{-1})\ \tilde{\gamma}^{0}_{\mu_N \nu_N}(\rho_N), \tag{3-2-20}$$

The general result that $R^{\ell}_{\mu 0}(\hat{\rho}^{-1}) = [4\pi/(2\ell+1)]^{1/2}\ Y_{\ell\mu}(\hat{\rho}^{-1})$ [16] indicates that $R^{0}_{\mu 0}(\hat{\rho}^{-1}) = 0$ for all $\mu \neq 0$ and $R^{0}_{\mu 0}(\hat{\rho}^{-1}) = 1$ for $\mu = 0$. Then Equation (3-2-20) becomes,

$$\tilde{\Gamma}^{00}_{\lambda_N}(\vec{\rho}_N) = C_0^{(\nu)}(z)\ z^{\nu} / (N_{00}\ \nu!). \tag{3-2-21}$$

Since the detector is at infinity, $\rho = \vec{\rho}_d \to \infty$, $C_0(\infty) \to 1$, $C_0^{(\nu)}(\infty) = 0$ for all $\nu \neq 0$, and $C_0^{(\nu)}(\infty) = 1$ for $\nu = 0$. Hence from Equations (3-2-20) and (3-2-21), $\tilde{\Gamma}^{00}_{\lambda_N}(\rho_N \to \infty) = 1$, and we have a final generally useful form not discussed previously:

$$W^{00,L_f}_{\lambda_N,\lambda_1}(\vec{\rho}_1) = \Gamma^{L_f}_{\lambda_1}(\vec{\rho}_1) = \gamma^{\ell_f}_{\mu_1\nu_1}(\rho_1)\ R^{\ell_f}_{\mu_1 m_i}(\hat{\rho}_1). \tag{3-2-22}$$

Note that W does not finally depend on the location of the detector through $\vec{\rho}_d$, although it does depend on the orientation of $\hat{\epsilon}$ through the rotation in $R^{\ell_f}_{\mu_1 m_i}(\hat{\rho}_1)$.

3.2.1. The Single-Scattering Intensity in Photoelectron Diffraction:

As a first example of the application of this formalism, we consider the single-scattering intensity $I^{(1)}$ in photoelectron

emission from a general $n_i L_i = (n_i, \ell_i, m_i)$ core sublevel, a case introduced by R-A [13] and also discussed using the R-A approach by Friedman and Fadley [17]. This can be written directly from Equation (3-2-1) for N = 2 as

$$I^{(1)}(\vec{k}, n_i, \ell_i, m_i) \propto \frac{d\sigma}{d\Omega}(n_i, \ell_i, m_i \rightarrow E_{kin}, \vec{k}, \ell_{i\pm1}, m_i)$$
$$\propto \Big| \sum_{L_f=(\ell_{i\pm1}, m_i)} m_{L_f,c}(\hat{\epsilon}) \exp(i\delta^c_{\ell_f}) \times \Big[G^{(0)}_{00,L_f}(\vec{R}_d \rightarrow \infty) + G^{(1)}_{00,L_f}(\vec{R}_j, \vec{R}_d \rightarrow \infty) \Big] \Big|^2 \qquad (3\text{-}2\text{-}23)$$

with the emitter as usual at the origin, $\vec{\rho}_j = k\vec{R}_j$, $\vec{\rho}_d = k\vec{R}_d$ in the first or direct wave term and $\vec{\rho}_d = k(\vec{R}_d - \vec{R}_j)$ in the second or scattered wave term.

$G^{(1)}_{00,L_f}$ must involve a sum over all single-scattering path choices of j = 1,2, ... ,M, where M is the number of single-scattering centers at positions $\vec{R}_1$, $\vec{R}_2$, ... ,$\vec{R}_M$. ($\vec{R}_1$, $\vec{R}_2$,.... here thus have a slightly different meaning from the general-path $\vec{R}_i$'s in Equation (3-2-1) and Figure 3.1.) The first sum on $G^{(0)}_{00,L_f}(\vec{R}_d)$ thus represents what can be termed the "direct" or "unscattered" wave ϕ_0, and the second sum on $G^{(1)}_{00,L_f}$ represents all of the singly scattered waves ϕ_j. Since a non-s core level will, in general, have $(2\ell_i+1)$ degenerate sublevels, the final intensity observed must sum over emission from them to yield

$$I^{(1)}_{n_i\ell_i}(\vec{k}) \propto \frac{d\sigma_{n_i\ell_i}(\vec{k})}{d\Omega} - \sum_{m_i=-\ell_i}^{\ell_i} \frac{d\sigma}{d\Omega}(n_i,\ell_i,m_i \rightarrow E_{kin},\vec{k},\ell_{i\pm1},m_i). \quad (3\text{-}2\text{-}24)$$

For the $\ell_f = \ell_i - 1$ channel, there will only be $2(\ell_i-1) + 1$ terms in this sum. For the $\ell_f = \ell_i + 1$ channel, $(2\ell_i+1)$ terms must be included.

First we concentrate on the direct-wave which is represented by the Green's function $G^{(0)}_{00,L_f}(\vec{R}_d)$. From Equations (3-2-8) and (3-2-9), it is a simple matter to show that [15,16]:

$$G^{(0)}_{00,L_f}(\vec{R}_d) = [\exp\{i\rho_d\}/\rho_d]\ (4\pi)^{1/2}\ Y_{\ell_f m_i}(\theta_k,\phi_k), \quad (3\text{-}2\text{-}25)$$

where (θ_k,ϕ_k) are the angles of $\vec{k}$ (or $\vec{R}_d$) measured with respect to the polarization vector $\hat{\epsilon}$ as the z axis.

The single-scattering Green's function, $G^{(1)}_{00,L_f}(\vec{R}_j,\vec{R}_d)$, can now be expressed, using Equation (3-2-8), as follows:

$$G^{(1)}_{00,L_f}(\vec{R}_j,\vec{R}_d) = \sum_{\{j\},\{L_j\}} G_{00,L_j}(\vec{\rho}_d)\ t_{\ell_j}(\vec{R}_j)\ G_{L_j,L_f}(\vec{\rho}_j). \quad (3\text{-}2\text{-}26)$$

Now using Equations (3-2-9) and (3-2-10), one gets the following final expression for $G^{(1)}_{00,L_f}$:

$$G^{(1)}_{00,L_f}(\vec{R}_j,\vec{R}_d) = \sum_{\{j\},\{L_j\}} [\exp\{i\rho_d\}/\rho_d] \sum_{\mu'} R^0_{0\mu'}(\hat{\rho}_d^{-1})$$
$$\times \left[\sum_{\nu'=0}^{[0,\ell_j-|\mu'|]} \tilde{\gamma}^0_{\mu'\nu'}(\rho_d)\ \gamma^{\ell_j}_{\mu'\nu'}(\rho_d)\right]$$
$$\times R^{\ell_j}_{\mu' m_j}(\hat{\rho}_d)\ t_{\ell_j}(\vec{R}_j)\ [\exp\{i\rho_j\}/\rho_j] \sum_{\mu''} R^{\ell_j}_{m_j\mu''}(\hat{\rho}_j^{-1})$$
$$\times \left[\sum_{\nu''=0}^{[0,\ell_j-|\mu''|]} \tilde{\gamma}^{\ell_j}_{\mu''\nu''}(\rho_j)\ \gamma^{\ell_f}_{\mu''\nu''}(\rho_j)\right] R^{\ell_f}_{\mu'' m_i}(\hat{\rho}_j). \qquad (3\text{-}2\text{-}27)$$

Another useful simplification arises since $\vec{R}_d \gg \vec{R}_j$: if θ_j is the single scattering angle at site j, the exponentials in Equation (3-2-27) can be written as $\exp\{i\rho_d\}\exp\{i\rho_j\} = \exp\{i(k|\vec{R}_d| - \rho_j\cos\theta_j + \rho_j)\} = \exp\{ik|\vec{R}_d|\}\exp\{i\rho_j(1-\cos\theta_j)\} = \exp\{i\rho_d\}\exp\{i\rho_j(1-\cos\theta_j)\}$, with $\rho_d = k|\vec{R}_d|$ now defined as in the direct wave case considered earlier. $\rho_j(1-\cos\theta_j)$ is thus simply the phase difference between the direct wave and the j^{th} scattered wave as caused by the path length difference $|\vec{R}_j|(1-\cos\theta_j)$, and it appears directly in numerous prior discussions of the theory of photoelectron diffraction [1-3]. Equation (3-2-27) can thus be written as

$$G^{(1)}_{00,L_f}(\vec{R}_j,\vec{R}_d) = [\exp\{i\rho_d\}/\rho_d] \sum_{j,\{L_j\}} [\exp\{i\rho_j(1-\cos\theta_j)\}/\rho_j]$$
$$\times \sum_{\lambda'\lambda''} R^0_{0\mu'}(\hat{\rho}_d^{-1})\ \tilde{\gamma}^0_{\lambda'}(\rho_d)\ t_{\ell_j}(\vec{R}_j)\ \gamma^{\ell_j}_{\lambda'}(\rho_d)\ R^{\ell_j}_{\mu' m_j}(\hat{\rho}_d)\ R^{\ell_j}_{m_j\mu''}(\hat{\rho}_j^{-1})$$
$$\times \tilde{\gamma}^{\ell_j}_{\lambda''}(\rho_j)\ \gamma^{\ell_f}_{\lambda''}(\rho_j)\ R^{\ell_f}_{\mu'' m_i}(\hat{\rho}_j). \qquad (3\text{-}2\text{-}28)$$

By considering explicit sums on ℓ_j and m_j and by realizing that $R^0_{0\mu'}(\alpha,\beta,\gamma) = (4\pi)^{1/2}\, Y_{0\mu'}(\beta,\gamma)$ is defined only when $\mu'=0$, one can simplify this expression. The facts that $\gamma^0_{0\nu'}(\rho_d) = C_0^{\nu'}(z_d)\, z_d^{\nu'} / \nu'!$ (cf. Equation (3-2-11)) and $C_0(z_d) = 1$ imply that $\gamma^0_{0\nu'}(\rho_d) \neq 0$ only when $\nu' \neq 0$. This makes $\nu' = 0$ the only surviving term in that summation. Hence $\lambda' = (\mu',\nu') = (0,0)$ for single-scattering. This makes $R^0_{00}(\hat{\rho}_d) = 1.0$ and $\tilde{\gamma}^0_{00}(\rho_d) = 1.0$ and we have

$$G^{(1)}_{00,L_f}(\vec{R}_j,\vec{R}_d) = [\exp\{i\rho_d\}/\rho_d] \sum_j [\exp\{i\rho_j(1-\cos\theta_j)\}/\rho_j]$$
$$\times \sum_{\ell_j} t_{\ell_j}(\vec{R}_j)\, \gamma^{\ell_j}_{00}(\rho_d) \sum_{\lambda''} R^{\ell_j}_{0\mu''}(\hat{\rho}_d,\hat{\rho}_j^{-1})\, \tilde{\gamma}^{\ell_j}_{\lambda''}(\rho_j)$$
$$\times \gamma^{\ell_f}_{\lambda''}(\rho_j)\, R^{\ell_f}_{\mu''m_i}(\hat{\rho}_j). \qquad (3\text{-}2\text{-}29)$$

Equation (3-2-29) becomes in the alternate notation of F's and W's introduced before:

$$G^{(1)}_{00,L_f}(\vec{R}_j,\vec{R}_d) = [\exp\{i\rho_d\}/\rho_d] \sum_j [\exp\{i\rho_j(1-\cos\theta_j)\}/\rho_j]$$
$$\times \sum_{\lambda''} F_{00,\lambda''}(\vec{\rho}_d,\vec{\rho}_j)\, W^{00,L_f}_{00,\lambda''}(\vec{\rho}_j) \qquad (3\text{-}2\text{-}30a)$$

where Equation (3-2-18) gives

$$F_{00,\lambda''}(\vec{\rho}_d,\vec{\rho}_j) = \sum_{\ell=0}^{\ell_{max}} t_\ell(\vec{R}_j)\ \gamma_{00}^{\ell}(\rho_d)\ R_{0\mu''}^{\ell}(\hat{\rho}_d,\hat{\rho}_j^{-1})\ \tilde{\gamma}_{\lambda''}^{\ell}(\rho_j), \quad (3\text{-}2\text{-}30b)$$

and Equation (3-2-22) gives,

$$W_{00,\lambda''}^{00,L_f}(\vec{\rho}_j) = \gamma_{\lambda''}^{\ell_f}(\rho_j)\ R_{\mu''m_i}^{\ell_f}(\hat{\rho}_j). \quad (3\text{-}2\text{-}30c)$$

As an interesting special case of this single-scattering result, the total intensity for emission into a <u>single</u> final state $L_f=(\ell_f,m_f)$ is thus:

$$I_{L_f}^{(1)}(k,\theta,\phi) \propto \Big| (-i)^{\ell_f} \exp(i\delta_{\ell_f}^{c})\ R_{\ell_f}(E_{kin})\ \langle \ell_f m_i | 10 | \ell_i m_i \rangle \times \left[G_{00,L_f}^{(0)}(\vec{R}_d) + G_{00,L_f}^{(1)}(\vec{R}_j,\vec{R}_d) \right] \Big|^2, \quad (3\text{-}2\text{-}31)$$

where we have now let $\theta_k = \theta_d \rightarrow \theta$ and $\phi_k = \phi_d \rightarrow \phi$ for simplicity. We have also cancelled out a trivial factor of $\exp\{-i\rho_d\}\ \exp\{i\rho_d\}/\rho_d^{\,2} = \rho_d^{-2}$ that simply allows for the spherical-wave character of the outgoing flux. Examples of such single final states would be the p-wave final state in s ($L_i = (0,0)$) photoelectron emission to p ($L_f = (1,0)$) (noting again that we take $\hat{\epsilon} \parallel \hat{z}$) and the often used s-wave final state approximation for Auger electron emission ($L_f = (0,0)$). For such cases, the excitation matrix elements and phase shifts in Equation (3-2-31) can simply be omitted, as they yield only constant factors in the intensity.

In a more general case such as p-wave initial state photoemission into s- and d-wave final states, one has to add final amplitudes with correct relative phases and to sum over the various m_i excitations possible. In general, the final intensity in this case can be written with Equation (3-2-24) as

$$I^{(1)}_{n_i\ell_i}(k,\theta,\phi) \propto \sum_{m_i} \Big| \sum_{\ell_f}^{\ell_i\pm1} (-i)^{\ell_f} \exp(i\delta^c_{\ell_f}) R_{\ell_f}(E_{kin}) \langle \ell_f m_i | 10 | \ell_i m_i \rangle \times [G^{(0)}_{00,L_f}(\vec{R}_d) + G^{(1)}_{00,L_f}(\vec{R}_j,\vec{R}_d)] \Big|^2. \qquad (3\text{-}2\text{-}32)$$

The explicit form of Equation (3-2-32) is

$$I^{(1)}_{n_i\ell_i}(k,\theta,\phi) \propto \sum_{m_i} \Big| \sum_{\ell_f}^{\ell_i\pm1} (-i)^{\ell_f} \exp(i\delta^c_{\ell_f}) R_{\ell_f}(E_{kin}) \langle \ell_f m_i | 10 | \ell_i m_i \rangle \times \Big[(4\pi)^{1/2} Y_{\ell_f m_i}(\theta,\phi) + \sum_{j=1}^{M} [\exp\{i\rho_j(1-\cos\theta_j)\}/\rho_j] \times \sum_{\lambda''} F_{00,\lambda''}(\vec{\rho}_d,\vec{\rho}_j) W^{00,L_f}_{00,\lambda''}(\vec{\rho}_j) \Big]^2. \qquad (3\text{-}2\text{-}33)$$

which is a generalization to non-s emission of the equivalent Equation (26) in Reference 13.

We also note that W is dependent only on the initial (L_f = (ℓ_f,m_f)) and final ($L_d = L_N = (0,0)$) states. Thus only one set of W's has to be calculated for a given L_f channel, whether the event considered passes through a single or a multiple scattering path.

The range of the index ν is given in Equation (3-2-10): 0 to $\min[\ell,\ell'-|\mu|]$. So far we have not imposed restrictions on the summation index μ. The dependence of the coefficients $\tilde{\gamma}_{\mu\nu}(\rho)$ and $\gamma_{\mu\nu}(\rho)$ on ρ implies that $F_{\lambda\lambda'}(\vec{\rho},\vec{\rho}') \propto (\rho)^{-(2\nu+\mu)} (\rho')^{-(2\nu'+\mu')}$ for large ρ and ρ' [13]. $\rho_j = kR_j$ is generally greater than unity, even for the smallest bond lengths, since nearest neighbor distances are always several atomic units and k for excitation above threshold is greater than the Fermi momentum k_f (≈ 1.0 in atomic units). This suggests the possibility of truncating the summations on μ and ν, and we now consider several levels for doing this. Keeping only the largest matrix element yields the effective curved-wave scatttering amplitude $F^{(0)}_{00,00}$ for point scattering (a result that is zeroth order in $1/\rho$) and a (1×1) matrix. Going beyond this requires recalling the restrictions on (μ,ν) set by prior definitions:

$$|\mu| \leq \ell, \tag{3-2-34a}$$

with $\ell = 0,1,2, \ldots \ell_{max}$ unless otherwise restricted at path termination points or by the following relations:

$$\nu \geq 0, \tag{3-2-34b}$$

$$\nu + |\mu| \leq \ell. \tag{3-2-34c}$$

A calculation that is first order in $1/\rho$ for large ρ can thus contain only non-zero terms corresponding to $(\mu,\nu) = (0,1)$, $(+1,0)$ and $(-1,0)$,

leading to a (3×3) symmetric matrix for $F^{(1)}_{\lambda\lambda'}$ whose elements are given in single scattering by Equation (3-2-30b). Going to second order in $1/\rho$ permits including the additional non-zero (μ,ν) = (0,1), (2,0) and (-2,0) to yield a symmetric (6×6) matrix whose elements are again given by Equation (3-2-30b).

We have gone only up to the second order in $1/\rho$ in all of calculations described here, because prior work by both Rehr and Albers [13] for x-ray absorption fine structure and by Bullock [18] for single scattering photoelectron diffraction has demonstrated that this level of approximation should be fully adequate, especially for energies above about 100 eV. As one example of these tests, single scattering calculations by Bullock [18] shown in Figure 3.2 involve the fictitious case of f emission from one atom in a two-atom chain with single Cu scatterer. The case of f emission into a single final g channel was selected to represent a more stringent convergence test. The wave vector $\vec{k}$ is kept parallel to the radiation polarization vector, as shown in the inset. At 100.0 eV the difference between the zeroth and second order approximation is noticeable over the whole range of the scattering angle. However, the second and eighth order curves are within a few % of one another over the whole range. In fact the only minor differences between the second and eighth orders occur for energies of ~300 eV or less and for angles $\leq 30^{\circ}$ that are near the forward-scattering cone. At 1000.0 eV, which represents a typical x-ray photoelectron diffraction (XPD) kinetic energy, the second and eighth orders are identical. Overall, we thus believe that

the second-order R-A method is fully adequate for work from 50-100 eV upward.

3.2.2. The Multiple-Scattering Intensity for a General Initial State:

We here discuss emission from a general $L_i = (\ell_i, m_i)$ initial state to a set of general final states, but with the important addition that multiple-scattering paths of arbitrary order are considered. The direct wave in this case is identical to that given in Equation (3-2-25). A multiple-scattering path contains the emitter and more than one scatterer, and a typical path is shown in Figure 3.1. Our notation for the various vectors needed to unambiguously describe a complete set of multiple-scattering paths will be more explicit than that of R-A, although we will remain as close to it as possible. Specifically, the emitter is still taken to be at $\vec{R}_0 = 0$, with the vectors of all other scatterers $\vec{R}_j$ and the detector $\vec{R}_d$ being measured with respect to the emitter. We will now increment the meaning of N by unity so that it now represents the order of the scattering (rather than (N-1) as before), so that a typical path is now $\vec{R}_0, \vec{R}_1, \vec{R}_2 \ldots \vec{R}_N, \vec{R}_{N+1} = \vec{R}_d$. In order to keep track of a given scatterer in a typical path, we will designate all possible first scatterers by $\vec{R}_{j_1}$, all possible second scatterers by $\vec{R}_{j_2}$, etc., up to a general k^{th} order $\vec{R}_{j_k}$. The vector used in the arguments of the F and W matrices we can then calculate from $\vec{\rho}_{j_k j_{k-1}} = k(\vec{R}_{j_k} - \vec{R}_{j_{k-1}})$, with two indices now required due to the many paths involved. For the

first step in a path, this is simply $\vec{\rho}_{j_1} = k\vec{R}_{j_1} = \vec{\rho}_j$, as in the single-scattering discussion of the prior section. For the last step in any N-event path, $\vec{\rho}_{d,j_N} = k(\vec{R}_d - \vec{R}_{j_N}) \simeq \vec{\rho}_d$ for simplicity, since this vector always points from the last scatterer to the detector at ∞. In multiple-scattering, there may be several consecutive scattering events, including those in which the photoelectron is scattered off the emitter at some point after a first scattering event on another site. In this case, we will treat the emitter as a neutral atom, even though it contains a core hole. The presence of this core hole could affect the phase shifts $\delta_\ell(\vec{R}_0)$ somewhat, but final state screening is expected to reduce this effect, so we have chosen to ignore it here. (In any case, our computer code is flexible enough to permit using different δ_ℓ's for the emitter if desired). The restriction on $\vec{\rho}_{j_k j_{k-1}}$ is that $j_k \neq j_{k-1}$ for all k: that is, the photoelectron cannot be scattered off the same atom twice in a row. In this notation, j_k can represent any atom of the M atoms in the cluster, including the emitter. The summations in any of the multiple-scattering paths to follow will thus at each step be over (M-1) j_k values at each order in a path, with the restriction that $j_k \neq j_{k-1}$ for all k. We will not write this restriction explicitly in equations, but indicate such sums only with the set of indices $\{j_i\}$.

The N^{th} order multiple-scattering Green's function in photoemission to a unique state $L_f = (\ell_f, m_i)$, can now be written in the revised notation from Equation (3-2-8) as,

$$G^{(N)}_{00,L_f}(\vec{R}_{j_1},\vec{R}_{j_2},\ \ldots\ ,\vec{R}_{j_N},\vec{R}_d) =$$

$$\sum_{\{j_i\},\{L_i\}} G_{00,L_N}(\hat{\rho}_d)\ t_{\ell_N}(\vec{R}_{j_N})\ G_{L_NL_{N-1}}(\hat{\rho}_{j_Nj_{N-1}})\ldots\ldots\ldots$$

$$\ldots\ t_{\ell_2}(\vec{R}_{j_2})\ G_{L_2L_1}(\hat{\rho}_{j_2j_1})\ t_{\ell_1}(\vec{R}_{j_1})\ G_{L_1L_f}(\hat{\rho}_{j_1}). \qquad (3\text{-}2\text{-}35)$$

This general Green's function can now be written in terms of the prior W and F matrices.

The steps leading to a specific evaluation of this $G^{(N)}_{00,L_f}$ are very similar to those shown in detail for the single-scattering cases. Therefore, we will omit details here and directly write from Equations (3-2-17) and (3-2-35):

$$G^{(N)}_{00,L_f}(\vec{R}_{j_1},\vec{R}_{j_2},\ \ldots\ ,\vec{R}_{j_N},\vec{R}_d) =$$

$$\sum_{\{j_i\}} [\exp\{i\rho_d+\rho_{j_Nj_{N-1}}+\ldots+\rho_{j_1}\}/(\rho_d\ \rho_{j_Nj_{N-1}}\ldots\rho_{j_1})]$$

$$\times \sum_{\{\lambda_i\}} F_{00,\lambda_N}(\vec{\rho}_d,\vec{\rho}_{j_Nj_{N-1}})\ F_{\lambda_N\lambda_{N-1}}(\vec{\rho}_{j_Nj_{N-1}},\vec{\rho}_{j_{N-1}j_{N-2}})\ldots.$$

$$\ldots\ldots\ F_{\lambda_2\lambda_1}(\vec{\rho}_{j_2j_1},\vec{\rho}_{j_1})\ W^{00,L_f}_{00,\lambda_1}(\vec{\rho}_{j_1}). \qquad (3\text{-}2\text{-}36)$$

First we consider the exponential prefactors involving path length differences and thus containing all of the structural information. These can be written in terms of two angles. The notation we use for these angles is as follows:

$$\theta_{j_k j_{k-1}} = \text{angle between vectors } \hat{\rho}_{j_{k+1} j_k} \text{ and } \hat{\rho}_{j_k j_{k-1}}, \qquad (3\text{-}2\text{-}37a)$$

which is the true scattering angle for the event at $\vec{R}_{j_k}$, and

$$\theta'_{j_k j_{k-1}} = \text{angle between vectors } \hat{\rho}_d \text{ and } \hat{\rho}_{j_k j_{k-1}}, \qquad (3\text{-}2\text{-}37b)$$

which is the angle required for calculating the path length difference along $\hat{\rho}_{j_k j_{k-1}}$ leading to the event at $\vec{R}_{j_k}$. Then, by repeated usage of the argument used to obtain Equation (3-2-28), we can show that

$$\exp\{i\rho_d + \rho_{j_N j_{N-1}} + \ldots + \rho_{j_1}\} \,/\, (\rho_d\, \rho_{j_N j_{N-1}} \ldots \rho_{j_1}) =$$
$$(\exp\{i\rho_d\}/\rho_d) \prod_{k=1}^{N} [\exp\{i\rho_{j_k j_{k-1}} (1-\cos\theta'_{j_k j_{k-1}})/\rho_{j_k j_{k-1}}]. \qquad (3\text{-}2\text{-}37c)$$

After the last scattering event, the photoelectron escapes towards the detector. This last event, or the first event in a time reversed sense, involves a finite and an infinite distance and is represented by $F_{00,\lambda_N}(\vec{\rho}_d, \vec{\rho}_{j_N j_{N-1}})$. This F matrix is identical in structure to the one we worked out in the single-scattering case. Also, the W matrix as defined in Equation (3-2-30) depends only on the polarization of the incoming radiation and the position of the first scatterer relative to the emitter; thus it does not require any modification either. The only other factors left to calculate are the matrices $F_{\lambda_k \lambda_{k-1}}(\vec{\rho}_{j_k j_{k-1}}, \vec{\rho}_{j_{k-1} j_{k-2}})$ involving two finite distances.

The general form of these is identical to that given in Equation (3-2-18).

Thus we have finally,

$$G^{(N)}_{00,L_f}(\vec{R}_{j_1},\vec{R}_{j_2},\ \ldots\ ,\vec{R}_{j_N},\vec{R}_d) =$$

$$(\exp\{i\rho_d\}/\rho_d) \sum_{\{j_i\}} \Big[\prod_{k=1}^{N} [\exp\{i\rho_{j_k j_{k-1}}(1-\cos\theta'_{j_k j_{k-1}})\}/\rho_{j_k j_{k-1}}]$$

$$\times \sum_{\{\lambda_i\}} F_{00,\lambda_N}(\vec{\rho}_d,\vec{\rho}_{j_N j_{N-1}})\ F_{\lambda_N\lambda_{N-1}}(\vec{\rho}_{j_N j_{N-1}},\vec{\rho}_{j_{N-1} j_{N-2}}) \cdots\cdots$$

$$\times F_{\lambda_2\lambda_1}(\vec{\rho}_{j_2 j_1},\vec{\rho}_{j_1})\ W^{00,L_f}_{00,\lambda_1}(\vec{\rho}_{j_1})\Big] \qquad (3\text{-}2\text{-}38)$$

where,

$$F_{00,\lambda_N}(\vec{\rho}_d,\vec{\rho}_{j_N j_{N-1}}) = \sum_{\ell} t_\ell\ \gamma^{\ell}_{00}(\rho_d)\ R^{\ell}_{0\mu_N}(\hat{\rho}_d,\hat{\rho}^{-1}_{j_N j_{N-1}})\ \tilde{\gamma}^{\ell}_{\lambda_N}(\rho_{j_N j_{N-1}}),$$

$$F_{\lambda_k,\lambda_{k-1}}(\vec{\rho}_{j_k j_{k-1}},\vec{\rho}_{j_{k-1} j_{k-2}}) =$$

$$\sum_{\ell_{k-1}=0}^{\ell_{\max}} t_{\ell_{k-1}}\ \gamma^{\ell_k}_{\lambda_k}(\rho_{j_k j_{k-1}})\ R^{\ell_k}_{\mu_k\mu_{k-1}}(\hat{\rho}_{j_k j_{k-1}},\hat{\rho}^{-1}_{j_{k-1} j_{k-2}})\ \tilde{\gamma}^{\ell_{k-1}}_{\lambda_{k-1}}(\rho_{j_{k-1} j_{k-2}}),$$

and,

$$W^{00,L_f}_{00,\lambda_1}(\vec{\rho}_{j_1}) = \gamma^{\ell_f}_{\lambda_1}(\rho_{j_1})\ R^{\ell_f}_{\mu_1 m_i}(\hat{\rho}_{j_1}).$$

As a specific example of applying this result, we write it out explicitly for fifth-order multiple-scattering:

$$
\begin{aligned}
G^{(5)}_{00,L_f}(\vec{R}_{j_1},\vec{R}_{j_2},\vec{R}_{j_3},\vec{R}_{j_4},\vec{R}_{j_5},\vec{R}_d) = \\
= (\exp\{i\rho_d\}/\rho_d) \sum_{\{j_i\}} \Big[[\exp\{i\rho_{j_1}(1-\cos\theta'_{j_1})\}/\rho_{j_1}] \\
\times [\exp\{i\rho_{j_2j_1}(1-\cos\theta'_{j_2j_1})\}/\rho_{j_2j_1}] \; [\exp\{i\rho_{j_3j_2}(1-\cos\theta'_{j_3j_2})\}/\rho_{j_3j_2}] \\
\times [\exp\{i\rho_{j_4j_3}(1-\cos\theta'_{j_4j_3})\}/\rho_{j_4j_3}] \; [\exp\{i\rho_{j_5j_4}(1-\cos\theta'_{j_5j_4})\}/\rho_{j_5j_4}] \\
\times F_{00,\lambda_5}(\vec{\rho}_d,\vec{\rho}_{j_5j_4}) \; F_{\lambda_5\lambda_4}(\vec{\rho}_{j_5j_4},\vec{\rho}_{j_4j_3}) \; F_{\lambda_4\lambda_3}(\vec{\rho}_{j_4j_3},\vec{\rho}_{j_3j_2}) \\
\times F_{\lambda_3\lambda_2}(\vec{\rho}_{j_3j_2},\vec{\rho}_{j_2j_1}) \; F_{\lambda_2\lambda_1}(\vec{\rho}_{j_2j_1},\vec{\rho}_{j_1}) \; W^{00,L_f}_{00,\lambda_1}(\vec{\rho}_{j_1}) \Big]. \qquad (3\text{-}2\text{-}39)
\end{aligned}
$$

In some of our numerical simulations involving small clusters of ≤ 40 atoms, we have used equivalent expressions upto tenth-order multiple scattering.

The overall expression for the intensity for a single final-state $L_f = (\ell_f, m_i)$ is thus

$$
\begin{aligned}
I^{(N_{max})}_{L_f}(k,\theta,\phi) \propto \sum_{m_i} \Big| \Big[G^{(0)}_{00,\ell_f m_i}(\vec{R}_d) + G^{(1)}_{00,\ell_f m_i}(\vec{R}_{j_1},\vec{R}_d) + \\
\sum_{N=2}^{N_{max}} G^{(N)}_{00,\ell_f m_i}(\vec{R}_{j_1},\vec{R}_{j_2},\ \ldots\ ,\vec{R}_{j_N},\vec{R}_d) \Big] \Big|^2. \qquad (3\text{-}2\text{-}40)
\end{aligned}
$$

On the right hand side, the first term represents the direct wave, the second the singly-scattered waves and the final summation the multiply-scattered waves up to a maximum order of N_{max} (≤ 10 in this work).

For emission from all of the initial magnetic sublevels $\ell_i m_i$ into two final state chanels $\ell_f = \ell_i \pm 1, m_i$ we have the fully general result

$$I_{n_i\ell_i}^{(N_{max})}(k,\theta,\phi) \propto \sum_{m_i} \left| \sum_{\ell_f}^{\ell_i \pm 1} (-i)^{\ell_f} \exp(i\delta_{\ell_f}^{c}) R_{\ell_f}(E_{kin}) \langle \ell_f m_i | 10 | \ell_i m_i \rangle \right.$$
$$\times [G_{00,\ell_f m_i}^{(0)}(\vec{R}_d) + G_{00,\ell_f m_i}^{(1)}(R_{j_1},\vec{R}_d) +$$
$$\left. \sum_{N=2}^{N_{max}} G_{00,\ell_f m_i}^{(N)}(\vec{R}_{j_1},\vec{R}_{j_2}, \ldots ,\vec{R}_{j_N},\vec{R}_d)] \right|^2. \quad (3\text{-}2\text{-}41)$$

Equation (3-2-41) can be written more explicitly as,

$$I_{n_i\ell_i}^{(N_{max})}(k,\theta,\phi) \propto \sum_{m_i} \left| \sum_{\ell_f}^{\ell \pm 1} (-i)^{\ell_f} \exp(i\delta_{\ell_f}^{c}) R_{\ell_f}(E_{kin}) \langle \ell_f m_i | 10 | \ell_i m_i \rangle \right.$$
$$\times \left[(4\pi)^{1/2} Y_{\ell_f m_i}(\theta) + \right.$$
$$\sum_{j_1} [\exp\{i\rho_{j_1}(1-\cos\theta_{j_1})\}/\rho_{j_1}] \sum_{\lambda_1} F_{00,\lambda_1}(\vec{\rho}_d,\vec{\rho}_{j_1})\, W_{00,\lambda_1}^{00,L_f}(\vec{\rho}_{j_1}) +$$
$$\left. \sum_{N=2}^{N_{max}} \sum_{\{j_i\}} \left[\prod_{k=1}^{N} [\exp\{i\rho_{j_k j_{k-1}}(1-\cos\theta'_{j_k j_{k-1}})\}/\rho_{j_k j_{k-1}}] \right. \right.$$

$$\times \sum_{\{\lambda_i\}} F_{00,\lambda_N}(\vec{\rho}_d,\vec{\rho}_{j_N j_{N-1}})\, F_{\lambda_N\lambda_{N-1}}(\vec{\rho}_{j_N j_{N-1}},\vec{\rho}_{j_{N-1} j_{N-2}})\cdots\cdots$$

$$\cdots\cdots\cdots F_{\lambda_2\lambda_1}(\vec{\rho}_{j_2 j_1},\vec{\rho}_{j_1})\, W^{00,L_f}_{00,\lambda_1}(\vec{\rho}_{j_1})\Big]\Big|^2, \qquad (3\text{-}2\text{-}42)$$

where F_{00,λ_N}, $F_{\lambda_k\lambda_{k-1}}$, and $W^{00,L_f}_{00,\lambda_1}$ are given with Equation (3-2-38).

3.2.3. Inclusion of Inelastic Scattering, Vibrational Effects, Instrumental Angular Averaging, Unpolarized Radiation and Auger Emission:

We now consider the inclusion of several additional effects that are essential for a quantitative comparison of theory and experiment: damping due to inelastic scattering, damping due to vibrational effects, intrumental angular averaging, the possible use of unpolarized radiation, and the treatment of Auger emission.

A fully rigorous method for including inelestic attenuation is so far not available, and thus we use the common phenomenological approach of an exponential decay of the amplititude of each component of the photoelectron wave with the distance travelled in the solid before escaping through the "surface" [1,3]. The surface here is a plane used to define both the cutoff of inelastic scattering and the location of possible refraction effects due to the inner potential V_0 (as discussed below). If the distance travelled along a given path is L and the inelastic attenuation length for photoelectron <u>intensity</u> is Λ_e, then the exponential decay factor for the <u>amplitude</u> is $\exp\{-L/2\Lambda_e\}$

[1,3]. If we define $\vec{R}_{0S}$ as the vector from the emitter to the surface in the direction of $\vec{k}$, $\vec{R}_{j_k j_{k-1}} = \vec{R}_{j_k} - \vec{R}_{j_{k-1}} = \vec{\rho}_{j_k j_{k-1}}/k$, and $\vec{R}_{j_N S}$ as the vector from atom j_N to the surface in the direction of $\vec{k}$ (see Figure 3.1(c)), such factors can be incorporated into Equation (3-2-42) to yield:

$$
\begin{aligned}
I^{(N_{max})}_{n_i \ell_i}(k,\theta,\phi) \;\alpha\; & \sum_{m_i} \Big| \sum_{\ell_f} (-i)^{\ell_f} \exp(i\delta^c_{\ell_f})\, R_{\ell_f}(E_{kin}) \,\langle \ell_f m_i \; 10 | \ell_i m_i \rangle \\
\times \Big[& (4\pi)^{1/2}\, Y_{\ell_f m_i}(\theta)\, \exp\{-|\vec{R}_{0S}|/2\Lambda_e\} + \\
& \sum_{j_1} [\exp\{i\rho_{j_1}(1-\cos\theta_{j_1})\}/\rho_{j_1}]\, \exp\{-|\vec{R}_{j_1 S}|/2\Lambda_e\}\, \exp\{-|\vec{R}_{j_1}|/2\Lambda_e\} \\
& \times \sum_{\lambda_1} F_{00,\lambda_1}(\vec{\rho}_d, \vec{\rho}_{j_1})\, W^{00,L_f}_{00,\lambda_1}(\vec{\rho}_{j_1}) + \\
& \sum_{N=2}^{N_{max}} \sum_{\{j_i\}} \Big[\prod_{k=1}^{N} [\exp\{i\rho_{j_k j_{k-1}}(1-\cos\theta'_{j_k j_{k-1}})\}/\rho_{j_k j_{k-1}}]\, \exp\{-|\vec{R}_{j_N S}|/2\Lambda_e\} \\
& \times \exp\{-|\vec{R}_{j_N j_{N-1}}|/2\Lambda_e\} \,..\, \exp\{-|\vec{R}_{j_2 j_1}|/2\Lambda_e\}\, \exp\{-|\vec{R}_{j_1}|/2\Lambda_e\} \\
& \times \sum_{\{\lambda_i\}} F_{00,\lambda_N}(\vec{\rho}_d, \vec{\rho}_{j_N j_{N-1}})\, F_{\lambda_N \lambda_{N-1}}(\vec{\rho}_{j_N j_{N-1}}, \vec{\rho}_{j_{N-1} j_{N-2}}) \,..... \\
& \qquad ..... F_{\lambda_2 \lambda_1}(\vec{\rho}_{j_2 j_1}, \vec{\rho}_{j_1})\, W^{00,L_f}_{00,\lambda_1}(\vec{\rho}_{j_1}) \Big] \Big]\Big|^2 . \qquad (3\text{-}2\text{-}43)
\end{aligned}
$$

Thermal vibrations can be treated most simply in an isotropic uncorrelated fashion, although anisotropic correlated vibrations are a more accurate description for the more important near-neighbor scatterers [3,7]. There is no generally applicable yet accurate model

for including both anisotropy and correlation in single or multiple scattering calculations, although different methods for approximating these effects have been discussed previously by Sagurton et al. [3] and by Barton et al. [7].

In the simplest case of isotropic uncorrelated vibrations, inclusion of them in Equation (3-2-43) can be effected by multiplying each scattered amplitude by a simple Debye-Waller factor $W^{uc}_{j_k}$ representing the motion of a given scatterer j_k; if $\Delta\vec{k}_{j_k j_{k-1}}$ is the change in $\vec{k}$ on scattering at the j_k^{th} atom, $\theta_{j_k j_{k-1}}$ is the scattering angle defined in equation (3-2-37(a)) and $\overline{U^2_{j_k}}$ is the absolute mean square displacement of the j_k^{th} atom, this simple uncorrelated Debye-Waller factor is given by [3]

$$W^{uc}_{j_k} = \exp\{-\Delta k^2_{j_k j_{k-1}} \overline{U^2_{j_k}}\} = \exp\{-2k^2(1-\cos\theta_{j_k j_{k-1}})\, \overline{U^2_{j_k}}\}. \qquad (3\text{-}2\text{-}44)$$

But for correlated vibrations, this factor is expected to depend on the distance between the present scatterer and the previous scatterer. We represent this by $W^{c}_{j_k j_{k-1}}$. When the distance between the present and the previous scatterer is large enough, $W^{c}_{j_k j_{k-1}}$ will approach the uncorrelated $W^{uc}_{j_k}$. But in general, it will depend on the displacement of atom j_k relative to the previous scatterer, which we denote by $\vec{U}_{j_k j_{k-1}}$. (The displacement relative to the emitter may also play a role, but we will here simplify the problem by neglecting it.) With

the definition of the effective mean square displacement with thermal averaging (indicated by $\langle\cdots\rangle$) of $\sigma^2_{j_k j_{k-1}} = \langle(\Delta\hat{k}_{j_k j_{k-1}} \cdot \vec{U}_{j_k j_{k-1}})\rangle$, the equivalent correlated Debye-Waller-type attenuation factor is given by [3]:

$$W^c_{j_k j_{k-1}} = \langle\exp(-i\Delta\vec{k}_{j_k j_{k-1}} \cdot \vec{U}_{j_k j_{k-1}})\rangle = \exp(-1/2\langle(\Delta\vec{k}_{j_k j_{k-1}} \cdot \vec{U}_{j_k j_{k-1}})^2\rangle)$$
$$= \exp(-1/2(\Delta k_{j_k j_{k-1}})^2 \sigma^2_{j_k j_{k-1}}) = \exp(-k^2(1-\cos\theta_{j_k j_{k-1}})\sigma^2_{j_k j_{k-1}}). \quad (3\text{-}2\text{-}45)$$

$\sigma^2_{j_k j_{k-1}}$ we have calculated from a sum over phonon modes in the "substrate" crystal, usually neglecting surface-specific effects. The method is one due to Beni and Platzmann [19], but with simplifications introduced by Sagurton et al. [3]. The relevant equation is [3]:

$$\sigma^2_{j_k j_{k-1}} = \frac{3(h/2\pi)^2}{2M_S k_B \theta_D q_D^2}\left(q_D^2 + \frac{4q_D^2}{\alpha^2}\left[\frac{\pi^2}{6} - \sum_{n=1}^{\infty}\left(\frac{1}{n^2} + \frac{\alpha}{n}\right) e^{-\alpha n}\right]\right.$$
$$- \frac{2}{|\vec{R}_{j_k} - \vec{R}_{j_{k-1}}|^2}(1-\cos\beta_{j_k j_{k-1}})$$
$$+ \frac{4q_D}{|\vec{R}_{j_k} - \vec{R}_{j_{k-1}}|\alpha}\sum_{n=1}^{\infty}\frac{1}{n^2 + (\beta_{j_k j_{k-1}}/\alpha)^2}\left(e^{-na}\left[n\sin\beta_{j_k j_{k-1}}\right.\right.$$
$$\left.\left. + (\beta_{j_k j_{k-1}}/\alpha)\cos\beta_{j_k j_{k-1}}\right] - \beta_{j_k j_{k-1}}/\alpha)\right) \quad (3\text{-}2\text{-}46)$$

where M_S is the substrate or "average-atom" atomic mass, k_B is the Boltzmann constant, θ_D is the effective or "average-atom" Debye

temperature, q_D is the associated Debye wave vector, $\alpha = \theta_D/T(K)$, and $\beta_{j_k j_{k-1}} = q_D|\vec{R}_{j_k} - \vec{R}_{j_{k-1}}|$. Additional details of calculating $W_{j_N j_{N-1}}$'s including the allowance for surface-specific affects are found elsewhere [3,7]. In the calculations reported here, the $W_{j_N j_{N-1}}$'s have been determined from Equations (3-2-45) and (3-2-46) and then inserted into Equation (3-2-43) as follows:

$$
\begin{aligned}
I_{n_i \ell_i}^{(N_{max})}(k,\theta,\phi) \;\alpha\; & \sum_{m_i} \Big| \sum_{\ell_f} (-i)^{\ell_f} \exp(i\delta_{\ell_f}^{c}) \, R_{\ell_f}(E_{kin}) \, \langle \ell_f m_i \; 10 | \ell_i m_i \rangle \\
\times \Bigg[& (4\pi)^{1/2} \, Y_{\ell_f m_i}(\theta,\phi) \, \exp\{-|\vec{R}_{0S}|/2\Lambda_e\} + \\
& \sum_{j_1} [\exp\{i\rho_{j_1}(1-\cos\theta_{j_1})\}/\rho_{j_1}] \, \exp\{-|R_{j_1 S}|/2\Lambda_e\} \, \exp\{-|\vec{R}_{j_1}|/2\Lambda_e\} \, W_{j_1 0} \\
& \times \sum_{\lambda_1} F_{00,\lambda_1}(\vec{\rho}_d, \vec{\rho}_{j_1}) \, W_{00,\lambda_1}^{00,L_f}(\vec{\rho}_{j_1}) + \\
& \sum_{N=2}^{N_{max}} \sum_{\{j_i\}} \Bigg[\prod_{k=1}^{N} [\exp\{i\rho_{j_k j_{k-1}}(1-\cos\theta'_{j_k j_{k-1}})\}/\rho_{j_k j_{k-1}}] \, \exp\{-|\vec{R}_{j_N S}|/2\Lambda_e\} \\
& \qquad \times \exp\{-|\vec{R}_{j_N j_{N-1}}|/2\Lambda_e\} \, .. \, \exp\{-|\vec{R}_{j_2 j_1}|/2\Lambda_e\} \, \exp\{-|\vec{R}_{j}|/2\Lambda_e\} \\
& \qquad \times W_{j_N j_{N-1}} \, W_{j_{N-1} j_{N-2}} \, \ldots\ldots\ldots\ldots \, W_{j_2 j_1} \, W_{j_1 0} \\
& \times \sum_{\{\lambda_i\}} F_{00,\lambda_N}(\vec{\rho}_d, \vec{\rho}_{j_N j_{N-1}}) \, F_{\lambda_{N-1}\lambda_{N-2}}(\vec{\rho}_{j_N j_{N-1}}, \vec{\rho}_{j_{N-1} j_{N-2}}) \ldots\ldots \\
& \qquad \ldots\ldots\ldots F_{\lambda_2 \lambda_1}(\vec{\rho}_{j_2 j_1}, \vec{\rho}_{j_1}) \, W_{00,\lambda_1}^{00,L_f}(\vec{\rho}_{j_1}) \Bigg] \Bigg]^2 ,
\end{aligned}
\qquad (3\text{-}2\text{-}47)
$$

where the physical origin of each $W_{j_k j_{k-1}}$ factor is indicated in Figure 3.1(c).

In addition, we must also include the important effects of instrumental angular averaging due to the finite aperture of the detector. This is done by summing the photoelectron intensities over a grid of points on a circular aperture centered on the nominal emission direction as defined by $\vec{k}$. The direct wave and the singly-scattered waves have to be recalculated for each grid point on the aperture. For multiply scattered waves, only the path length differences represented by $\rho_{j_k j_{k-1}}(1-\cos\theta'_{j_k j_{k-1}})$ and the last scattering matrix represented by $F_{00,\lambda_N}(\vec{\rho}_d,\vec{\rho}_{j_N j_{N-1}})$ need to be recalculated (cf. Equation (3-2-30b). This calculation has been made much more efficient by further assuming that the scattering matricies are slowly varying functions of the angles (θ,ϕ) in $\vec{k}$. Then only the geometric phase factors due to path length differences need to be recalculated.

If (θ,ϕ) are now taken to be the mean angles of the nominal emission direction $\vec{k}$ and $\sum_b$ is a sum over the (θ_b,ϕ_b) combinations on a grid spanning the acceptance aperture, usually in a centered circular pattern, we can include angular broadening in Equation (3-2-47) as:

$$\bar{I}^{(N_{max})}_{n_i \ell_i}(k,\theta,\phi) \propto \sum_b \sum_{m_i} \left| \sum_{\ell_f} (-i)^{\ell_f} \exp(i\delta^c_{\ell_f}) R_{\ell_f}(E_{kin}) \langle \ell_f m_i | 10 | \ell_i m_i \rangle \right.$$

$$\times \left[(4\pi)^{1/2} Y_{\ell_f m_i}(\theta_b,\phi_b) \exp\{-|\vec{R}_{0S}|/2\Lambda_e\} + \right.$$

$$\sum_{j_1} [\exp\{i\rho_{j_1}(1-\cos\theta_{bj_1})\}/\rho_{j_1}] \exp\{-|\vec{R}_{j_1 S}|/2\Lambda_e\} \exp\{-|\vec{R}_{j_1}|/2\Lambda_e\} W_{j_1 0}$$

$$\times \sum_{\lambda_1} F_{00,\lambda_1}(\vec{\rho}_d, \vec{\rho}_{j_1}) \, W^{00,L_f}_{00,\lambda_1}(\vec{\rho}_{j_1}) +$$

$$\sum_{N=2}^{N_{max}} \sum_{(j_1)} \left[\prod_{k=1}^{N} [\exp\{i\rho_{j_k j_{k-1}}(1 - \cos\theta'_{bj_k j_{k-1}})\}/\rho_{j_k j_{k-1}}] \right.$$

$$\times \exp\{-|\vec{R}_{j_N S}|/2\Lambda_e\} \exp\{-|\vec{R}_{j_N j_{N-1}}|/2\Lambda_e\} .. \exp\{-|\vec{R}_{j_2 j_1}|/2\Lambda_e\}$$

$$\times \exp\{-|\vec{R}_{j_1}|/2\Lambda_e\} W_{j_N j_{N-1}} W_{j_{N-1} j_{N-2}} \cdots\cdots\cdots\cdots W_{j_2 j_1} W_{j_1 0}$$

$$\times \sum_{(\lambda_i)} F_{00,\lambda_N}(\vec{\rho}_d, \vec{\rho}_{j_N j_{N-1}}) \, F_{\lambda_{N-1}\lambda_{N-2}}(\vec{\rho}_{j_N j_{N-1}}, \vec{\rho}_{j_{N-1} j_{N-2}}) \cdots\cdots$$

$$\left. \cdots\cdots F_{\lambda_2 \lambda_1}(\vec{\rho}_{j_2 j_1}, \vec{\rho}_{j_1}) \, W^{00,L_f}_{00,\lambda_1}(\vec{\rho}_{j_1}) \right] \Big]^2 . \qquad (3\text{-}2\text{-}48)$$

The direct wave is thus recalculated for each grid point (θ_b, ϕ_b) but only the phase differences due to path length difference are recalculated for each scattered wave, as indicated by the added "b" subscript.

An additional correction incorporated at the end of the calculation is that all of the external exit angles with respect to the surface θ_{ext} have been adjusted relative to the internal angles of propogating to the surface θ_{int} using the following refraction equation [1];

$$\theta_{ext} = \tan^{-1}[(\sin^2\theta_{int} - V_0/E'_{kin})^{1/2}/\cos\theta_{int}], \qquad (3\text{-}2\text{-}49)$$

where V_0 is the inner potential and E'_{kin} is the internal kinetic energy such that $E_{kin}(\text{external}) = E'_{kin}(\text{internal}) - V_0$.

Finally, all of the above equations are valid only for radiation of a definite polarization, as usual with the coordinates chosen so that $\hat{\epsilon} \parallel \hat{z}$. Normally, we choose this polarization vector $\hat{\epsilon}$ to lie somewhere in the plane defined by the directions of the incoming radiation ($\hat{k}_{h\nu}$) and the outgoing electron ($\hat{k}$). However, if the source is unpolarized, a second polarization $\hat{\epsilon}'$ perpendicular to other plane must be considered, with $I(\text{unpolarized}) = I(\hat{\epsilon}) + I(\hat{\epsilon}')$. However, our past experience with single-scattering calculations has shown that the other direction can in most cases safely be neglected; this is because $\hat{\epsilon}$ in most experimental geometries is usually aproximately parallel to $\hat{k}$, and thus more strongly excites the direct and scattered waves towards it, whereas $\hat{\epsilon}'$ is perpendicular to $\hat{k}$ and therefore is much less important.

We have used Equations (3-2-48) and (3-2-48) in all of the photoelectron diffraction calculations discussed here. For simulations of Auger electron diffraction, the program was simply forced by the input choices of R_{ℓ_f} and $\delta^c_{\ell_f}$ to treat a fictitious case of p emission into a single s channel. This method yields the correct final state for scattering if it is assumed that the final state of the Auger process is an s-wave [10-12].

3.2.4. Comparison to the Multiple-Scattering Treatment by Barton and Shirley:

We now briefly compare the Rehr-Albers [13] approach utilized here to another truncated spherical-wave multiple-scattering method based upon pioneering work by Barton and Shirley (B-S) [7]. Both of these methods are cluster based in contrast to traditional LEED multiple-scattering methods which rely on the translational symmetry of the system under investigation. We will first introduce the essential elements of the Barton-Shirley method briefly.

This method is based upon a Taylor series magnetic-quantum-number expansion (TS-MQNE). These authors note that the addition formula for the translation of spherical waves can be derived by first taking the Fourier transform of the spherical wave and then doing the inverse transform. They then return to the transform and expand it in a Taylor series about the origin-shift vector $\vec{a}$, which is the bond vector of a particular scatterer. The z-axis is also rotated parallel to $\vec{a}$ to simplify the calculation, just as in the R-A method. They finally obtain an angular momentum series when each term in the translation is subjected to the inverse Fourier transform. This is done to obtain a workable approximation to the Gaunt-integral summations that normally makes the calculation of $G_{L,L'}(\vec{\rho},\vec{\rho}')$ so time comsuming. This results in the following expression for the single-scattering portion of a p-wave final state at the detector ($\vec{R}_d$)

due to an atom at $\vec{a}$ with respect to the emitter [7], the case we will treat as our comparative example:

$$\psi_a^{(1)}(\vec{R}_d) = -ik\,[\exp(i\rho_d)/\rho_d]\,[\exp(i\rho_a(1-\cos\theta_{aR_d}))/\rho_a] \sum_{q=-1}^{1} \sum_{p=0}^{1-|q|} F_{pq}^{00}(\vec{\rho}_a,\vec{\rho}_d)\, e^{iq\phi_{\epsilon aR_d}}\, P_{10}^{pq}(\hat{a},\hat{\epsilon}), \tag{3-2-50}$$

where $\hat{\epsilon}$ is the radiation polarization, $\phi_{\epsilon aR_d}$ is the azimuth of $\hat{R}_d$ with respect to $\hat{\epsilon}$ as rotated around $\vec{a}$ or $\vec{\rho}_a$,

$$F_{pq}^{00}(\vec{\rho}_a,\vec{\rho}_d) = \frac{1}{ik} \sum_{\ell=|q|}^{\ell_{max}} i\,(2\ell+1)\, t_\ell(\vec{a})\, H_\ell^{pq}(\rho_a)\, P_\ell^{|q|}(\cos\theta_{aR_d}),$$

$$P_{10}^{pq}(\hat{a},\hat{\epsilon}) = N_{\ell q}\, R^{(1)}_{|q|0}(0,\theta_{\epsilon a},\pi-\phi_{x\epsilon a})\, C^{1}_{pq}\ ,$$

$$H_\ell^{pq}(\rho_a) = \frac{(\ell+q)!}{(\ell-q)!}\,\frac{(-1)^p}{(i\rho_a)^{q+p}}\,\frac{p!}{q!}\sum_{s=0}^{p}\frac{(q+p-s)!}{s!\,(p-s)!}\,(\rho_a)^s\,\frac{\partial^s C_\ell(\rho_a)}{[\partial(\rho_a)]^s}\ ,$$

$P_\ell^{|q|}(\cos\theta_{aR_d})$ is an associated Legendre polynomial, θ_{aR_d} is the angle between $\vec{a}$ and $\vec{R}_d$, $N_{\ell q}$ is a normalization constant for spherical harmonics, $R^{(1)}_{|q|0}(0,\theta_{\epsilon a},\pi-\phi_{x\epsilon a})$ is a rotation matrix element with angle defined in the same format, $\theta_{\epsilon a}$ and $\phi_{x\epsilon a}$ are the polar and azimuthal angles of $\vec{a}$ with respect to $\hat{\epsilon} \parallel \hat{z}$, and

$$C^{l}_{pq} = \frac{(\ell+|q|+p)!}{(\ell-|q|-p)!} \frac{1}{p!\ (2|q|+2p)!!} .$$

The expansion index q is found to correct the zeroth order origin-shift term in an arc perpendicular to the bond vector that moves away from the center of the scattering potential, whereas the index p corrects outward from the center along this bond vector [7].

One can compare the above equation with our Equation (3-2-30) by making some minor modifications to the latter. With $\vec{R}_j$ replaced by $\vec{a}$ and ρ_j by ρ_a, Equation (3-2-30) becomes

$$G^{(1)}_{00,10}(\vec{a},\vec{R}_d) = [\exp(i\rho_d)/\rho_d]\ [\exp(i\rho_a(1-\cos\theta_{aR_d}))/\rho_a] \times \sum_{\lambda''} F_{00,\lambda''}(\vec{\rho}_d,\vec{\rho}_a)\ W^{00,10}_{00,\lambda''}(\vec{\rho}_a) \qquad (3\text{-}2\text{-}51)$$

where, with some additional simplifications in both F and W, we have [15],

$$F_{00,\lambda''}(\vec{\rho}_d,\vec{\rho}_a) = e^{i\mu''\gamma} \sum_{\ell=0}^{\ell_{max}} t_\ell(\vec{a})\ \gamma^{\ell}_{00}(\rho_d)\ d^{\ell}_{0\mu''}(\theta_{aR_d})\ \tilde{\gamma}^{\ell}_{\lambda''}(\rho_a),$$

and

$$W^{00,10}_{00,\lambda''}(\vec{\rho}_a) = \gamma^{1}_{\lambda''}(\rho_a)\ d^{1}_{\mu''0}(\theta_{\epsilon a}),$$

where the $d^{\ell}_{\mu\nu}(\theta)$ is a standard function in calculating rotation matrices.

We note at once some similarities between these two expressions. The summation limits in Equation (3-2-50), which is a first order Taylor Series in m, and Equation (3-2-51), which is a second order expansion in the parameter $1/\rho$, lead to an equivalant number of terms. In Equation (3-2-50), q = -1, 0, +1 and p = 0, 1, and these are in fact equal to the allowed values for $\mu"$ and $\nu"$ in $\lambda" = (\mu",\nu")$. It is also evident that the summations in Equations (3-2-50) and (3-2-51) can be broken into two major factors. The first factors, $F^{00}_{pq}(\vec{\rho}_a,\hat{\rho}_d)$ $e^{iq\phi_{\epsilon aR_d}}$ in Equation (3-2-50) and $F_{00,\lambda"}(\vec{\rho}_d,\vec{\rho}_a)$ in Equation (3-2-51), are independent of the exact initial and final states involved, while the second factor, $P^{pq}_{10}(\hat{a},\hat{\epsilon})$ in Equation (3-2-50) and $W^{00,10}_{00,\lambda"}(\vec{\rho}_a)$ in Equation (3-2-51) (which we have already noted also depends on $\hat{\epsilon}$), are not. Also, the "effective scattering factors" in the two approximations are similar in that both $F^{00}_{pq}(\vec{\rho}_a,\hat{\rho}_d)$ and $F_{00,\lambda"}(\vec{\rho}_d,\vec{\rho}_a)$ represent the scattering of a given angular momentum component ((p,q) or $(\mu",\nu")$ respectively) incident on scatterer "a" into the correct (0,0) component at the detector.

To compare these models further, we modify Equation (3-2-51) further. First we substitute explicit expressions for γ and $\tilde{\gamma}$. Also the $d^{\ell}_{\mu\nu}$'s can be written in terms of the associated Legendre polynomials P^{m}_{ℓ}. Then we get,

$$F_{00,\lambda"}(\vec{\rho}_d,\vec{\rho}_a) = e^{i\mu"\gamma}\,[4\pi]^{1/2} \sum_{\ell}^{-} (2\ell+1)\; t_\ell(\vec{a}) \times [C_\ell(z_a)\;(\partial^{\nu"} C_\ell(z_a)/\partial z_a^{\nu"})\; z_a^{\nu"}/\nu"!] \times P_\ell^{|\mu"|}(\cos\theta_{aR_d}). \qquad (3\text{-}2\text{-}52)$$

and,

$$W^{00,10}_{00,\lambda"}(\vec{\rho}_a) = [(-1)^{\nu"}\; N_{1\mu"}\; [\partial^{\nu"+\mu"} C_1(z_a)/\partial z^{\nu"+\mu"}]\; z^{\nu"+\mu"} / (\nu"+\mu")!]\; d^1_{\mu"0}(\theta_{\epsilon a}). \qquad (3\text{-}2\text{-}53)$$

Now, if we compare the effective scattering factor $F_{00,\lambda"}(\vec{\rho}_d,\vec{\rho}_a)$ in Equation (3-2-52) with that of $F^{00}_{pq}(\vec{\rho}_a,\vec{\rho}_d)$ in Equation (3-2-50), it is evident that they have some similarities, but also some important differences. Both involve the t-matrix elements t_ℓ and the associated Legendre polynomials $P^m_\ell(\cos\theta_{aR_d})$. But the Barton-Shirley method has a sum of derivatives of the C_ℓ's in H^{pq}_ℓ, and the Rehr-Albers formalism contains products of C_ℓ's and their derivatives.

In comparing $W^{00,10}_{00,\lambda"}(\vec{\rho}_a)$ in Equation (3-2-53) with $P^{pq}_{10}(\hat{a},\hat{\epsilon})$ in Equation (3-2-50), we note that, while $W^{00,10}_{00,\lambda"}(\vec{\rho}_a)$ is dependent on the distance between the emitter and the first scatterer, $P^{pq}_{10}(\hat{a},\hat{\epsilon})$ is independent of any distance. This is also true for the analogous multiple-scattering comparisons. For example, we can compare double-scattering terms in a similar manner, and it is clear that they exhibit such differences.

From the point of view of computational time, inspection of the number and types of factors to be calculated in the two methods in single-scattering indicates a comparable amount of numerical work. However, in general multiple-scattering, the cleaner separability of the $F_{\lambda_k,\lambda_{k-1}}(\vec{\rho}_k,\vec{\rho}_{k-1})$ for each scattering vertex defined by $\vec{R}_k \leftarrow \vec{R}_{k-1} \leftarrow \vec{R}_{k-2}$ would appear to furnish a computational advantage in the R-A approach.

As final comparative comments, we believe that the R-A approach has better convergence and formal properties, as discussed also eleswhere [13]. In particular, the R-A formalism reduces to effective curved-wave scattering amplitudes in a point scattering approximation [13] in zeroth order (i.e., (1x1)), whereas that of B-S does not. For a given degree of convergence smaller matrices should be needed in R-A calculations. The R-A method also does not distinguish between forward and backward scattering, whereas the B-S method appears to converge faster in back scattering [7]. The R-A method at the (6x6) level assumed here also should be applicable to a broader range of energies, with the B-S approach representing more of a low-energy Taylor expansion. We will illustrate some of these comments in subsequent numerical calculations with the R-A method.

In conclusion, the R-A and B-S methods have certain simililarities in form but are fundamentally different in the kind of truncation/approximation they make in the expansion of $G_{L,L'}(\vec{\rho})$. The R-A separation appears to be more quickly convergent, to be inherently applicable to a broader range of energies, to be more readily

generalizable to higher order expansions (even though the second order (6×6) seems fully adequate to date), and to be more easily adopted to a variety of situations such as, e.g., emission from a general $n_i\ell_i$ subshell treated here (a case which to our knowledge has not yet been dealt with using the B-S approach).

3.2.5. The Computer Code and Input Parameters:

We have a single code capable of doing both scanned-angle photoelectron (PD) and Auger electron diffraction (AED), and scanned-energy photoelectron diffraction (ARPEFS). Multiple-scattering up to tenth order events can be included; single-scattering output is an option in any run. For photoelectron diffraction, emission from any $n_i\ell_i$ subshell also can be treated. This is thus the most general cluster-based code for such diffraction calculations of which we are aware. This program presently operates on both supercomputers (e.g., the Cray Y-MP/864 at the San Diego Supercomputer Center) and work stations (e.g., a Sun SPARCstation), although to date most calculations have been done on the supercomputer. As an estimate of the program size, the present version requires about 75 kWords of high speed memory (1 Word = 64 bytes) and about 5 MWords of fast disk storage.

In order to avoid calculating negligibly small multiple scattering events, all events over 3^{rd} order are subjected to a user-selected cutoff criterion $x_N(\%)$. Specifically, the amplitude of

each 3^{rd} order scatterd wave is computed, and x_N is a selected percentage of the maximum amplitude among all 3^{rd} order events. All 3^{rd} order events above the x_3 cutoff are continued to 4^{th} order. At 4^{th} order, a cutoff x_4, again based on the maximum 3^{rd} order amplitude is used to decide which events are continued to 5^{th} order. This process is then repeated for x_5, x_6, ... up to the maximum order considered. Thus we do not depend on less accurate indicators of intermediate wave strengths such as the total path length [7,13]. A sufficiently accurate set of cutoffs is found to be $x_3 = x_4 = x_5 = \ldots\ldots = x_N = 5\%$, which is found to yield excellent convergence judged against test calculations with smaller cutoff choices. The program also outputs the number of events at each order so that convergence can also be judged by having a negligible number of events at or below the N_{max} order. We discuss the order required to achieve convergence for several of the applications considered below.

The non-structural input parameters to each calculation and our sources for them are: the radial matrix elements ($R_{\ell_i \pm 1}$) and phase shifts ($\delta^c_{\ell_i \pm 1}$) (from Reference 14), the scattering phase shifts δ_ℓ (from the program MUFPOT of Reference 21), the inelastic attenuation length (from various sources), the inner potential V_0 (from various sources also), the geometric parameters of the experiment, the type of scan involved (θ,ϕ, or $h\nu$), the vibrational parameters necessary for using Equation (3-2-46) (from various sources), the maximum order of scattering to be included N_{max}, the order of the R-A approximation to be used (found to be fully adequate at 2^{nd} order or (6×6) scattering

matrices), and the cutoff (in %) at each level above 3^{rd} order measured with respect to the largest 3^{rd} order event.

3.2.6. Tests Against Scanned-Energy (Angle-Resolved Photoemission Fine Structure) Results for c(2×2)S on Ni(001):

We here compare two angle-resolved photoemission fine structure (ARPEFS) experimental curves for the c(2×2)S overlayer on Ni(001) due to Barton et al. to a multiple-scattering cluster spherical-wave (MSC-SW) analysis of this data by the same authors [7(b)], and to our reanalysis of this work using the present method. In both experiments, the photon incidence direction, the polarization $\hat{\epsilon}$, the [001] surface normal, and the electron emission direction lie in the same plane, normal to the surface. Our calculations made use of clusters of 40 atoms and non-structural inputs as described elsewhere in a SSC-SW analysis of the same data by Sagurton et al. [3].

In the first case, the incoming photon beam makes an angle of $\theta_{h\nu} = 70^{\circ}$ with respect to the surface normal and the detector is placed in the direction of the surface normal ($\theta_{e-} = 0^{\circ}$). (Hence, this has been termed normal photoelectron diffraction or NPD.) The photon energy was scanned from 50 to 420 eV. Figure 3.3(a) shows the experimental curve superimposed on the MSC-SW simulation by Barton et al. [7(b)] for an optimized structure with sulfur 1.30 Å above the first Ni layer and a first-to-second Ni-Ni interlayer distance of 1.84 Å that is expanded by 4.5% with respect to the bulk value of 1.76 Å. Figure

3.3(b) shows a similar comparison of our SS and MS results to experiment. In SS, several peak positions and intensities are not predicted correctly (e.g., l, m and o, as well as the valley between k and l). By contrast, our MSC-SW simulations are in excellent agreement with the experiment, and appear to provide an overall better description of the data than the earlier calculations shown in (a). In perticular, we are better able to predict the intensities of peaks o and p, and the positions of peaks r and s are also in better agreement with experiment.

The second case is very similar to the first, except that the incoming photons are oriented at $\theta_{h\nu} = 45^{\circ}$ away from the surface normal and the detector is at $\theta_{e-} = 45^{\circ}$ away from the surface normal. (This has been termed off-normal photoelectron diffraction or OPD.) Figure 3.4(a) again shows the experimental curve and the MSC-SW simulation by Barton et al. [7(b)] for the optimized structure. Figure 3.4(b) shows our SS and MS results compared to the same experimental data. In SS, the position and intensity of the valley between peaks a and b are not well reproduced. For peak c, the calculated intensity is too small. Also peak i in the SS simulation is displaced by several eV. In our MS results however, the only major disagreement compared to the simulati,n by Barton et al. [7(b)] is the intensity of peak f, which is overestimated. But our simulation of peaks e and j is in better agreement with experiment than that of these prior calculations [7(b)].

The χ-scale ordinates on both Figures 3.3 and 3.4 are set by the experimental data and our calculations have not been rescaled to fit experiment. This is an important point, as prior SSC-SW results due to Sagurton et al. [3] have an adjusted χ-scale which is more expanded than the experimental scale. This difference is due to the different sets of correlated vibrational parameters used in the two calculations, which evidently oversuppressed the diffraction oscillations in the earlier work. Our parameters correspond to the alternate "correlated model 1" discussed by Sagurton at al. [3].

As a final comment concerning our calculations, we note that convergence is achieved at 4^{th} order as judged from final intensities, although events through 5^{th} order were included in the calculation. The number of scattering events versus order for several cases disscussed in this paper are given in Table 3.1, with points of convergence as judged by intensities or by number of events indicated.

Overall, the MSC-SW results obtained using these two different methods agree very well with themselves and with experiment. This indicates that the Rehr-Albers approach [13] is reliable over low to medium energies of photoelectron diffraction and that it can provide at least as good a description of such experimental data as the method of Barton and Shirley, if not somewhat better.

3.2.7. Tests Against Scanned-Angle X-ray Photoelectron Diffraction Results for c(2×2)S/Ni(001):

As a final comparison of our calculations to prior experimental data and MS theory, we consider an experimental study by Sinkovic et al., who used the intermediate kinetic energy range from 230 to 900 eV to study adsorbate core-level azimuthal photoelectron diffraction [22]. The adsorbate/substrate system employed in this study was again the well-defined c(2×2)S overlayer on Ni(001). Again the photon incidence direction, the polarization, the [001] surface normal, and the electron emission direction were in a single plane normal to the surface. They utilized two polarization orientations: s-polarization lying in the (001) surface and a specially selected p-polarization only 18° off the surface normal that maximally emphasized substrate Ni scattering relative to the primary wave. A grazing electron takeoff angle of $\theta = 10^{\circ}$ with respect to the surface was used in both cases, with the azimuthal angle ϕ being scanned. The experimental geometry for p polarization is shown in the inset of Figure 3.5.

The s-polarization results with $\hat{\epsilon}$ only 10° away from the electron emission direction and thus yielding a very strong primary wave were reasonablly well reproduced by a quite simple single-scattering cluster plane-wave (SSC-PW) model [22]. The corresponding p-polarization results were markedly different however. In order to be semiquantitatively described by the theory, the p-polarization data required a reduction in the PW scattering amplitudes and the inclusion

of double-scattering events [22]. These p-polarization data were later analyzed by Sagurton et al. [23] using a single-scattering cluster spherical-wave approach, but there was no significant improvement in the agreement. From this prior work, it was concluded that the p-polarization geometry with its weaker primary wave showed evidence of MS effects [22].

Tang [9] subsequently performed a multiple-scattering spherical-wave analysis on this system and agreed in concluding that MS is required for the accurate description of the p-polarization data. Tang's computational method is based on an inverse-LEED type final state, as described eleswhere by Tong et al. [6,24]; this method takes the translational symmetry of the system into account and thus requires the assumption of long range order. Hence it is fundamentally different from the cluster-based methods used by Barton et al. [7] and in this work. We have now performed multiple-scattering cluster spherical-wave (MSC-SW) calculations on the same system and Figure 3.5 compares this p-polarization experimental data to various theoretical curves. We considered a cluster of 36 atoms. We see that SSC-SW theory fails to predict the peak observed in the [110] direction, and yields very poor positions for the other two peaks in experiment at $\phi \sim 22^{\circ}$ and 67°. By contrast the two MS curves agree much better with experiment, and also very well with one another. Tang's MS curve has a peak in the [110] direction, but it is too strong in relative intensity. The other peaks and shoulders at $\phi \sim 10^{\circ}$ and 80° in his curve are in good

agreement with experiment. Our MS curve has a wider double peak along [110]. This may be due to our small cluster size of 36 atoms and/or our neglect of the finite aperture of the detector. But the relative intensity of our central peak is in better agreement with the experiment than that predicted by Tang [9]. The rest of the structure in our MS curve away from [110] is in excellent agreement with experiment. The strong disagreement of our SS results with experiment is consistent with the prior conclusions by both Sinkovic et al. [22] and Tang [9] concerning the need for MS for this particular geometry. Finally, we note that convergence for this case was reached at 4^{th} order, as indicated by the numbers in Table 3.1.

3.3. APPLICATION TO AUGER AND PHOTOELECTRON DIFFRACTION FORM ATOMIC CHAINS:

3.3.1. Straight and Bent Chains:

We now consider single-scattering and fully converged multiple-scattering results for simple linear chains of different atoms, an illustrative type of test case discussed first by Xu, Barton, and Van Hove [10(b)]. To illustrate the type of diffraction pattern one expects from such chains, we show in Figure 3.6 a simplified drawing applicable to high-energy scattering where forward peaking is dominant and the scattering phase shift is small (here assumed to be zero). Both the 0^{th} order (forward scattering) peak and

the higher-order diffraction peaks are labelled. In a real n-atom chain these features will be distorted somewhat by scattering phase shifts that depend on scattering angle, by the resulting imperfect overlap of different orders from different scatterers, by inelastic attenuation effects, and by multiple-scattering effects.

We begin by considering Cu atoms placed at 45° with respect to a fictitious "(001) surface", as shown in the inset of Figure 3.7. The 2.56 Å nearest neighbor distance is chosen to simulate emission along a [101] direction. The surface is used only to determine that region of space over which an exponential decay of intensity due to inelastic scattering is included. These chains represent the nearest-neighbor [101] direction in the fcc Cu crystal, with a single emitting atom at the bottom of the chain. The total emission from such a [101] chain in the metal would thus be the sum over the intensities of all of these emitters from the surface inward to the end of the chain. Cu LMM Auger emission at 917.0 eV is simulated using the aforementioned approximation of an s outgoing wave (ℓ_f=0 only). Λ_e is taken to be 11.7 Å at 917 eV and 3.9 Å at 100 eV in results to be discussed later. Refraction at the surface due to the inner potential V_0 has not been included. The resulting curves for 2-10 atom linear chains are shown in Figure 3.7. Figure 3.8 shows other information derived from these curves, in particular the forward-scattering along-chain intensities in both SS and MS and, in the lower panel, the amount of MS "defocussing", which is defined as $D(\%) = 100 \times [I^{SS}(\text{along chain}) -$

I^{MS}(along chain)] / I^{SS}(along chain), all as a function of chain length n.

From these two figures, it is evident that the longer the chain is, the greater are the MS effects: the forward-scattering peak height systematically diminishes as the number of atoms in the chain increases, eventually falling by about 6 atoms to a level equal to the background on either side of the chain axis. Such intensity reductions were termed "defocussing" in the first discussion of this effect by Tong and co-workers [6]. It is also interesting to note that the MS peak widths are consistently narrower than those of corresponding SS peaks, becoming systematically smaller in FWHM as the number of atoms in the chain is increased. This can be qualitatively understood from a classical picture in which only those electrons with very small deflections (i.e., with large impact parameters at the edge of the scattering potential) can avoid being driven into defocussing pathways in passing several scattering centers. By contrast, for a 2-atom chain and at this high energy, MS effects are negligible, a simplifying result which is applicable to emission from an oriented diatomic molecule such as the system CO/Fe that is to be discussed later. The 4- to 10-atom cases are applicable to multilayer substrate emission or to grazing-angle emission from adsorbate/substrate systems, since in both of these cases, emitters can have more or less linear rows of atoms between them and the detector for a certain direction of emission. In such cases, one thus expects that intensity along linear or nearly-linear chains of atoms with small interatomic

distances will be significantly reduced. By contrast to the MS results, the SS intensity only begins to reduce after n = 4-5 due to both interference effects and inelastic attenuation. But even at n = 10, the SS intensity shows a pronounced forward-scattering peak and is much too strong compared to the MS intensity.

These calculations provide another test of the accuracy of our method and the computer code, because a similar set of curves for the same case were reported earlier by Xu and Van Hove [10(a)] for 2-, 3- and 5-atom Cu [101] chains at 917.0 eV; they have used the TS-MQNE method of Barton and Shirley [7] in their work. The good agreement between these two different approaches to MS is very encouraging: in fact, excellent agreement is obtained if we allow fully for the differing degrees of angular broadening used in the two sets of calculations.

We have also performed calculations on such Cu chains at the much lower energy of 100.0 eV. There is no Cu Auger peak at 100.0 eV and this energy was simply chosen to investigate the low energy behavior of multiple-scattering effects, again for an outgoing s-wave. As shown in Figures 3.9 and 3.10, the SS and MS forward-scattering intensities decay at a more nearly comparable rate than those at 917.0 eV. This is due to the lack of a strongly forward-peaked scattering factor, as well as to the shorter electron mean free path at this energy, which tends to attenuate MS effects with longer total path lengths. Although both defocussing loss of intensity and peak narrowing with increasing chain length are still present, they are

less pronounced than at 917 eV and we expect this to be a general comparison between lower (~100 eV) and higher (≥ 500 eV) energies with an emitter at the end of the chain.

A further noteworthy effect at lower energies is that the peak maximum systematically moves to higher takeoff angles so that it is 2-5° away from the chain axis. This is due to peak distortion by the stronger exponential damping of intensities by inelastic effects, which will go as $\exp(-Z_n/\Lambda_e \sin\theta)$, if Z_n is the depth of the emitter in the n-atom chain below the surface.

Another interesting case is that of bent chains, results from which are shown in Figure 3.11 for 917.0 eV and in Figure 3.12 for 100.0 eV. The amount of defocussing vs. the bend angle β for 2- 3- and 5-atom chains is presented. The dropoff of defocussing to zero for 917 eV at β ~25°-30° is consistent with the fact that the forward peak in the plane-wave scattering factor dies away to essentially "background" level by this angle [1]. At 100 eV, however, the forward peak is much broader, but the SS and MS intensities still converge at about the same angle. Thus, events more than about 30° off axis are expected to be rather SS in character over a broad range of energy, although we note that the chain geometry we have used here does not allow for back scattering from atom(s) just below the emitter, an effect which could become important by 100 eV.

We now investigate the dependence of these MS effects in chains on different crystallographic directions and materials. In Figures 3.13 and 3.14, we first look at 917 eV emission along the much more

open [111] direction in the fcc Cu lattice, which has a nearest-neighbor distance of d_{n-n} = 6.27 Å compared to 2.56 Å for the [101] direction considered previously. In this case, the chain is placed at 35.3° with respect to a fictitious (001) surface and hence the forward-scattering peak is very close to that angle with respect to the surface. The intensities along the chain fall more rapidly with increasing chain length due to inelastic attenuation, which now goes as $\exp(-Z_n/\Lambda_e \sin(35.3^\circ))$. These inelastic effects are enhanced because the interatomic distance and thus Z_n is about 2.5 times larger than that for the [101] chains at a given n. We note here also that enhanced inelastic attenuation has shifted the peak position about 2° toward higher takeoff angles. Also, the SS and MS results are much closer to one another for [111] chains because of the increased nearest-neighbor distance and a concomitant reduction of MS defocussing effects; thus the importance of this type of MS effect will depend strongly on the direction of observation. Nonetheless, up to 50% defocussing is seen for the longest chain, and the same sort of peak narrowing in MS is observed. Both SS and MS peaks are very small after about eight atoms and hence major contributions to the photoelectron intensity are coming from the top eight layers in each case.

To further investigate the effects of interatomic distances on defocussing, we have finally studied Cu [001] chains (d_{n-n} = 3.62 Å) which are less dense than [101] chains but more dense than [111] chains . We see from Figures 3.15 and 3.16 that both single and

multiple scattering intensities for [001] chains are in between those for [101] and [111] cases, but closer in behavior to the [101] case, consistant with the interatomic distances being closer.

As a final comment concerning these results for various Cu chains at 917 eV kinetic energy, we note that the higher-order diffraction features occuring for emission angles more than 10-15° away from the chain axis are always predicted reasonably well by SS theory, even though the MS curves exhibit some additional fine structure about an average that is very close to the companion SS curves. This is another indication that SS becomes a reasonable approximation for angles sufficiently far from a near-linear chain of scatterers. (cf. also discussion of Figures 3.11 and 3.12.) One potentially useful implication of this observation is in the recently-suggested holographic inversion of θ,ϕ intensity plots to yield images of atomic positions [25]. Since bond-distance information in these inversions is present only in the higher-order features, SS may prove to be an at least semiquantitative usefully accurate way to model the images expected, and this has been demonstrated in recent preliminary work [26].

We now turn to examples of chains for different materials, and first show in Figures 3.17 and 3.18 results for linear [101] Al chains at 1336.0 eV, which corresponds to MgK_{α}-excited Al 2s emission. We have here assumed $\hat{\epsilon}$ and $\hat{k}$ to be parallel. Defocussing effects are again obvious, since the SS curves show a pronounced peak for an emitter as deep as ~10 layers in the solid, but the MS intensity goes

essentially to background level when the emitter is about eight layers deep. Peak narrowing as chain length increases is also evident. Note also that defocussing sets in more slowly for Al than for Cu as a function of chain length, with about an additional 2 chain atoms being required to yield the same effect in Al.

A second case of Ge [11$\bar{1}$] chains is also interesting and related to a recent x-ray photoelectron diffraction study by our group of a surface phase transition on Ge(111) [27]. In this study, the intensity of a forward-scattering peak along a [11$\bar{1}$] direction at 19.0° with respect to the Ge(111) surface was monitored as a function of temperature, and it was found to show an abrupt decrease at a previously-observed surface phase transition temperature. The Ge [11$\bar{1}$] chains on which we have carried out MS calculations represent this direction. As shown in Figures 3.19 and 3.20, even though the SS peak has contributions from more than ten layers (five (111) double layers in the usual notation), the MS signal is seem to come from the top eight layers (four double layers) only. Both defocussing intensity reduction and peak narrowing are again seen. The smooth-curve average behavior of the defocussing effects in Figure 3.20 also make it appear that Ge defocusses intensity more rapidly than Cu.

Figure 3.20 illustrates another interesting effect in Ge: the "saw tooth" variation of the curves as the chain length increases, which is found in both the SS and MS curves. This is explained by the alternating short-long-short-long nature of the interatomic distances

along this chain. That is, within a double layer d_{n-n} is 2.45 Å, but between them it is three times this or 7.35 Å. The chains with odd numbers of atoms thus have a gap of 7.35 Å between the emitter and the nearest forward scatterer, and then two foward scatterers with d_{n-n} = 2.45 Å along the chain. Chains with even numbers of atoms have a single nearest-neighbor scatterer at d_{n-n} = 2.45 Å, and then a long gap of 7.35 Å to the next scatterer. The enhanced intensity for even numbers is thus due to having a strong forward-focussing scatterer very close to the emitter. This oscillatory effect on intensity, which has not been discussed previously, could be useful in studying semiconductor epitaxial growth. The "stairstep" form of the defocussing curve also has the same origin, in that increasing from even to odd adds only a long distance scatterer that is very ineffective at defocussing.

In Figure 3.19, SS peak centroids are found to shift to higher takeoff angles by about 3° due to previously discussed inelastic effects. We do not observe such distortions in the MS peak. This is due to the less severe inelastic distortions on the narrower MS peaks.

We continue this discussion on chains by investigating the dependence of these strong forward-scattering defocussing effects on some of the non-structural parameters used in the simulations.

First, we consider the size of the muffin-tin radius which is used in the program generating the scattering phase shifts δ_{ℓ}. This is motivated by recent work by Aebisher et al. [28] who have theoretically investigated the material dependence of such MS effects

along chains. They concluded that the different amounts of defocussing in Cu and Al chains at a given chain length (cf. our more detailed results of this type in Figures 3.7-3.10, 3.13, and 3.14-3.20) are not due to the choice of non-structural input parameters but rather are primarily due to the differences in the scattering strengths of the constituent atoms (i.e., their atomic numbers and the resultant set of δ_ℓ's). However, an additional parameter related to the δ_ℓ's that depends on the nature of the material and also has a certain degree of arbitrariness in its choice is the muffin-tin radius R_{MT} used in the calculation of the δ_ℓ's. The usual choice is the touching-sphere radius and hence R_{MT} is clearly dependent on the lattice parameters of a given material.

We have thus investigated the effects of muffin-tin radius on the final intensities for a five-atom Cu chain, as shown in Figure 3.21. Here we have chosen two non-touching radii which are 30% and 15% smaller than the touching radius, the touching radius, and two overlapping radii which are 15% and 30% larger than the touching radius. The magnitude of the SS forward intensity increases monotonically with the size of the muffin-tin radius. This can be qualitatively explained in terms of a potential of greater radial extent being capable of better focusing the photoelectrons in the forward direction, since forward-scattering is primarily controlled by the outer portion of the potential corresponding to larger impact parameters. But the MS intensities show a much weaker variation with

R_{MT} that is, if anything, the inverse of the SS intensities; that is, the strongest forward scattering in SS (the largest R_{MT}) gives the strongest defocussing and the lowest MS intensity along the chain. This can be explained via a potential of greater radial extent causing stronger defocussing and thus being capable of directing photoelectrons away from the forward direction through multiple-scattering effects. However it is evident from Figure 3.21 that the choice of muffin-tin radius has only minor effects on defocussing. Hence, the choice of muffin-tin radius alone is not sufficient to account for the different amounts of defocussing in different materials; our results show that these differences are mainly due to a combination of the differing atomic scattering strengths and the change in interatomic distance along chains of atoms, in agreement with the work of Aebisher et al. [28].

As a final comment on Figure 3.21, we note that, for angles more than 10-15^{o} away from the chain axis, the diffraction structure is negligiblly affected by the choice of the muffin-tin radius in either SS or MS. This is useful, because as noted previously, it is such higher-order structure that contains bond length information, or via holographic inversion, also atomic image positions.

There are other non-structural parameters that could influence chain intensities such as the precise choice of the inelastic attenuation length of the photoelectron, the finite aperture of the photoelectron detector and the inner potential. Varying the first two parameters over a reasonable range is found to cause changes in

relative peak intensities of only about 1-10%; peak positions are very little affected. Increasing the inner potential is responsible for moving peak positions to lower takeoff angles due to refraction, an effect that is strong for lower energies and/or lower takeoff angles. When the inner potential is increased, the peak positions move away from the surface normal according to Equation (3-2-49). But the single and multiple scattering peaks are found to move together with no relative displacement.

The various tests we have made to insure that our cutoff criteria were adequate and that full MS convergence was reached are discussed eleswhere [15]. But in connection with calculations on linear chains at higher energies $\geq$ 100 eV, there is one useful rule of thumb: the highest order of scattering can be estimated as the maximum number of forward-scattering events in sequence, that is, (n-1) for an n-atom chain. For example, all of the Al chains in Figure 3.17 are found to obey this (n-1) rule. This is illustrated for a 9-atom chain in Table 3.1, for which a small number of 9^{th} order events exceed the 5% cutoff, but convergence as judged by intensities is reached at 8^{th} order. We do however, have evidence that for chains of much higher atomic number such as W, orders beyond this rule might need to be included. Thus, testing its validity at least against the next higher n^{th} order is advisable in any case.

3.3.2. Effect of the Initial State:

As indicated previously our approach to multiple-scattering can be extended to include the correct initial and final states in photoemission as allowed by dipole selection rules. This is done with a very small amount of extra computer time as one has to recalculate only the W matrix for each final quantum number L_f.

We now look at the effects of photoemitting from different initial states (that is, into different final states ℓ_f) for two- and three-atom Cu chains at two different kinetic energies (100.0 and 1000.0 eV) and in both single and multiple scattering. For purposes of illustration only, the $\ell_f = \ell_i + 1$ channel is included. In general, the ℓ_i-1 channel is expected to be weaker due to the smaller radial matrix element associated with it. (Our code can, of course, treat the full problem with $\ell_f = \ell_i \pm 1$ if the matrix elements are known.) The polarization $\hat{\epsilon}$ was kept fixed along the electron emission direction $\hat{k}$. No inelastic attenuation was included. These results are shown in Figures 3.22 (E_{kin} = 100 eV) and 3.23 (E_{kin} = 1000 eV), where we have plotted the normalized function $\chi = (I(\vec{k}) - I_0(\vec{k}))/I_0(\vec{k})$, with I_0 equal to the unscattered intensity. In addition to the possible ℓ_i+1 final states for photoelectron diffraction, we have also included the $\ell_f = 0$ approximate final state for Auger electron diffraction, so that all of ℓ_f = 0,1,2,3, and 4 are considered.

In Figure 3.22, the first set of curves are for a two-atom Cu chain at 100.0 eV with SS only. This case was examined earlier using a single-scattering formalism by Friedman and Fadley [17], and our results agree completely with theirs. In particular, the forward-scattering intensity steadily decreases as the initial angular momentum increases and the intensity for larger scattering angles shows the oscillatory behavior typical of higher-order diffraction peaks (cf. Figure 3.6), but with phases that change by as much as π as ℓ_f changes from 0 to 4. Also the effect of the photoelectron parity is clear in the backward direction, with odd and even parity curves being grouped together. As expected [10,11], there are almost no MS effects in a two-atom case, as we can see also from Figure 3.22. Hence, these observations should also be valid for a full MS calculation.

The second set of curves in Figure 3.22 is for a three-atom SS chain at 100.0 eV. First, we observe an enhancement of intensity for all ℓ_f in the forward scattering direction due to the presence of an extra atom in the chain. However, the forward-scattering intensity still shows a decrease with increasing ℓ_f. Second, the absolute value of the back-scattering intensity is now reduced, but it still shows the grouping of waves according to parity. Relative to the 2-atom case, we also observe a splitting or fine structure in the first order interference peaks occuring over about 20°-45°. This is due to the well understood interference of waves from each scatterer, since the orders from different scatterers do not occur at the same angle, but

rather overlap roughly as 1^{st} order of the 1^{st} scatterer and 2^{nd} order of the 2^{nd} scatterer. However, the presence of scattering phase shifts makes this correspondence only approximate. The bottom set of curves are for the same case, but now MS effects are included. The forward-scattering peaks are now defocused, but they exhibit the same decrease as ℓ_f is increased that was seen in SS. There is also an enhancement of the amplitudes of features in the off-forward directions that must be present in order to yield a net conservation of flux. This enhancement of diffraction effects in the off-forward directions is expected to be more pronounced for longer chains as the defocussing of forward-scattering peak is more severe for those chains (cf. Figures 3.7 and 3.9). From these curves, it is evident that the use of the correct final ℓ_f states is very important at kinetic energies as low as 100.0 eV. Note however, that for scattering angles $\geq 25^{\circ}$, the diffraction fine structure is very nearly the same in both SS and MS for all angular momenta; this reiterates a point made earlier that SS is still a reasonable approximation for angles away from any forward scattering cone.

In Figure 3.23, we present the high energy (1000.0 eV) counterparts of the curves shown in Figure 3.22. As expected, the forward-scattering intensities are much higher at high energies. The decrease in the forward scattering strength as ℓ_f is increased is still present, but it is much smaller in magnitude compared to that at low energy. The first few peaks in the higher-order diffraction features out to about 35°-40° show a weaker dependence on ℓ_f than at

100 eV, with a general tendency to simply be smeared out as ℓ_f increases. However, the weaker higher-order diffraction features at intermediate-to-large scattering angles are not as close to one another between SS and MS as they were for 100 eV. The grouping by parity at the back-scattering end of the curves is still true at high energy, even though the amplitudes of these oscillations are now smaller compared to the low energy case. (Notice that the left ordinate of Figure 3.22 is identical to the right expanded ordinate of Figure 3.23). The effects of defocussing are also clear in the 3-atom curves: forward scattering is decreased and off-forward features are in general increased somewhat. From these curves, one can conclude that, at kinetic energies as high as 1000.0 eV, the correct final state is not so important for scattering geometries that emphasise forward scattering. Also, beyond the reduction of the forward scattering peaks, MS is not found to radically alter the fine structure over the most significant region up to ~40° scattering angle; SS calculations thus may reproduce experimental data reasonably well, as has been noted in numerous studies [1].

In longer chains, MS effects would be expected to cause drastic reductions in the forward-scattering intensity (cf. Figures 3.7, 3.9, 3.13, 3.15, 3.17 and 3.19). This should result in a larger increase in the relative amplitudes of the large-angle oscillations.

As a further test case concerning the effects of the final photoelectron angular momenta, we consider the $(\sqrt{3}\times\sqrt{3})R30^\circ$ Ag overlayer on Si(111) to be discussed in detail in Section 3.5.2. For

this still controversial structure, Bullock et al. [29] have used azimuthal x-ray photoelectron diffraction data and SSC-SW calculations to suggest that the Ag atoms are buried 0.2 Å below the top Si layer in what has been termed a Ag-honeycomb missing-top-layer (MTL) model (cf. Figure 3.24). Two closely-related domain types are postulated for this structure, with about a 40:60 mixture of type 1:type 2 being suggested. For this model, Ag photoelectrons are thus expected to show strong forward scattering from near-neighbor Si atoms for low takeoff angles (short arrows). Also, there are some short nearly-linear Ag-Si_3 chains in this geometry (see long arrow) that might be expected to lead to MS effects (a topic to which we will return later). The kinetic energy for the Ag $3d_{5/2}$ photoelectrons studied is 1114 eV for this system. In Figures 3.25 and 3.26 we compare SS and MS curves for $\ell_f = 1$ and fully interfering $\ell_f = 3 + 1$ as calculated for the final optimized geometry with two domains. In agreement with our earlier prediction, there are no significant changes in going from the approximate p-wave final state to the correct d+s-wave final state. This also has been seen in Ni $2p_{3/2}$ emission from a Ni(001) substrate [30(c)], a case to be discussed in Section 3.4.2., and another example where high energy forward-scattering is dominant.

3.4. APPLICATION TO EPITAXIAL OVERLAYER GROWTH AND SUBSTRATE EMISSION:

3.4.1. Auger Diffraction from Epitaxial Cu(001) on Ni(001):

The experimental data we will consider was obtained by Chambers et al. [31] and made use of the forward scattering of high-energy Auger electrons for studying vertical interlayer relaxations in epitaxially-grown overlayers. In this experiment, 6 Å or about 3 ML of Cu was grown epitaxially on a Ni(001) substrate. Due to the 2.56% lattice mismatch between Cu and Ni, it was expected that the Cu layers would relax vertically. The polar-angle dependence of the Cu Auger peak was measured in the [001] → [101] → [100] azimuth, and compared to single-scattering plane-wave calculations in which the vertical distance between Cu layers was varied to simulate interlayer relaxations [31].

We present in Figure 3.27 both the experimental data and prior theoretical curves, as well as single- and fully-converged multiple-scattering spherical-wave counterparts to the plane-wave calculations by Chambers et al [31]. A cluster of about 40 atoms was used for both our SS and MS calculations to permit isolating only those effects due to MS. There is in general very good agreement between our SS curves and those of Chambers et al., with more fine structure appearing in the latter, probably due to the larger cluster used in these prior calculations. The MS results for the [101] peak

exhibit the effects of defocussing and narrowing noted earlier, but importantly still exhibit the same shift in peak position with vertical relaxation that is seen in the SS curves. Thus, MS does not appear to prevent the use of this peak position for estimating the interlayer relaxation as Chambers et al. have done. However, our theoretical curves agree best with the position of this peak for an interlayer distance of 3.71 Å that is slightly different from their value of 3.80 Å. As a final comment, the FWHM of the [101] peak is reduced by about 10° in going from single- to multiple-scattering, but the width of the single-scattering curve in fact agrees better with experiment, perhaps due to the presence of disorder and/or vibrational effects beyond our model. Overall, we thus conclude that the single-scattering level of Auger electron-scattering theory is adequate for studying vertical layer relaxations in thin epitaxial overlayers via the positions of strong forward scattering peaks, but that correctly predicting all relative intensities will require including multiple-scattering effects.

3.4.2. X-ray Photoelectron Diffraction from Ni(001):

Stewart et al. [30(a)] have reported high angular resolution x-ray photoelectron diffraction patterns for Ni $2p_{3/2}$ emission from a Ni(001) substrate. Osterwalder et al. [30(b) and (c)] have performed an extensive set of SS calculations to simulate this experimental data. The agreement between experiment and the simulations was often

good, but was not as satisfactory for several angles. We thus in Figures 3.28(a) and 3.28(b) compare different types of SS and MS calculations with experiment, focussing on those angles for which discrepancies were noted. The cluster size was ~40 atoms with emitters in up to four layers. In increasing order of accuracy and complexity, the theoretical curves are SSC-PW (p final state), SSC-SW(p final state), SSC-SW (d+s final state), and MSC-SW (p final state). The MS theory curves shown are thus for a simple s -> p transition to simulate the correct p -> d + s transition; as noted earlier we do not expect this to affect the results strongly for such a high energy emphasizing forward scattering. And this is borne out by the near identity of the single scattering SW curves with p and d+s final states in the figure.

Due to the presence of long atomic chains in single crystal substrates it is expected, based on our experience with atomic chains, that the inclusion of MS will improve the agreement between theory and experiment along linear or nearly linear chain directions. For example, one approaches such chains at $\theta = 7^{\circ}$ and $\phi = 45^{\circ}$, where the experiment has a valley but all of the SS theory curves predict a peak. Grazing emission at $\phi = 45^{\circ}$ corresponds to emission along nearest-neighbor <110> directions for which MS effects should be strongest (cf. Figure 3.7). And indeed multiple scattering is found to very much reduce this peak in the calculated spectrum for $\theta = 7^{\circ}$, and to overall enhance the agreement with experiment. The same is true at $\theta = 10^{\circ}$ and $\phi = 45^{\circ}$, with the linear chain still in the [110]

direction. Again the agreement is best as to peak positions and fine strucure in MS, although a large cluster may be needed to accurately predict all relative intensities.

For $\theta = 18.4^{\circ}$ the agreement between SS theory and the experiment is satisfactory. This may be due to the fact that now the emission direction is nearly 20° away from the nearest-neighbor chain axis and hence that the MS effects are reduced. This was illustrated earlier using bent Cu chains (cf. Figure 3.11).

The next low-index chain axis as θ is increased is [111] at $\theta = 35.3^{\circ}$ and $\phi = 45^{\circ}$. We have previously noted that the [111] direction in Cu has a large enough nearest-neighbor distance that MS effects are much reduced compared to [101] or [001] (cf. Figures 3.7 and 3.13). However, looking along the [111] axis through an fcc unit cell, we find that there are in fact two equilateral triangles of 6 total scatterers comprised of the face centering atoms in the unit cell that have scattering angles small enough with respect to [111] (19.5° and 35.3°) to potentially complicate calculations along this axis through MS. In fact, in this direction, the experiment shows a prominent peak, but all of the single scattering theories show either a valley or only a very small peak. Including multiple-scattering is able to produce the correct peak shape along [111], but the peak height is still too small. Further study of this direction with larger clusters and the correct d + s final states is called for.

For the final example at $\theta = 45^{\circ}$, multiple scattering effects are expected to be most prominent along the nearest-neighbor [101] azimuth

for which $\phi = 0^{\circ}$. All of the theory curves here show at least qualitative agreement with experiment in predicting two strong peaks at $\phi = 0^{\circ}$, 90° and a weaker triplet at $\phi = 45^{\circ}$. However, all disagree in predicting a strong splitting of the $\phi = 0^{\circ}$, 90° peaks into doublets. The SSC-SW (p final state) and MSC-SW (p final state) curves agree best with experiment. Again, larger clusters and the correct d + s final states may be necessary to describe these data adequatly.

In general, these results for Ni(001) indicate that MS has improved the agreement between theory and experiment for these problem directions, suggesting that MS calculations will be of use in fully simulating x-ray photoelectron diffraction involving substrate emission. This agreement may be improved by using larger clusters, and correct final states, as well as including correlated vibrations and angular broadening.

3.5. APPLICATION TO ADSORBED OVERLAYERS:

3.5.1 CO/Fe(001) System:

In this section we assess the multiple-scattering effects arising for the case of an adsorbed molecule: CO on Fe(001). This system has recently been studied by Saiki et al. [32] using x-ray photoelectron diffraction. From previous studies including NEXAFS measurements [33], it was known that, for the α_3 state of this system, the C-O

bond is tilted away from the Fe(001) surface normal by about $45\pm10^{\circ}$. However, the tilt angle was not very precisely known and there was no information available on the azimuthal preference of this tilting. By comparing experimental polar and azimuthal results for C 1s emission to spherical-wave single-scattering results for a 7-atom cluster of $COFe_5$, it was possible to determine more precisely both aspects of structural information mentioned [32], as shown in the inset in Figure 3.29: the tilt is $55\pm2^{\circ}$ from the surface normal and it is preferentially along [100] azimuths. Single-scattering calculations have also been performed on much larger CO/Fe clusters but these results are very similar to those for the $COFe_5$ cluster [34]. In order to further estimate the vertical height of the C atom with respect to the first Fe plane, Saiki et al. used the intensity ratio I'/I of the 0^{th} and higher order diffraction peaks at $\phi = 0^{\circ}$ and 45° respectively. Comparison of experiment and single-scattering theory then suggested a C vertical height of either about 0.3 or about 0.6 Å.

In order to assess the influence of MS effects on this analysis, we have performed azimuthal multiple-scattering calculations for the 7-atom $COFe_5$ cluster. C 1s emission induced by a single polarization vector in the plane of x-ray incidence and electron emission was considered; the angle between photon incident and electron emission was 72°. Although the experiment was done with unpolarized radiation, prior experience indicates that the intensity due to the second polarization vector perpendicular to this plane is negligible. Once

again, no allowance was made for the finite angular acceptance cone of the spectrometer.

In Figure 3.29, we compare single-scattering and multiple-scattering results, including the ratio I'/I as a function of the C vertical distance. The single and multiple scattering curves are very similar, and as indicated in Table 3.1, the first order scattering level is where convergence is seen. This indicates that multiple-scattering effects are not major factors in using such high-energy x-ray photoelectron diffraction to determine the structural parameters of such a small-molecule/substrate system. This is fully consistent with our previous observation that there are no significant multiple-scattering contributions in high energy emission from two-atom clusters (cf. Figures 3.7, 3.9, 3.15, 3.17, and 3.19).

The numbers in Table 3.1 for this system also illustra that our 5% cut off criteria (which are based on the maximum amplitude in 3^{rd} order scattering) are too conservative for this case. That is all events up to 3^{rd} order are calculated even though those at 2^{nd} and 3^{rd} order are expected to be neglegible, and this leads also to calculating some 4^{th} order and 5^{th} order events. For this case, therefore our conservative cutoffs beginning after 3^{rd} order nonetheless included unnecessary higher order terms.

3.5.2. Scanned-Angle X-ray Photoelectron Diffraction Results for $(\sqrt{3}\times\sqrt{3})R30^\circ$ Ag on Si(111):

The Ag/Si(111) system has been studied using almost every technique in surface science, including Ag 3d x-ray photoelectron diffraction [29,35]. The most recent study by x-ray photoelectron diffraction [29] indicated that the Ag cannot be more than 0.5 Å below the surface, and furthermore concluded from an R-factor analysis of azimuthal Ag 3d results and SSC-SW calculations that the structure consists of two closely related types of Ag honeycomb domains that grow on the second Si layer, with the top Si layer missing. This geometry has been shown in Figure 3.24. For this geometry, linear Ag-Si-Si-Si chains can be seen, e.g., along the long arrow at $\phi \sim 160^\circ$. Especially at low photoelectron emission angles relative to the surface, these chains could cause defocussing or other MS effects near the chain axis and hence the resulting MS intensity patterns could be different from their SS counterparts.

We have thus simulated azimuthal intensity patterns for three take-off angles of 4.1°, 10.0° and 14.7° spanning the range studied as a function of the percentage of domain 1 (see Figure 3.24). As noted previously, the kinetic energy for the Ag $3d_{5/2}$ photoelectrons is 1114 eV. The proper $d \rightarrow f + p$ final state with interference is considered. The Ag photoemitter is placed 0.2 Å below the surface and the compression parameter s for the Ag trimers is 0.86 Å, with both parameters being found via a SS R-factor analysis [29].

The corresponding R-factors are shown in Figure 3.30. The shape of the individual R-factor curves are very simillar in SS and MS, although the SS minima are lower and the MS curves are generally flatter about their minima. The total R-factor is a sum of individual R-factors for the three θ values involved, with each R value being weighted by the experimental anisotropy at that θ. The total SS R-factor, which is smaller than the total MS R-factor, indicates a mixture of 40% of domain 1 to 60% of domain 2. The ratio indicated by the MS total R-factor is nearly 50:50. The experiment-theory comparison in Figure 3.26 is for the SS-derived value of 40% of domain 1. Including MS yields only minor changes relative to SS, and the overall fits to experiment are very little different for the two sets of curves (as indicated in Figure 3.26), even though the total SS R-factor is slightly lower. The remaining small discrepancies between experiment and theory could be due to: the use of too small a cluster (here 22 atoms for SS and MS), the need to more accurately allow for vibrational attenuation of diffraction effects, slight errors in the calibration of the experimental theta scale, and/or the need for further structural refinement.

Finally, the event count versus order in Table 3.1 makes it clear that, for this particular geometry of Ag/Si(111), at least 3^{rd} order events must be included. These results thus cast doubt on the recent use by Fujikawa and Hosoya [36] of only 2^{nd} order events in analyzing another proposed structure for this system.

3.6. CONCLUSIONS:

When adapted to a multiple-scattering treatment of photoelectron diffraction and Auger electron diffraction, the new separable Green's function approach of Rehr and Albers yields results that are in excellent agreement with prior multiple-scattering results in the literature spanning energies from ~80 eV to 1000 eV. This approach also has certain advantages as to the versatility and speed of convergence. The code we have written to implement it should be applicable to a broad range of both scanned-angle and scanned-energy problems. Multiple-scattering is important when scattering along linear chains of atoms is involved, with the most obvious effect being a loss of intensity due to defocussing, but peak narrowing also being seen. From calculations on linear chains, we conclude that the amount of MS defocussing along the chain axis depends on the interatomic distances as well as the strength of the scatterer (i.e., its atomic number). Other parameters such as the radius of the muffin-tin potential, the inner potential, the electron mean free path, and the degree of angular broadening have a relatively minor effect on this defocussing. Incorporating the correct final ℓ_f state is not important in geometries emphasizing high-energy forward scattering, but is quite important for larger scattering angles and/or lower energies. This was demonstrated for Cu chains and for $(\sqrt{3}\times\sqrt{3})R30^\circ$ Ag on Si(111). In Ni $2p_{3/2}$ emission from a Ni(001) substrate, the agreement between theory and experiment was improved for certain

near-chain directions when multiple-scattering was included. But for CO/Fe(001), where no long chains of atoms are present, single-scattering theory was adequate. For the case of a recently proposed structure for ($\sqrt{3}\times\sqrt{3}$)R30° Ag on Si(111), the difference between single- and multiple-scattering is minor and both analyses point to the same two-domain model.

REFERENCES:

[1]. (a) C.S. Fadley, Prog. in Surf. Sci. 16 (1984) 275;
(b) C.S. Fadley, Physica Scripta T 17 (1987) 39;
(c) C.S. Fadley, in: Synchrotron Radiation Research: Advances in Surface Science, Ed. R.Z. Bachrach (Plenum, New York, 1990), in press.

[2]. (a) S.A. Chambers, I.M. Vitomirow, S.B. Anderson, H.W. Chen, T.J. Wagener, and J.H. Weaver, Superlatt. and Microstruct. 3 (1987) 563, and references therein; (b) R.A. Armstrong and W.F. Egelhoff, Surf. Sci. 154 (1985) L225.

[3]. M. Sagurton, E.L. Bullock, and C.S. Fadley, (a) Phys. Rev. B 30 (1984) 7332; and (b) Surf.Sci. 182 (1987) 287.

[4]. A. Liebsch, Phys. Rev. Lett. 32 (1974) 1203; A. Liebsch, Phys. Rev. B 13 (1976) 544.

[5]. T. Fujikawa, J. Phys. Soc. Jpn. 50 (1981) 1321; 51 (1982) 251; 54 (1985) 2747; J. Elect. Spect. 26 (1986) 4350.

[6]. S.Y. Tong, H.C. Poon, and D.R. Snider, Phys. Rev. B 32 (1985) 2096.

[7]. (a) J.J. Barton and D.A. Shirley, Phys. Rev. B 32 (1985) 1892; J.J. Barton and D.A. Shirley, Phys. Rev. B 32 (1985) 1906; J.J. Barton, Ph.D. Thesis, University of California at Berkeley (1985); (b) J.J. Barton, S.W. Robey and D.A. Shirley, Phys. Rev. B 34 (1986) 778.

[8]. W.F. Egelhoff, Phys. Rev. Lett. 59 (1987) 559.

[9]. J.-C. Tang, J. Vac. Sci. Technol. A 5 (1987) 658.

[10]. (a) M.-L. Xu and M. Van Hove, Surf. Sci. 207 (1989) 215;
(b) M.-L. Xu, J.J. Barton, and M.A. Van Hove, Phys. Rev. B 39 (1989) 8275.

[11]. A.P. Kaduwela, G.S. Herman, D.J. Friedman, C.S. Fadley, and J.J. Rehr, Physica Scripta 41 (1990) 948.

[12]. H. Hilferink, E. Lang, and K. Heinz, Surf. Sci. 93 (1980) 398; R.G. Weissman and K. Muller, Surf. Sci. Repts. 1 (1981) 251; P.J. Orders, R.F. Connelley, N.F.T. Hall, and C.S. Fadley, Phys. Rev. B 24 (1981) 6161.

[13]. J.J. Rehr and E.A. Albers, Phys. Rev. B 41 (1990) 8139; with additional details provided in J.J. Rehr and J. Mustre de Leon, private communication.

[14]. S.M. Goldberg, C.S. Fadley, and S. Kono, J. Electron Spectrose. Relat. Phenom., 21 (1981) 285.

[15]. A.P. Kaduwela, Ph.D. Dissertation, University of Hawaii (1991), Chapter 2. Various details concerning the derivation of equations and the structure and use of the computer program are found here.

[16]. K. Gottfried, Quantum Mechanics Volume 1: Fundamentals, 6th ed. (Wiley, New York,1970).

[17]. D.J. Friedman and C.S. Fadley, J. Electron Spectrosc. Relat. Phenom. 51 (1990) 689.

[18]. E.L. Bullock, unpublished results.

[19]. G. Beni and P.M. Platzmann, Phys. Rev. B 14 (1976), 1514

[20]. P.A. Lee, Phys. Rev. B 13 (1976) 5261.

[21]. J.B. Pendry, Low Energy Electron Diffraction (Academic, London, 1974) and private communication.

[22]. B. Sinkovic, P.J. Orders, C.S. Fadley, R. Trehan, Z. Hussain and J. Lecante, Phys. Rev. B 30 (1984) 1833.

[23]. M. Sagurton and C.S. Fadley, unpublished results.

[24]. S.Y. Tong and C.H. Li, Critical Review in Solid State and Materials Science (Chemical Rubber, Cleveland, 1981), p. 209.

[25]. A. Szoke in: Short Wavelength Coherent Radiation: Generation and Application, Eds. D.T. Attwood and J. Bokor, AIP Conference Proceedings No. 147 (American Institute of Physics, New York, 1986); J.J. Barton, Phys. Rev. Lett. 61 (1988) 1356; G.R. Harp, D.K. Saldin, and B.P. Tonner, Phys. Rev. Lett. 65 (1990) 1012.

[26]. B.P. Tonner, private communication; S. Thevuthasan, private communication.

[27]. T.T. Tran, D.J. Friedman, Y.J. Kim, G.A. Rizzi, and C.S. Fadley, to appear in the "Structure of Surfaces III" in the Springer Series in Surface Science, Eds. S.Y. Tong, M.A. Van Hove, K. Takayanagi, and X.D. Xide, (Springer-Verlag, Berlin, 1991).

[28]. H.A. Aebischer, T. Greber, J. Osterwalder, A.P. Kaduwela, D.J. Friedman. G.S. Herman, and C.S. Fadley, to appear in Surf. Sci.

[29]. E.L. Bullock and C.S. Fadley, Phys. Rev. B 41 (1985) 1212.

[30]. (a) E.A. Stewart, MS Thesis, University of Hawaii (1987);
(b) J. Osterwalder, E.A. Stewart, D. Cyr, C.S. Fadley,

J. Mustre de Leon, and J.J. Rehr, Phys Rev B 35 (1987) 9859; (c) J. Osterwalder, A. Stuck, D.J. Friedman, A. Kaduwela, C.S. Fadley, J. Mustre de Leon, and J.J Rehr, Physica Scripta 41 (1990) 990.

[31]. S.A. Chambers, I.M. Vitomirow, S.B. Anderson, H.W. Chen, T.J. Wagner, and J.H. Weaver, Phys. Rev. B 33 (1986) 8810.

[32]. R.S. Saiki, G.S. Herman, M. Yamada, J. Osterwalder, and C.S. Fadley, Phys. Rev. Lett. 63 (1989) 283.

[33]. D.W. Moon, S. Cameron, F. Zaera, W. Eberthardt, R. Carr, S.L. Bernasek, J.L. Gland, and D.J. Dwyer, Surf. Sci. 180 (1987) L123.

[34]. G.S. Herman and C.S. Fadley, unpublished results.

[35]. S. Kono, K. Higashiyama, and T. Sagawa, Surf. Sci. 165 (1986) 21.

[36]. T. Fujikawa and M. Hosoya, J. Phys. Soc. Jpn. 59 (1990) 3750.

Table 3.1.

Indication of the number of events versus scattering order and the convergence with order for various cases considered here. A cutoff of 5% of the maximum 3rd order amplitude is used for continuing to 4th, 5th, and higher order events.

Case:	S/Ni(001)	S/Ni(001)	S/Ni(001)	Al Chain	CO/Fe(001)	Ag/Si(111)
Figure:	3.3	3.4	3.5	3.17	3.29	3.26
Cluster size:	39	37	36	9	7	23
Number of events#:						
1st	3838	2701	560	648	360+	861
2nd	145844	99937	19600	5184	2160	9261
3rd	5542072	3697669	686000	41472	12960	379701+
4th	4184712+	2203646+	38780+	36288	2880	2583max
5th	429400max	450475max	31675max	44960	2160max	-
6th	-	-	-	31136	-	-
7th	-	-	-	12656	-	-
8th	-	-	-	3136+	-	-
9th	-	-	-	360*	-	-
10th	-	-	-	0max	-	-

Actually equal to the number of cycles of retrieving elements in the scattering matricies at each order.

+ Already converged at this order as judged by equality of intensities to within 1.0% between this order and the next order.

* Convergence judged by the number of events.

max Maximum order considered.

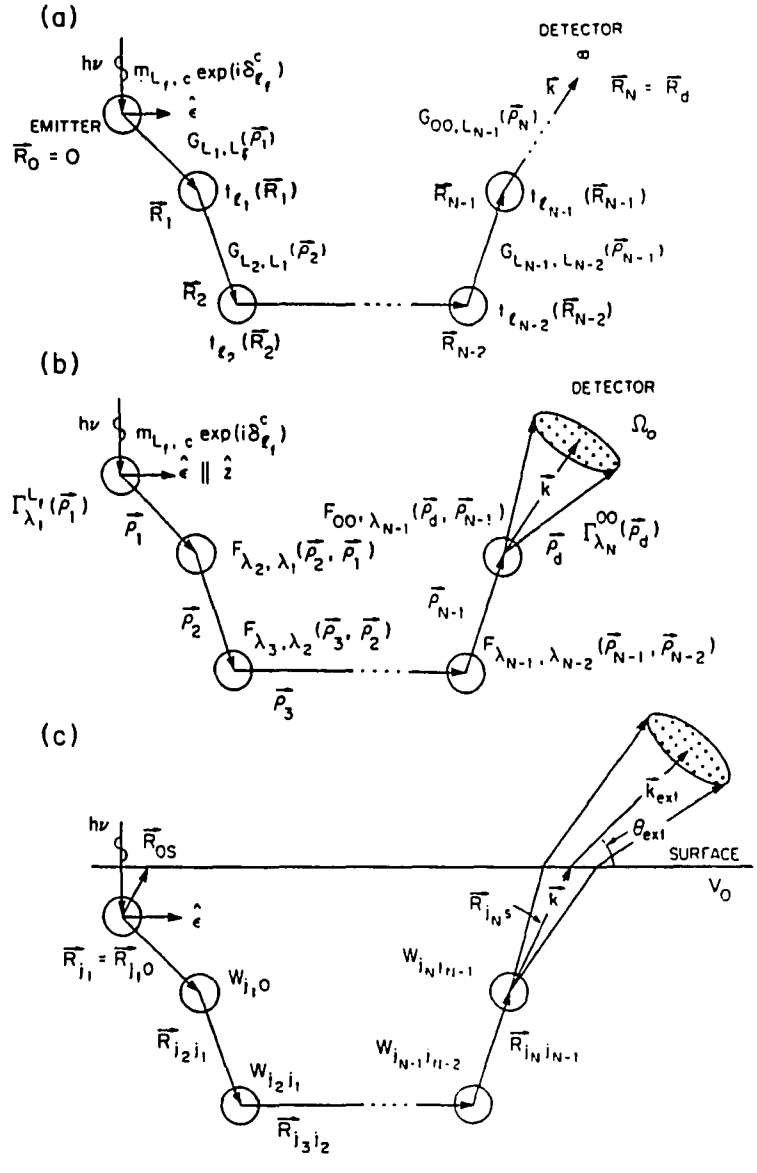

Figure 3.1. The geometry of the scattering process: (a) the initial general expression in terms of the free particle propagator $G_{L,L'}$ and the t-matrix elements t_ℓ; (b) the separation into scattering matrices $F_{\lambda,\lambda'}$ and termination factors $\Gamma^{L_f}_{\lambda_1}$ and $\Gamma^{00}_{\lambda_N}$ that is obtained in the Rehr-Albers method [13]; (c) the inclusion of Debye-Waller and inelastic damping, with $\vec{R}_N$ now defined for convenience as the last scatterer instead of the detector as in (a) and (b).

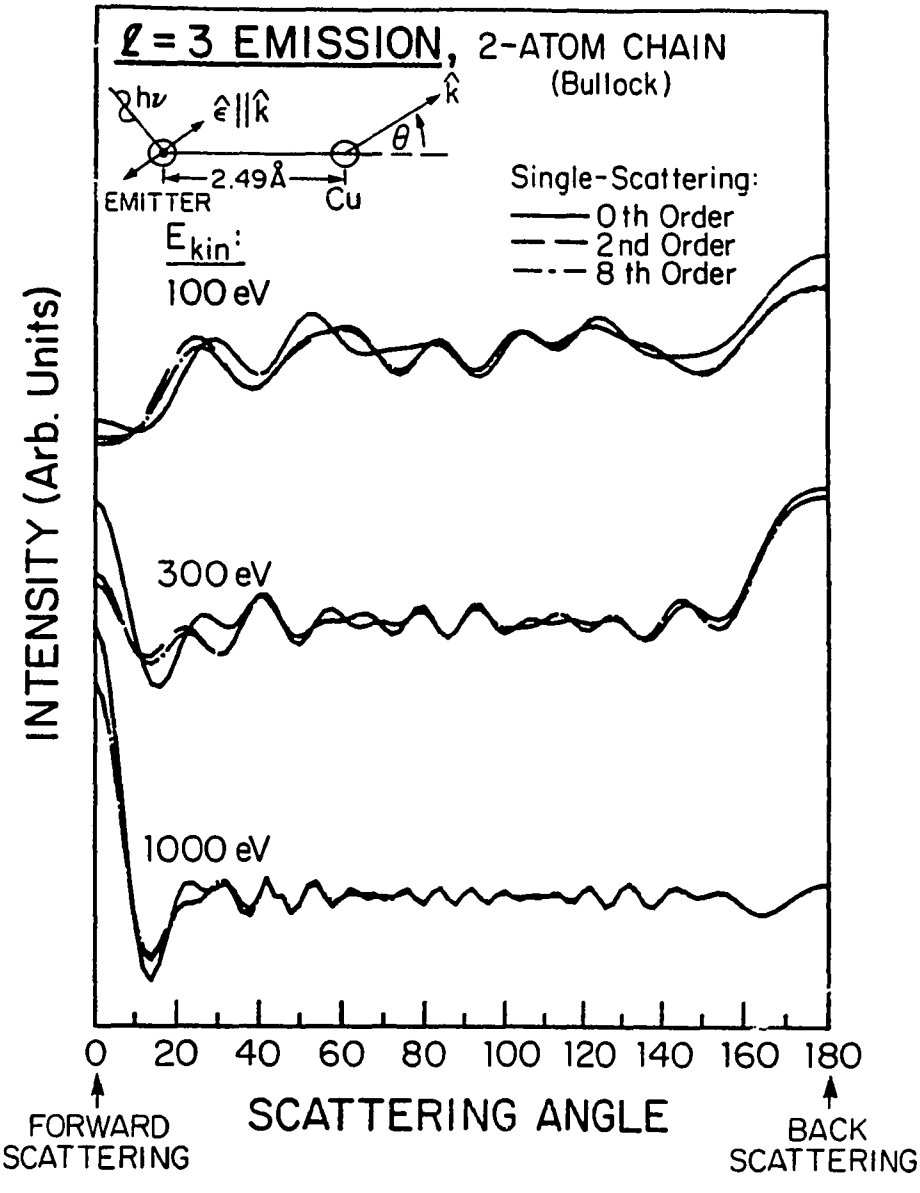

Figure 3.2. The degree of convergence with order in the Rehr-Albers approximation. Model single-scattering calculations are shown at 0^{th} order, 2^{nd} order (the order used throughout this paper), and a much higher 8^{th} order for hypothetical f → g emission from a 2-atom chain a with Cu scatterer (from Bullock, reference 18). Results are shown at 100 eV, 300 eV, and 1000 eV.

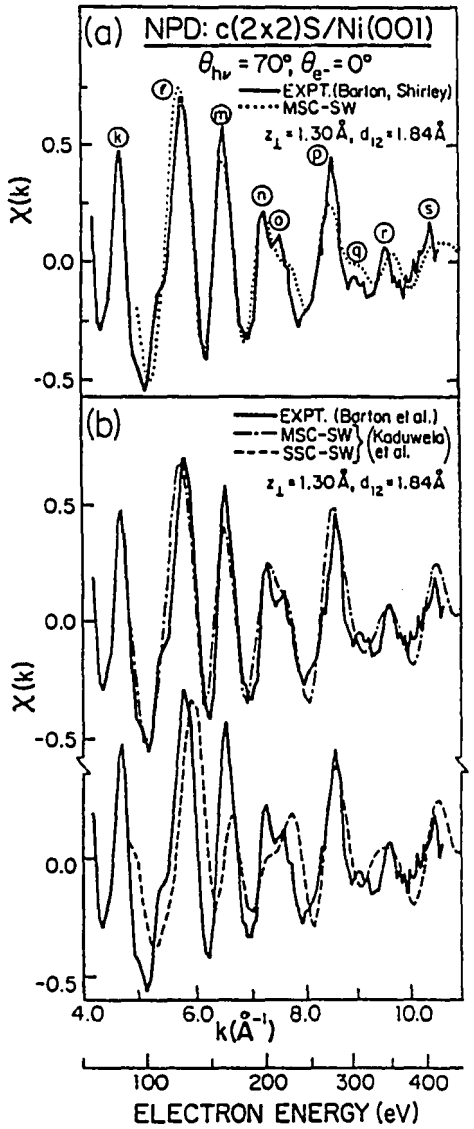

Figure 3.3. (a) Experimental and theoretical scanned-energy (ARPEFS) curves for S 1s emission from c(2x2)S/Ni(001) by Barton et al. [7(b)]. The incoming radiation makes a 70° angle with the surface normal, and the photoelectrons are emitted along the surface normal. (b) Single and multiple-scattering simulations of the experimental data in (a) using the present method.

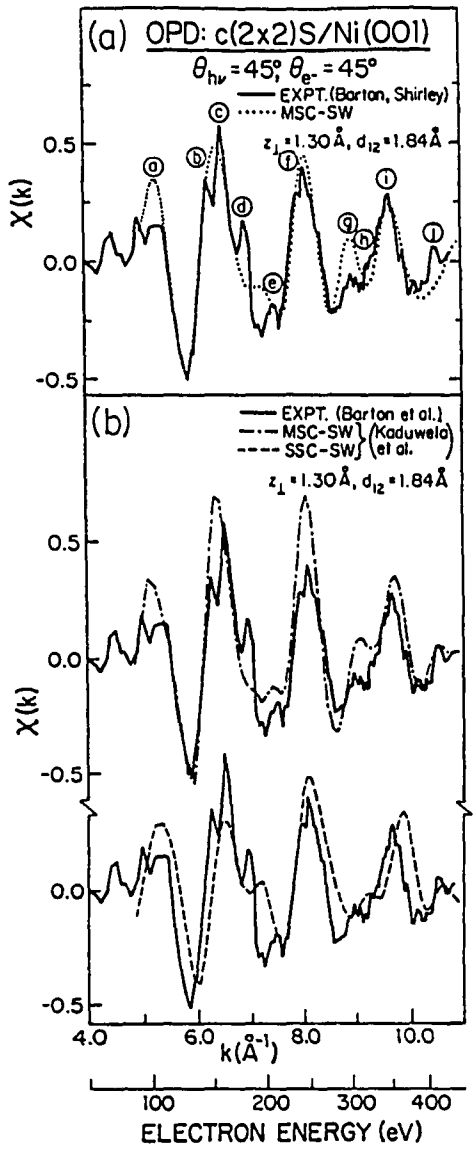

Figure 3.4. (a) Experimental and theoretical scanned-energy (ARPEFS) curves for S 1s emission from c(2×2)S/Ni(001) by Barton et al. [7(b)]. The incoming radiation makes a 45° angle with the surface normal, and the photoelectrons are emitted at a 45° angle with respect to the surface normal. (b) Single and multiple-scattering simulations of the experimental data in (a) using the present method.

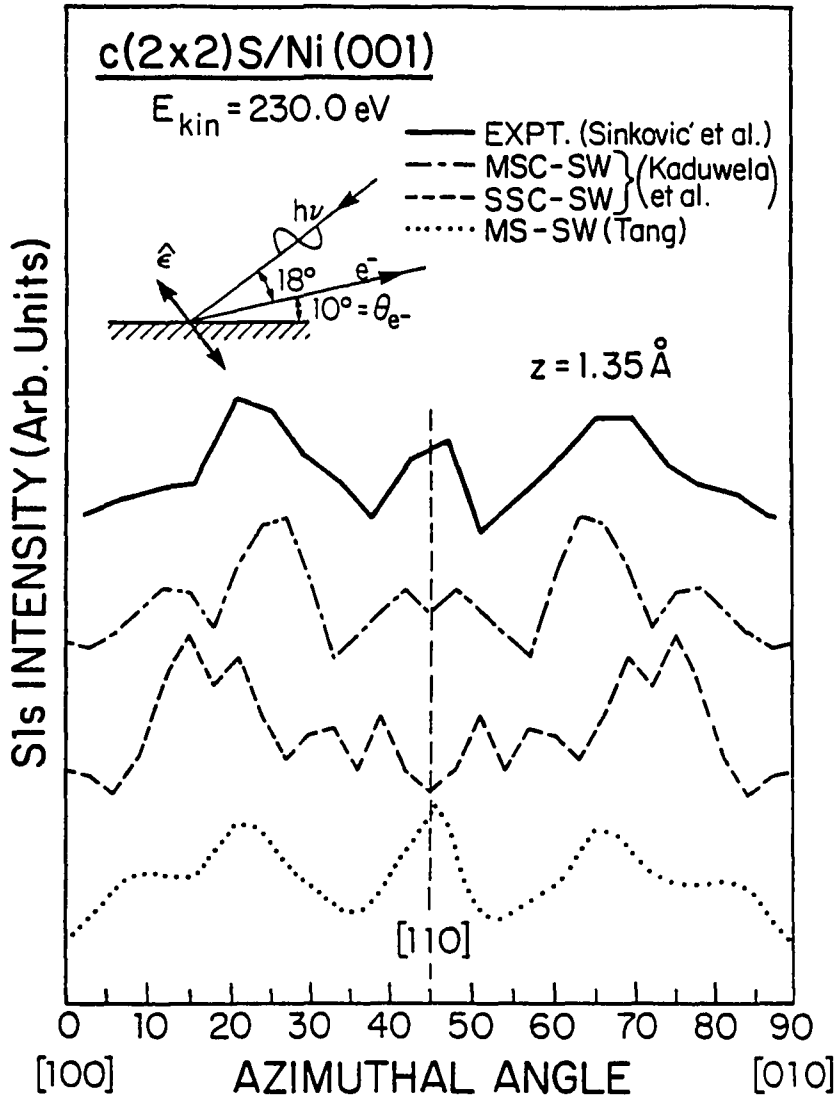

Figure 3.5. Azimuthal photoelectron diffraction for S 1s emission from c(2×2)S/Ni(001) at 230.0 eV. The experimental geometry is shown in the inset. The experimental data are from Reference 22, the bottom MS-SW curve is from Reference 9, and the rest of the theoretical curves are from this work.

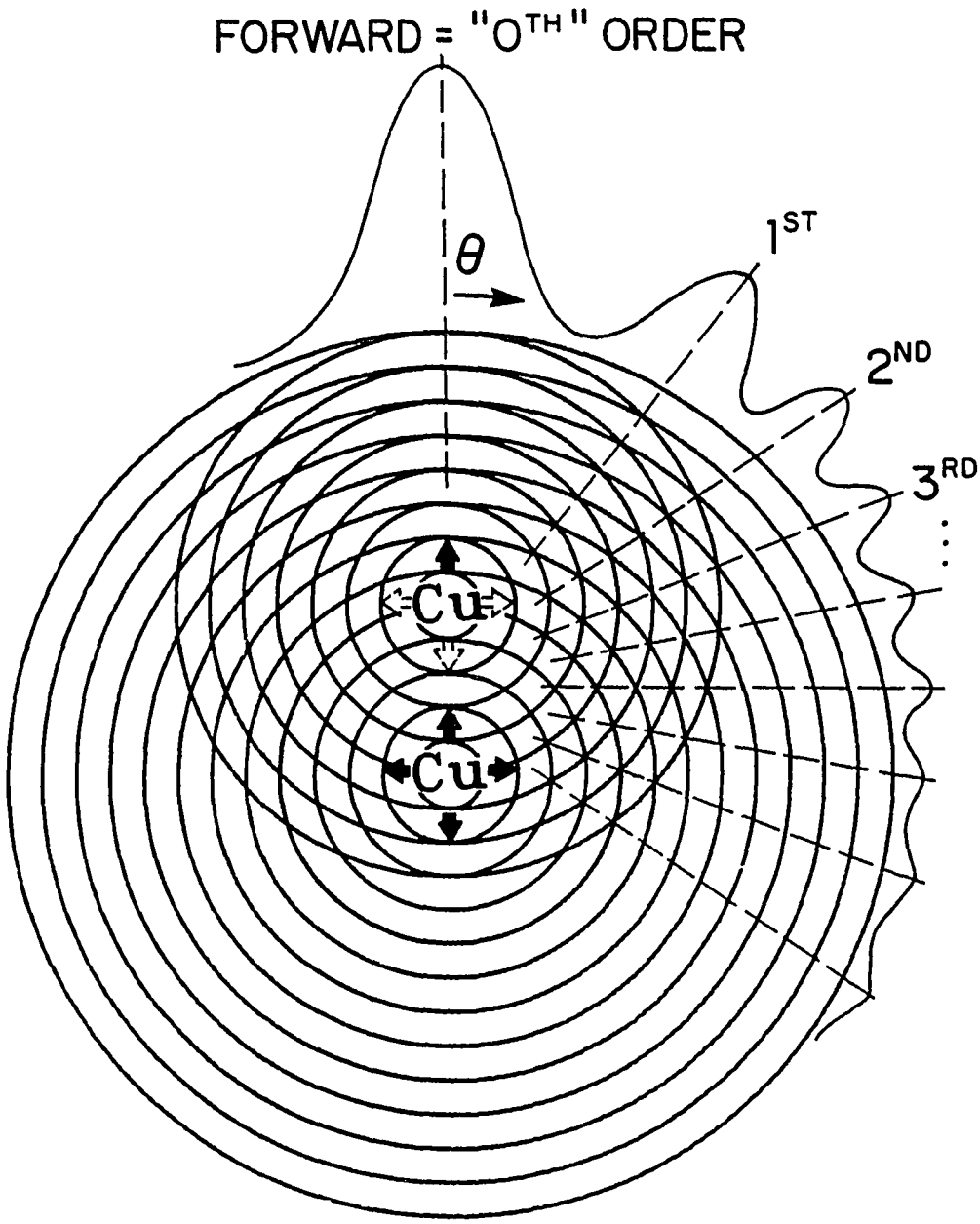

Figure 3.6. Illustration of the origin of the diffraction features expected in emission from a 2-atom chain, with the 0^{th} order (forward scattering) peak and the higher-order peaks labelled. The scattering phase shift is for simplicity assumed to be zero.

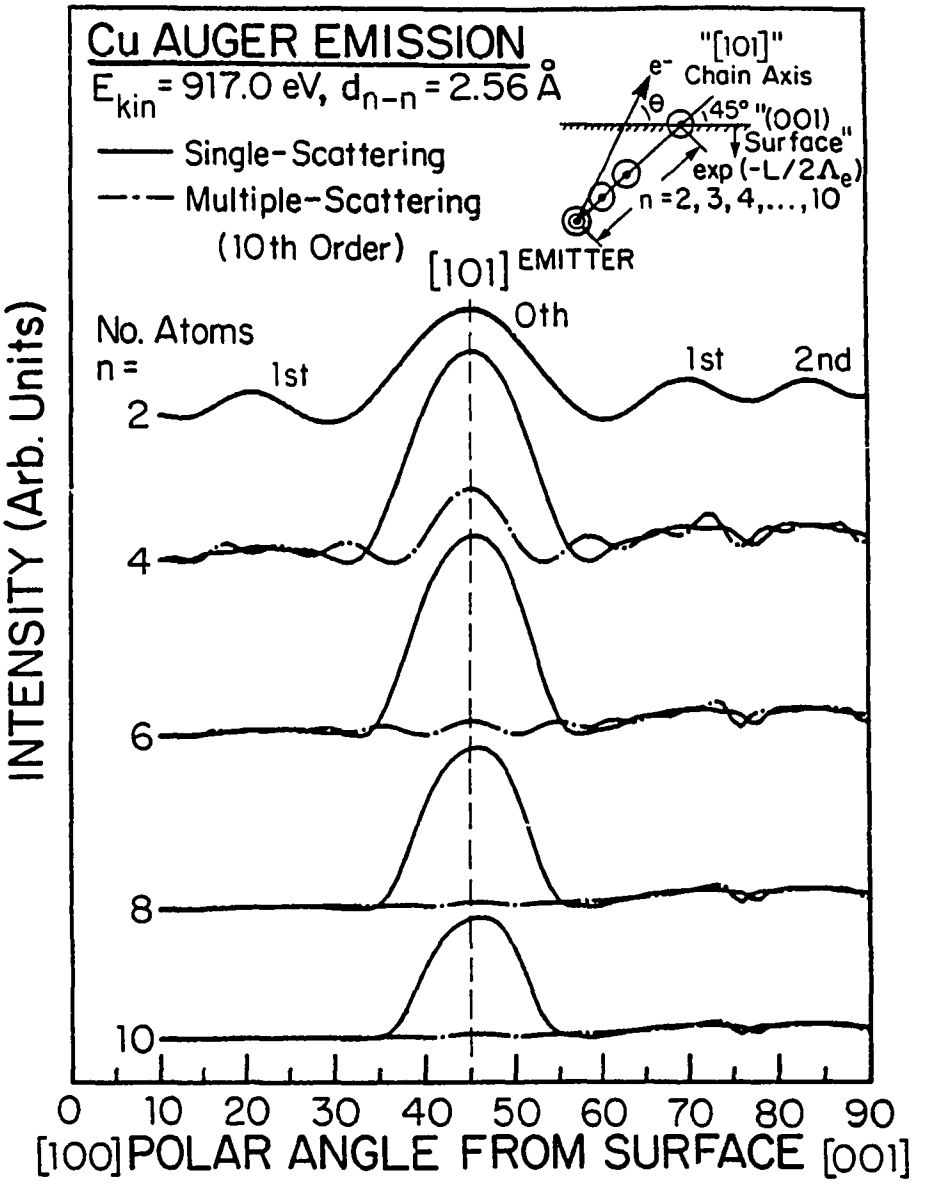

Figure 3.7. Single and multiple scattering calculations of Auger electron diffraction from linear Cu [101] chains at 917.0 eV.

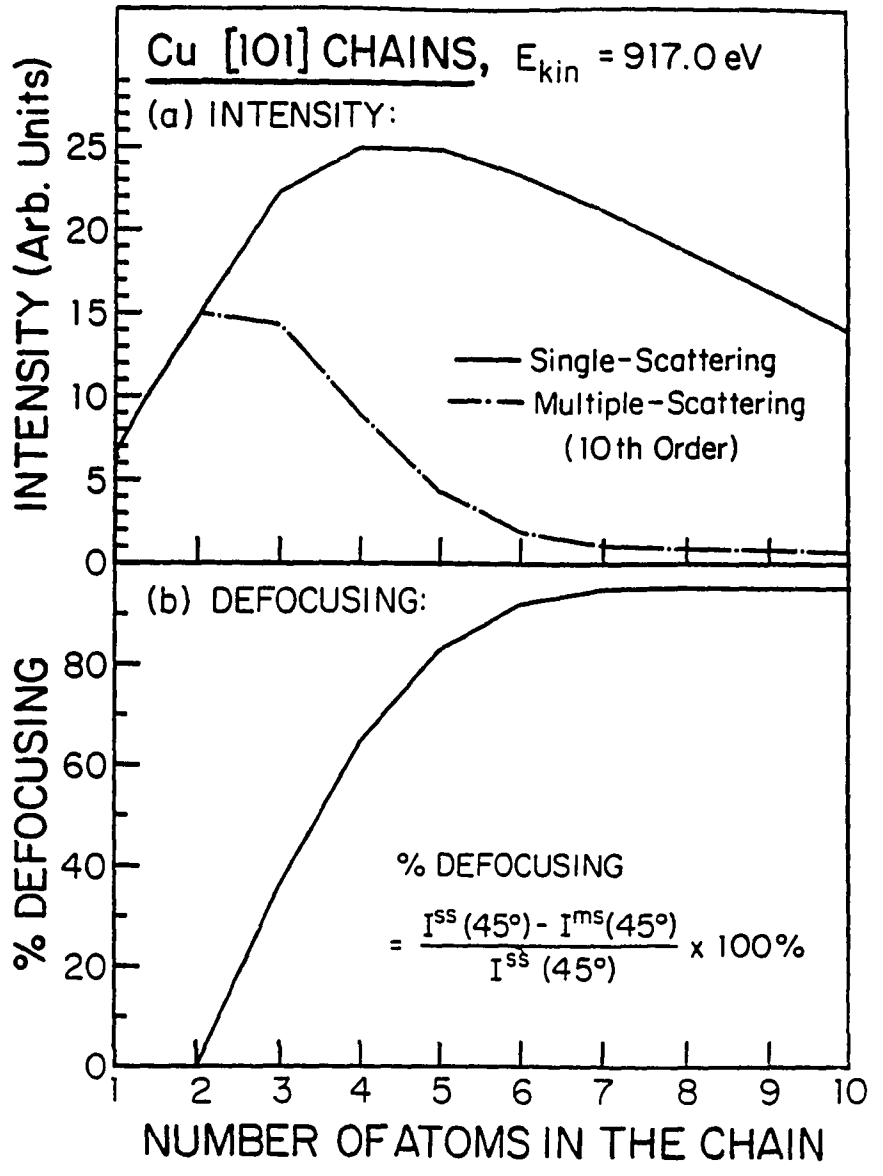

Figure 3.8. (a) Single and multiple scattering Auger electron diffraction intensities direcly along linear Cu [101] chains at 917 eV as a function of the number of atoms in the chain. (b) The % defocussing (defined in the inset) in Auger electron diffraction intensity along linear chains of Cu [101] at 917 eV.

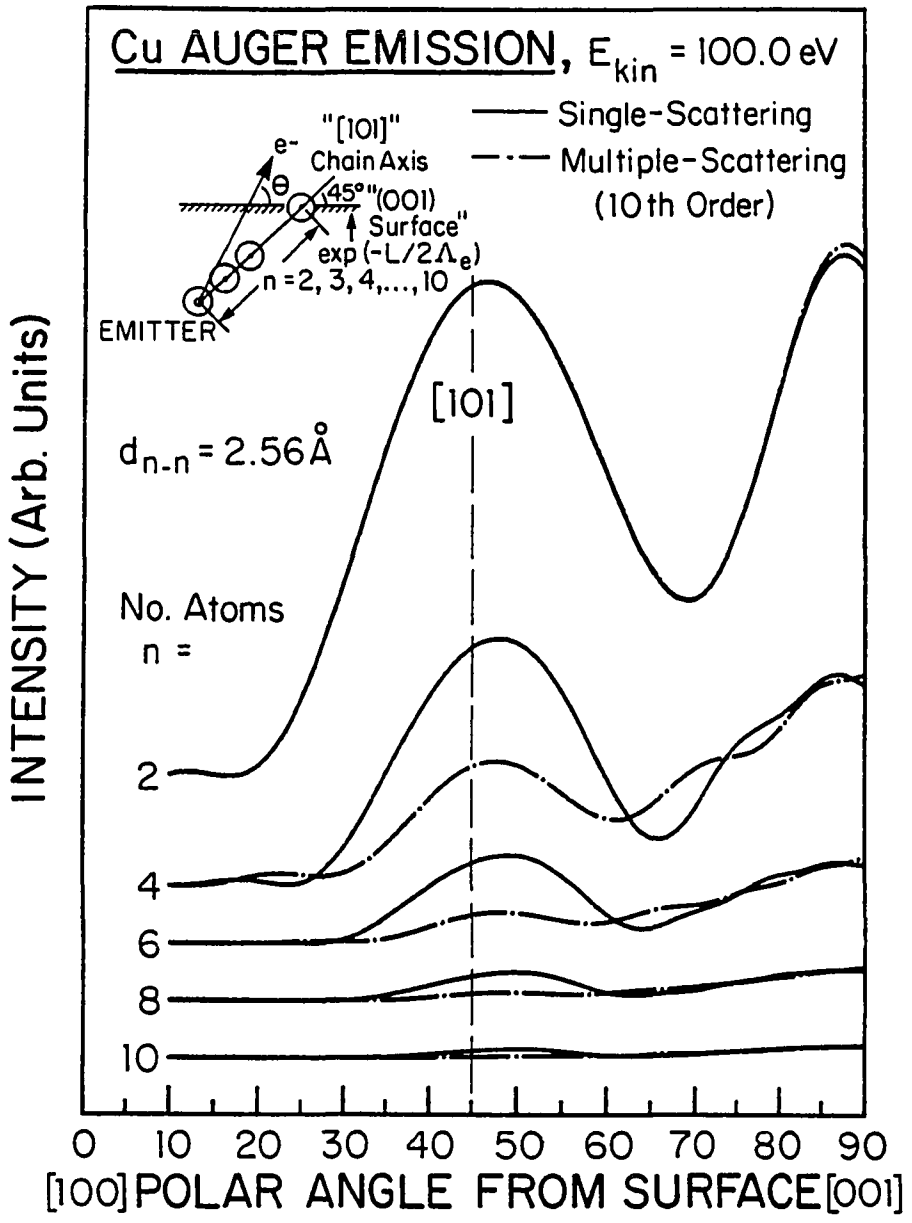

Figure 3.9. Same as Figure 3.7, but for 100 eV.

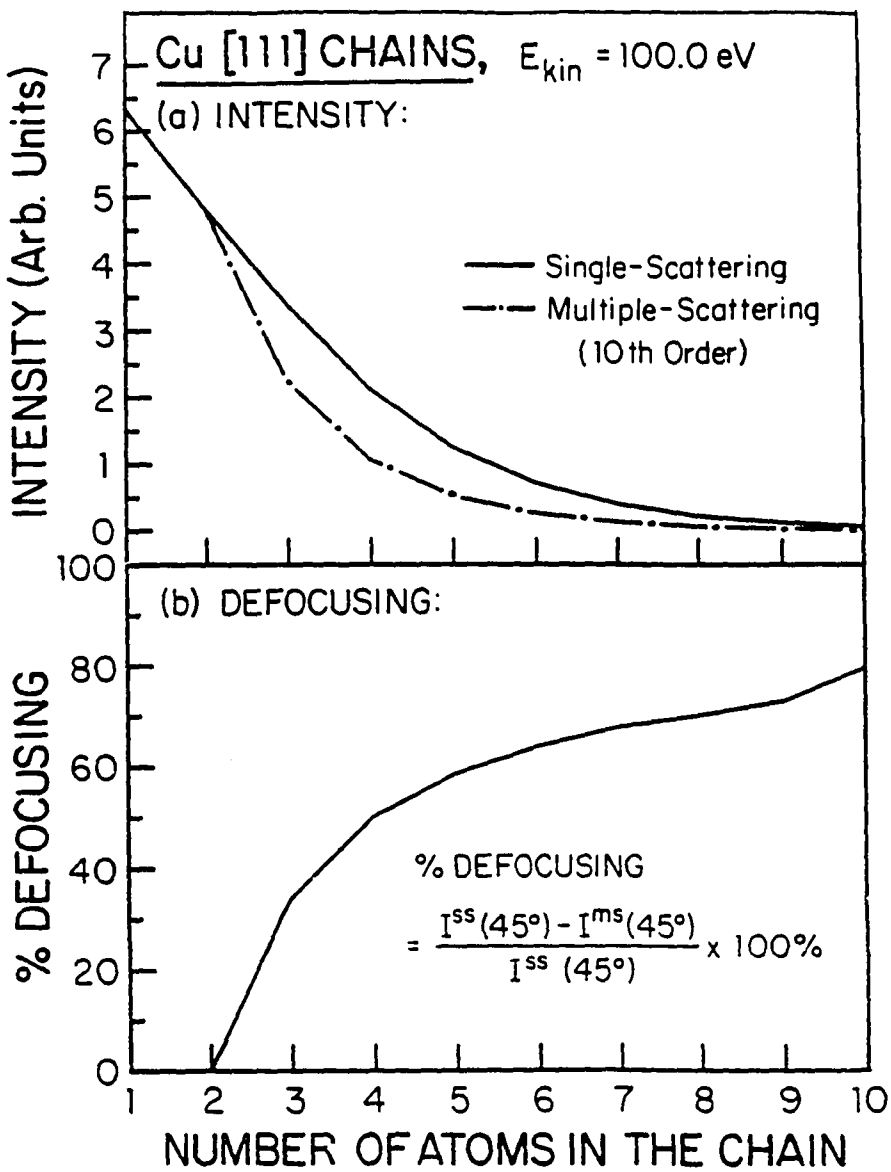

Figure 3.10. (a) Same as Figure 3.8(a), but for 100 eV. (b) Same as Figure 3.8(b), but for 100 eV.

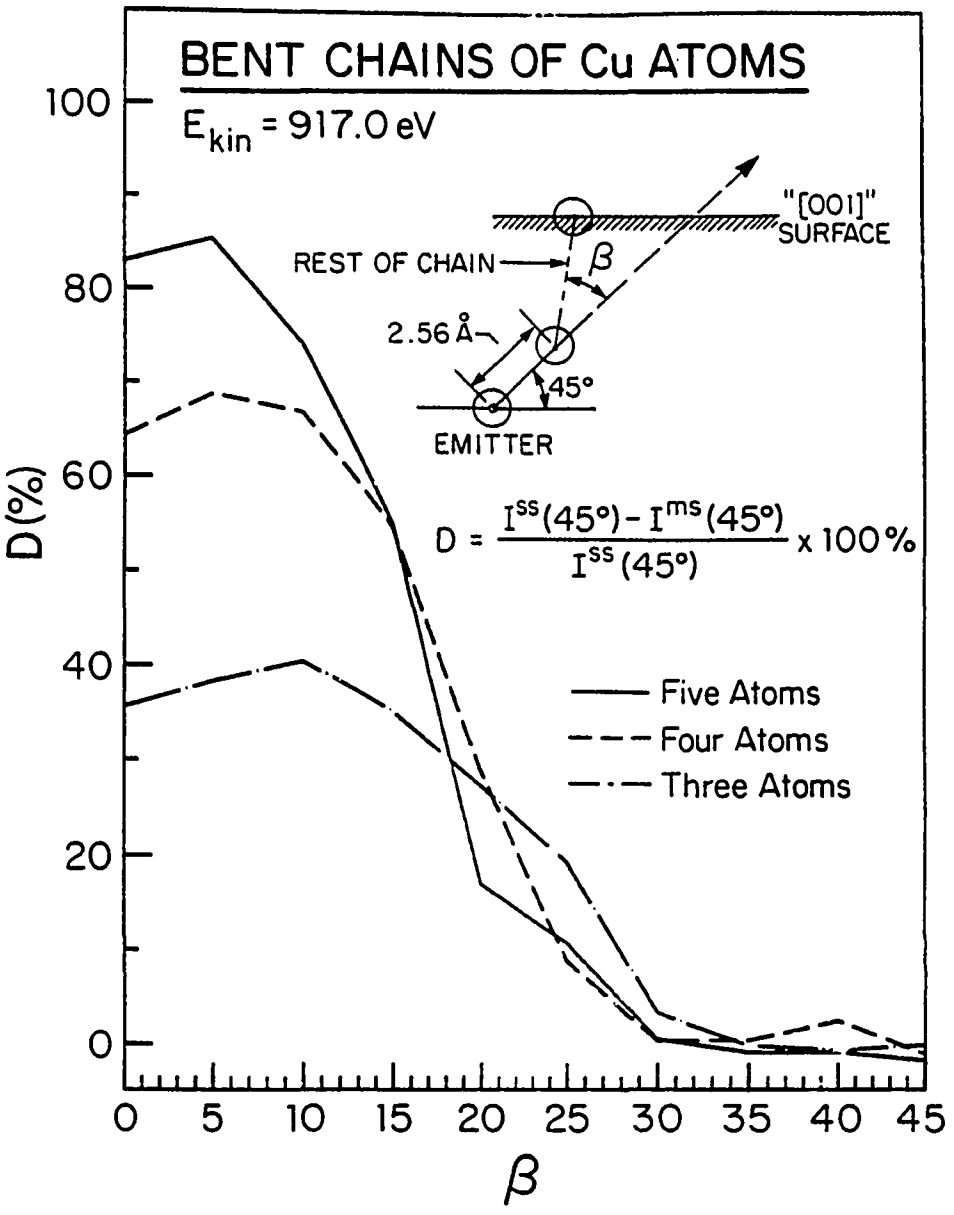

Figure 3.11. Defocussing of the Auger electron diffraction intensity at 917 eV in bent Cu [101] chains as a function of the bend angle.

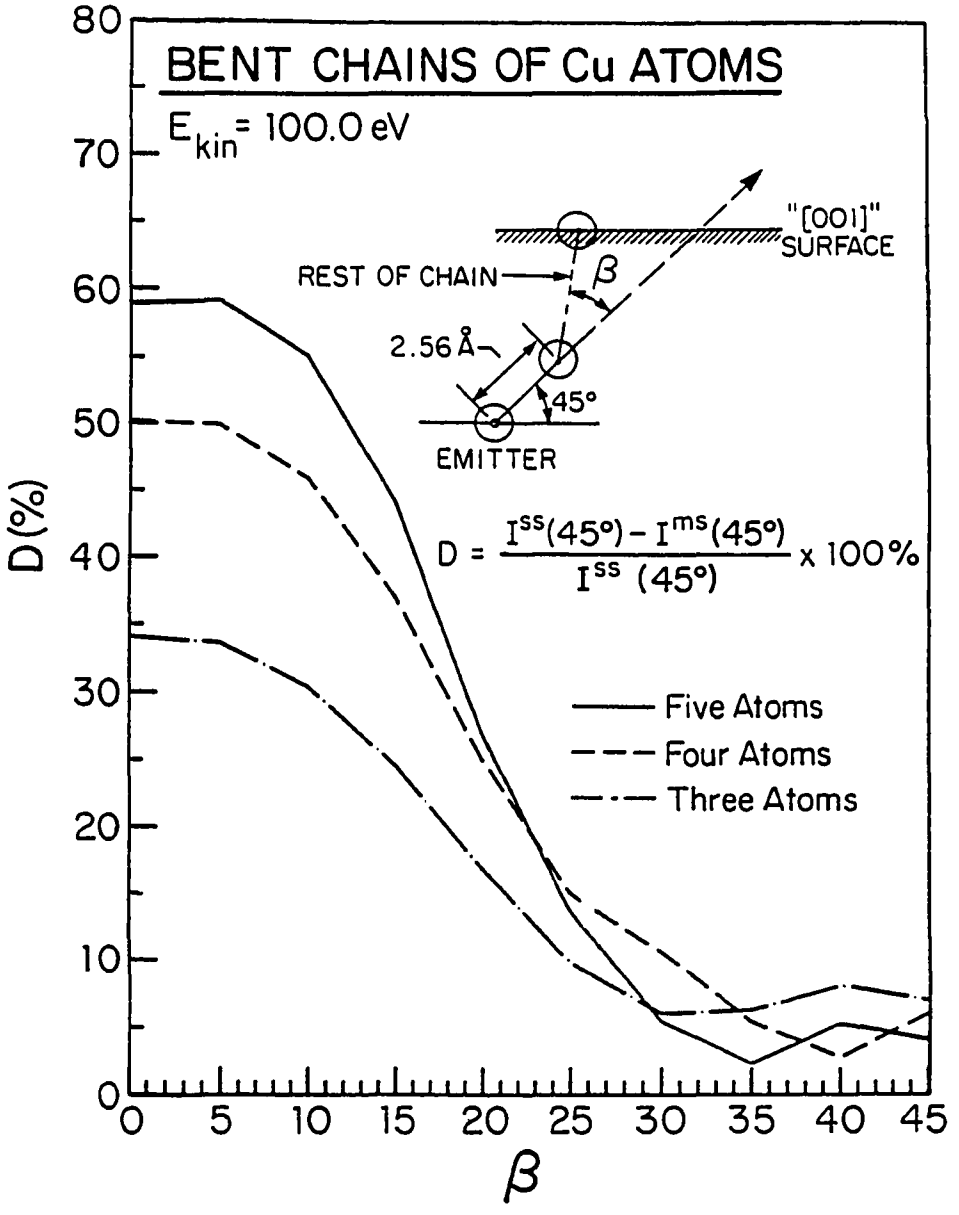

Figure 3.12. Same as Figure 3.11, but for 100 eV.

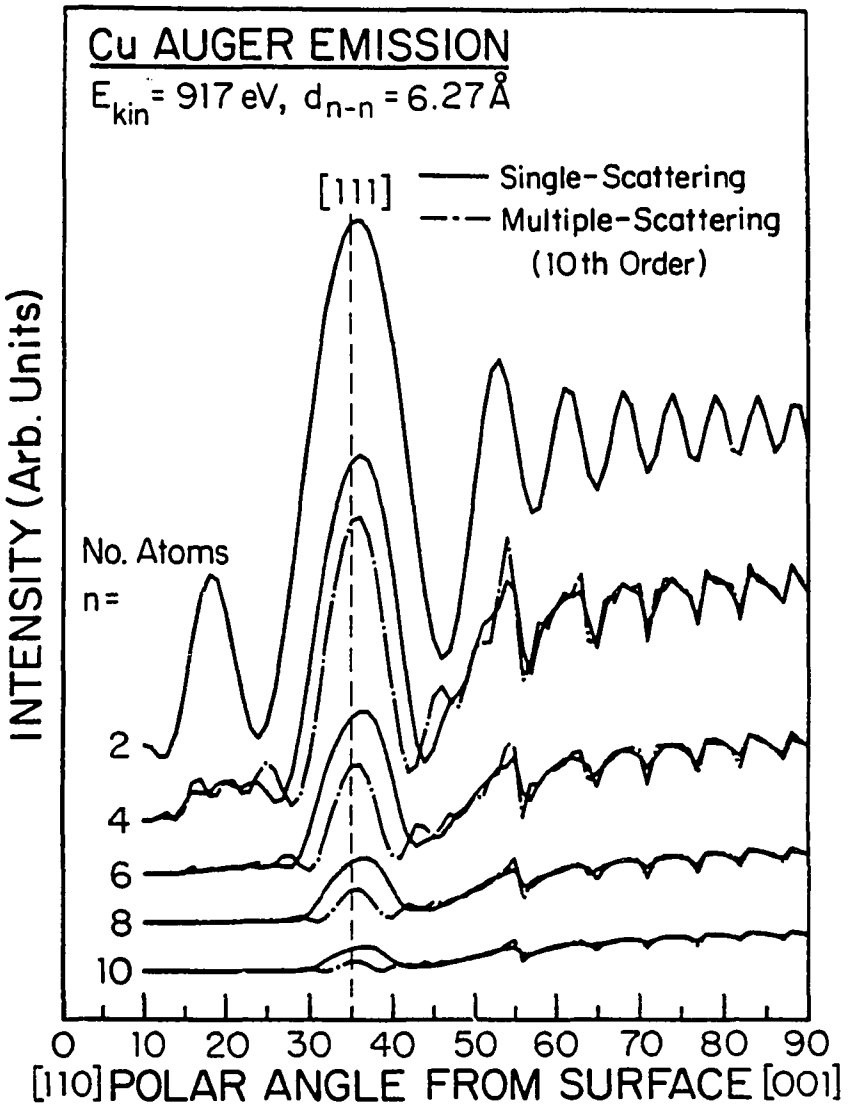

Figure 3.13. Same as Figure 3.7, but for Cu [111] chains.

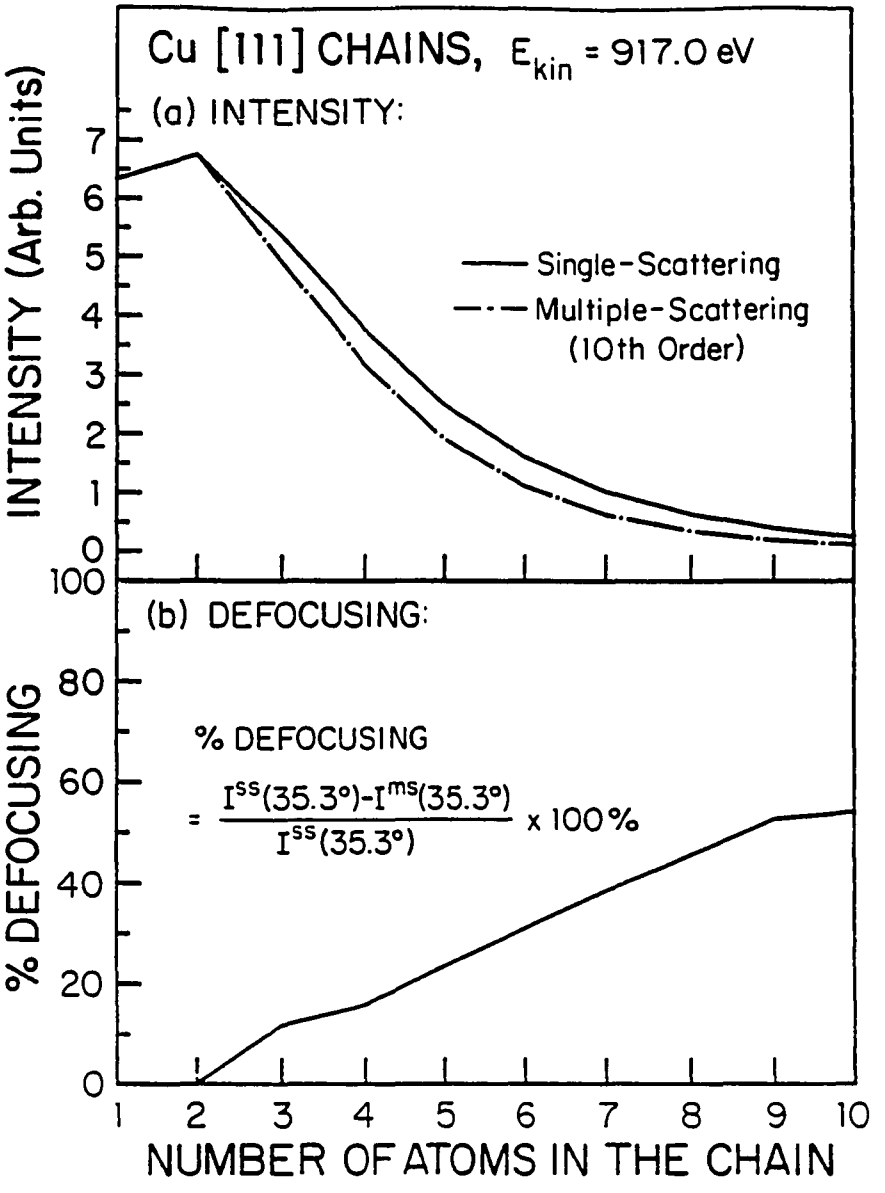

Figure 3.14. Same as Figure 3.8, but for Cu [111] chains.

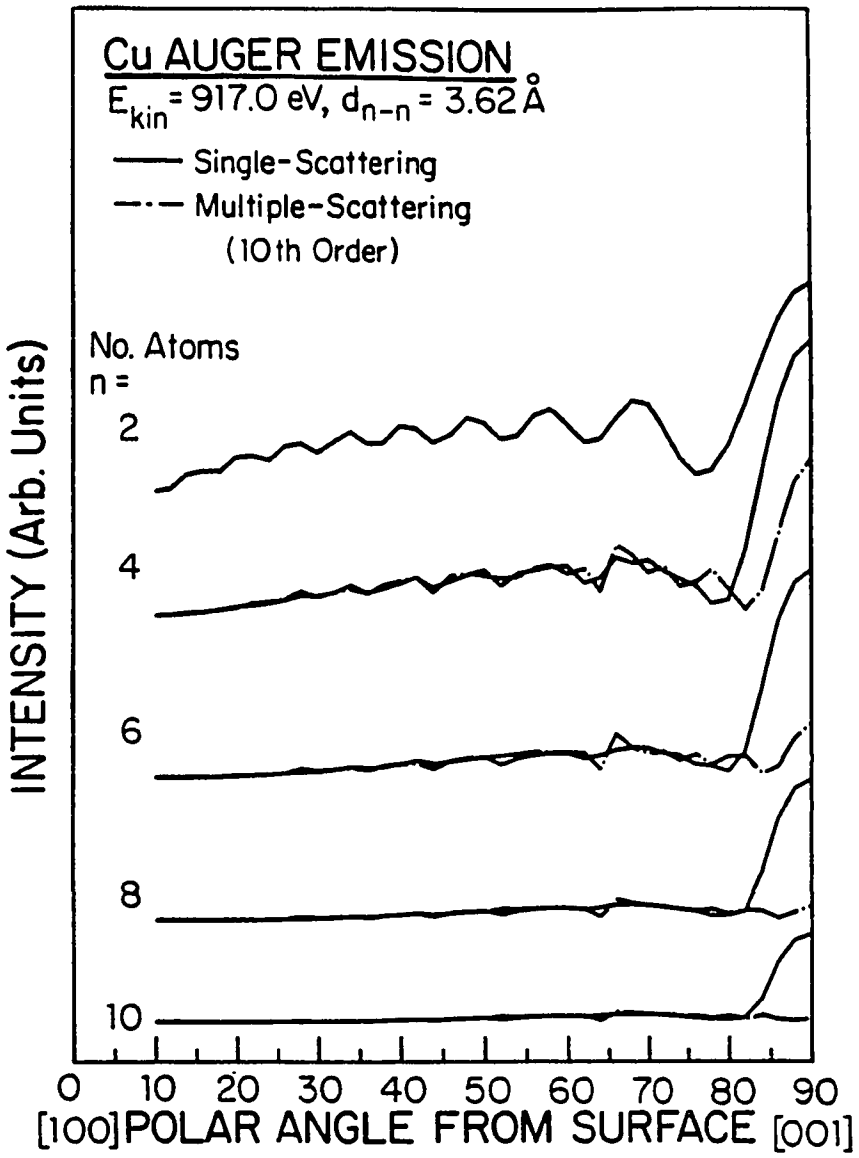

Figure 3.15. Same as Figure 3.7, but for Cu [001] chains.

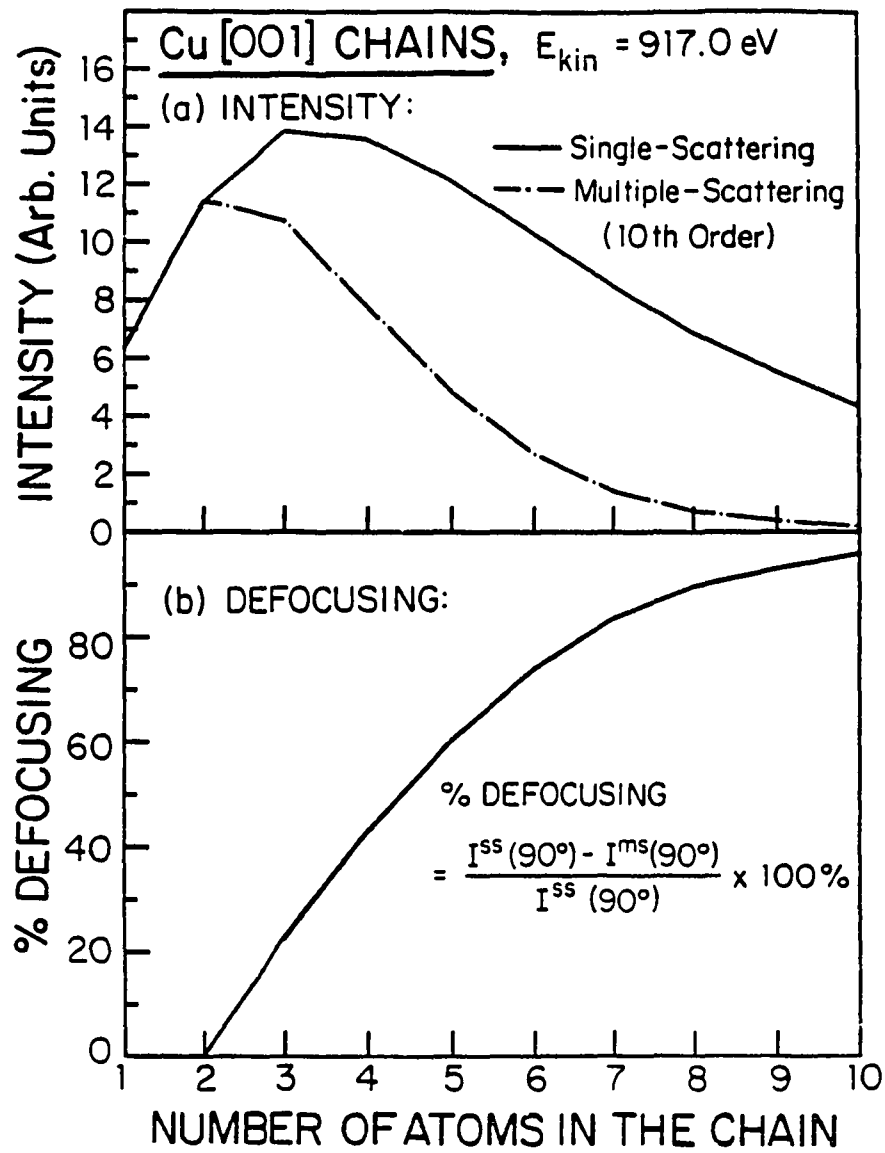

Figure 3.16. Same as Figure 3.8, but for Cu [001] chains.

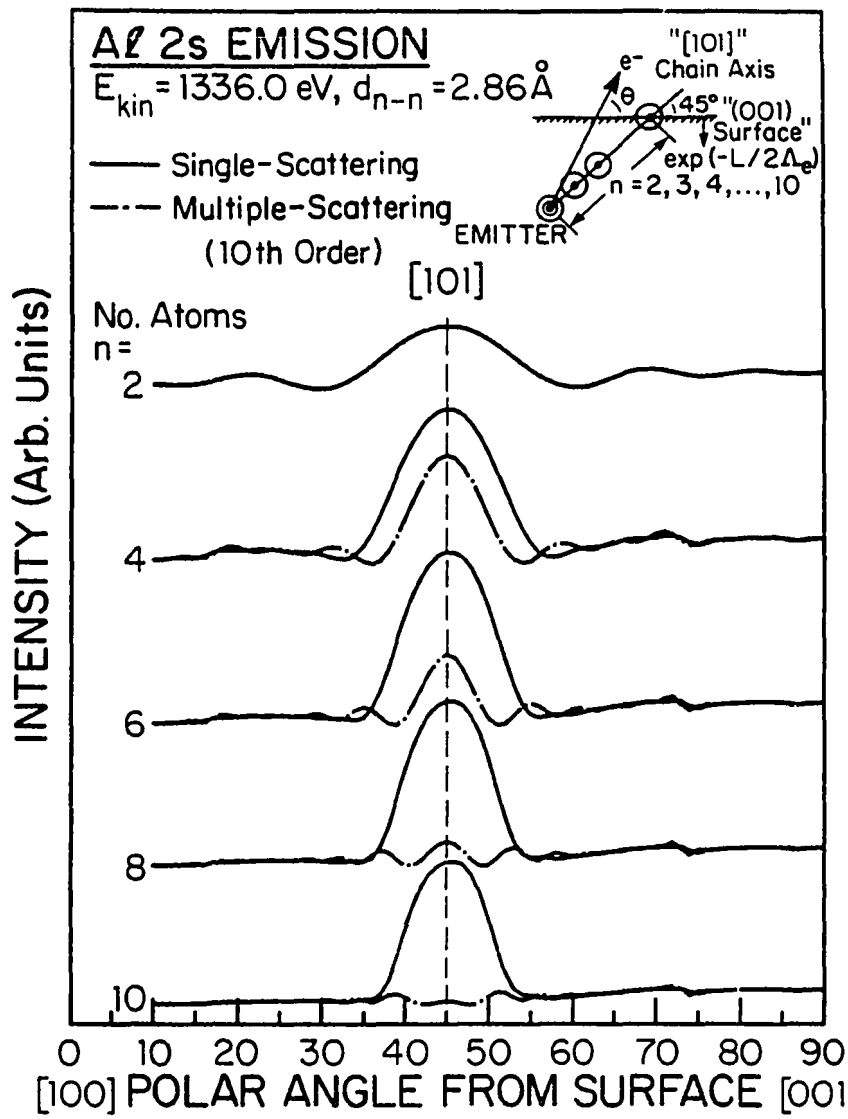

Figure 3.17. Single and multiple scattering calculations of Al 2s photoelectron diffraction from a linear Al [101] chain at 1336.0 eV. The emitter is at one end of the chain, as shown in the inset.

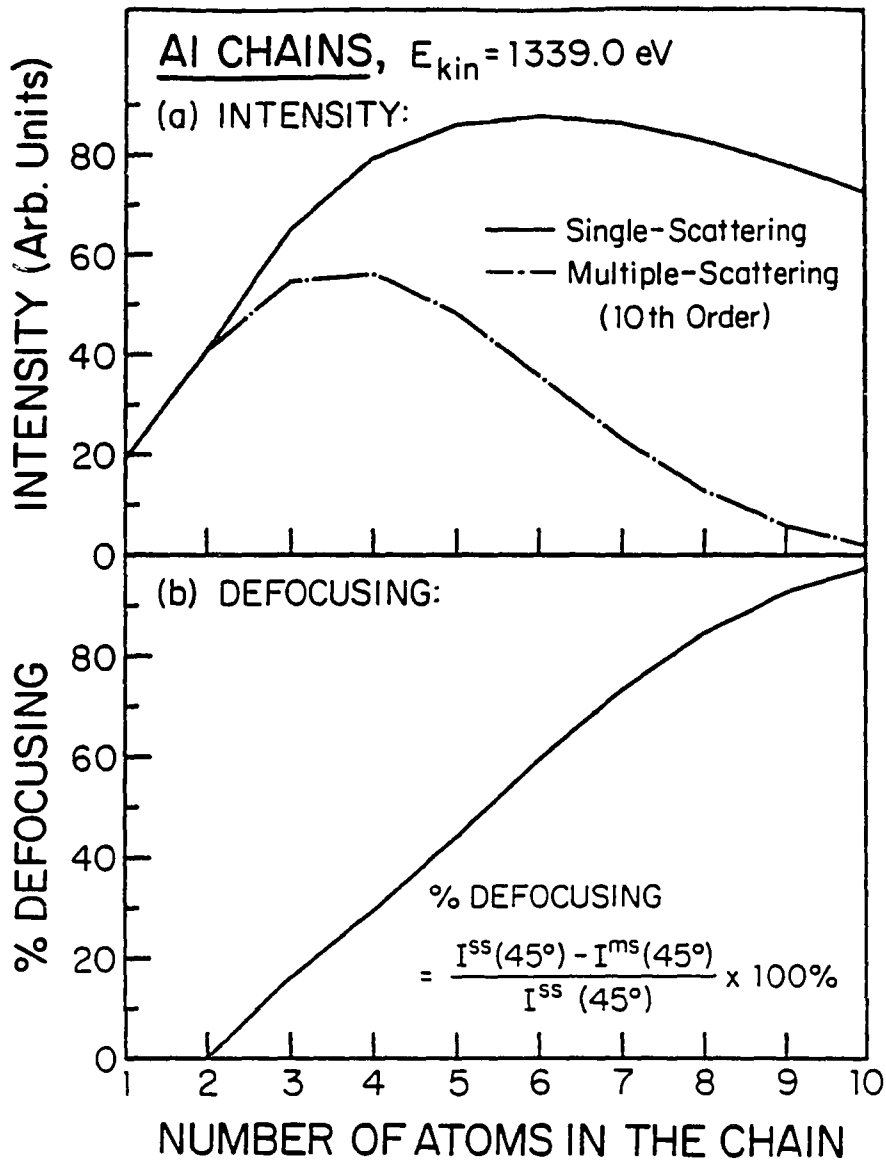

Figure 3.18.(a) Al 2s photoelectron diffraction intensity at 1336.0 eV directly along linear Al [101] chains as a function of number of atoms in the chain. (b) The % defocussing in 2s photoelectron diffraction intensity, based upon the results in (a).

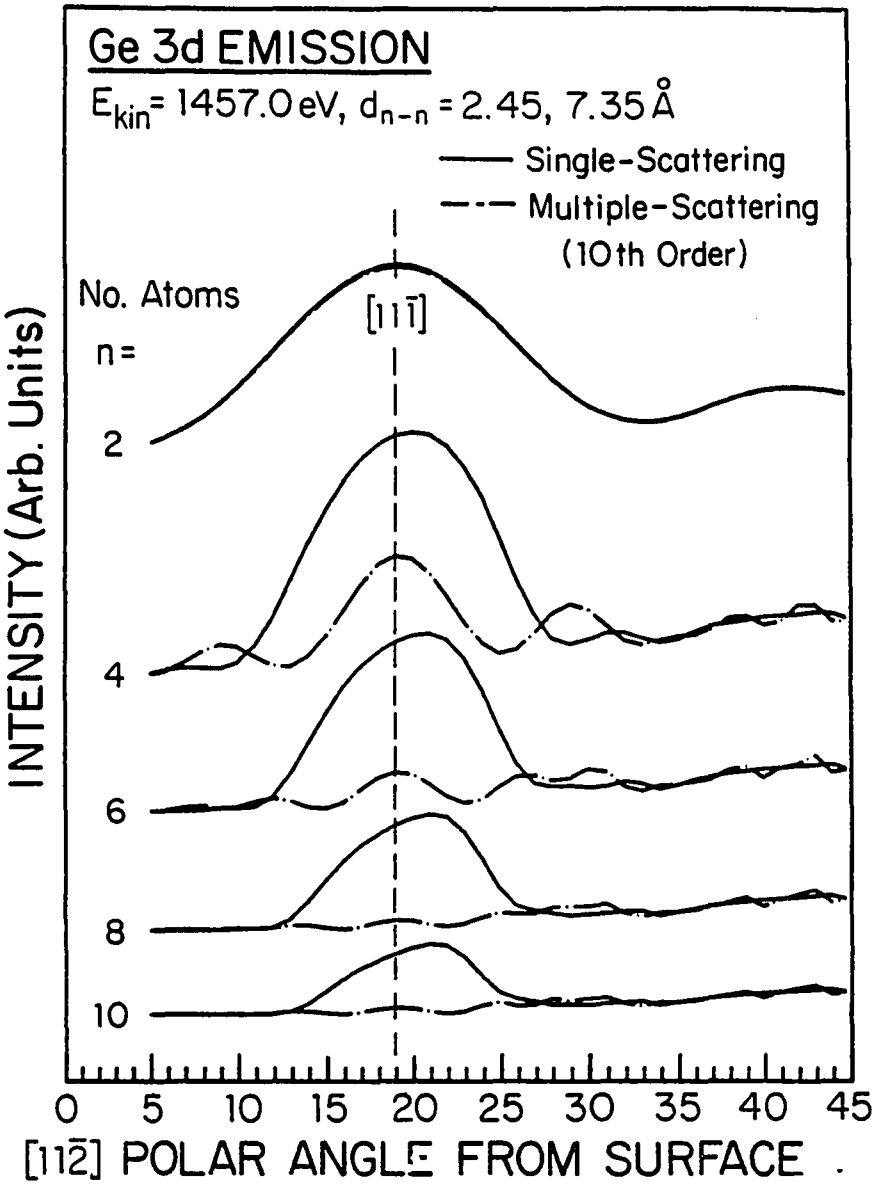

Figure 3.19. Single and multiple scattering calculations of Ge 3d photoelectron diffraction at 1457.0 eV from linear Ge [11$\bar{1}$] chains. The emitter is at one end of the chain.

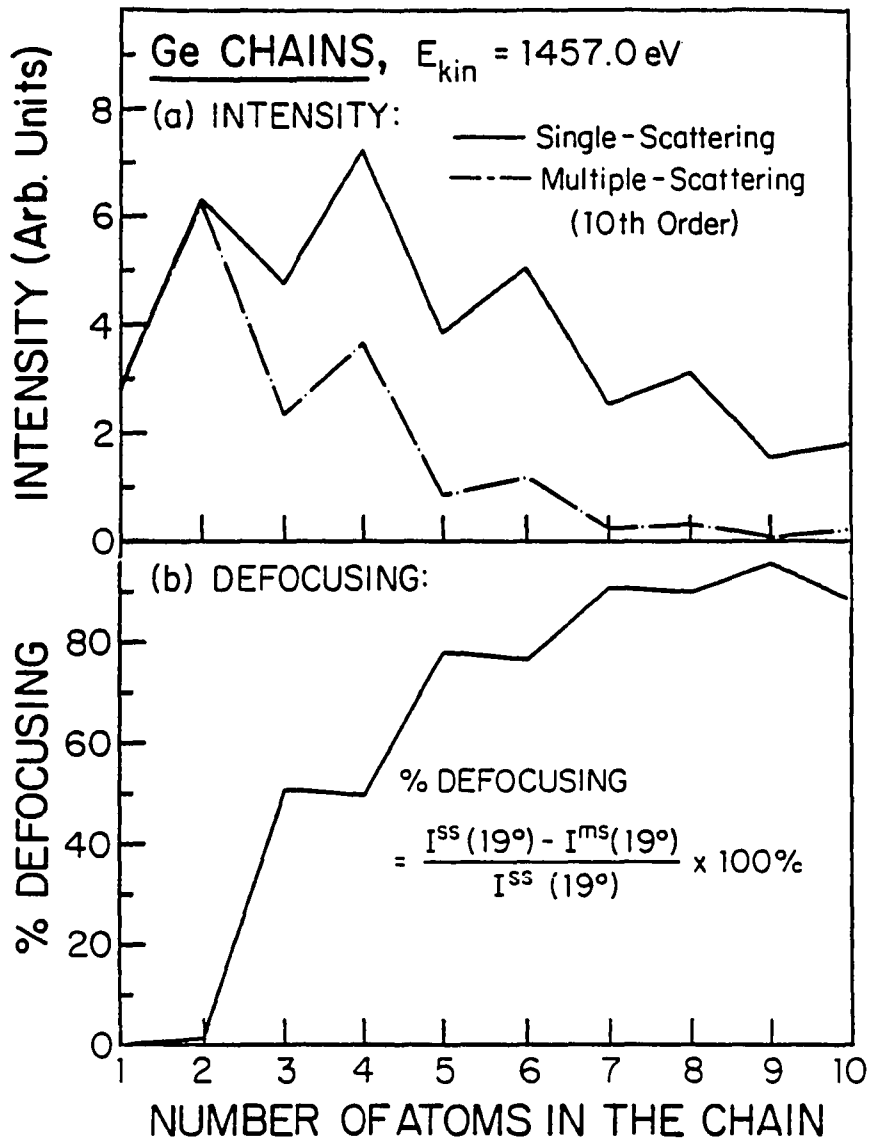

Figure 3.20.(a) Ge 3d photoelectron diffraction intensity from linear Ge [11$\bar{1}$] chains at 1457.0 eV as a function of the number of atoms in the chain. (b) The % defocussing in 3d photoelectron diffraction intensity based upon the results of (a).

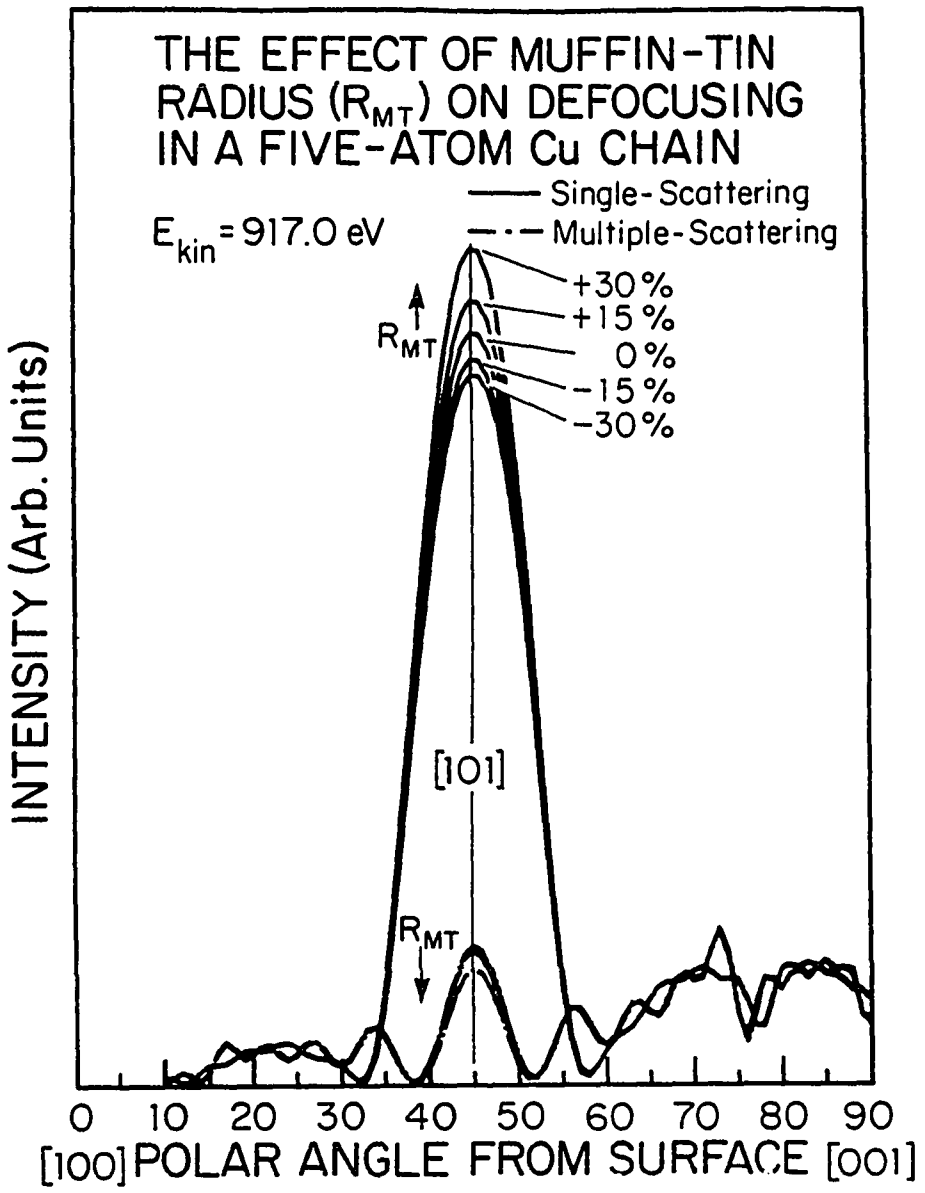

Figure 3.21. The effect of changing muffin-tin radius (R_{MT}) on defocussing in a five atom Cu [101] chain at 917.0 eV. The multiple scattering curves all cluster very close together at the bottom of the figure.

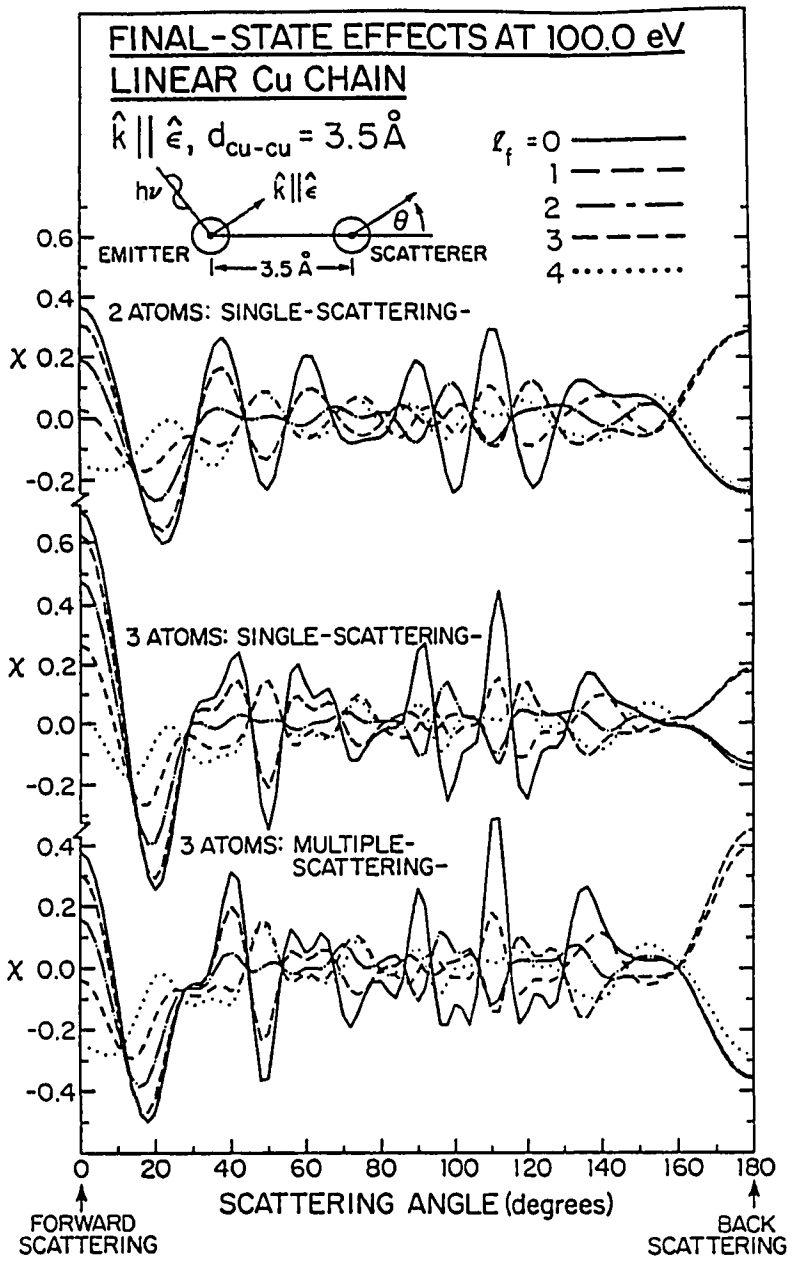

Figure 3.22. Effects of final state angular momenta ℓ_f on photoelectron diffraction from two- and three-atom Cu chains with an interatomic spacing of 3.5 Å and a kinetic energy of 100.0 eV. Single and multiple scattering calculations are shown for ℓ_f = 0,1,2,3, and 4. For 2 atoms, the single and multiple scattering results are essentially identical. For three atoms, we show both sets of curves.

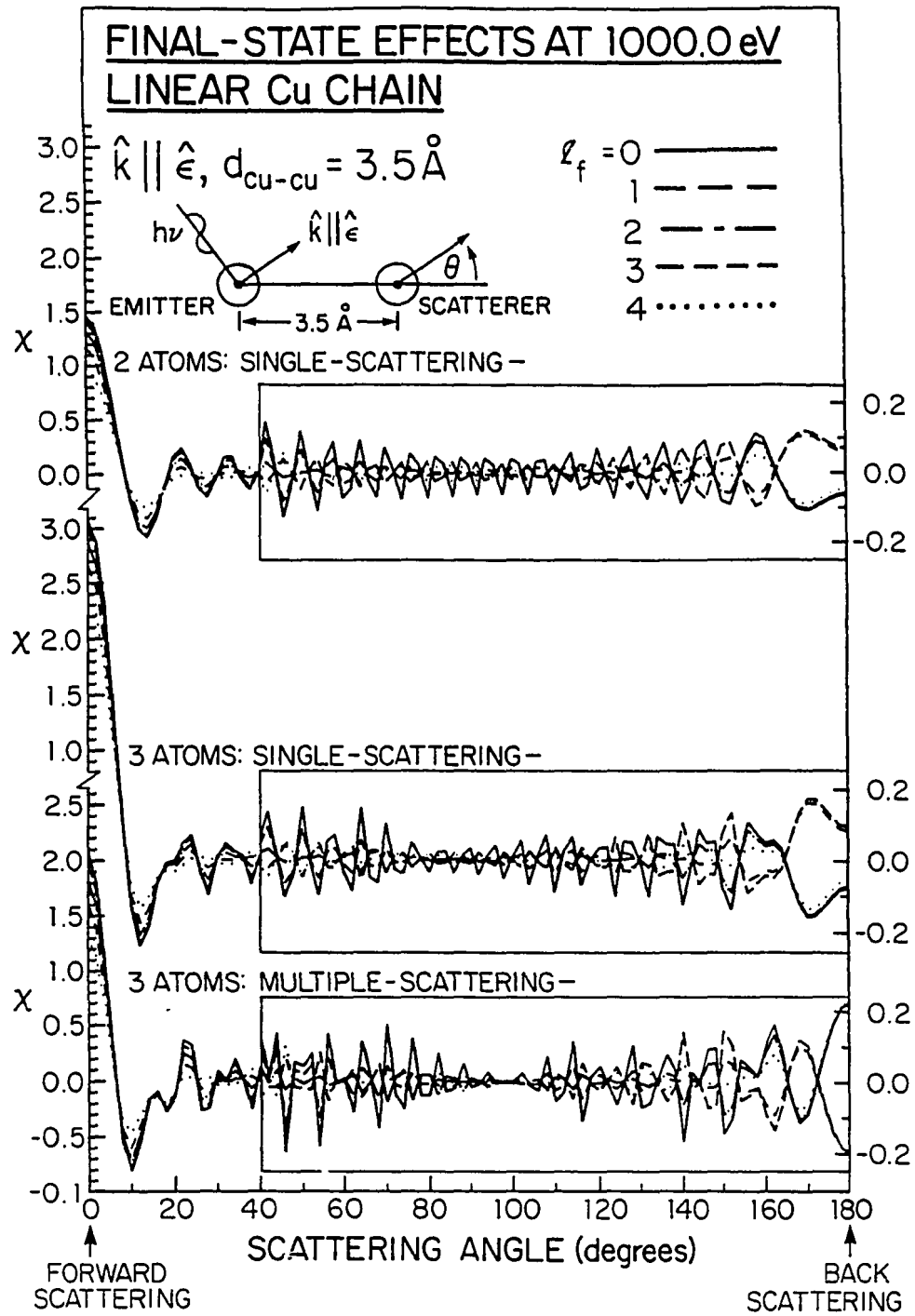

Figure 3.23. Same as Figure 3.22, but at 1000.0 eV.

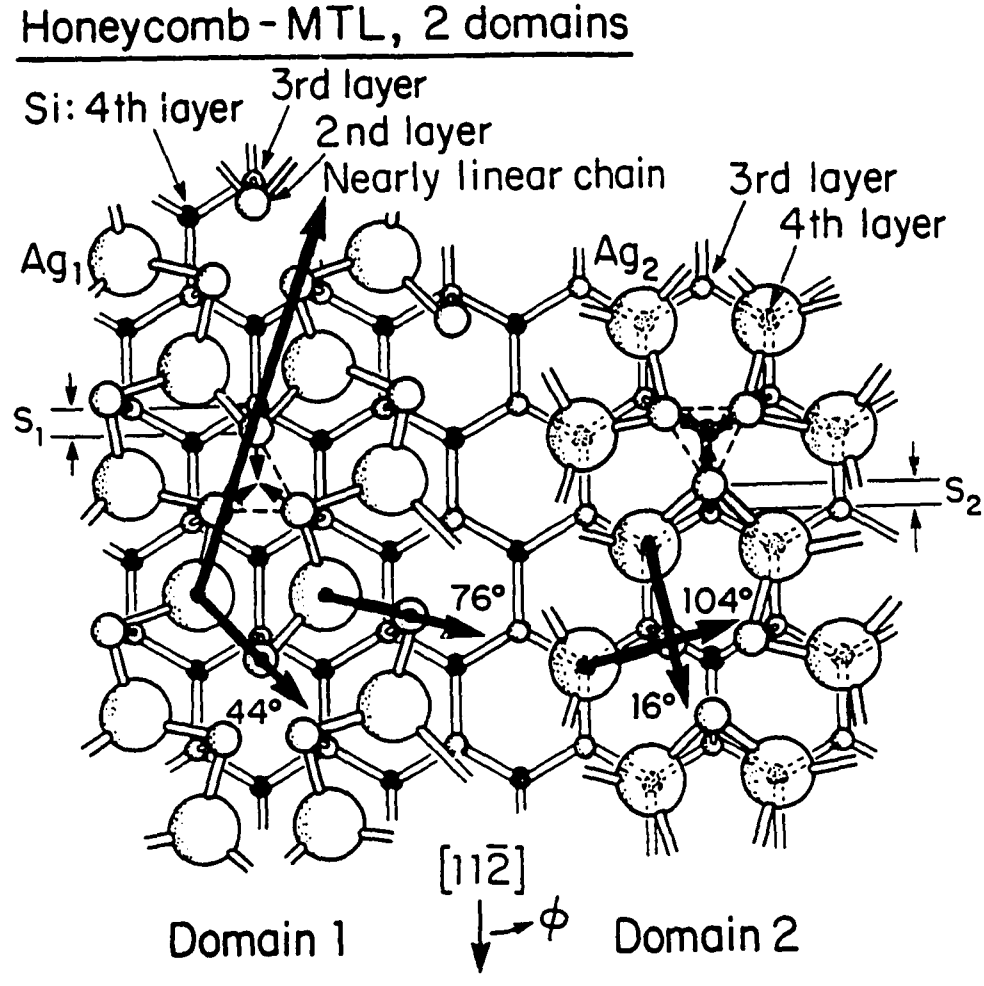

Figure 3.24. The 2-domain Ag-honeycomb missing top layer model proposed in Reference 30 for the ($\sqrt{3}\times\sqrt{3}$)R30° Ag on Si(111). The four short arrows indicate the strong nearest-neighbor forward scattering peaks expected in this model. A typical nearly linear Ag-Si-Si-Si chain along which enhanced MS effects might occur is shown by the long arrow in domain 1.

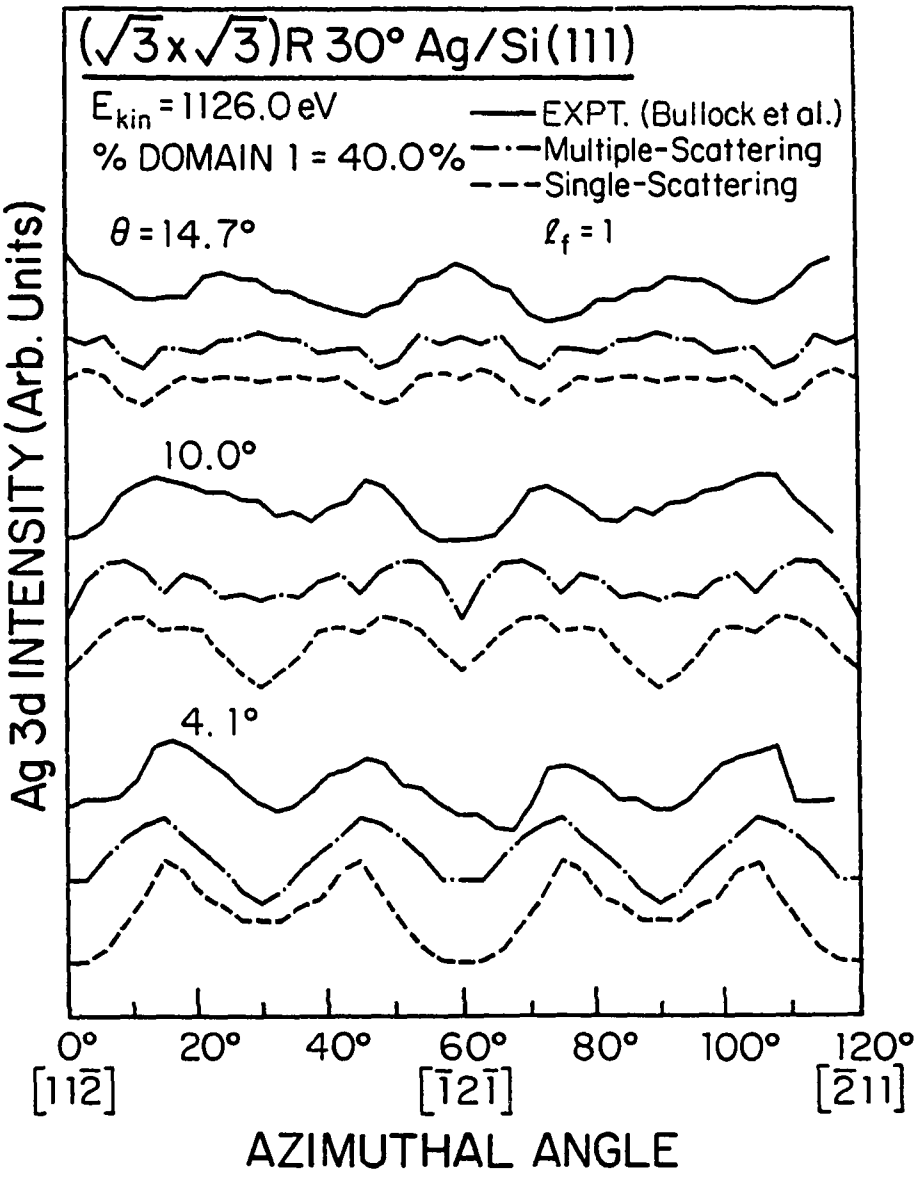

Figure 3.25. Comparison of experimental Ag 3d azimuthal x-ray photoelectron diffraction data and single and multiple scattering theoretical curves for this system with an assumed domain mix of Domain 1:Domain 2 = 40:60. Simulations are for an s → p transition.

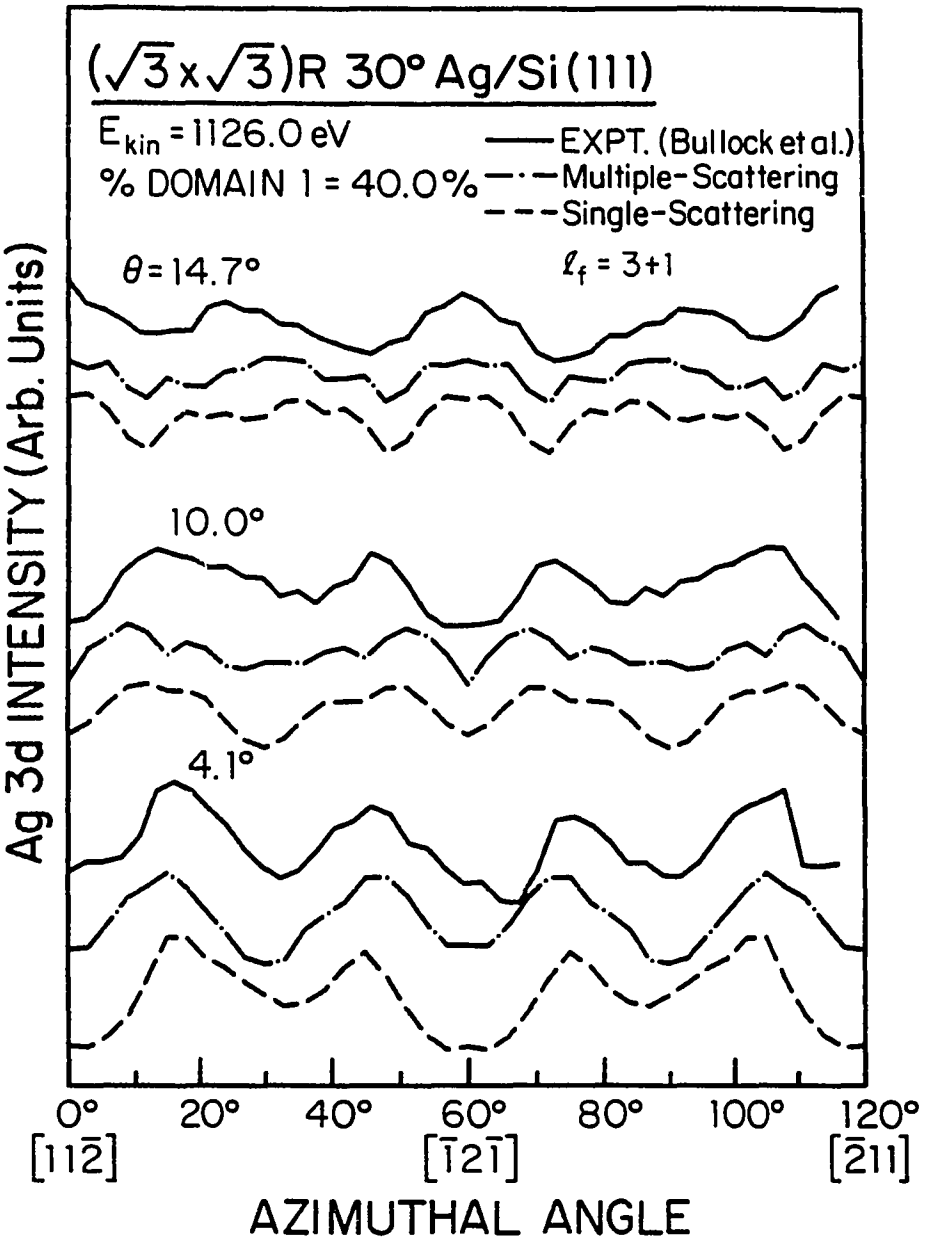

Figure 3.26. Same as 25, but for the correct d → f + p transitions.

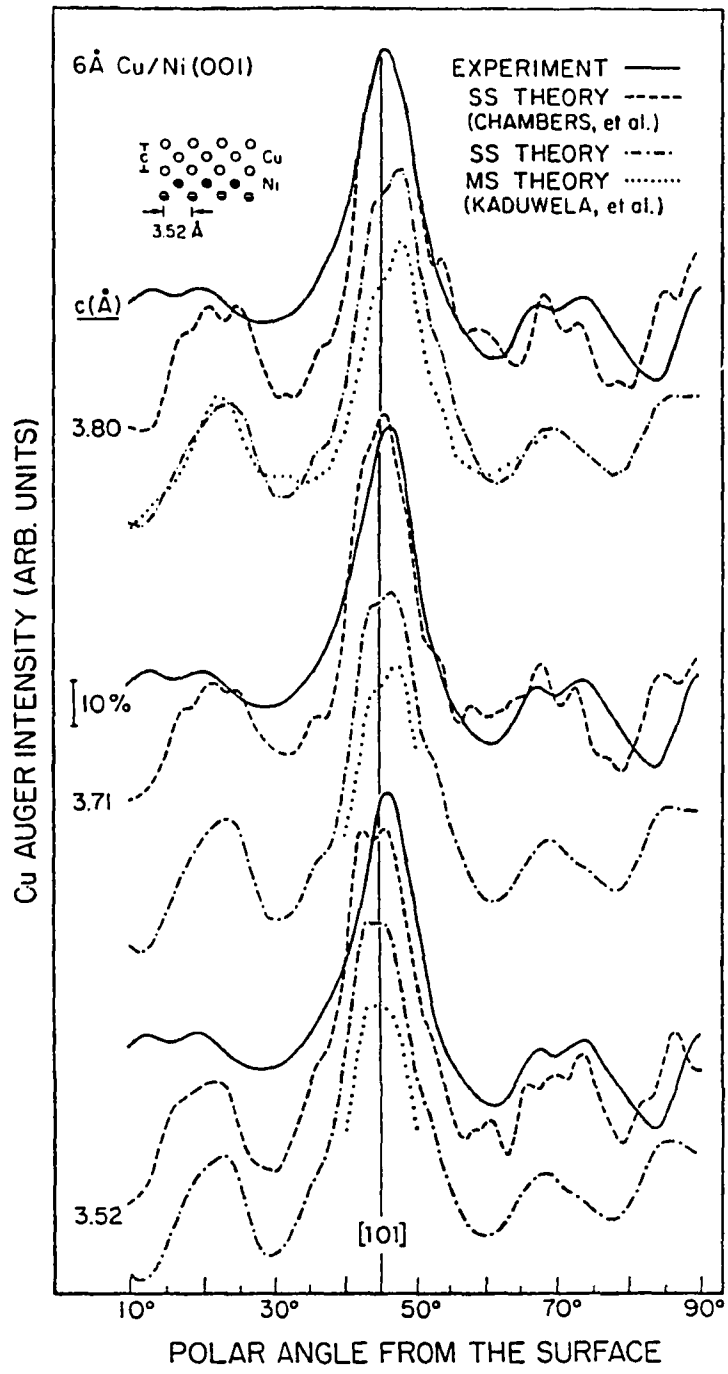

Figure 3.27. Polar-angle dependence of Cu LMM Auger emission at 917.0 eV from 3 ML of pseudomorphic Cu grown on Ni(001). Experimental data and SS calculations with PW scattering are from Reference 32. Also shown are SSC-SW and MSC-SW calculations from this work.

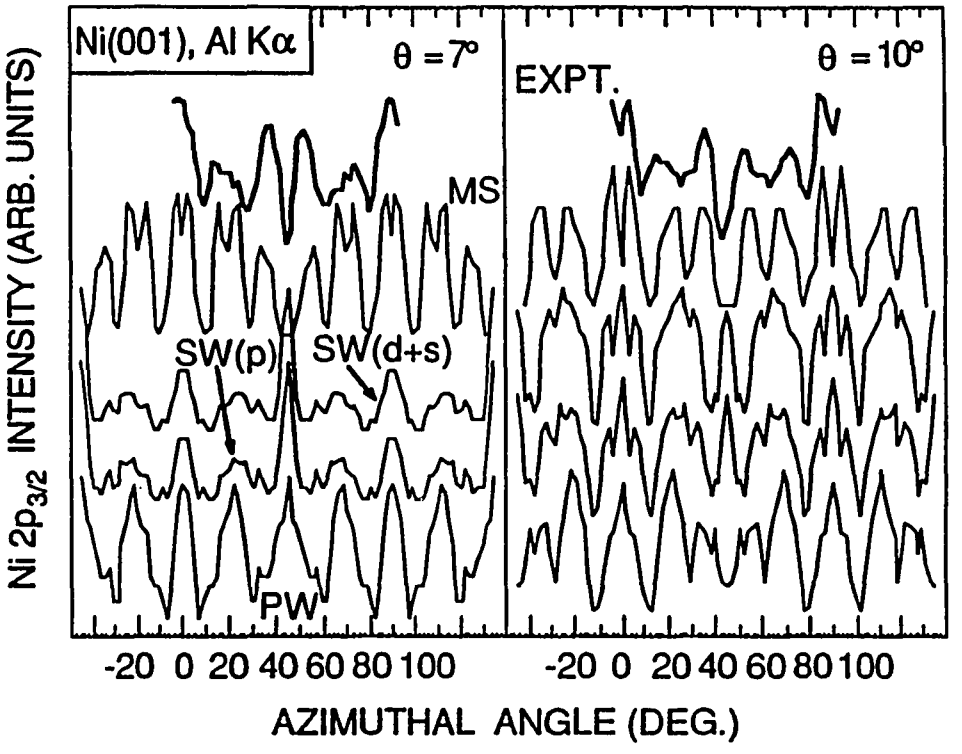

Figure 3.28. Ni $2p_{3/2}$ azimuthal x-ray photoelectron diffraction data obtained at high angular resolution from a Ni(001) substrate at 629 eV are compared to theoretical calculations at several levels of approximation: SSC-PW (s → p), SSC-SW (s → p), SSC-SW (p → d+s), and MSC-SW (s → p). (a) results for takeoff angles of 7.0° and 10.0°.

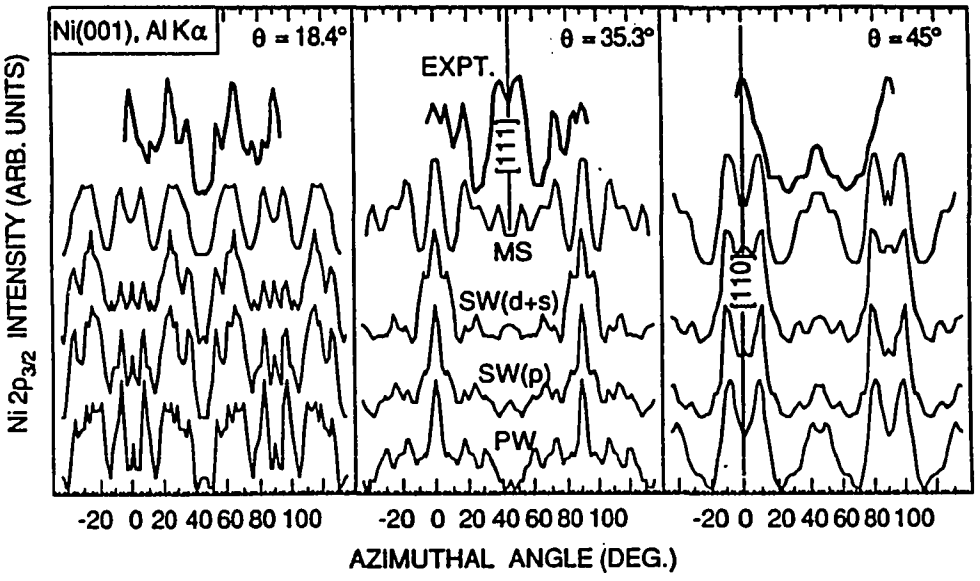

Figure 3.28.(b) Same as in (a), but results for takeoff angles of 18.4°. 35.3° (passing through [111]) ,and 45.0° (passing through [101]). (See also Reference 31(c).)

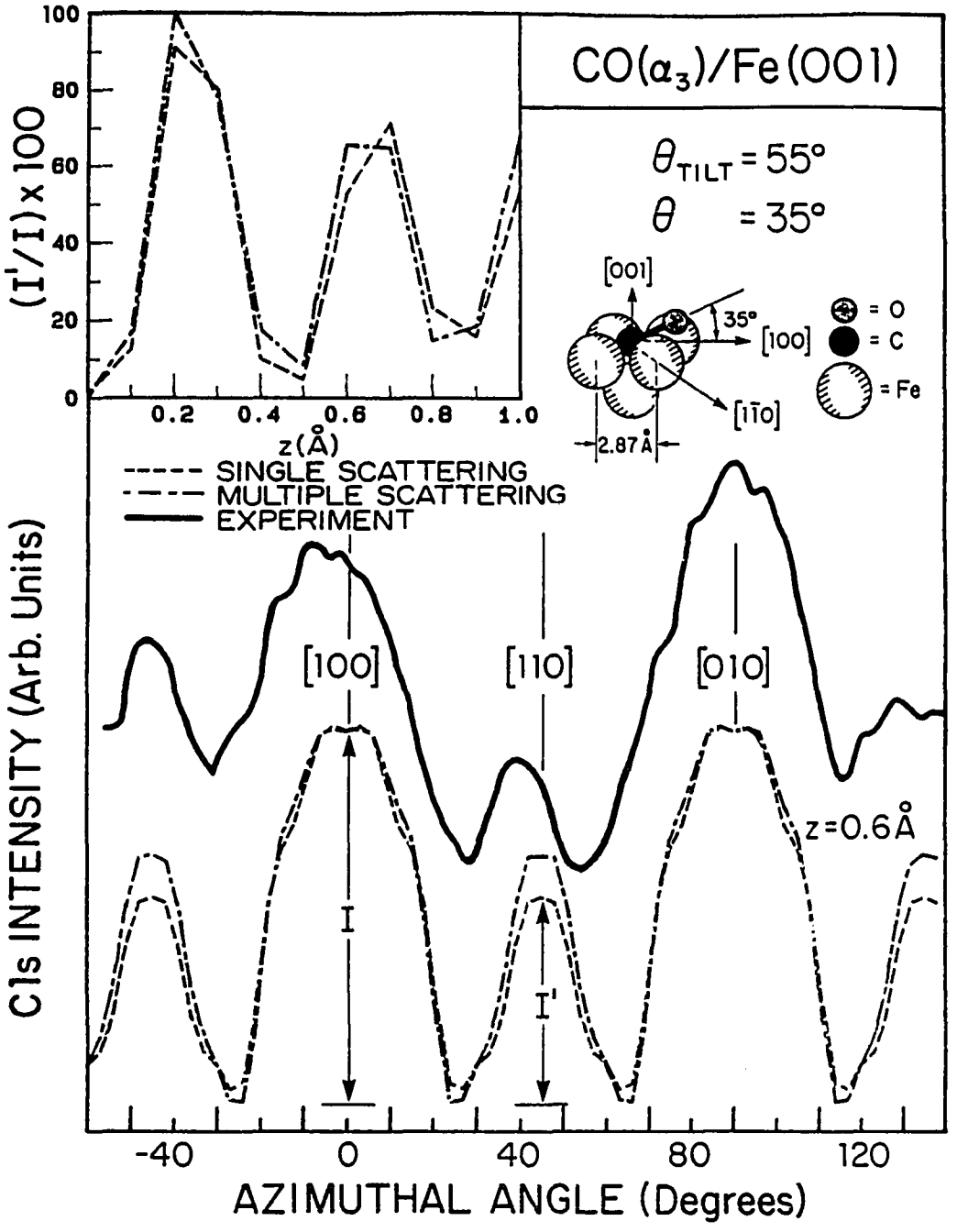

Figure 3.29. Azimuthal dependence of the C 1s photoelectron intensity from the α_3 state of CO on Fe(001). The ratio of the intensities I' and I is also shown in the inset as a function of the distance z of the C atom above the first Fe layer. The geometry of the cluster used in the calculation is also shown.

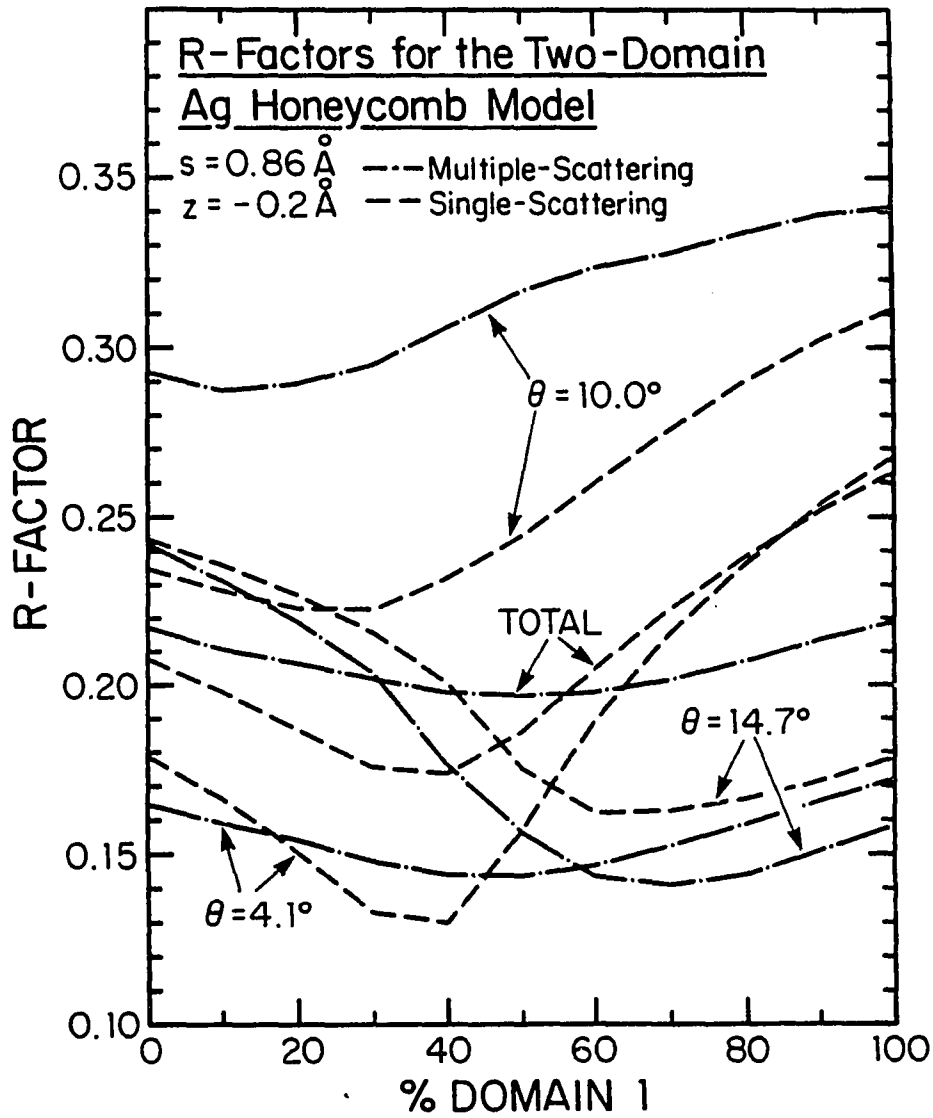

Figure 3.30. SS and MS R-factors for Ag $3d_{5/2}$ x-ray photoelectron diffraction from ($\sqrt{3}\times\sqrt{3}$)R30° Ag on Si(111) as a function of the percentage of domain 1.